INDIRECT REACTION METHODS FOR NUCLEAR ASTROPHYSICS: EXPLORING CHARGE-EXCHANGE AND TRANSFER REACTION MODELS

By

Terri Elizabeth Poxon-Pearson

A DISSERTATION

Submitted to
Michigan State University
in partial fulfillment of the requirements
for the degree of

Physics — Doctor of Philosophy

2020

ABSTRACT

INDIRECT REACTION METHODS FOR NUCLEAR ASTROPHYSICS: EXPLORING CHARGE-EXCHANGE AND TRANSFER REACTION MODELS

By

Terri Elizabeth Poxon-Pearson

Indirect reaction methods play an important role in probing many astrophysical nucleosynthetic processes in cases where a direct measurement in the laboratory is technically challenging or not possible. However, the resulting astrophysical data is only as good as the quality of the reaction theories used to extract it from experimental measurements. In this thesis we explore two indirect reaction methods, transfer and charge-exchange reactions, with an emphasis on the reaction theory models used to interpret the measurement.

Deuteron induced transfer reactions are a useful tool for probing single particle capture reactions. We discuss a methodology that has been developed to extract spectroscopic factors from transfer to low lying resonances. Spectroscopic factors are used to experimentally constrain the astrophysical reaction rate of interest via the resonance strength. Here, we present results of three transfer reaction studies: ^{30}P(d,n) to extract the ^{30}P(p,γ) reaction in classical novae, ^{23}Al(d,n) to extract the ^{23}Al(p,γ) reaction in type-I x-ray bursts, and ^{56}Ni(d,n) to extract the ^{56}Ni(p,γ) reaction, also important in x-ray bursts. In all of these cases, the transfer data was able to reduce the uncertainty in the astrophysical reaction rate and this marks the first experimental constraints on the ^{30}P(p,γ) reaction rate.

Charge-exchange reactions have diverse applications to astrophysical processes, ranging from constraining electron capture rates in core collapse supernovae, to probing the nuclear symmetry energy, important to understanding neutron stars and their mergers. However, the reactions models which describe charge-exchange reactions remain relatively underdeveloped

compared to those used to describe other reactions. In this thesis we present an initial study exploring several aspects of charge-exchange reaction models.

We conduct a systematic study of charge-exchange transitions to 0^+ isobaric analog states over a range of targets and beam energies using the distorted wave Born approximation. We use a two-body framework, which is characterized by a nucleon-target Lane potential, and a three-body framework, which uses an NN interaction to describe charge-exchange between a scattering nucleon and a valence nucleon bound to an inert core. We explore the impact of different interactions, varying both the potential which mediates the charge-exchange and the interaction which describes the incoming and outgoing distorted waves.

We find that the two-body formalism was better able to describe both the shape and magnitude of charge-exchange data, capturing 31% of the data within the error band created by normalized calculations using two different optical potentials. This is opposed to describing less that 15% of the data in the three-body model. Although there was a 50% difference, on average, between the charge-exchange cross sections produced using Koning-Delaroche [1] and Chapel-Hill [2] parameter sets, neither parameter set is preferred by the data.

The shape of the angular distributions produced by the three-body framework differ significantly from their two-body counterparts and from experimental data. We determined that this difference arises from a selection of different partial waves between the formalisms. The Lane interaction in the two-body framework selects lower partial waves, indicating a more central interaction, while the Gogny and AV8' interactions select higher partial waves, resulting in a reaction located near the surface of the target where the active nucleons are in close proximity. Overall, the charge-exchange cross section is very sensitive to the choice of interaction, indicating that charge-exchange could be a useful tool to further constrain nuclear interactions.

ACKNOWLEDGMENTS

First I want to thank my advisor, Filomena Nunes, for all of her support and guidance over the past six years. While I have at times questioned my abilities and my goals, I have never questioned my choice of advisor. Filomena has helped me grow professionally, listening intently as I discerned my career goals, and connecting me with people and opportunities that support that growth. She has helped me foster resilience and grit, lending me confidence and reassurance when I was in doubt. At the same time, Filomena has supported me as a whole person, encouraging my involvement in science outreach and WaMPS and affording me the flexibility to nurture a long distance relationship and marriage. Thank you.

I want to thank my parents, without whom, I would not have been possible. Their support throughout my life was been unwavering, regardless of what endeavor I was pursing, because they have never really cared what I chose to do as long as I was happy and healthy. I am grateful to have been unburdened by their expectations and uplifted by their pride in my accomplishments. Of course, I need to thank my husband, Michael Swift, who has been my loudest cheerleader and strongest support since I began this process. Thank you for calming me down when I was overwhelmed, celebrating every small victory and milestone, moving from sunny California to less sunny Michigan while I finished my degree, and, most of all, for loving me.

I am grateful for the support offered by the NSCL, from the camaraderie of lab graduate students, all the way up to the highest levels of leadership which has intentionally supported graduate student initiatives, such as WaMPS, both with their words and financially. I am grateful for the opportunity to work as a lab tour guide and for Zach Constan's support of graduate student guides. Showing off this facility and the amazing research performed here

has reinvigorated my passion for my work on more than one occasion.

I would like to thank my guidance committee members, Remco Zegers, Alex Brown, Pawel Danielewicz, and Laura Chomiuk for their advice and input. In particular, I am grateful for the time Remco has taken to share some of his deep knowledge of charge-exchange reactions, offering particularly helpful guidance, and for Pawel whose help was indispensable in getting my reaction code running. I am grateful for the insights gleaned from conversations with several colleagues, particularly Bob Wiringa. Finally, I am grateful for the support of Jolie Cizewski who is a fierce advocate for young scientists and has been a great support in moving into the next stage of my career.

While graduate school was not always easy for me, I never lacked good friends and a strong support system of fellow graduate students. Specifically, I want to thank Brandon Elman (and honorary graduate student, Alice Mills), Chris Izzo, Andrew LaJoie, Dennis Foren, Justin Lietz, Rachel Sandler, Amy Lovell, and Christa Haverly for their friendship and support. I am grateful for every meal, drink, game, and conversation we shared.

I wanted to thank the members of the few-body reactions group, past and present, for all of their feedback on practice talks, company during travel, and opportunities to pass on some of my knowledge: Amy Lovell, Gregory Potel, Weichuan Li, Linda H'lophe, Luke Titus, Alaina Ross, Nick Cariello, Manuel Catacora-Rios, Jimmy Rotureau, Garrett King, Paul Wright, and Simon Sundberg.

Finally, this work would not have been possible without the funding sources that have supported my research, including the National Science Foundation, the National Nuclear Security Administration Stewardship Science Academic Alliance program through the Department of Energy, Michigan State University, and the National Superconducting Cyclotron Laboratory.

TABLE OF CONTENTS

LIST OF TABLES

LIST OF FIGURES

Chapter 1

Introduction

1.1 Indirect Reactions for Nuclear Astrophysics

Nuclear astrophysics is a unique field which links the fundamental interactions of protons and neutrons across length and energy scales with the evolution of elements in stars throughout the universe. Although the field has been very successful in creating a general picture of how heavy elements have built up since the time of the big bang, there remain many open lines of investigation, including understanding the complex dynamics of supernovae, verifying astrophysical sites for different nucleosynthetic processes, and gaining an understanding of the most exotic nuclear matter through the study of neutron stars and their mergers. Exploring all of these research areas requires large amounts of nuclear physics data, from reaction rates to masses, and requires extensive reaction networks, models, and simulations to link astrophysical observations with underlying physics.

This process is further complicated by the fact that many nucleosynthetic processes of interest involve incredibly short lived nuclei and reactions at sub-Coulomb energies, making them difficult, or even impossible, to recreate in the lab. Without the ability to directly measure these nuclear properties, the field must rely on indirect reaction methods which measure a different, more accessible, reaction process that can probe some aspect of the reaction of astrophysical interest. Indirect reaction methods require reaction and structure

theory to link measured quantities to the reaction rates required for astrophysical calculations and simulations. Because of this, the extracted value of astrophysical interest is only as good as the theory tools used to link it to the experimentally measured observable. In this thesis we will discuss how charge-exchange has been used as an indirect probe for electron capture and the nuclear equation of state, and how transfer reactions can be used to probe proton capture reactions. In both cases, we will be focusing on the reaction theory used to describe these processes.

1.2 Transfer Reactions as a Probe of Astrophysical Proton Capture

Single-particle capture reactions are ubiquitous in a wide range of astrophysical environments. Many of these processes are illustrated in Figure 1.1. Along the proton dripline, nucleosynthesis of light to medium mass nuclei can proceed through the rapid proton capture process (rp-process) in environments such as Oxygen Neon (ONe) novae explosions [22] and x-ray bursters [23]. In these hydrogen rich environments, the reaction network consists of proton captures followed by β^+ decays back towards stability.

On the neutron rich side of the chart of the nuclei, the slow neutron capture process (s-process) builds up elements heavier than lead in Asymptotic Giant Branch (AGB) and red giant stars through a chain of neutron captures, followed by beta decay back towards stability [24]. In these environments, the neutron density is low enough that beta decay rates can compete with the neutron capture rate, creating a reaction chain that clings closely to the valley of stability and stalls out with the production of lead and bismuth.

The recent observation of a neutron-star merger by LIGO and subsequent multi-messenger

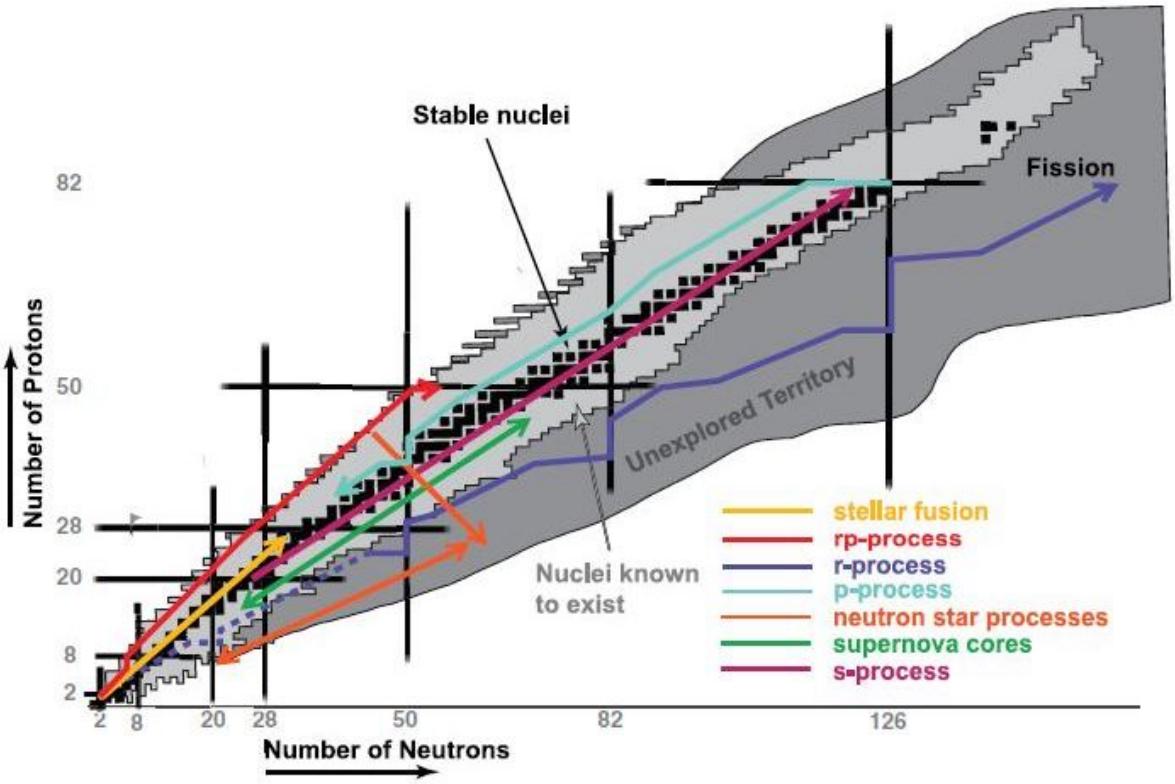

Figure 1.1: The chart of the nuclides with various nucleosynthetic processes shown schematically. The rp-process is shown in red along the proton dripline, the s-process is shown in pink close to the valley of stability, and the r-process is shown in purple, reaching out towards the neutron drip line. Figure from [8].

observations of the remnant kilonova have confirmed neutrons stars as a site of the rapid neutron capture process (r-process) [25]. In this scenario, there is a very high density of excess neutrons, allowing for many subsequent neutron captures, resulting in highly exotic nuclei which eventually beta decay back towards stability, forming the heaviest elements.

These astrophysical capture processes involve thousands of reaction and decay rates, many of which are essential to understanding the observed isotopic abundances. However, in all but a few cases, direct measurement in the laboratory is impossible. Astrophysical proton capture reactions proceed below the Coulomb barrier, leading to plummeting cross sections. As an additional complication, many of these captures are on unstable nuclei, limiting the

experiments to relatively low beam rates accessible through current rare isotope beams. The situation is even more dire when studying neutron capture onto rare r-process isotopes. In this scenario, both the target isotope and the neutron are unstable, meaning that neither can be made into a target for an experiment. Instead, these processes must be explored through an indirect probe and, in both of these cases, (p,γ) and (n,γ), transfer reactions provide a helpful tool.

A(d,p)B and C(d,n)D transfer reactions have the same initial and final state as their corresponding A(n,γ)B and C(p,γ)D astrophysical reactions, but are experimentally much more feasible. For reactions involving an unstable target, the experiment runs in inverse kinematics, with a deuterated target and a rare isotope beam. Unlike direct proton capture experiments, these experiments can run well above the Coulomb barrier ($>$ 30 MeV/u) and still occupy the low lying final state resonances relevant to nuclear astrophysics. Once transfer to these final states is measured, a variety of theoretical techniques can be used to connect the transfer data to the astrophysical capture process of interest, including extraction of the asymptotic normalization coefficient (ANC) or spectroscopic factor (S), which will be discussed in greater detail throughout this work.

1.3 Charge-Exchange Reactions as an Astrophysical Probe

Charge-exchange reactions are isobaric transitions where a neutron in the target is exchanged with a proton in the projectile, or vice-versa. These reactions can be performed using single-nucleon probes, such as (n,p) or (p,n) reactions but, experimentally, it is often advantageous to use composite probes such as (t,^{3}He) or (d,^{2}He), or even heavy-ion probes such as (^{12}C, ^{12}N) and (^{7}Li, ^{7}Be). These reactions are mediated by the strong nuclear force via meson-

exchange but populate the same initial and final states as processes mediated by the weak force and, therefore, can be used as a probe in regions where β decay or beta delayed neutron emission (β-n) data is unavailable or energetically forbidden (see Figure 1.2). In general, charge-exchange reactions provide insight into two aspects of nuclear astrophysics: they serve as an indirect probe for stellar electron-capture processes and as a tool for exploring bulk properties of nuclear matter, such as the nuclear equation of state, which is central to understanding neutron stars and their mergers. First, we will introduce charge-exchange in the context of electron-capture.

1.3.1 Electron Capture in Supernovae

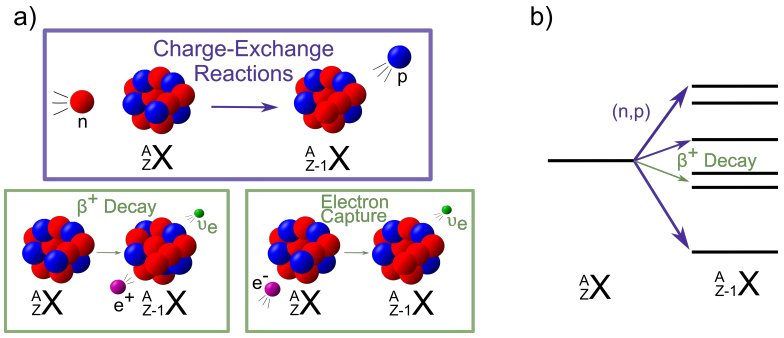

Figure 1.2: a) (n,p) charge-exchange reactions populate the same initial and final states as electron-capture and β^+ decay, although charge-exchange proceeds through the strong nuclear force and electron-capture and β decay are mediated by the weak force. b) Charge-exchange is a versatile probe of B(GT) because it is able to populated final states in the Z-1 isobar up to high excitation energies, while β^+ decay is limited to final states in the Z-1 daughter with excitation energies smaller than the β^+ Q-value. Figure is from [9]

Supernovae are an important site for nucleosynthesis and produce significant amounts of elements heavier than Iron. In both core-collapse and type Ia supernovae, electron-capture reactions on nuclei in the pf shell (Z $\sim$ 21-40), neutronize the nuclear material, affecting the dynamics of the nuclear explosion [26]. Understanding these electron-capture reactions are a key component for interpreting the observed isotopic abundances produced in these

stellar explosions. In most cases, relevant electron-capture rates cannot be measured directly, but can be estimated with knowledge of the Gamow-Teller transition strengths in the β^+ direction. Gamow-Teller transitions are mediated by the $\boldsymbol{\sigma\tau}$ operator and change the total spin (S) and isospin (T) of the nucleus, but not the orbital angular momentum (L) (ΔL=0, ΔS=1, ΔT=1). Charge-exchange reactions have become an important tool to probe Gamow-Teller transition strengths (B(GT)) because they can be used to excite transitions that are energetically blocked to β decay (see Figure 1.2).

Extracting B(GT) from charge-exchange reaction cross sections relies upon an approximate proportionality relation between these two quantities, first established by [27] and expressed as

$$\left[\frac{d\sigma}{d\Omega}(q=0)\right]_{ST} = \hat{\sigma} B(ST) \tag{1.1}$$

where $\frac{d\sigma}{d\Omega}$ is the charge-exchange cross section, ST specifies the transition of interest (Gamow-Teller, Fermi, etc), and q is the momentum transfer. A key ingredient is the unit cross section ($\hat{\sigma}$) which can be determined by direct comparison to β decay data, when available, or by extraction from a well defined correlation between mass number and unit cross section (e.g. [28, 29, 30]). This proportionality in Eq. 1.1 is only valid at energies where a single-step process can be assumed. These studies are commonly performed at $\sim$ 100 MeV/u, where the single-step approximation is warranted, although its region of validity could extend down to $\sim$ 50 MeV. At lower energies, multistep reactions become increasingly important. It has also been extended to, and experimentally verified for, a wide range of charge-exchange probes including (p,n) [28], (n,p) [31], (d,^{2}He) [32, 33], (t,^{3}He)/(^{3}He,t) [34, 30], and (^{7}Li,^{7}Be) [35, 36].

Undoubtedly, there has been great success using charge-exchange reactions to constrain astrophysical models. Although core-collapse supernovae models incorporate a large network of electron-capture reactions, sensitivity studies such as [37] guide experimental efforts by determining which reactions have the greatest impact on observables such as peak neutrino luminosity. The study in Sullivan et al. [37] highlighted the "high-sensitivity region" near the N=50 shell gap closure. Guided by this and other sensitivity studies [38, 39], B(GT) was extracted from the ^{86}Kr(t,^{3}He)^{86}Br charge-exchange reaction and introduced in the calculation of stellar electron-capture rates [40]. The extracted electron-capture rates were significantly smaller than those often derived from a simple single-state approximation often used in regions without experimental results or high quality structure inputs. When input into core-collapse supernovae simulations, this difference leads to a reduction in the deleptonization in the core-collapse, which has effects on observables such as peak neutrino luminosity and the frequency of gravitational waves emitted from the collapsing star [41]. Both of these are potentially important signals for understanding core-collapse supernovae as we move into the multimessanger era of astronomy.

In this work, we are only considering transitions between 0^+ isobaric analog states and, therefore, do not explore these Gamow-Teller transitions. Still, Fermi transitions can be important for electron capture in supernovae. High stellar temperatures allow for the population of excited states and Fermi transitions from these states become possible [42]. Extraction of electron capture rates are one of the most important applications of charge-exchange calculations and future extension of the framework presented in this thesis should be made to additionally include Gamow-Teller transitions.

1.3.2 Neutron Stars and the Nuclear Equation of State

Charge-exchange reactions are also a versatile tool for exploring several aspects of bulk nuclear matter. These constraints are vital to modeling neutron stars and their mergers, which were recently confirmed as a central site for the production of r-process elements. One way charge-exchange reactions constrain bulk nuclear matter is by placing limits on the nuclear symmetry energy [43]. The symmetry energy encompasses the energy penalty for an imbalance of neutrons and protons within nuclear matter and is directly linked to the nuclear equation of state, a key component for modeling the behavior of neutrons stars. Understanding the evolution of the symmetry energy with changes to the neutron-proton asymmetry is essential for extrapolating from experimental observations of nuclei, with relatively low levels of asymmetry, to the extreme of asymmetric nuclear matter in neutron stars. In uniform nuclear matter, with neutron density ρ_n, proton density ρ_p, and total density $\rho = \rho_n + \rho_p$, the energy per nucleon can be expressed as

$$\frac{E}{A} = \frac{E_0}{A}(\rho) + S(\rho)\Big(\frac{\rho_n - \rho_p}{\rho}\Big)^2. \tag{1.2}$$

E_0 represents the energy of symmetric nuclear matter and $S(\rho)$ is the density dependent symmetry energy. $S(\rho)$ can then be expanded around nuclear saturation density, ρ_0 as

$$S(\rho) = a_a^V + \frac{L}{3}\frac{\rho - \rho_0}{\rho_0} + ... \tag{1.3}$$

where a_a^V is the symmetry energy at normal nuclear density and L is the slope of the symmetry energy. These values directly impact quantities, such as the pressure of nuclear matter, which inform the nuclear equation of state [44].

Knowledge of the neutron skin thickness, defined as the difference between the root mean square radii of proton and neutron distributions inside nuclei, constrains the symmetry energy [45, 46]. Because of this, precise measurements of the neutron skin thickness have become a goal for many types of reaction probes. However, while neutron stars contain a vast imbalance of excess neutrons, ordinary nuclear matter, even the unstable nuclei accessible with rare isotope beams, have relatively small proton-neutron asymmetry. This small asymmetry shrinks the neutron skin thickness, making its precise determination difficult. Charge-exchange reactions allow access points to this difference of proton and neutron densities, referred to as the isovector density.

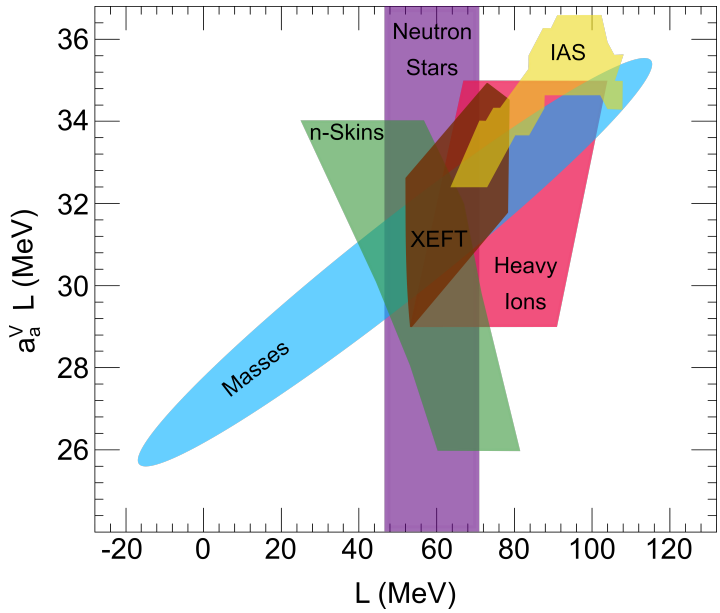

Figure 1.3: Constraints from different theoretical and experimental sources on the symmetry energy at saturation density (a_a^V) and the slope of the symmetry energy at the saturation density (L). The constraints from the isobaric analog state (IAS) study by Danielewicz et al. are shown in yellow [10] and predictions from neutron matter calculations within chiral effective field theory (χEFT) in N^3LO are shown in brown [11]. Constraints from observables include neutron skin (n-skins) thickness [12] shown in green, neutron-star observations [13] shown in purple, nuclear masses [14] shown in blue, and heavy-ion collisions [15] shown in pink. Figure is an adaptation from [10], first presented in [9].

Fermi transitions (ΔL=0, ΔS=0, ΔT=1) between isobaric analog states (IAS) provide a

unique tool for exploring isovector densities. In (p,n)-type reactions, the IAS maintains the same structure as the target nucleus, except replacing one neutron with a proton. Isospin symmetry holds that the excitation energy of the IAS will be approximately equal to the Coulomb energy of the incoming proton. This energy matching means that Fermi transitions to the IAS are often considered to be "elastic" in nature, except that the isospin projection of the projectile is flipped by the isovector term of the interaction potential, transforming a proton to a neutron or vice-versa. There have been several theoretical efforts, informed by measurements of IAS reactions, to explore the isovector properties of nuclei.

These isospin flipping transitions to the IAS can be described using the Lane optical potential [47]

$$U(r) = U_0(r) + \frac{\boldsymbol{\tau}\boldsymbol{T}}{4A}U_1(r), \tag{1.4}$$

where $\boldsymbol{\tau}$ is the isospin operator which acts on the scattering particle and $\boldsymbol{T}$ is the isospin operator which acts on the target nucleus. Additionally,

$$U_1(r) \propto U_n(r) - U_p(r) \tag{1.5}$$

is the isovector term which drives the IAS transition. Phenomenological potentials fit to proton/neutron elastic scattering data on a wide variety of targets and scattering energies are often used for $U_{p/n}(r)$. They take the form of Woods-Saxon potentials with real and imaginary terms, as well as terms to describe absorption at the surface of the target and a spin-orbit interaction. Adjusting the radius and diffuseness of these potentials will affect the shape of both the elastic and charge-exchange reaction cross sections they produce. Recent work by Danielewicz et al. [10] allowed the radius and diffuseness parameters for

a particular parameterization [1] of $U_{p/n}(r)$ to vary in order to simultaneously fit data for proton elastic scattering, neutron elastic scattering, and charge-exchange to the IAS. The modified potential parameters from this procedure are then compared to the values fit only to elastic scattering data. These values were then related to various aspects of the symmetry energy, notably, the symmetry energy at normal nuclear density (a_a^V) and the slope of the symmetry energy as a function of density, evaluated at saturation density (L). Figure 1.3 demonstrates the constraints the work by Danielewicz et al. [10] put on these properties of the symmetry energy (labeled IAS) as well as other theoretical and experimental efforts, including calculations using ab-initio nuclear interactions [11], measurements of nuclear masses [14], heavy-ion collisions [15], neutron skin thicknesses [12], and neutron star observations [13].

Similar theoretical efforts use a more microscopic approach. In this vein, charge-exchange transitions to the IAS are studied within the folding model where effective NN interactions are integrated over the proton and neutron densities of target nuclei. In the case of (^{3}He,t) reactions, this potential is also folded over the projectile nucleus in the so-called double-folding model [48, 49, 50, 51, 52]. These calculations require neutron and proton densities for the target which can be taken from experiment or calculated using a realistic nuclear interaction. The radius parameter of the proton and neutron densities can then be adjusted to best produce IAS charge-exchange data. From these adjusted potentials, a neutron skin thickness can be extracted [51].

In particular, (^{3}He,t) reactions are of interest because some argue that the spatial overlap between the probe and target could create nuclear densities close to or above the nuclear saturation density, allowing a unique probe of nuclear symmetry energy. By varying the sensitivity of the effective interaction to isovector density and comparing these results with observational constraints from x-ray bursters, Ref. [50] concluded that equations of state

with a "soft" density dependence on isovector density are unrealistic and data favored a stiffer equation of state.

One challenge in this field is that current IAS data comes from measurements on stable targets. Then, results based on these measurements must be extrapolated to the limits of nuclear asymmetry inside neutron stars. In order to more effectively probe the nuclear symmetry energy, there is a need for high quality measurements of IAS transitions on neutron rich nuclei, such as those that will be produced by the Facility for Rare Isotopes Beams. It is notable, however, that such measurements will create new experimental challenges, as these reactions must be run in inverse kinematics. The IAS has been measured successfully measured in unstable, neutron rich isotopes, such as ^{16}C [53]. Because neutrons are also unstable, (n,p) type reactions will require the use of composite probes such as (d,^{2}He), although this is limited to measuring Gamow-Teller transitions.

1.4 Motivation

Although there have been significant efforts to improve precision and validate new charge-exchange probes in the experimental regime, there are many opportunities to explore additional complications in the reaction mechanics. For example, almost exclusively, charge-exchange calculations are performed assuming a single-step process in the framework of the distorted wave Born or impulse approximation (see Section 2.3), regardless of the beam energy of the reaction. When comparing to experiments at intermediate energies ($\sim$100 MeV/u), a single-step process is likely a good approximation. This is evidenced by a relatively good description of the g shape (although, for the case of composite probes, not necessarily the magnitude) of experimental angular distributions. However, charge-exchange

reaction experiments which investigate the population of the have been performed at ∼25-50 Mev/u (see [17, 18]). While DWBA is within its region of validity for the electron-capture studies run at ∼100 Mev/u, it will become increasingly less accurate with decreased beam energy and dedicated study is necessary to understand where this approximation breaks down. As with all indirect reaction methods, an incomplete understanding of charge-exchange reaction theory will impact the quality of extractions made for astrophysical applications.

Investigations of reaction dynamics in charge-exchange has not yet implemented recent developments in the realm of other reactions such as the incorporation of non-local interactions (see [54, 55, 56, 57, 58]). In this work we hope to begin to broaden our understanding of charge-exchanges reactions, including the impact of using two-body versus three-body reaction formalisms, and the effect of nuclear interactions on charge-exchange observables.

There are several opportunities to explore the impact of interactions which mediate isospin transitions in charge-exchange. Most commonly, for experimental charge-exchange studies, the effective nucleon-nucleon (NN) interaction parameterized by Love and Franey [59, 60] is used to describe the isospin transition. This phenomenological potential has an operator form, and uses a sum of real and imaginary Yukawa potentials. Of course, the choice of the effective NN interaction will directly affect the shape and magnitude of the calculated cross section. The Love and Franey potential is best constrained above about 100 MeV. It would be informative to explore the effects of different effective interactions, including microscopic and non-local potentials. In particular, in this initial study we will be looking at reactions in the 25-45 MeV energy range, where LF interaction has not been parameterized. In this thesis, we take this as an opportunity to investigate the effect of other NN interactions on charge-exchange observables. Having this goal in mind, the reaction code developed here is not restricted to interactions with Yukawa form factors. In future reac-

tion studies, however, it would be informative to implement the LF interaction for ease of comparison with calculations using different formalisms. Although studying the effects of non-local potentials is outside of the scope of this thesis, the code developed for this work, CHEX, can readily be extended to include non-local interactions.

In many IAS studies which have been used to study properties of nuclear matter, optical model potentials are used to construct, not only the incoming and outgoing scattering states, but also the Lane potential which describes the transition. It has been shown in the realm of transfer reactions that the phenomenological optical model potentials used to produce initial and final distorted wave functions are not very well constrained and produce large uncertainties [61]. In this work we begin to investigate the uncertainty derived from these phenomenological interactions, although similar, more rigorous, studies are needed in the realm of charge-exchange before uncertainties can be properly quantified.

Finally, we begin to explore the ways in which the reaction formalism effects charge-exchange observables. The two-body formalism which utilizes Lane potentials offers a simple way to explore charge-exchange transitions, but a three-body formalism can better describe microscopic transitions between single-particle states in the target. Instead of using a difference of proton and neutron optical potentials that adjusts the isospin projection of the target, we employ an NN potential that operates directly on the valence nucleon. In this work, we present a systematic study, over a variety of target nuclei and beam energies, to highlight the impact of various reaction formalisms in charge-exchange.

1.5 Outline

This thesis is organized in the following way: In Chapter 2, we begin by presenting the necessary reaction theory to build up to our description of transfer and charge-exchange reactions, including an introduction to optical model potentials, which are used throughout this work, and the fundamentals of elastic scattering theory. After this initial discussion, this thesis proceeds on a dual track, with the first part of each chapter discussing transfer reactions and the second half discussing how the topic of that chapter pertains to charge-exchange reactions. For example, after the general introductions, Chapter 2 goes on to introduce the reactions framework used for our transfer reaction studies, and the theoretical tools necessary to connect these reactions to astrophysical capture processes. Then, in the final section of Chapter 2, we introduce the reactions frameworks used to study charge-exchange in this thesis.

Chapter 3 discusses details of implementing the theoretical methods discussed in the previous chapter in reaction calculations. First, in Section 3.1, we discuss transfer calculations, including the bound state approximation which we have used to calculate transfer to unbound resonances. Then, in Section 3.2, we discuss the details of the charge-exchange reactions code, CHEX, developed for this thesis and the implementation of our two-body and three-body formalisms in that code, including a discussion of the various potentials explored in this work.

In Chapter 4 we present results for transfer and charge-exchange reactions. This thesis contains three separate transfer reaction studies, all utilizing a similar methodology. Section 4.1 highlights one of these transfer studies, the case of ^{30}P(d,n), in detail and discusses how this methodology was expanded in a study of ^{23}Al(d,n)^{24}Si. The remainder of the

transfer reaction results can be found in Appendix A, including a preliminary study for a proposed new method for constraining spectroscopic factors in transfer measurements using the Active Target Time Projection Chamber (AT-TPC). Section 4.2 discusses the results of our charge-exchange reaction study, for both the two-body and three-body frameworks presented here. Finally, Chapter 5 presents conclusions and outlooks for both the transfer and charge-exchange studies discussed in this thesis.

Some of the more technical developments made for this thesis have been included here in the appendices. In addition to the aforementioned transfer results in Appendix A, Appendix B contains the full derivation of the two-body charge-exchange T-matrix presented in this work. Similarly, Appendix C contains T-matrix derivations for each of the operators considered in the three-body charge-exchange framework: isospin central, isospin tensor, isospin spin-spin, and isospin spin-orbit. Finally, Appendix D presents the tests performed to benchmark and check the charge-exchange code, CHEX, developed for this thesis.

Chapter 2

Reaction Theory

Regardless of which astrophysical process we are probing, reliable results can only be extracted if there is an adequate and valid reaction theory used in the extraction. In this chapter we will build up to more complicated reaction descriptions by, first, introducing the basics of scattering theory, starting with the introduction of optical potentials and elastic scattering, and then expand on these topics to describe the transfer and charge-exchange formalism used in this thesis.

2.1 Optical Model Potentials

The effective nuclear interaction between a projectile nucleon and an A-body target results from a complicated, many-body problem and, although there are current efforts to develop scattering potentials from a many-body framework (e.g. [62]), it is not currently feasible to describe the full dynamics of complex reactions using an ab-initio framework. Therefore, throughout this work, in both the realms of transfer and charge-exchange reactions, interactions between the projectile/ejectile and the target/residual nucleus are described using optical model potentials (OMP). These are phenomenological potentials fit to reproduce elastic scattering data. They have real components, as well as imaginary terms which account for flux loss to non-elastic processes. The optical model effectively imposes a two-body approximation, freezing the A-body target into an inert object in its ground state. This implies

that many-body effects such as NN-correlations and anti-symmeterization are incorporated into the phenomenological fit via a strong mass and beam energy dependence [63, 64, 65].

When data is available, these fits can be developed for a particular projectile/target pair at the energy of interest. However, for many cases, this data is unavailable and global optical potentials are used instead. Global potentials are created by simultaneously fitting elastic scattering for a wide range of targets over a large energy range. These fits produce potentials which vary smoothly over mass and energy, allowing for interpolation or extrapolation to targets and energies without dedicated fits (Examples include [66, 1, 2]). Although these potentials are able to capture general trends over different mass and energy regions, it is worth noting that they are fit to stable nuclei and their validity for unstable nuclei has not been demonstrated. Despite this, they are currently used to describe reactions on unstable targets, because there are no better alternatives available.

Typically optical potentials follow a common form which can be expressed as

$$U(R) = V(R) + i(W(R) + W_s(R)) + V_{SO}(R) + V_C(R), \tag{2.1}$$

where $V(R)/W(R)$ are real/imaginary central terms, $W_s(R)$ is the imaginary surface term, $V_{SO}(R)$ is the real spin-orbit term, and $V_C(R)$ is the Coulomb term. Most terms are parameterized by a Woods-Saxon potential or its derivative. The central real and imaginary terms have the form

$$V(R) = -\frac{V_r}{1 + e^{(R-R_r)/a_r}}, \tag{2.2}$$

where V_r (W_r for imaginary central) is the depth parameter which specifies the strength of the potential, R_r is the radius term defined by $R_r = r_r A^{1/3}$, and a_r is the diffuseness.

The surface term has only an imaginary contribution and accounts for reactions that occur at the surface of the target (usually strongest at low energies). It takes the form of the derivative of a Woods-Saxson such that

$$W_s(R) = -4a_s \frac{d}{dR} \frac{W_s}{1 + e^{(R-R_s)/a_s}}, \tag{2.3}$$

with $R_s = r_s A^{1/3}$.

The spin-orbit term is typically real and also has a derivative form expressed as

$$V_{SO}(R) = \Big(\frac{\hbar}{m_\pi c}\Big)^2 \frac{2\boldsymbol{L}\cdot\boldsymbol{s}}{R} \frac{d}{dR} \frac{V_{SO}}{exp[(R - R_{SO})/a_{SO}]}, \tag{2.4}$$

where m_π is the pion mass [67]. Finally, for potentials where both the projectile and target are charged, there is an additional Coulomb term. Outside of the Coulomb radius defined as $R_C = r_c A^{1/3}$, a simple point-Coulomb potential is valid, defined by

$$V_C(R) = \frac{Z_p Z_t e^2}{R}, \tag{2.5}$$

where Z_p is the projectile charge and Z_t is the target charge. Inside R_c, the point approximation is no longer valid and a homogeneous charge distribution is taken for the target, resulting in:

$$V_C(R) = \frac{Z_p Z_t e^2}{R_C}\Big(\frac{3}{2} - \frac{R^2}{2R_C^2}\Big). \tag{2.6}$$

Here, we will simply note that optical potential fits for each target and energy contain a large number of fit parameters ($\sim$ 12) and these fits are not unique, even when these parameters have limited ranges of applicability. This introduces large uncertainties that

propagate through to the observables calculated with these potentials as inputs (e.g. transfer cross-sections). Recent efforts to quantify this uncertainty using Bayesian methods have found that the uncertainty is larger than previously assumed, at times larger that 100% [68]. This insight is important to note when comparing calculations using these potentials to experimental results.

2.2 Elastic Scattering

We will begin with a description of two-body, elastic scattering of projectile, p, with target, t, under the influence of a spherically symmetric potential. The reduced mass of the system is μ and the center of mass scattering energy is E. The dynamics of the system are dependent on the wave function that describes the scattering particle, so we must therefore solve the Schrödinger equation

$$[\hat{T} + U(R) - E]\psi(R, \theta) = 0, \tag{2.7}$$

where $U(R)$ is the nuclear potential, and T is the kinetic energy operator. In general, we can fix the incoming particle momentum along the z-axis. In this picture, the incoming wave function is modeled as a plane wave, characterized by its momentum. After interacting with $U(R)$, the outgoing wave function is a superposition of the incoming plane wave and an outgoing spherical wave according to the relation

$$\psi^{asym}(R, \theta) = e^{ikz} + f(\theta)\frac{e^{ikR}}{R}, \tag{2.8}$$

where $f(\theta)$ is the scattering amplitude which characterizes the strength of the interaction

where, for example, $U(r) = 0$ would lead to a scattering amplitude $f(\theta)$=0. When both short-range nuclear interactions and Coulomb potentials are present, the total scattering amplitude is equal to the sum of both the Coulomb scattering amplitude, $f_c(\theta)$ and the nuclear scattering amplitude, under the influence of Coulomb, $f_n^{(c)}(\theta)$. Because the Coulomb interaction is long range, but the nuclear potential goes to 0 at far distances, we use different methods to calculate these scattering amplitudes. The effect of the nuclear interaction can be found by expanding in Legendre polynomials, $P_L(\cos\theta)$, which is known as a partial wave decomposition. The expansion takes the form

$$\psi(R,\theta) = \sum_{L=0}^{\infty}(2L+1)i^L P_L(\cos\theta)\frac{1}{kR}\chi_L(R), \tag{2.9}$$

where k is the projectile momentum. The Legendre polynomials (P_L) are a convenient choice for this expansion because they are eigenfunctions of both the $\hat{L}^2$ and $\hat{L}_z$ operators with eigenvalues $L(L+1)$ and $m_L = 0$ for the case of a central potential, respectively. Thus, we are able to solve the Schrödinger equation for each partial wave separately. This means that equation 2.7 can be decomposed to give

$$\Big[-\frac{\hbar^2}{2\mu}\Big(\frac{d^2}{dR^2} - \frac{L(L+1)}{R^2}\Big) + U(R) - E\Big]\chi_L(R) = 0. \tag{2.10}$$

Solving this expression is then straightforward. Inside the range of the interaction, Equation (2.10) can be solved using a trial wave function $u_L(R)$ according to a chosen numerical method utilizing the constraints that the wave function must go to 0 at $R = 0$ and have a non-zero derivative at $R = 0$. Once this solution, $u_L(R)$, is found, it can be matched to the the behavior at large distances (R>a), outside of the range of the nuclear potential. The true wave function is $\chi_L(R) = B_L u_L(R)$, where we impose a normalization consistent with

the plane wave for the non-interaction process. Outside the range of the nuclear force, there are still effects from the long ranged Coulomb interaction, so the external form of the wave function, as given in [67], is

$$\chi_L(R > a) = \frac{i}{2}[H_L^-(\eta, kR) - \boldsymbol{S}_L H_L^+(\eta, kR)]. \tag{2.11}$$

In this expression, $H_L^{\pm}(\eta, kR)$ are the Hankel functions as defined in [67], η is the dimensionless Sommerfeld parameter defined as

$$\eta = \frac{Z_p Z_t e^2}{\hbar}\Big(\frac{\mu}{2E}\Big)^{1/2}, \tag{2.12}$$

and $\boldsymbol{S}_L$ is the S-matrix for each individual partial wave. The S-matrix can be calculated through the use of the R-matrix which matches the logarithmic derivatives of the true and trial wave functions at the matching radius a such that

$$\boldsymbol{R}_L = \frac{1}{a}\frac{\chi_L(a)}{\chi'_L(a)} = \frac{1}{a}\frac{u_L(a)}{u'_L(a)} \tag{2.13}$$

and

$$\boldsymbol{S}_L = \frac{H_L^- - a\boldsymbol{R}_L H_L'^-}{H_L^+ - a\boldsymbol{R}_L H_L'^+}. \tag{2.14}$$

Finally, the nuclear scattering amplitude (under the influence of a Coulomb potential) can be written as

$$f_n(\theta) = \frac{1}{2ik}\sum_{L=0}^{\infty}(2L+1)P_L(\cos\theta)e^{2i\sigma_L(\eta)}(\boldsymbol{S}_L - 1), \tag{2.15}$$

where $\sigma_L(\eta)$ is the Coulomb phase shift defined as

$$\sigma_L(\eta) = arg\Gamma(1 + L + i\eta). \tag{2.16}$$

the point Coulomb scattering amplitude is given in [67] as

$$f_c(\theta) = \frac{-\eta}{2ksin^2(\theta/2)} exp[-i\eta ln(sin^2(\theta/2)) + 2i\sigma_0(\eta)] \tag{2.17}$$

and the total differential cross section is given by

$$\frac{d\sigma}{d\Omega} = |f_c(\theta) + f_n(\theta)|^2. \tag{2.18}$$

2.3 Transfer Reaction Formalism and DWBA

For many reactions, a two-body description is insufficient to describe the complexities of the reaction process. This is particularly true in cases where mass partitions are rearranged, such as in (d,N) transfer reactions. For both transfer and charge-exchange reactions, we will therefore employ a three-body formalism which freezes an inert core within the target, but allows for the rearrangement of the other two particles during the reaction. We will begin by introducing the three-body formalism used to describe transfer reactions, such as A(d,n)B, where a proton is transferred from the scattering deuteron to the inert target. For these reactions, it is useful to use the T-matrix formalism, which is based on integral relations, as opposed to the S-matrix used in the previous section, which is based on asymptotic matching.

The T-matrix can be described equivalently using either the initial (prior form) or final (post form) coordinates of the system (see Figure 2.1) which correspond to the mass partition

rearrangement during this process.

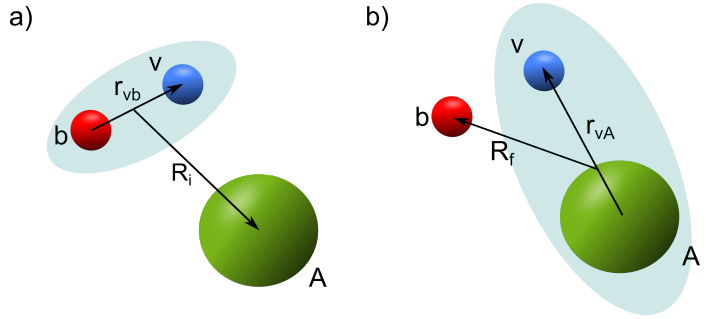

Figure 2.1: Coordinates for A(a,b)B transfer reactions in the a) initial channel (prior form) and b) final channel (post form) where a=b+v and B=A+v

Using these coordinates, the prior T-matrix can be expressed as [67]

$$T^{exact}_{prior} = \langle \Psi^{(-)exact}(\boldsymbol{r}_{vA}, \boldsymbol{R}_f) | V_{vA} + V_{bA} - U_i | \Phi_{I_b:I_a}(\boldsymbol{r}_{vb}) \chi_i(\boldsymbol{R}_i) \rangle \tag{2.19}$$

and the post T-matrix can be written as

$$T^{exact}_{post} = \langle \Phi_{I_A:I_B}(\boldsymbol{r}_{vA}) \chi_f(\boldsymbol{R}_f) | V_{vb} + V_{bA} - U_f | \Psi^{exact}(\boldsymbol{r}_{vB}, \boldsymbol{R}_i) \rangle \tag{2.20}$$

where $\Phi_{I_i:I_f}$ is the overlap between the i and f wave functions, V_{if} is the interaction between the ith and fth bodies, U is an optical potential between the scattering body and the target in either the initial or final channels, χ is a distorted scattering wave produced using U, and Ψ^{exact} is the exact three-body wave function. The last two terms of the interaction, $V_{bA} - U_i$ in the prior formalism and $V_{bA} - U_f$ in the post formalism, are referred to as the remnant term. In the case of deuteron induced transfer reactions, the two potentials in the post-form remnant term have similar magnitudes, and it is often a good approximation to neglect it. Therefore, we will continue using the post T-matrix form.

Ψ^{exact}_i is the solution to the three-body Shrödinger equation such that

$$[T_{R_i} + T_{r_{vb}} + V_{bv} + V_{bA} + V_{vA} - E]\Psi^{exact} = 0, \tag{2.21}$$

where T_{R_i} is the kinetic energy operator of the scattering vb system, and $T_{r_{vb}}$ is the kinetic energy of the internal motion of particles v and b.

Similarly to Equation (2.11), we can formulate an expression for Ψ^{exact} at far distances for each set of quantum numbers in the initial and final channels (α_i/α) with the form

$$\psi(R_f) = \delta_{\alpha\alpha_i} F_{L_i}(\eta_L, k_f R_f) + \boldsymbol{T}_{\alpha\alpha_i} H_L^+(\eta_L, k_f R_f) \tag{2.22}$$

where F_L is the regular Coulomb function, H_L^+ is the Hankel function, and $\boldsymbol{T}_{\alpha\alpha_i}$ is the T-matrix. It is often challenging to solve for this exact wave function, so there are a number of approximations that can be made to simplify the T-matrix expression. Most commonly, the Distorted Wave Born Approximation (DWBA) is applied. In DWBA, Ψ^{exact} is simplified to the elastic channel, a product of the scattering distorted wave and the corresponding bound state wave function. This simplification models the reaction as a single-interaction process and will generally break down at low scattering energy. Applying the DWBA and neglecting the remnant term, transforms Equation (2.20) into

$$T_{post}^{DWBA} = \langle \Phi_{I_A:I_B}(\boldsymbol{r}_{vA}) \chi_f(\boldsymbol{R}_f) | V_{vb} | \Phi_{I_b:I_v}(\boldsymbol{r}_{vb}) \chi_i(\boldsymbol{R}_i) \rangle. \tag{2.23}$$

Once the T-matrix is calculated, it can be easily related to the scattering amplitude by

$$f_{\mu_t\mu_p}^{\mu_{t_i}\mu_{p_i}}(\boldsymbol{k_i}; \boldsymbol{k_f}) = \frac{\mu_\alpha}{2\pi\hbar^2} \boldsymbol{T}_{\mu_t\mu_p}^{\mu_{t_i}\mu_{p_i}}(\boldsymbol{k_i}; \boldsymbol{k_f}), \tag{2.24}$$

where $\mu_{p/t}$ is the spin projection of the projectile and target and μ_α is the reduced mass of

the system. Finally, averaging over initial state spin projections and summing over final spin projections, gives us the cross section

$$\sigma(\theta) = \frac{1}{\hat{I}_{p_i}^2 \hat{I}_{t_i}^2} \sum_{\mu_{p_i}\mu_{t_i}\mu_p\mu_t} |f_{\mu_t\mu_p}^{\mu_{t_i}\mu_{p_i}}(\boldsymbol{k_i}; \boldsymbol{k_f})|^2, \tag{2.25}$$

where $\hat{I} = \sqrt{(2I+1)}$.

2.3.1 Adiabatic Distorted Wave Approximation

Often, DWBA is not sufficient to describe deuteron induced reactions accurately. The deuteron is weakly bound (2.2 MeV) and, therefore, has a large probability for breakup in the potential field of the target nucleus. Theoretical studies have demonstrated that taking this breakup into account is critical for reproducing experimental observations [69]. In DWBA, the exact incoming wave function is simplified as the product of the deuteron ground state wave function and the deuteron distorted wave, which means that this breakup is not included, apart for its influence on the optical potential which describes the deuteron elastic scattering. The adiabatic distorted wave approximation (ADWA) allows for the consideration of deuteron breakup, but offers a less computationally expensive alternative to including the full three-body wave function.

ADWA is based on a separation of scales between the deuteron beam energy and its internal binding energy ($E >> \epsilon_i$, where ϵ_i is the excitation energy of the n/p system). With this separation of scales, the excited states of the deuteron can be taken as essentially degenerate with the ground state. To ensure accuracy, the deuteron beam energy should be above about 20 MeV to ensure the separation of scales between the beam and internal energies. One consequence exploited by [70, 71] is that the three-body wave function is only

necessary within the relatively short range of the deuteron binding potential, V_{np}. Within that limited range, the exact wave function can be expanded in some choice of basis functions. In this case Weinberg states [72], $\phi_i(r)$, are used to describe the relative motion inside the deuteron and are complete within the range of the deuteron interaction. $\chi_i(R)$ are used to describe the relative target-deuteron motion. This expansion can be expresses as

$$\Psi^{exact} \approx \Psi^{ADWA} = \sum_{i=0}^{\infty} \phi_i(r)\chi_i(R). \tag{2.26}$$

ADWA retains only the first term of this expansion, $\Psi^{ADWA} \approx \phi_0(r)\chi_0(R)$, where $\phi_0(r)$ is an eigenfunction of the internal deuteron Hamiltonian with the deuteron binding energy as its eigenenergy and $\chi_0(r)$ is referred to as the adiabatic scattering wave function. Retaining just the first term has been shown to be a good approximation for our purposes [73]. $\chi_0(r)$ is calculated using the adiabatic potential which is defined using neutron-target and proton-target optical potentials. It is worth noting that this adiabatic potential is no longer useful to describe elastic scattering. The final ADWA T-matrix for (d,N) transfer is written as

$$T_{post}^{ADWA} = \langle \Phi_{I_A:I_B}(\boldsymbol{r}_{vA})\chi_f(\boldsymbol{R}_f)|V_{vb}|\Psi^{ADWA}\rangle. \tag{2.27}$$

2.3.2 Spectroscopic Factors and Resonance Strengths

Once transfer cross sections have been calculated, a theoretical framework must be used to connect this value to the astrophysical capture process. Commonly, and for the cases discussed throughout this thesis, this is achieved through the extraction of spectroscopic factors. From a theory perspective, the single-nucleon spectroscopic factor is defined as the norm of the single-nucleon overlap function:

$$S = |\langle \phi_f | \phi_i \rangle|^2, \tag{2.28}$$

where ϕ_i and ϕ_f are the radial parts of $\Phi_{I_i:I_f}$ from equations (2.19) and (2.20).

In an intuitive sense, the spectroscopic factor can be thought of as a measure of how well a given state can be well described in a "single-particle" picture where the transferred nucleon occupies a single orbital in the mean field of the target. For states that are highly single-particle in nature, S will be close to one, and a small S can be interpreted as a more fractured structure that involves the participation of nucleons in several orbitals. Therefore, the full wave function overlap for the composite A+1 nucleus in both the single-particle transfer reaction or the particle capture reaction that it correlates to, can be related to the overlap in a single-particle picture ψ_{sp} by the relation

$$\phi(r_{AN}) = S^{1/2} \psi_{sp}(r_{AN}), \tag{2.29}$$

where r_{AN} is the coordinate that connects the target nucleus with the transferred (captured) nucleon. As shown in Equation (2.27) the transfer cross section is proportional to this overlap squared. Because the experimentally measured transferred cross section will contain information about the full wave function overlap, and our calculations were performed by modeling the final bound state with a single-particle, Woods-Saxon potential, the spectroscopic factor can easily be obtained by normalizing the experimental cross section to the theoretical value as shown below:

$$S = \frac{d\sigma/d\Omega|_{exp}}{d\sigma/d\Omega|_{th}}. \tag{2.30}$$

Practically, this normalization is often performed at the first peak of the differential cross section. In many cases, in (d,n) reactions where the outgoing neutron is difficult to measure, angular information is unavailable and the comparison must be performed by simply taking the ratio of the full angle-integrated cross sections.

Once the spectroscopic factor is extracted, it can be used to place constraints on the astrophysical capture rate of interest. For particle capture cases where the final state resonances are narrow and isolated (often the case for proton captures into low lying resonances) the reaction cross section to a isolated state is described by a Breit-Wigner resonance. It can be shown that the astrophysical reaction rate is [74]

$$N_a\langle\sigma\nu\rangle \propto (T)^{-3/2}\sum_i(\omega\gamma)_i e^{-\frac{E_i}{kT}} \tag{2.31}$$

where $N_a\langle\sigma\nu\rangle$ is the reaction rate, T is the temperature of the astrophysical environment, E_i is the excitation energy of the final resonance states, and $\omega\gamma_i$ is the resonance strength. The negative exponent in Equation (2.31) dictates that only low lying resonances will contribute significantly to the reaction rate. For most cases of interest, these excitation energies have been measured experimentally, however, $\omega\gamma_i$ remains relatively unconstrained. The resonance strength $\omega\gamma$ is described by the relationship

$$\omega\gamma_{if} = \frac{(2J_f+1)}{(2j_p+1)(2J_i+1)}\frac{\Gamma_p\Gamma_\gamma}{\Gamma_p+\Gamma_\gamma}, \tag{2.32}$$

where J_f is the spin of the final state, J_i is the spin of the initial state, j_p is the spin of the captured proton, Γ_γ is the gamma decay width for the final state and Γ_p is the proton decay width for the final state. However, for many of these low lying resonances, the Coulomb barrier reduces the proton decay width by orders of magnitude relative to the gamma decay

width, such that the resonance strength can, to very good approximation, be expressed as

$$\omega\gamma_{if} \approx \frac{(2J_f+1)}{(2j_p+1)(2J_i+1)}\Gamma_p. \tag{2.33}$$

Finally, the proton decay width can be related to the single-particle decay width through the spectroscopic factor such that

$$\Gamma_p = C^2 S \Gamma_{sp}. \tag{2.34}$$

In this expression, C is a Clebsch-Gordan coefficient and Γ_{sp} is the single-particle decay width. Γ_{sp} is obtained by calculating elastic scattering from a central Woods-Saxon potential where the depth is adjusted to reproduce the energy of the resonance of interest and is easily calculated. By these means, the spectroscopic factor extracted from the transfer reaction can be used to constrain the calculation of the proton decay width and, therefore, directly constrain the proton capture reaction rate.

2.4 Charge-Exchange Framework

Similar to the reaction framework presented here for transfer reactions, charge-exchange reactions can be described using a T-matrix formalism. Within this work we have employed a two-body and a three-body framework, both using single step DWBA, to analyze charge-exchange reactions to the isobaric analog state. Here, we will introduce both of these methods, and more in depth derivations of the relevant T-matrix expressions can be found in Appendices B and C.

2.4.1 Two-Body Formalism

The first description of charge-exchange reactions involves a two-body formalism where the charge-exchange transition is caused by changes in a bulk optical potential which describes the interaction between the projectile nucleon and the target. The coordinates for two-body charge-exchange are show in Figure 2.2. Because charge-exchange is an isobaric transition, the mass difference between the target and residual nucleus is neglected and we utilize the same scattering coordinate, R_{1A}, in the initial and final channel. For (p,n) reactions, the projectile, 1, is a proton in the incoming channel, and a neutron in the outgoing channel, representing a isospin flip interaction.

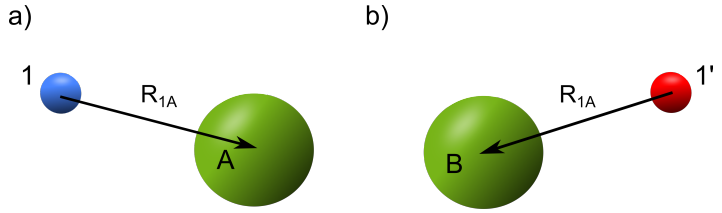

Figure 2.2: Coordinates for A(p,n)B charge-exchange reactions where the residual nucleus, B, is an isobar of the target, A.

In this formalism, the transition potential is defined using the Lane potential [47] which is cast in the form

$$U(R_{1A}) = U_0(R_{1A}) + \frac{\boldsymbol{\tau} \cdot \boldsymbol{T}}{4A} U_1(R_{1A}), \tag{2.35}$$

where $U_0(R_{1A})$ is the isoscalar potential which drives elastic scattering, $U_1(R_{1A})$ is the isovector potential which drives the charge-exchange transition, and $\boldsymbol{\tau}$ and $\boldsymbol{T}$ are the isospin operators which act on the projectile nucleon and target nucleus, respectively. The dot product of the isospin operators can be expanded as

$$\boldsymbol{\tau} \cdot \boldsymbol{T} = \tau_z T_z + \tau_+ T_- + \tau_- T_+. \tag{2.36}$$

where $\tau_{+/-}$ are the isospin raising/lowering operators.

Throughout this work, we use the convention that neutrons have isospin projection $\frac{1}{2}$ and protons have isospin projection $-\frac{1}{2}$. The first term in Equation (2.36) can be neglected in charge-exchange reactions, because it will not cause an isospin-flip. The third term will produce 0 because $\tau_-|\frac{1}{2} - \frac{1}{2}\rangle = 0$. Therefore, only the second term, which increases the isospin projection of the proton and lowers the isospin projection of the target, can contribute. The factors in Equation (2.35) are chosen such that it can be rearranged to express elastic scattering of neutrons and protons:

$$U_{n,p} = U_0(R_{1A}) \pm \frac{N-Z}{A} U_1(R_{1A}) \tag{2.37}$$

where the upper sign corresponds to neutron scattering potentials and the lower sign corresponds to protons. Neutron number, N, charge number, Z, and mass number, A, pertain to the target nucleus. This makes it clear that the isovector part of the Lane potential can be written in terms of proton and neutron elastic scattering potentials giving us

$$U_1(R_{1A}) = \frac{A}{2(N-Z)}[U_n(R_{1A}) - U_p(R_{1A})]. \tag{2.38}$$

U_n and U_p are typically taken to be optical potentials with a form similar to that introduced in Section 2.1. The choice of optical potential, however, is not unique and we will discuss the potentials used in this study more thoroughly in the next chapter.

The transition matrix element for charge-exchange can been expressed simply as

$$T_{2B}^{CE} = \langle \chi_f(\boldsymbol{R_{1A}})|2\frac{\sqrt{|N-Z|}}{A}U_1(R_{1A})|\chi_i(\boldsymbol{R_{1A}})\rangle. \tag{2.39}$$

$\chi_i(\boldsymbol{R_{1A}})$ and $\chi_f(\boldsymbol{R_{1A}})$ represents the p+A/n+B distorted waves, which are calculated using an optical potential. As discussed earlier, the incoming and outgoing scattering wave functions can be expanded in partial waves, giving us a T-matrix expression of

$$\begin{aligned} T_{2B}^{CE} = \langle \chi_f(\boldsymbol{R_{1A}})|2\frac{\sqrt{|N-Z|}}{A}U_1(R_{1A})|\chi_i(\boldsymbol{R_{1A}})\rangle = \int \sum_{L_f J_f M_f L_i J_i} \\ {}_i{}^{L_i - L_f} e^{i\sigma_{L_i}} (-1)^{L_i-(M_f-\mu_1')+J_f-M_f} \frac{(4\pi)^{3/2}\hat{L}_i}{k_f k_i} C^{J_i\mu_1}_{Li0I_1\mu_1} C^{J_f M_f}_{L_f(M_f-\mu_1')I_1\mu_1'} \\ \left[Y^{L_f}(\hat{R}_{1A})\Xi^{I_1}(-\xi_1)\right]^{J_f}_{-M_f} \left[Y^{L_i}(\hat{R}_{1A})\Xi^{I_1}(\xi_1)\right]^{J_i}_{\mu_1} Y^{L_f}_{-(M_f-\mu_1')}(\hat{k}_f) \\ \frac{\chi_{L_i J_i}(R_{1A})\left(2\frac{\sqrt{|N-Z|}}{A}U_1(R_{1A})\right)\chi^*_{L_f J_f}(R_{1A})}{R_{1A}^2} d\Omega_{1A} d\xi_1 dR_{1A}. \end{aligned} \tag{2.40}$$

where primed variables have undergone an isospin transition.

This expression can be simplified using a number of properties, including the fact that the Lane potential is a scalar operator, so the total angular momentum in the initial and final channels must couple to 0. Once the expression is fully simplified, we are left with

$$\begin{aligned} \langle \chi_f(\boldsymbol{R_{1A}})|2\frac{\sqrt{|N-Z|}}{A}U_1(R_{1A})|\chi_i(\boldsymbol{R_{1A}})\rangle = \\ \int \sum_{L_i J_i} e^{i\sigma_{L_i}} \frac{(4\pi)^{3/2}}{k_f k_i} \hat{L}_i \frac{\chi_{L_i J_i}(R_{1A})\left(2\frac{\sqrt{|N-Z|}}{A}U_1(R_{1A})\right)\chi^*_{L_f J_f}(R_{1A})}{R_{1A}^2} \\ C^{J_i\mu_1}_{Li0I_1\mu_1} C^{J_i\mu_1}_{L_i(\mu_1-\mu_1')I_1\mu_1'} Y^{L_i}_{\mu_1-\mu_1'}(\hat{k}_f) dR_{1A}. \end{aligned} \tag{2.41}$$

To get the cross section, we average over initial state projections, and sum over the final projections to give us

$$\frac{d\sigma}{d\Omega} = \sum_{\mu_1 \mu_1' \mu_A \mu_B} \frac{k_f}{k_i} \frac{\mu_1 \mu_f}{4\pi^2 (\hbar c)^4} \frac{1}{\hat{J}_A \hat{\mu}_1} |T^{\mu_1}_{\mu_1'}|^2 \tag{2.42}$$

where J_A and J_B are the initial and final spin of the target and equal 0 in the case of 0^+ transitions.

2.4.2 Three-Body Formalism

The two-body formalism discussed previously offers a simple way to explore charge-exchange transitions but freezing the target into an inert, single body, necessarily erases interesting phenomenon introduced by the internal structure of the target. Although in most cases of interest computing reactions using the full, A+1 body system remains intractable, we will introduce an additional complication into the formalism by now expressing the target as an inert core with a valence nucleon. This three-body formalism can describe transitions between single-particle states in the target. Instead of using a difference of proton and neutron optical potentials that adjusts the isospin projection of the target, we will now employ an NN potential that operates directly on the valence nucleon.

The coordinates for the three-body charge-exchange formalism are show in Figure 2.3. The valence particle, 2, occupies a well defined single-particle state with a given value of l and j, which we assume can be described by a Woods-Saxon potential.

In this description, the formalism is built on two coordinates, R_{1A} which runs from the projectile/ejectile to the target/residual, and r_{2c} which runs from the valence nucleon to the inert core. The NN interaction discussed above will, therefore, run along the coordinate r_{12},

which connects the projectile and valence nucleons. Because this coordinate is different than the basis coordinates which describe our wave functions, it poses an additional complication. In our work, the NN potential is expanded in a multipole expansion.

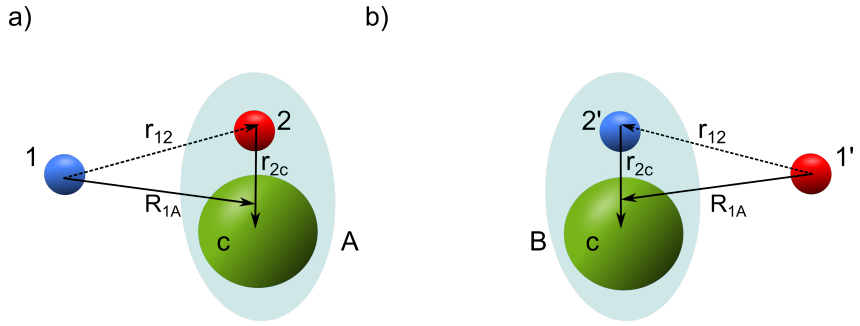

Figure 2.3: Coordinates for A(p,n)B charge-exchange reactions within the three-body reaction formalism.

NN potentials utilized in this three-body framework must be cast in an operator form in coordinate space. Because we are interested in charge-exchange reactions, we will only include terms of the potential which contain the $\boldsymbol{\tau} \cdot \boldsymbol{\tau}$, Fermi operator where, in the three-body framework, the operator acts on the projectile and valence nucleons. These potentials contain a radial dependence that can be phenomenologically fit to charge-exchange data or derived from a more ab-initio approach. They can be wholly real or contain a mixture of real and imaginary components. Some interactions are energy dependent while others are not. In addition to a central isospin term, these potentials can contain other isospin operators such as the spin-spin, $(\boldsymbol{\sigma} \cdot \boldsymbol{\sigma})(\boldsymbol{\tau} \cdot \boldsymbol{\tau})$, operator or the spin-orbit operator, $(\boldsymbol{L} \cdot \boldsymbol{S})(\boldsymbol{\tau} \cdot \boldsymbol{\tau})$, among others. The choice of potential will be discussed in more detail in the next chapter.

The charge-exchange three-body T-matrix can be written in a similar form as the two-body T-matrix:

$$T_{3B}^{CE} = \langle \chi_f(\boldsymbol{R_{1A}}) \Phi_{I_c:I_{2'}}(\xi_c, \xi_2, \boldsymbol{r_{2c}}) | t_{NN} | \Phi_{I_c:I_2}(\xi_c, \xi_2, \boldsymbol{r_{2c}}) \chi_i(\boldsymbol{R_{1A}}) \rangle, \tag{2.43}$$

where now the target/residual wave functions have a dependence on the core spin components, the valence spin components, and the internal coordinate r_{2c}. The Lane potential is replaced by an NN potential. As previously mentioned, the NN potential is directed along the r_{12} coordinate which runs from the projectile proton to the valence neutron. Various NN potentials are parameterized using different terms, but only terms that contain the $\boldsymbol{\tau_1 \cdot \tau_2}$ operators will contribute to charge-exchange. For example, the AV8' potential considered in this work ([75]) has 8 terms, 4 of which contain isospin operators. Because all of the operators I discuss for charge-exchange contain the isospin operators, I will often drop this from the description of the operators and refer to them, instead, as the central, tensor, spin-spin, and spin-orbit terms. In this case, t_{NN} is written as

$$\begin{aligned} t_{NN} = {} & V_C(r_{12}) \boldsymbol{\tau_1 \cdot \tau_2} + V_T(r_{12}) \sqrt{\frac{24\pi}{5}} (\boldsymbol{\tau_1 \cdot \tau_2}) \Big[Y_2(\hat{r}_{12}) \cdot [\boldsymbol{\sigma_1} \otimes \boldsymbol{\sigma_2}]_2 \Big] \\ & + V_{SS}(r_{12}) (\boldsymbol{\sigma_1 \cdot \sigma_2}) (\boldsymbol{\tau_1 \cdot \tau_2}) + V_{LS}(r_{12}) (\boldsymbol{L \cdot S}) (\boldsymbol{\tau_1 \cdot \tau_2}) \end{aligned} \tag{2.44}$$

where $V_C(r_{12})$, $V_T(r_{12})$, $V_{SS}(r_{12})$, and $V_{LS}(r_{12})$ give the radial dependence of the central, tensor, spin-spin, and spin-orbit terms, respectively. An expression for the three-body charge-exchange T-matrix with an isospin central interaction is given here, along with a brief commentary on the expressions involving the isospin-tensor, isospin-spin-spin, and isospin-spin-orbit operators. For a full derivation of these expressions, see Appendix C. For the case of only an isospin central term, Equation (2.44) simplifies to

$$t_{NN} = V_C(r_{12})\boldsymbol{\tau_1} \cdot \boldsymbol{\tau_2} \tag{2.45}$$

In addition to making the isospin flip, the isospin operators will give a factor of $\frac{1}{2}$ and we will also add a $(2j+1)$ factor to account for all available neutrons in the valence shell. Now, we must express this quantity using an expansion in our current coordinates using the method from [67]. The relationship between the two coordinate vectors and $\boldsymbol{r}_{12}$ is

$$\boldsymbol{r}_{12} = \boldsymbol{R}_{1A} - \frac{m_c}{m_A}\boldsymbol{r}_{2c}, \tag{2.46}$$

where m_c is the mass of the core and m_A is the mass of the target. The potential only depends on the magnitude of $\boldsymbol{r}_{12}$, so we can calculate r_{12}^2

$$r_{12}^2 = R_{1A}^2 + \frac{m_c^2}{m_A^2}r_{2c}^2 - \frac{2m_c}{m_A}R_{1A}r_{2c}z, \tag{2.47}$$

where $z = \cos\theta_{12}$ and θ_{12} is the angle between $\boldsymbol{R}_{1A}$ and $\boldsymbol{r}_{2c}$. Then we can build a multipole function, F_λ, using the potential so that:

$$F_\lambda(R_{1A}, r_{2c}) = \frac{1}{2}\int_{-1}^{1} V_{NN}(r_{12})P_\lambda(z)dz, \tag{2.48}$$

where P_λ are Legendre Polynomials. Then, our final potential is

$$t_{NN} = V(r_{12})\frac{(2j+1)}{2} = \sum_\lambda (2\lambda+1)F_\lambda(R,r)\frac{4\pi}{2\lambda+1}\sum_{m_\lambda} Y_{\lambda,m_\lambda}(\hat{r}_{2c})^* Y_{\lambda,m_\lambda}(\hat{R}_{1A})\frac{(2j+1)}{2}. \tag{2.49}$$

As before, we can expand our incoming and outgoing wave functions in partial waves.

In addition to the scattering wave functions previously used in the two-body description, there will also be an expression for the internal valence-core wave function. Including all the appropriate factors, the T-matrix can be written as

$$\langle \chi_f(\boldsymbol{R_{1A}}) \Phi_{I_c:I_{2'}}(\xi_c, \xi_2, \boldsymbol{r_{2c}}) | t_{NN} | \Phi_{I_c:I_2}(\xi_c, \xi_2, \boldsymbol{r_{2c}}) \chi_i(\boldsymbol{R_{1A}}) \rangle = \int \sum_{\substack{L_f J_f M_f L_i J_i \\ m_{j_i} m_{j_f} \mu_c \mu_c'}} k_1$$
$$Y^{L_f}_{M_f}(\hat{k}_f) C^{J_f M_f + \mu_1'}_{L_f M_f I_1 \mu_1'} C^{J_i \mu_1}_{L_i 0 I_1 \mu_1} C^{J_A \mu_A}_{j_i m_{j_i} I_c \mu_c} C^{J_B \mu_B}_{j_f m_{j_f} I_c \mu_c'} \left[Y^{L_f}(R_{1A}) \Xi^{I_1}(-\xi_1) \right]^{J_f}_{-(M_f + \mu_1')}$$
$$\left[Y^{l_f}(r_{2c}) \Xi^{I_2}(-\xi_2) \right]^{j_f}_{-m_{j_f}} \left[Y^{L_i}(R_{1A}) \Xi^{I_1}(\xi_1) \right]^{J_i}_{\mu_1} \left[Y^{l_i}(r_{2c}) \Xi^{I_2}(\xi_2) \right]^{j_i}_{m_{j_i}} \Xi^{*I_c}_{\mu_c'}(\xi_c) \Xi^{I_c}_{\mu_c}(\xi_c)$$
$$\frac{\phi_{j_f}(r_{2c}) F_{L_f J_f}(R_{1A}) t_{NN} \phi_{j_i}(r_{2c}) F_{L_i J_i}(R_{1A})}{R_{1A}^2} R_{1A}^2 r_{2c}^2 dR_{1A} dr_{2c} d\Omega_{2c} d\Omega_{1A} d\xi_1 d\xi_2 d\xi_c, \tag{2.50}$$

where

$$k_1 = i^{L_f - L_i} (-1)^{L_i + L_f + M_f + \mu_1' + m_{j_f}} e^{i\sigma_{L_i}} \frac{\hat{L}_i (4\pi)^{\frac{3}{2}}}{k_f k_i}. \tag{2.51}$$

Ideally, we simplify all angular components of this integral in order to ease its implementation in our calculations. We can accomplish this by using a number of angular momentum identities and, again, taking advantage of the scalar nature of the central operators (see Appendix C). After all of these manipulations, we are left with a final expression that only contains a radial integral:

$$\langle\chi_f(\boldsymbol{R_{1A}})\Phi_{I_c:I_{2'}}(\xi_c,\xi_2,\boldsymbol{r_{rc}})|t_{NN}|\Phi_{I_c:I_2}(\xi_c,\xi_2,\boldsymbol{r_{2c}})\chi_i(\boldsymbol{R_{1A}})\rangle =$$
$$\int \sum_{\substack{L_f J_f M_f L_i J_i \\ M_J \lambda m_{j_i} m_{j_f} \mu_c}} k_5\; Y^{L_f}_{M_f}(\hat{k}_f) C^{J_f M_f+\mu_1'}_{L_f M_f I_1 \mu_1'} C^{J_i \mu_1}_{L_i 0 I_1 \mu_1} C^{\lambda M_J}_{J_f -(M_f+\mu_1') J_i \mu_1} C^{\lambda M_J}_{j_f -m_{j_f} j_i m_{j_i}}$$
$$C^{\lambda 0}_{L_i 0 L_f 0} C^{\lambda 0}_{l_f 0 l_i 0} C^{J_A \mu_A}_{j_i m_{j_i} I_c \mu_c} C^{J_B \mu_B}_{j_f m_{j_f} I_c \mu_c} \begin{Bmatrix} L_i & J_i & I_1 \\ J_f & L_f & \lambda \end{Bmatrix} \begin{Bmatrix} l_i & j_i & I_2 \\ j_f & l_f & \lambda \end{Bmatrix} \tag{2.52}$$
$$\frac{\phi_{j_f}(r_{2c}) F_{L_f J_f}(R_{1A}) F_\lambda(R,r) \phi_{j_i}(r_{2c}) F_{L_i J_i}(R_{1A})}{R^2_{1A}} R^2_{1A} r^2_{2c} dR_{1A} dr_{2c},$$

where

$$k_5 = i^{L_f+L_i}(-1)^{M_f+\mu_1'+m_{j_f}-M_J+J_i+I_1+j_i+l_f+I_2} e^{i\sigma_{L_i}}(2j_i+1)\frac{(4\pi)^{\frac{3}{2}}}{2k_f k_i}\frac{\hat{L_i}^2 \hat{L_f} \hat{J_i} \hat{J_f} \hat{j_i} \hat{j_f} \hat{l_i} \hat{l_f}}{\hat{\lambda}^2}. \tag{2.53}$$

Now the total cross section expression is

$$\frac{d\sigma}{d\Omega} = \sum_{\substack{\mu_1 \mu_1' \\ \mu_A \mu_B}} \frac{k_f}{k_i} \frac{\mu_1 \mu_f}{4\pi^2(\hbar c)^4} \frac{1}{\hat{J}^2_A \hat{\mu}^2_1} \tag{2.54}$$
$$\times \left|\langle\chi_f(\boldsymbol{R_{1A}})\Phi_{I_c:I_{2'}}(\xi_c,\xi_2,\boldsymbol{r_{2c}})|t_{NN}|\Phi_{I_c:I_2}(\xi_c,\xi_2,\boldsymbol{r_{2c}})\chi_i(\boldsymbol{R_{1A}})\rangle\right|^2,$$

where J_A and J_B are the initial and final spins of the target. A similar expression can also be worked out for additional terms in the interaction. Here, we just remark on a few unique features of each term considered in this work.

The spin-spin operator, which has the form

$$V_{Spin-Spin} = V_{SS}(r_{12})(\boldsymbol{\sigma_1} \cdot \boldsymbol{\sigma_2})(\boldsymbol{\tau_1} \cdot \boldsymbol{\tau_2}), \tag{2.55}$$

is relatively straightforward to consider because the additional operator, $\boldsymbol{\sigma_1} \cdot \boldsymbol{\sigma_2}$, acts only in spin space. The operator therefore factorizes and much of the T-matrix expression remains unchanged. This operator, often referred to as the Gamow-Teller operator or spin-flip operator, is capable of switching the spin projection of the projectile and valence nucleus, causing a net change of $\Delta S = 1$. However, like the $\boldsymbol{\tau} \cdot \boldsymbol{\tau}$ operator, it can be broken down into three terms: $\boldsymbol{\sigma_1} \cdot \boldsymbol{\sigma_2} = \sigma_{1z}\sigma_{2z} + \sigma_{1+}\sigma_{2-} + \sigma_{1-}\sigma_{2+}$. Because we are only considering Fermi transitions in this work, we only consider contributions from $\sigma_{1z}\sigma_{2z}$ (ΔS=0).

The tensor operator offers an additional challenge, however, because it mixes spin and position space operators. The tensor operator has the form

$$V_{Tensor} = V_T(r_{12})\sqrt{\frac{24\pi}{5}}(\boldsymbol{\tau_1} \cdot \boldsymbol{\tau_2})\Big[Y_2(\hat{r}_{12}) \cdot [\boldsymbol{\sigma_1} \otimes \boldsymbol{\sigma_2}]_2\Big], \tag{2.56}$$

where $Y_2(r_{12})$ is a rank two spherical harmonic directed along the r_{12} coordinate. Because our initial and final wave functions are written in the R_{1A} and r_{2c} coordinates, the tensor operator's spherical harmonic must be expanded in terms of the other two coordinates. This greatly complicates the expression. Details for this process can be found in Appendix C.

Finally, we also considered the spin-orbit operator. This operator has a similar complication to the tensor operator, where it operates both on spin space and angular momentum space (which contains an angular dependence). Unlike the spherical harmonic from the tensor operator, however, there is not a simple spherical harmonic expansion that can be used to express the angular momentum operator, $\boldsymbol{L}$, in terms of the coordinates we have chosen to express the problem. Although it is possible to express this term exactly, it would introduce

the need for a numerical angular integral in the T-matrix expression and require a significant alteration to the framework used for our calculations code. Therefore, we experimented with several approximate way of including the spin-orbit interaction which is described in detail in Appendix C. After these investigations, we felt we were unable to reliably extract meaningful information regarding the magnitude or shape of the spin-orbit contribution, so we have instead, chosen to not include this operator in our calculation and leave this as an open area for future development and investigation.

Once we have developed our formalism for charge-exchange reactions, the challenge is to operationalize these expressions in a reaction code. The next chapter discusses the code, CHEX, that has been developed to explore these reaction formalisms.

Chapter 3

Calculations and Inputs

3.1 Transfer Reactions with FRESCO

All transfer cross sections were calculated using the reaction code FRESCO [76]. Each of the different transfer reactions considered in this thesis followed the same basic prescription for calculating cross sections to various final states of interest. Any differences, if present, are noted in the discussion of the results. For all cases considered, (d,n) and (d,p) theoretical cross sections were calculated using the finite-range adiabatic approximation [70, 71] described in Section 2.3.1 which explicitly incorporates deuteron breakup in the field of the target. To implement the ADWA formalism, the adiabatic optical potential for the incoming channel must be constructed from proton and neutron optical potentials and then fed into FRESCO. The effective adiabatic potentials for (d,p) and (d,n) were computed with TWOFNR [77]. The CH89 [2] optical potential was used for the nucleon-target interactions in the initial and final channels.

The deuteron bound state in the initial channel is parameterized using the Reid soft core NN interaction [78] (built into FRESCO). For consistency, the V_{vb} interaction in the transition amplitude from Equation (2.27) is also from [78]. In these calculations, the target nucleus is taken as inert and the final state of the target-like nucleus is modeled by placing the transferred nucleon into a single-particle bound state described by a real Woods-Saxon

potential with central and spin-orbit terms. The radius and diffuseness of the Woods-Saxon are chosen to be standard values of r=1.25 fm and a=0.65, respectively, and the depth of the spin-orbit term is chosen to be 6 MeV. For further discussion of the shape of this potential, see Section A.2. In the case of bound final states, FRESCO automatically adjusts the depth of the central potential to reproduce the experimental binding energy. In the case of unbound resonances in the final channel, we implemented either continuum binning or a bound state approximation which we explore in further detail now.

3.1.1 Bound State Approximation

For all of the cases considered in this work, the final states of astrophysical interest are low-lying, positive energy, resonances where the transferred particle sits in an excited state above the one proton separation energy. Still, these low-lying resonances exhibit many aspects of a bound excited state, including a confined wave function and well defined excitation energy with a relatively small width. In these cases, there are a couple of different choices for representing the final states.

Resonance states can be represented with continuum bins [67]. Using this method, one can place the resonance at the exact experimental excitation energy and calculate a wave packet (the integral of the corresponding wave function over energy or momentum) within a chosen energy window around the resonance. In this configuration, the potential depth of the single-particle Woods-Saxon is not automatically adjusted by FRESCO. Therefore, we manually tuned the depth of the Woods-Saxon until the phase shift goes through $\pi/2$ at the appropriate resonance energy. For narrow proton resonances at low excitation energies, the complete transition from 0 to π in phase can happen over the span of less than 1 eV (as compared to the natural energy scale of MeV) and locating this resonance is often difficult.

Once the resonance is located, the width can be calculated by taking the derivative of the phase shift and determining the full width at half max. Although using FRESCO to determine widths is an accurate and reliable method, it is inefficient and, for the narrowest resonances, infeasibly time consuming.

For most results presented in this thesis, we have sidestepped this process by using a bound state approximation. In this approximation, a low lying resonance is artificially bound by about 0.001 MeV. This is based on the idea that a resonance which is just slightly unbound will have a similar spacial distribution as a very shallow bound state. This is particularly valid in the case of proton transfer where the Coulomb barrier contributes to an even more localized resonance state. Of course, at some point, this approximation will break down as the resonance energy increases. Although this approximation has been widely used prior to the applications presented in this thesis, its accuracy had not been rigorously tested. Below, we present the effect of the bound state approximation on reaction cross section results for the particular case of resonant states in ^{31}S, and note that these results generalize to other nuclei studied in this thesis.

A reasonable place to start is to check that the wave functions produced by the artificially bound states behave similarly to the wave functions calculated using continuum binning. Figure 3.1 shows this comparison for a $l = 1$ proton resonance in ^{31}S at $E_x = 6.833$ MeV ($E_{res} = 702$ keV). It is clear that the unbound resonance behaves very similarly to a shallowly bound state and, therefore, it is reasonable to expect similar cross sections produced by the two configurations.

Next, we examined the impact of the bound state approximation on the angle integrated transfer cross section which will be used to constrain the astrophysical capture rate (see Section 2.3.2). To evaluate whether or not the bound state approximation is accurate, it

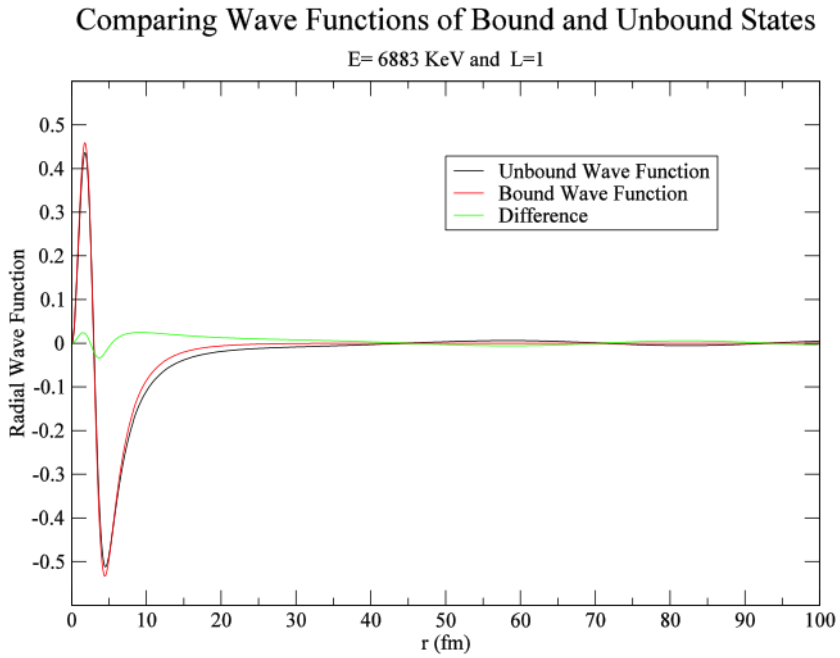

Figure 3.1: Comparing the single-particle wave functions created using the bound state approximation (red) and the exact calculation using continuum binning (black) for a proton resonance in ^{31}S at E_x=6833 keV. The green curve shows the difference between the two wave functions.

is important to compare the error introduced through this method with other errors and uncertainties present in our model. The main source of uncertainty in our calculations are the OMPs used to describe our incoming and outgoing distorted scattering waves. These optical potentials are obtained from fits to elastic scattering data between the nucleons and the initial (final) state nuclei at the initial (final) energies. However, for target and energy combinations for which this experimental information do not exist, one uses global optical potentials which are created by simultaneously fitting large data sets over a wide variety of energies and masses. These parameterizations describe trends across the nuclear chart, but are not necessarily valid for a given target at a particular energy, especially if it is unstable. Additionally, the parameterization for each potential contain around 15 different parameters and the choice of parameterization is not unique, leading to a large uncertainty, typically around 30%, but which has in some cases been shown to be over 100% [61].

Another, less rigorous, way to gauge the scale of the uncertainty introduced by the optical potential is to repeat the calculation using different global parameterizations and observe the effect on the angle integrated cross section. For example, all transfer results presented in this thesis use the parameterization by Varner et al. [2] (CH89), but these calculations can be repeated using another choice of global optical potential, such as the Becchetti-Greenlees parameterization [66]. When such a substitution is made, the propagated difference to the angle integrated cross section is at least on the order of about 10-15%, depending on the case. Errors from the bound state approximation will be independent of errors introduced by the optical potential and, thus, will be added in quadrature to those errors in our theoretical calculations. This means that the errors introduced through this bound state approximation should be significantly less than the errors introduced by the optical potentials to avoid a large proliferation of errors.

Table 3.1 shows the result of comparing the angle integrated transfer cross sections obtained using continuum bins to describe the unbound resonances and those obtained via the bound state approximation. As we would expect, the errors associated with this method increase as the resonance energy increases. Another clear trend is that the value of orbital angular momentum has a large impact on the effect of the approximation. For l=1 states the error is consistently higher than the error associated with l=2 or 3 states. This is not surprising as the potential barrier will be increased for larger values of angular momentum. This increased barrier will better mimic the potential of a bound state in an attractive potential well. This effect is evidenced in the single-particle widths calculated for these states. As the angular momentum increases, the resonances become narrower and behave more like bound states.

For ^{31}S, the error associated with the bound state approximation can be tolerated for

l=1 states including and below the resonance located at 226 keV, as we would expect the error to continue decreasing for lower energies. For l=1 states above that threshold, the bound state approximation introduces too large an error into our calculated cross sections, and continuum binning should be performed. Continuum binning is, however, much more feasible for these higher energy resonances with wider widths. It appears that the bound state approximation is safe to use for resonances with l >1 up to resonance energies of at least 450 keV. The error associated with the l=2 resonance with E_{res}=452 keV is only 2.4%, so it is reasonable to assume that the region of validity extends to significantly higher energies.

When applying this approximation to other systems, it will be imperative to locate the energy at which the error associated with the bound state approximation become too large. For l=0 and l=1 systems, this point seems to be much lower than was previously thought. For states with large orbital angular momentum, the approximation is very likely to hold for most resonances of interest.

Final State		Comparison				
E_{res} (keV)	E_x (keV)	n,l,j	Bound State Approximation xs (mb)	Continuum Binning xs (mb)	xs % Difference	Width (eV)
226.0	6357.0	2,1,1.5	1.52	1.43	6.13	3.67E-04
246.0	6377.0	1,3,3.5	6.68	6.75	-1.05	1.02E-06
262.0	6393.0	1,2,2.5	1.14	1.16	-1.39	2.64E-04
411.0	6542.0	2,1,1.5	1.04	0.92	12.05	1.02E00
452.0	6583.0	1,2,1.5	0.82	0.80	2.36	6.51E-02
702.0	6833.0	2,1,1.5	1.55	1.23	22.51	2.02E+02

Table 3.1: Comparison of angle integrated transfer cross sections to states in ^{31}S calculated using the bound state approximation and the continuum binning method. As the resonance energy increases, and the value of l decreases, the approximation breaks down.

3.2 Charge-Exchange Reactions with CHEX

All charge-exchange calculations presented here were produced using the reaction code, CHEX, developed for this thesis. Of course, there are a number of charge-exchange reaction

codes on the market, such as DW81 [79] for (p,n)/(n,p) reactions and FOLD [80] which can be used for the analysis of composite probes, such as (^{3}He,t). However, older codes, such as DW81, were not written with the expressed goal of exploring reaction dynamics and prove difficult for outside users to explore and extend. More modern codes such as FOLD are more accessible, but we decided it was necessary to build our code with components that we could fully understand and control, allowing for a stronger base for future extensions in the reaction mechanism. The goal of CHEX is for a flexible and user friendly tool that can be used for exploring and expanding the description of reaction dynamics for charge-exchange reactions. To this end, CHEX is built on a modular design where well described tasks occupy different subroutines. Additionally, CHEX utilizes a front end interface to solicit input parameters from the user. The general flow of CHEX calculations are shown in Figure 3.2.

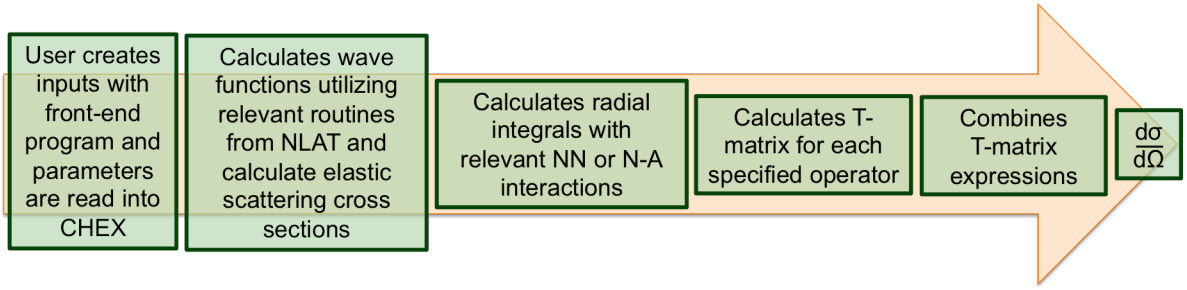

Figure 3.2: Flowchart showing the general organization of CHEX, the charge-exchange reaction code created for this thesis. The primary observables calculated by CHEX are charge-exchange cross sections.

The wave functions in CHEX are created using subroutines adapted from the NLAT reaction code [81]. NLAT (nonlocal adiabatic transfer) is a transfer reaction code which allows for the inclusion of non-local nucleon-target and bound state interactions. Within this context, the Schrödinger equation is solved using an iterative method. Although the effects of non-local potentials have not yet been explored in charge-exchange reactions, CHEX utilizes the NLAT Schrödinger equation solver to allow for an easy extension to including

effects from non-locality in future studies. Elastic scattering cross sections for the entrance and exit channels are also calculated. The remainder of this section will discuss some of the key inputs and methods used in CHEX charge-exchange calculations. For an outline of the benchmarks and checks performed for CHEX, see Appendix D.

3.2.1 Two-Body Calculations

As previously discussed, charge-exchange reactions described in a two-body framework utilize a Lane potential, defined in the equations in Section 2.4.1, which is proportional to the difference of neutron and proton optical potentials. The user is free to choose the form of these optical potentials. CHEX has incorporated Lane potentials based on the global potentials developed by Koning-Delaroche (KD) [1] and Varner et al. (CH89) [2]. Lane potentials derived from these OMPs have a non-zero range ∼7-8 fm, with the exact range depending on the case, and have real and imaginary components. As demonstrated in Figure 3.3 , Lane potentials derived from different optical potentials differ from one another significantly. In addition to the Lane interaction which mediates the charge-exchange, an optical potential must be chosen to describe the incoming and outgoing distorted waves. CHEX has built in options to use the KD or CH89 global potentials, or the user can input parameters for a specific OMP which is cast in the form discussed in 2.1.

In the two-body picture, the target has no internal structure and, therefore, bound-state wave functions do not enter into the cross-section calculations. Additionally, there is only an isospin central component. This greatly simplifies the two-body calculations and allows for short computation times.

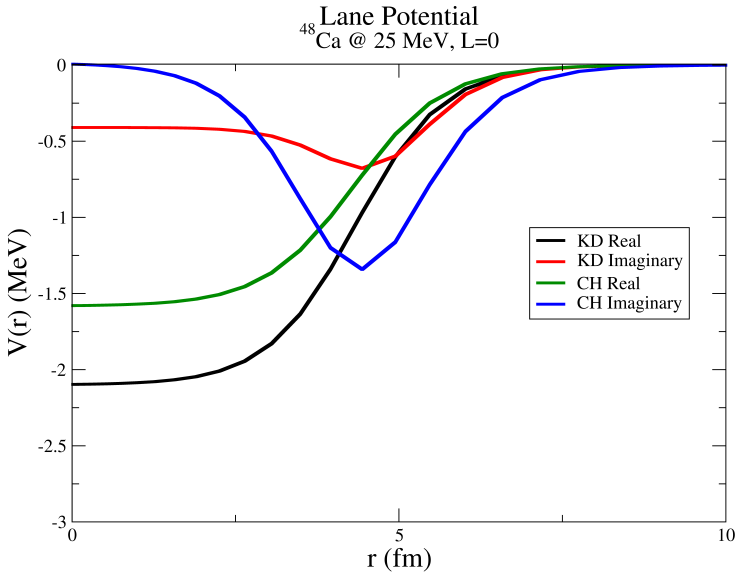

Figure 3.3: Plot of the radial form of the Lane potential calculated using parameters from KD and CH89. The case shown is for ^{48}Ca and L=0.

3.2.2 Three-Body Calculations

CHEX also includes the implementation of charge-exchange using the three-body formalism presented in this work. Similar to the two-body calculations described above, the user has the ability to specify the optical potential used to describe the incoming and outgoing distorted waves, and to specify the interaction that will mediate charge-exchange. CHEX has built in options to implement the isospin components of the NN interactions developed by Dechargé-Gogny (Gogny) [82] and Pudliner et al. (AV8'), which is based on the Argonne v_{18} potential [75, 83]. These potentials will be discussed in more detail in the following section. The user can also decide which operators to include in the calculation.

In the three-body picture, the target is comprised of an inert core with a valence particle in a well defined single-particle state. In this work we study nuclei that undergo transitions to their IAS. The IAS is the lowest energy excited state in the final nucleus with the same

isobaric spin, T, as the target nucleus. In a basic picture, the wave function of the IAS can be thought of as identical to the initial state, with a neutron replaced by a proton for the case of isospin lowering reactions or vice versa for isospin raising reactions. Unlike other reaction codes, such as DW81 and FOLD, the current version of CHEX does not input transition densities to many possible final states created by shell-model or other structure calculations. Instead, the user selects a specific initial and final single particle state with a value of l and j. This state is modeled using a Woods-Saxon potential with a radius of r_0=1.25 fm and a diffuseness of a=0.65. The user must adjust the depth of the potential to reproduce the experimental binding energies of these states. Because of this set up, CHEX is currently best suited to calculate specific microscopic transitions with well defined initial and final states.

3.2.3 Details of NN Potentials

One of the most important inputs in the charge-exchange calculations is the choice of NN interaction which mediates the charge-exchange reaction. One of the goals of this work is to explore the sensitivity of the charge-exchange observable to the choice of interaction. As a general note, CHEX is capable of incorporating any NN interaction which can be written in an operator form in position space. Most commonly, the effective NN interaction parameterized by Love and Franey (LF) [59, 60] is used to describe the isospin transition. LF is a phenomenological, energy dependent interaction that is cast in an operator form with isospin central, tensor, and spin-orbit terms. Each term uses a sum of real and imaginary Yukawa potentials with different ranges, correlating to π, ρ, and 2π meson exchange. The LF potential was fit to reproduce NN scattering data and, its updated form, includes in-medium effects which have been demonstrated to alter the bare NN potential [84]. LF has been tabulated for energies ranging from 50 MeV to 1000 MeV. The LF interaction has proven

to be a useful interaction for describing charge-exchange reaction data, although it is best constrained above about 100 MeV.

In the LF potential, the parameterization is chosen to explicitly and separately account for the knock-on exchange contributions to the transition amplitude. Exchange contributions arise from interchange of position of the projectile and valence nucleons [85]. The exchange contribution is estimated to be about 35% in [18]. At this time, CHEX does not implement an exchange term, either approximately or exactly. For this reason, the LF potential was not used in this analysis. Based on this, we impose the additional constraint that all NN interactions currently implemented in CHEX should not contain explicit parameterizations for knock-on exchange.

With this in mind, we selected two other NN interactions to implement in CHEX and explore the effect on charge-exchange cross sections. The first interaction chosen was AV8' [75]. AV8' is a reprojection of the Argonne v_{18} potential [83] which reduces the 18 terms to just 8, while still reproducing key features including the deuteron binding energy. v_{18} is a high-quality, bare, NN potential with 40 adjustable parameters that were fit to a database of thousands of nn, np, and pp scattering data, as well as the deuteron binding energy. Within this framework, v_{18} obtains a χ^2 per datum of 1.09 over an energy range of 0-350 MeV. Unlike the Lane and LF interactions, v_{18} is fully real and is not energy dependent. It can be written in an operator form with 18 distinct operators, half of which contain isospin operators.

A full implementation of the 9 relevant isospin terms for v_{18} is a complicated task and lies outside the scope of this thesis. Additionally, choosing to implement only some of those 9 operators is risky because v_{18} is not fit on an operator by operator basis and, therefore, it can be difficult to predict the effect of excluding operators. This effect is amplified by

the fact that reaction amplitudes from various components are able to add destructively. For this reason we, instead, implemented AV8'. AV8' has only 8 operator terms and can be expressed as

$$v'_{ij} = \sum_{p=1,8} v'_p(r_{ij}) O^p_{ij} \tag{3.1}$$

where the various operators are: central, isospin central, spin-spin, isospin spin-spin, tensor, isospin tensor, spin-orbit, and isospin spin-orbit. These operators are expressed as

$$O^{p=1,8}_{ij} = 1, (\boldsymbol{\tau_i} \cdot \boldsymbol{\tau_j}), (\boldsymbol{\sigma_i} \cdot \boldsymbol{\sigma_j}), (\boldsymbol{\sigma_i} \cdot \boldsymbol{\sigma_j})(\boldsymbol{\tau_i} \cdot \boldsymbol{\tau_f}), S_{ij}, S_{ij}(\boldsymbol{\tau_i} \cdot \boldsymbol{\tau_f}), (\boldsymbol{L} \cdot \boldsymbol{S}), (\boldsymbol{L} \cdot \boldsymbol{S})(\boldsymbol{\tau_i} \cdot \boldsymbol{\tau_f}), \tag{3.2}$$

respectively, and $v'_p(r_{ij})$ gives the radial form of each term. The strength of the radial forms are derived from a recombination of the first 14, charge-independence components of v_{18}. For the purpose of charge-exchange reactions, we only need to consider contributions from isospin dependent forms, reducing the potential which must be implemented to just four terms:

$$\begin{aligned} v'_{ij}(r_{ij}) = v'_2(r_{ij})(\boldsymbol{\tau_i} \cdot \boldsymbol{\tau_j}) + v'_4(r_{ij})(\boldsymbol{\sigma_i} \cdot \boldsymbol{\sigma_j})(\boldsymbol{\tau_i} \cdot \boldsymbol{\tau_f}) \\ + v'_6(r_{ij}) S_{ij}(\boldsymbol{\tau_i} \cdot \boldsymbol{\tau_f}) + v'_8(r_{ij})(\boldsymbol{L} \cdot \boldsymbol{S})(\boldsymbol{\tau_i} \cdot \boldsymbol{\tau_f}). \end{aligned} \tag{3.3}$$

The T-matrix for each operator is calculated in a separate subroutine in CHEX, and then combined. The radial form factors of the operators are implemented using a subroutine from [86] and are shown in Figure 3.4.

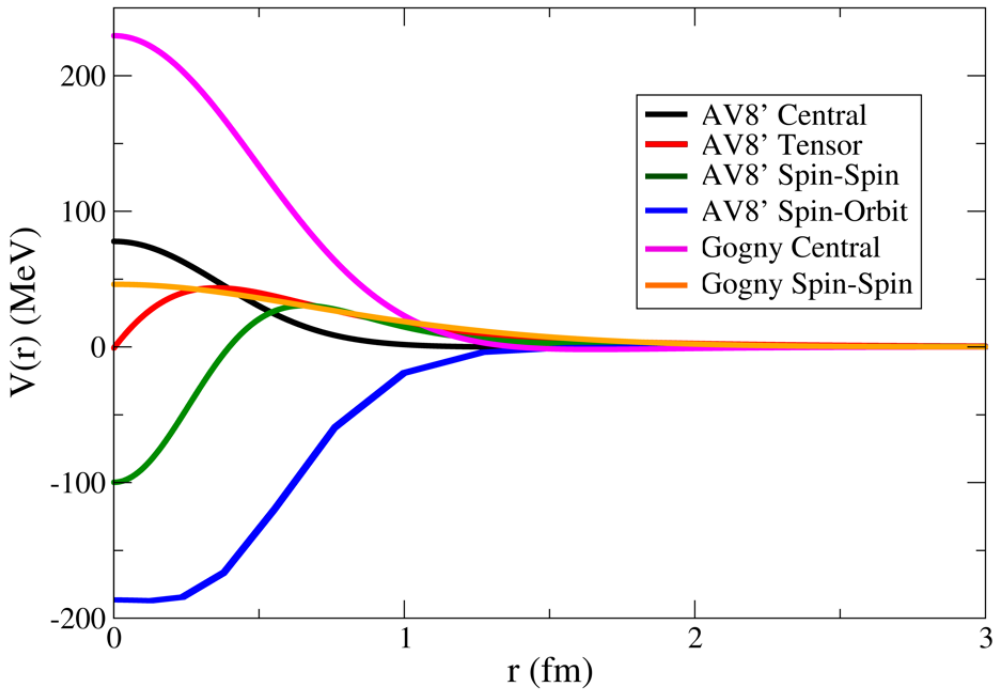

Figure 3.4: Plot of the radial form factors of the AV8' and Gogny potential operators considered in this work.

AV8' is a bare NN interaction, like v_{18}. We know that nucleons undergoing charge-exchange reactions will feel the effects of other nucleons in the target. However, one could imagine a scenario where, as the valence nucleon undergoing charge-exchange in our model becomes less and less bound, these effects might begin to decrease. For this reason, we would like to study the charge-exchange response to bare NN interactions. Additionally, for this work, we have chosen the Gogny interaction [82], which does include in-medium effects.

The Gogny interaction is a real, effective interaction. Although it also contains a density dependent and spin-orbit term, for our purposes studying charge-exchange reactions, it takes the simple form of the sum of Gaussians,

$$V(r) = \sum_{i=1,2} (HP_\tau - MP_\sigma P_\tau)_i e^{-r^2/\mu_i^2} \tag{3.4}$$

where r is the distance between the nucleons, M, H, and μ are parameters which specify the strength of the interaction, and $P_\tau = \frac{1}{2}(1 + \hat{\boldsymbol{\tau}}_\mathbf{1} \cdot \hat{\boldsymbol{\tau}}_\mathbf{2})$. Because we are only concerned with terms which can cause an isospin transition, this expression can be stated as

$$V(r) = \sum_{i=1,2} \frac{1}{2}(H(\hat{\boldsymbol{\tau}}_\mathbf{1} \cdot \hat{\boldsymbol{\tau}}_\mathbf{2}) - M(\hat{\boldsymbol{\sigma}}_\mathbf{1} \cdot \hat{\boldsymbol{\sigma}}_\mathbf{2})(\hat{\boldsymbol{\tau}}_\mathbf{1} \cdot \hat{\boldsymbol{\tau}}_\mathbf{2}))_i e^{-r^2/\mu_i^2}. \tag{3.5}$$

The Gaussians used simulate a short range and intermediate range interaction. Because the Gogny interaction seeks to describe in-medium effects, it was fit using a different, and much smaller set of nuclear data from AV8', including empirical data in nuclear matter, such as nuclear symmetry energy. The parameters used in these calculation are: $\mu_1 = 0.7$fm, $\mu_2 = 1.2$ fm, $H_1 = -496.2$ MeV, $H_2 = 37.27$ MeV, $M_1 = -32.56$ MeV, $M_2 = -68.81$ MeV and produce the forms shown in Figure 3.4.

Chapter 4

Results

4.1 Selected Transfer Results

This section contains a detailed look at the methods and results for a study of the ^{30}P(d,n)^{31}S reaction with applications to the astrophysical ^{30}P(p,γ)^{31}S capture reaction. Additionally, Section 4.1.4 discusses an extension of this method to study ^{23}Al(d,n)^{24}Si for applications to the ^{23}Al(p,γ)^{24}Si astrophysical reaction rate. The analysis of the ^{56}Ni(d,n)^{57}Cu and ^{56}Ni(d,p)^{57}Ni reactions are briefly summarized in Appendix A.1.

4.1.1 Motivation for Studying ^{30}P(p,γ)^{31}S via ^{30}P(d,n)^{31}S

The astrophysical proton capture reaction rate for ^{30}P(p,γ)^{31}S remains one of the largest uncertainties in models of oxygen neon (ONe) novae explosions. In these systems, an ONe white dwarf star is in a binary system with a hydrogen-rich companion star which accretes mass onto the surface of the white dwarf until the temperature and pressure build up enough to ignite an explosive thermonuclear runaway [87]. Nucleosynthesis in this environment follows the path of the rp-process discussed in Section 1.2, terminating with the production of elements near Ca. Although the rp-process involves a complex network of capture reactions and beta decays, it has been shown that uncertainty in the ^{30}P(p,γ)^{31}S reaction rate plays a key role in determining the synthesis of heavier elements in the rp-process [88].

Additionally, the structure of the final state nucleus, ^{31}S, remains largely unknown. Past experimental studies that examined this nucleus yielded conflicting results for the final state spins and parities [89, 90, 91] and updated shell model calculations which include the full *sd-pf* model space indicated that contributions from negative parity resonances are likely to dominate the proton capture reaction rate in the Gamow window [92, 93]. Determining the exact location and spins of these negative parity states is crucial to minimizing the large uncertainties remaining in the proton capture reaction rate.

However, direct measurements of ^{30}P(p,γ)^{31}S are not currently feasible. ^{30}P has a half life of 2.5 minutes, so experiments must be run in inverse kinematics with rare isotope beams. Beam energies must be well below the Coulomb barrier to directly populate the final states of interest ($E_p < 500$ keV), greatly suppressing the reaction cross section and rendering the radioactive isotope beam intensity insufficient for a direct measurement. For these reasons, the ^{30}P(d,n)^{31}S transfer reaction has been used to probe the astrophysical capture rate through the extraction of spectroscopic factors, as described in Section 2.3.2.

4.1.2 Experimental and Theoretical Methods

The experimental ^{30}P(d,n)^{31}S transfer cross sections were measured by our collaborators at the National Superconducting Cyclotron Laboratory at Michigan State University [94]. A 30 MeV/u beam of ^{30}P was created via in-flight fragmentation and impinged on a solid deuterated target, populating the excited states of interest in ^{31}S. These excited states quickly decay to bound states, releasing γ rays that were detected by GRETINA (Gamma-Ray Energy Tracking In-beam Array) which surrounded the target. GRETINA is a high-resolution, high-efficiency, γ ray detector capable of an energy resolution around 2-3 keV in the energy region of interest [95]. The heavy ^{31}S reaction products have a large forward

momentum and continue moving in the direction of the beam until detected in the S800 Spectrograph [96]. This method can be used to determine the transfer cross section to each of the excited states of interest through ^{31}S-γ coincidence. The cross section to the ground state, however, cannot be measured directly because it will not decay via γ emission. Additionally, the outgoing neutron is not detected and the γ ray statistics are insufficient to extract angular distribution information, so only the angle integrated cross section to each final state can be compared to theoretical calculations. This method was first validated for the case of ^{26}Al(d,n)^{27}Si, successfully reproducing known spectroscopic factors and resonance strengths [94].

We then calculated theoretical transfer cross sections for each observed state, according to the procedure described in Section 3.1. For each of the excited states of astrophysical interest, the bound state approximation provided sufficient accuracy. Spectroscopic factors for each transition were then extracted by taking the ratio of the experimental angle integrated cross section to the theoretical cross sections. In several cases where a transition was not observed in GRETINA, there was an upper bound placed on the cross section and, therefore, the spectroscopic factor. Once S is obtained, resonance strengths for each state that will significantly contribute to the astrophysical capture rate were calculated according to the procedure presented in Section 2.3.2.

4.1.3 Results and Conclusions

A summary of the results for the cross sections, spectroscopic factors, and relevant resonance strengths are summarized in Table 4.1. Full results for this work are available in [3].

A key result from this work is that the three strongest states measured in this experiment are all negative parity states and they correlate with the three states predicted to have the

E_x (keV)	E_{res} (KeV)	$J_i^\pi \rightarrow J_f^\pi$	σ_{exp} (mb)	σ_{th} (mb)	C^2S_{exp}	C^2S_{SM}	l	$\omega\gamma$
6138.6(6)	8.0(6)	$(3/2^+, 7/2^+) \rightarrow 7/2^+$	≤ 0.030	0.188	$\leq 0.16(7)$		0	
6158.5(5)	27.9(6)	$7/2^{(-)} \rightarrow 7/2^-$	0.177(33)	4.94	0.036(13)	0.26	3	
		$7/2^{(-)} \rightarrow 5/2^+$						
6255.3(5)	124.7(6)	$1/2^+ \rightarrow 1/2^+$	≤ 0.019	.0938	≤ 0.19		0	9.5×10^{-12}
6279.0(6)	148.4(6)	$3/2^+$	≤ 0.029	0.188	≤ 0.16		0	
6327.0(5)	196.4(6)	$3/2^- \rightarrow 1/2^+$	0.025(10)	1.07	0.023(12)	0.29	1	$3.5(19) \times 10^{-7}$
6357.3(2)	226.7(3)	$5/2-$	≤ 0.017	1.60	≤ 0.011		1	$\leq 1.4 \times 10^{-6}$
6376.9(4)	246.3(5)	$9/2^- \rightarrow 7/2^-$	0.32(5)	6.21	0.051(17)	0.39	3	
		$9/2^- \rightarrow 7/2^+$						
6390.2(7)	259.6(7)	$3/2^+$	≤ 0.042	0.189	≤ 0.22		0	2.4×10^{-5}
6392.5(2)	261.9(3)	$5/2^{(+)} \rightarrow 3/2^+$	0.034(9)	4.66	0.007(3)	0.0032	2	$4.8(21) \times 10^{-7}$
6394.2(2)	263.6(3)	$11/2^+$	≤ 0.018	1.20	≤ 0.002		4	
6541.9(4)	411.3(5)	$7/2^+$	≤ 0.037	6.21	$\leq 5.9 \times 10^{-3}$		2	$\leq 1.7 \times 10^{-4}$
6583.1(20)	452.5(20)	(7/2)	≤ 0.027	3.72	≤ 0.007		3	

Table 4.1: Summary of results from [3] for the study of ^{30}P(p,γ)^{31}S via ^{30}P(d,n)^{31}S. Transitions which were not observed in the experiment provide upper limits for the experimental cross sections and spectroscopic factors. Theoretical spectroscopic factors are shown for observed transitions and were produced via the shell model using the USDA Hamiltonian [4] for positive parity states and the WBP Hamiltonian [5] for negative parity states. Resonance strengths are shown for states that will contribute significantly to the proton capture reaction rate, noting that states with high l value will be suppressed.

largest spectroscopic factors by shell model calculations. It is notable however, that all of the measured spectroscopic factors corresponding to negative parity states are about an order of magnitude smaller than those predicted in the shell model. This indicates that the single-particle strength is, in fact, highly fragmented. This is not unreasonable given the complicated structure of the odd-odd nucleus, ^{30}P, which has many low-lying excited states. This result also indicates that the remaining single-particle strength must lie higher in excitation energy than about 6.7 MeV (about 0.5 MeV above the proton emission threshold). Above this energy, proton decays begin to compete with and dominate γ decay as a means to depopulate excited states in ^{31}S and, once this occurs, it is no longer a good approximation to purport that $\Gamma_\gamma \gg \Gamma_p$. In this case, the resonance strength becomes sensitive to both the proton decay width and gamma decay width, invalidating the approximation in Equation (2.33) and the experimental method.

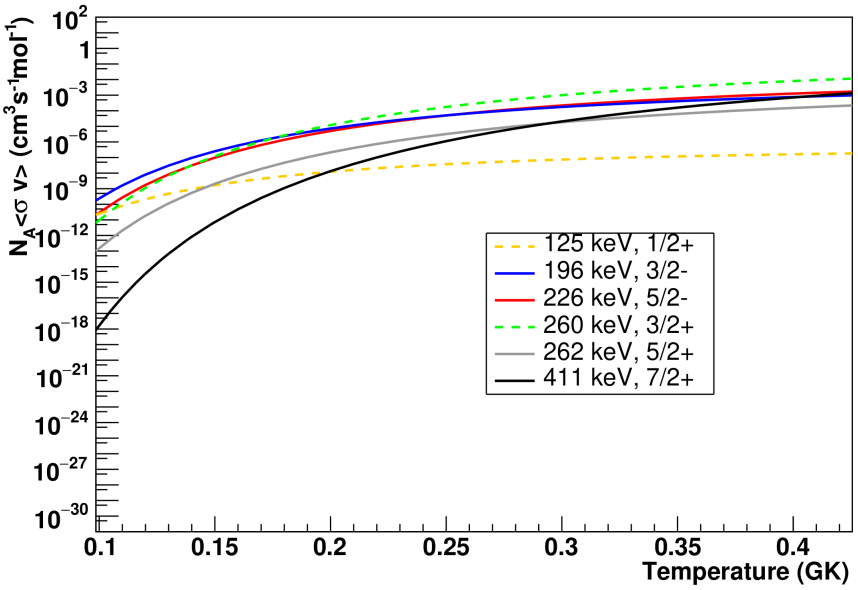

Figure 4.1: The proton capture reaction rate for various final states of ^{30}P(p,γ)^{31}S in the astrophysical temperature range relevant for novae. Solid lines indicate the use of spectroscopic factors extracted from this work. In cases where a final state was not observed, the spectroscopic factor is provided by theoretical shell model calculations. At low temperatures the $3/2^-$ state at 196 keV dominates the reaction rate, but at high temperatures, the $3/2^+$ state at 260 keV might become dominant, although this state was not observed in [3]. Figure adapted from [3].

The resonance strengths determined or constrained by upper limits in this study can then be used to calculate proton capture rates over the temperature range relevant for novae events. Those reaction rates are shown in Figure 4.1. States that were experimentally constrained by (d,n) in this study are shown in the full lines, while results from fully theoretical (p,γ) predictions are indicated by dashed lines. In particular, the resonance strength of the $3/2^+$ resonance at 260 keV comes from shell model calculations using the USDE interaction calculated in [89]. For temperatures between about 0.10 and 0.17 GK, the $3/2^-$ state at 196 keV which was first constrained by this work is expected to dominate the reaction rate. It is notable that, because the spectroscopic factor extracted here was much smaller than shell model predictions, this marks a significant decrease in the predicted reaction rate at low temperatures. Above about 0.17 GK, the $3/2^+$ resonance at 260 keV is predicted to

dominate the reaction rate. However, this state was not measured in the work presented here and, therefore, the reaction rate shown in Figure 4.1 is based solely on shell model predictions, which is likely to be significantly higher than the true reaction rate. Measuring this state will be crucial to further reducing the uncertainty in the ^{30}P(p,γ)^{31}S reaction rate. Nevertheless, this study marks the first experimental constraints of the ^{30}P(p,γ)^{31}S reaction rate and has reduced the overall uncertainty, particularly at temperatures between about 0.10 and 0.17 GK, in this key reaction for novae nucleosynthesis.

While this work was able to successfully constrain the spectroscopic factors for states in ^{31}S, it is oftentimes difficult to determine the correct l and j values for the single particle, final state, resonances. This information is encoded in the shape of the angular distribution, whose first peak is pushed towards higher angles for higher values of angular momentum transfer (l). This probably is particularly pronounced for targets with non-zero spin, allowing for more angular momentum couplings. Additionally, spectroscopic factors extracted at the first peak of the distribution, as opposed to from the total angle integrated cross section, are more exact. For this reason, an experimental advance that allowed for a measurement of angular distributions would be useful. This is difficult in the case of (d,n) transfer reactions where beam rates for radioactive isotopes are relatively low and, of course, detection of the emitted neutrons in the final state is much more difficult that charged particle detection.

4.1.4 ^{23}Al(d,n)^{24}Si

In type-I x-ray bursts (XRBs), a neutron star is in a binary system with a companion, low mass main sequence or red giant star, which is accreting hydrogen rich material onto the surface of the neutron stars. The transferred mass reaches high temperatures and densities until it eventually ignites thermonuclear runaway powered by hydrogen and helium burning

[23]. Recent advances in modeling XRBs could allow us to constrain neutron star properties, such as the mass and radius, but these models depend on nuclear reaction network inputs. Therefore, it is essential to reduce the large uncertainties in some key hydrogen and helium burning reaction rates in order to obtain meaningful neutron star properties from these models.

The ^{23}Al(p,γ)^{24}Si reaction rate has been shown by systematic studies to have a significant effect on the XRB light curve [97, 98]. These curves, which show luminosity over time, are the primary observables of XRBs. Similarly to the ^{30}P(p,γ) case, direct measurement of the proton capture reaction on ^{23}Al is not possible because of Coulomb suppression of the cross section to final excited states of interest. Additionally, ^{23}Al is unstable, with a half-life of about 0.47 seconds, so the experiment must be performed in inverse kinematics. Therefore, the ^{23}Al(d,n)^{24}Si transfer reaction is used as a probe for the astrophysical capture rate.

A similar procedure to that described in Section 4.1 was used to measure the ^{23}Al(d,n)^{24}Si, this time using a 48 MeV/u beam of ^{23}Al impinging on the deuterated target. As before, GRETINA was used to measure γ rays from the de-exciting final state in ^{24}Si in coincidence with heavy ion detection of ^{24}Si in the S800. Unique to this experiment was the addition of the low-energy neutron detector array (LENDA) to also measure the outgoing low energy neutrons from the (d,n) transfer. This setup allows for a complete measurement of the transfer reaction and, if enough neutrons are detected, could provide angular distribution information for the cross sections of various excited states, simplifying the comparison to theoretical calculations.

Theoretical transfer cross sections were produced in the ADWA framework using FRESCO and TWOFNR using the same potentials and procedures discussed in Section 3.1. As before, the theoretical spectroscopic factors were calculated in the framework of the shell model, this

time using the USDB interaction [4]. Because the ground state of ^{23}Al is $5/2^+$, there are many possible values of l transfer that couple to the appropriate initial and final spin of the target nucleus. Therefore, these theoretical cross sections for each l value were combined to obtain experimental spectroscopic factors according to the relation

$$C^2S^i_{exp} = \frac{C^2S^i_{theo} \times \sigma^i_{theo}}{\sum_{i'}(C^2S^{i'}_{theo} \times \sigma^{i'}_{theo})} \times \frac{\sigma_{exp}}{\sigma^i_{theo}} \tag{4.1}$$

where the sum over i' runs over all of the possible lj quantum number combinations for each of the final excited states. A summary of these results for the observed populations of states in ^{24}Si are shown in Table 4.1. The partial cross section listed for the ground state was obtained by subtracting the sum of all excited state cross sections measured in GRETINA from the total cross section measured in the S800. The state at 3471 keV has two possible spin assignments, 0^+ or 4^+, and no conclusion was made regarding this state, so both results are given. Resonance strengths are shown for the resonance states measured in this work.

E_x (keV)	E_{res} (KeV)	$J^\pi_i \rightarrow J^\pi_f$	σ_{exp} (μb)	σ_{th} (μb)	C^2S_{exp}	C^2S_{SM}	l	j	$\omega\gamma$
0			≤ 271	98	$\leq$2.8	3.44	2	5/2	
1874(3)		$2^+_1 \rightarrow 0^+_{g.s.}$	263(83)	139	0.6(2)	0.27	0	1/2	
				473	0.07(2)	0.03	2	3/2	
				411	0.4(1)	0.17	2	5/2	
3449(5)	156	$(2^+_2) \rightarrow 2^+_1$	78(41)	86	0.7(4)	0.45	0	1/2	4.2×10^{-5}
				402	0.002(1)	0.001	2	3/2	
				349	0.3(2)	0.176	2	5/2	
3471(6)	178	$(4^+_1) \rightarrow 2^+_1$	54(30)	722	0.07(4)	0.016	2	3/2	5.2×10^{-7}
				629	0.004(3)	0.001	2	5/2	
		$(0^+) \rightarrow 2^+_1$	54(30)	69	0.8(4)	0.24	2	5/2	5.0×10^{-6}

Table 4.2: Summary of results from [6] for the study of ^{23}Al(p,γ)^{24}Si via ^{23}Al(d,n)^{24}Si. Tentative spin allocations for states in ^{24}Si are shown in parenthesis and a final spin assignment could not be determined for the 3471 keV state. The ground state cross section represents an upper limit. Theoretical spectroscopic factors were produced in the shell model framework using the USDB interaction [4] and theoretical spectroscopic factors were determined using the relation given in Equation (4.1).

Unfortunately, due to low reaction yield, there were only about 100 counts registered in

LENDA between 6 and 16 MeV at the measured angles. With these low statistics, it was not possible to distinguish individual neutron distributions for the various final states measured in ^{24}Si. However, the total differential cross section could still be used to independently verify the results obtained from the GRETINA/S800 measurement. Each of the single l transfer theoretical cross sections could be weighted by their respective experimental spectroscopic factors and summed to create a total differential cross section and compared to the total cross section measured in LENDA. This comparison is shown in Figure 4.2 where the dashed lines indicate the uncertainty in the experimental spectroscopic factors. The agreement between the two measurements is remarkable and demonstrates the potential of using this method to extract all of the required information for astrophysical reaction rates with one experiment.

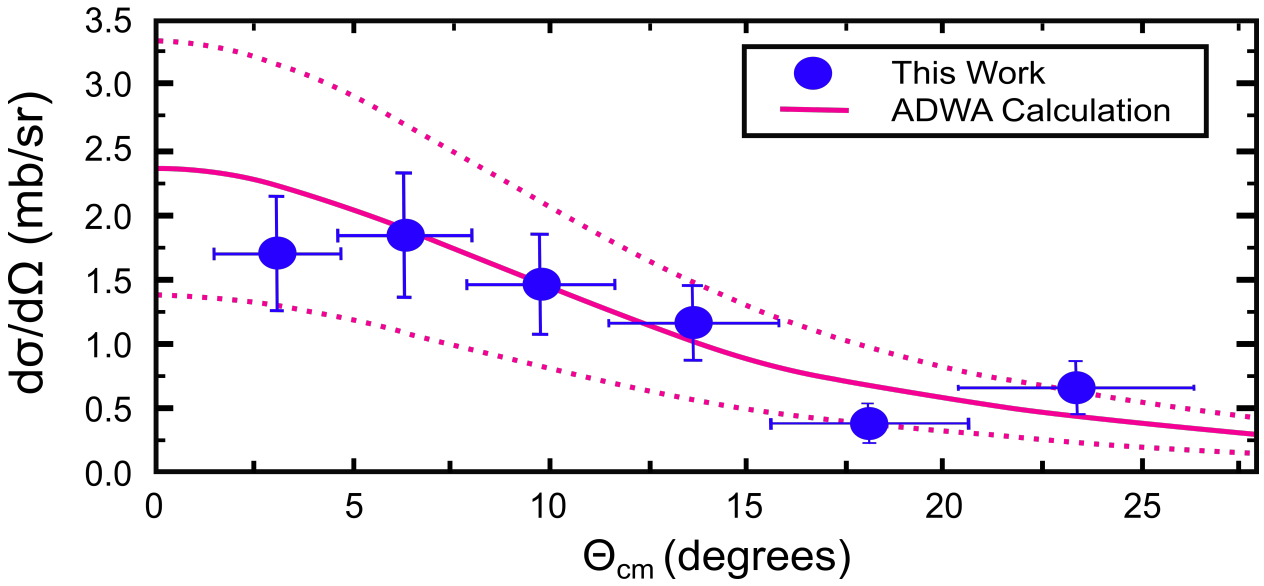

Figure 4.2: Differential cross section for ^{23}Al(d,n)^{24}Si in the center of mass system using the LENDA detector (blue dots) compared with the sum of theoretical distributions calculated using ADWA, weighted by experimental spectroscopic factors (solid pink). The error bands (dashed lines) are due to the uncertainty in the experimental spectroscopic factors. Figure adapted from [6].

When the results of this work are applied to the astrophysical reaction rate for ^{23}Al(p,γ)^{24}Si, the uncertainty is reduced by as much as 3-4 orders of magnitude in the temperature region

relevant for XRBs. This is shown in Figure 4.3. This reduction in uncertainties will allow for improved constrains on neutron-star compactness from XRB observations.

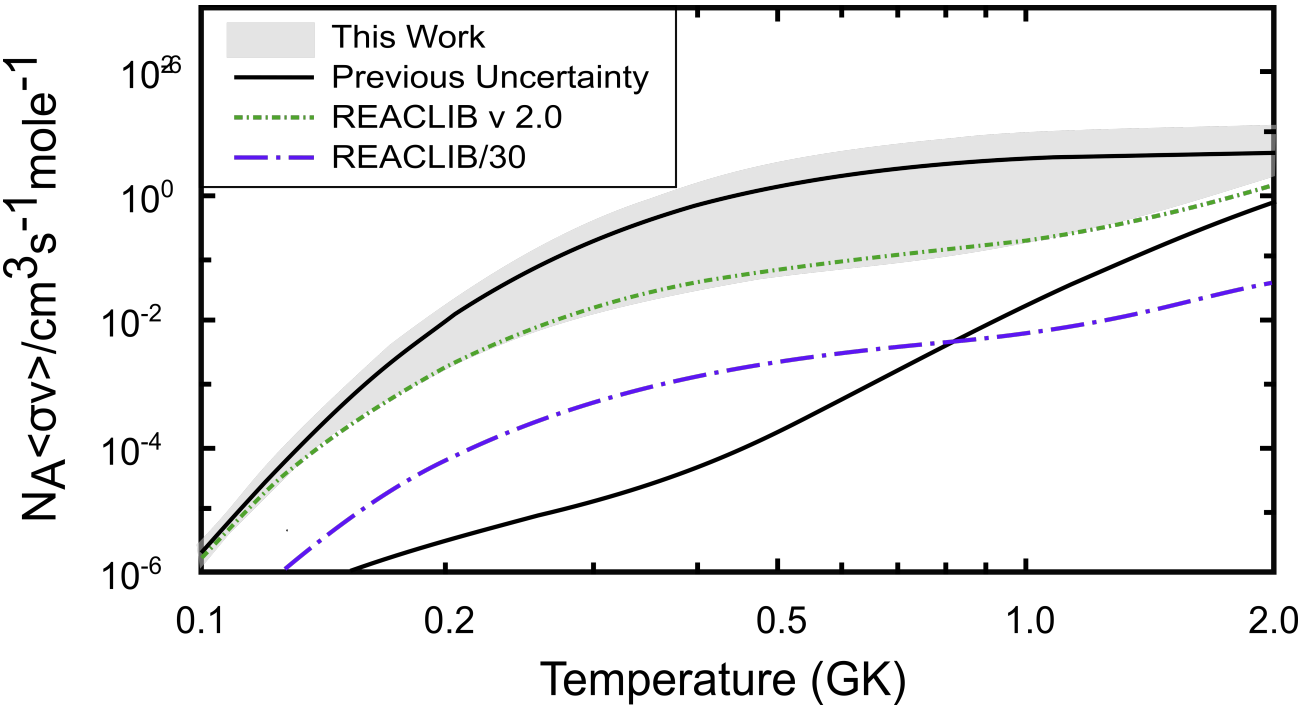

Figure 4.3: The 1-σ uncertainty band of the reaction rate determined by [6] is shown in grey, compared with the previous 1-σ uncertainty outlined in black. The green dashed line shows the recommendations from the REACLIB database which contain reaction rates to be used in astrophysical model calculations. The blue line shows the REACLIB value decreased by a factor of 30, which fell within previous uncertainties, but would be able to remove the by pass of material from the ^{22}Mg waiting point [16]. Figure adapted from [6].

4.2 Charge-Exchange Results

Investigation of charge-exchange reaction dynamics has not yet incorporated some of the recent developments developed for other reaction channels, such as transfer reactions and Coulomb dissociation (see [99, 55, 56, 57, 58]). In this work, we have begun some of these explorations and, in this chapter, we present the results of this initial study. In this work, we examined many facets of charge-exchange through a reaction theory lens, including the sensi-

tivity to the interaction which mediates charge-exchange and what effect the charge-exchange formalism has on the resulting cross sections (i.e. two-body vs. three-body framework).

We focused on (p,n) charge-exchange reactions to IAS in ^{14}C, ^{48}Ca, and ^{90}Zr. These targets were chosen because they span a large range of nuclear masses, their valence nucleons occupy shells with a large range of orbital angular momentum values (l), their final IAS are bound and, therefore, amenable to being modeled by our three-body formalism, and there is experimental charge-exchange cross section data available for each target's IAS transition. Each of these reactions are studied at three different lab energies: E=25, 35, and 45 MeV. It is worth noting that this energy range is much lower than charge-exchange reaction experiments typically used to extract transition strengths (i.e. B(GT)) using relations such as Equation (1.1). We chose to focus on this energy regime for a couple different reasons. First, in our current study we chose to study transitions between 0^+ IAS. Experimental data for these types of transitions are most common in this 20-50 MeV energy region. Additionally, a large motivation for studying charge-exchange reactions is to probe properties of the isovector density, which is most efficient with lower energy projectiles which probe the surface region of the target.

Experimental cross sections for ^{14}C(p,n) are taken from Taddeucci et al., where the reaction to the IAS was measured at E_{lab} = 25.7, 35 and 45 MeV [17]. Experimental error bars were estimated to be around 10% for all data points. Experimental charge-exchange cross section for ^{48}Ca(p,n) and ^{90}Zr(p,n) come from Doering et al., in which transitions were measured at E_{lab} = 25, 35 and 45 MeV for both targets [18]. For most data points in these sets, a 7% error bar was reported, although some data points, usually at large angles, have a larger percent error.

The charge-exchange results are organized in the following way: Section 4.2.1 presents

the results from our study of the two-body formalism introduced in Section 2.4.1. Calculations were performed using CHEX. This work is similar to the (p,n) reactions calculated in Danielewicz et al.[10], but here we will extend our calculations to explore the effect of utilizing different OMPs in the Lane potential which mediates the charge-exchange. We present results utilizing KD and CH89 optical potentials [1, 2]. Additionally we compare these results to experimental data.

Next, in section 4.2.2 we will present the results for charge-exchange reactions in the three-body framework introduced in Section 2.4.2. First, we comment on overall features of the cross sections in the framework, including trends with beam energy, target mass, and angular momentum of the valence nucleon. In this work we also explore the effect of various NN potentials, specifically the Gogny and AV8' interactions [82, 75, 83] and the effect of using different OMPs for the scattering wave functions. Finally, we compare these results to data and discuss the quality of that description.

In Section 4.2.3 we will explore the differences between results produced in the two-body and three-body calculations. Specifically, we explore the cause of significant differences in the magnitude and shapes of the angular distributions from two-body and three-body calculations. Finally, Section 4.2.5 discusses the limitations of this study, and the models used herein. We explore the possible effects of these constraints and present key areas for future exploration and extension.

4.2.1 Two-Body Results

In the first part of our charge-exchange study we calculated IAS charge-exchange transitions using a two-body formalism and a Lane-type potential to mediate the charge-exchange transition, as introduced in Section 2.4.1. For all cases presented here, we calculated the

charge-exchange cross section using two choices for the OMPs (KD and CH89). For consistency, the given parameter set was used to calculate both the distorted waves for the projectile-like nucleon and the Lane potential. Calculations for each of the cases studied here required less than 10 partial waves to converge and each calculation takes only a few seconds to run. In addition to the charge-exchange presented here, each run calculates the elastic scattering cross section for the incoming and outgoing nucleon. Although it does not effect the charge-exchange results presented here, we note that, as a general rule, the CH89 parameter set requires more partial waves than KD to converge the elastic scattering cross sections. This could be relevant to future work which makes use of these elastic scattering cross sections, particularly in applications to uncertainty quantification.

The two-body charge-exchange cross sections for each of the targets considered in this work are shown in left hand panels of Figures 4.4 (^{14}C), 4.5 (^{48}Ca), and 4.6 (^{90}Zr). Panels (a), (b), and (c) show the results for $E_{lab} = 25$, 35, and 45 MeV, respectively. Insets show the same information in a log scale, which is particularly helpful for clarifying behavior at large angles where cross sections are typically small. First we will remark on general properties of the results. Notably, all calculations are peaked at forward angles, which is compatible with the data that indicates a direct reaction process.

When comparing cross sections produced with KD versus CH89, it is clear that the choice of OMP has a large impact on the angular distributions that are produced. Although the general features of the cross sections for all targets and energy are preserved, the magnitude can change drastically between KD and CH89. Additionally, the diffraction patterns in the angular distributions are often shifted relative to one another, which is to be expected because the diffraction pattern is closely related to the radius parameter of the interaction (r_0) which varies between OMPs. One way to quantify the spread caused by the choice of

OMP is to look at the percent difference in the value of the cross section at the first peak. This percent difference ranges from 21% for ^{48}Ca(p,n) at 25 MeV, to 140% for ^{90}Zr(p,n) at 25 MeV. There is no clear trend with either target mass or projectile energy. The average percent difference over all of the cases presented here is 50%. As mentioned earlier, the variation produced through various choices of OMP gives a rough idea of the uncertainty in the calculation. The 50% value mentioned here is similar magnitude to the standard 30% uncertainties that are often cited in transfer reactions [100]. Of course, this is a very rough estimate and the 50% value here is the result of a given choice of two OMPs. This value would surely be different if we compared two different parameter sets. Still, this variation is sizable and a more rigorous uncertainty quantification effort, like those by Lovell et al. [68] which apply Bayesian methods to uncertainty quantification in transfer reactions, should be applied to charge-exchange. The full results for the percent difference are shown in the column labeled '2-Body Δ_{OMP}' in Table 4.3.

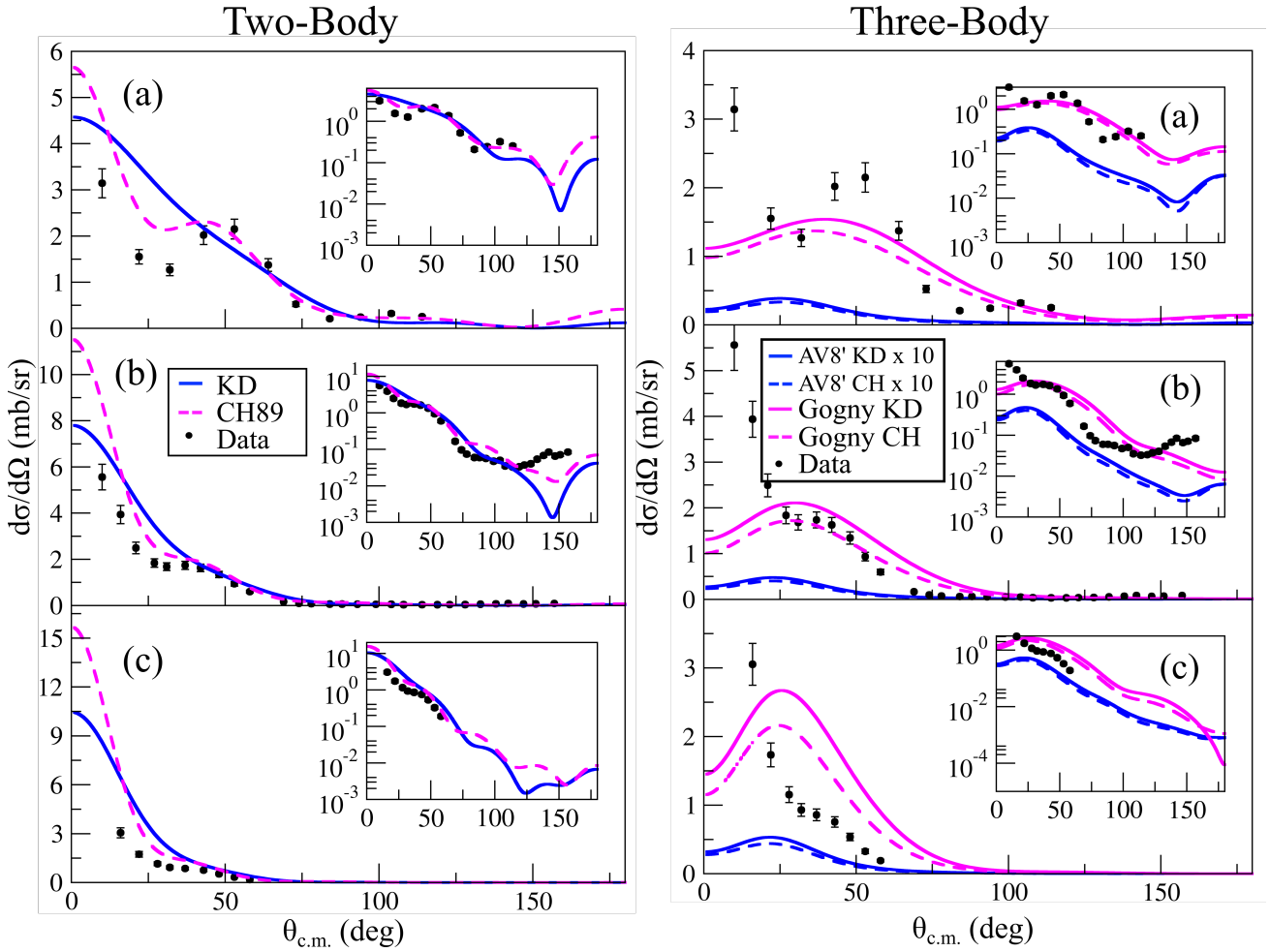

Figure 4.4: Charge-exchange cross sections for the ^{14}C(p,n)^{14}N^{IAS} transition at E_{lab} = 25 (a), 35 (b), and 45 (c) MeV. The left column shows the results for calculations using a two-body formalism with Lane potentials using OMP parameters from KD (solid blue) and CH89 (dashed pink). The right column shows the results for calculations using a three-body formalism. The solid/dashed blue lines utilized the AV8' NN interaction and distorted waves derived from KD/CH89. The solid/dashed pink lines utilized the Gogny NN interaction and distorted waves derived from KD/CH89. Insets show the same results in a log scale. Experimental data from [17] is shown in black.

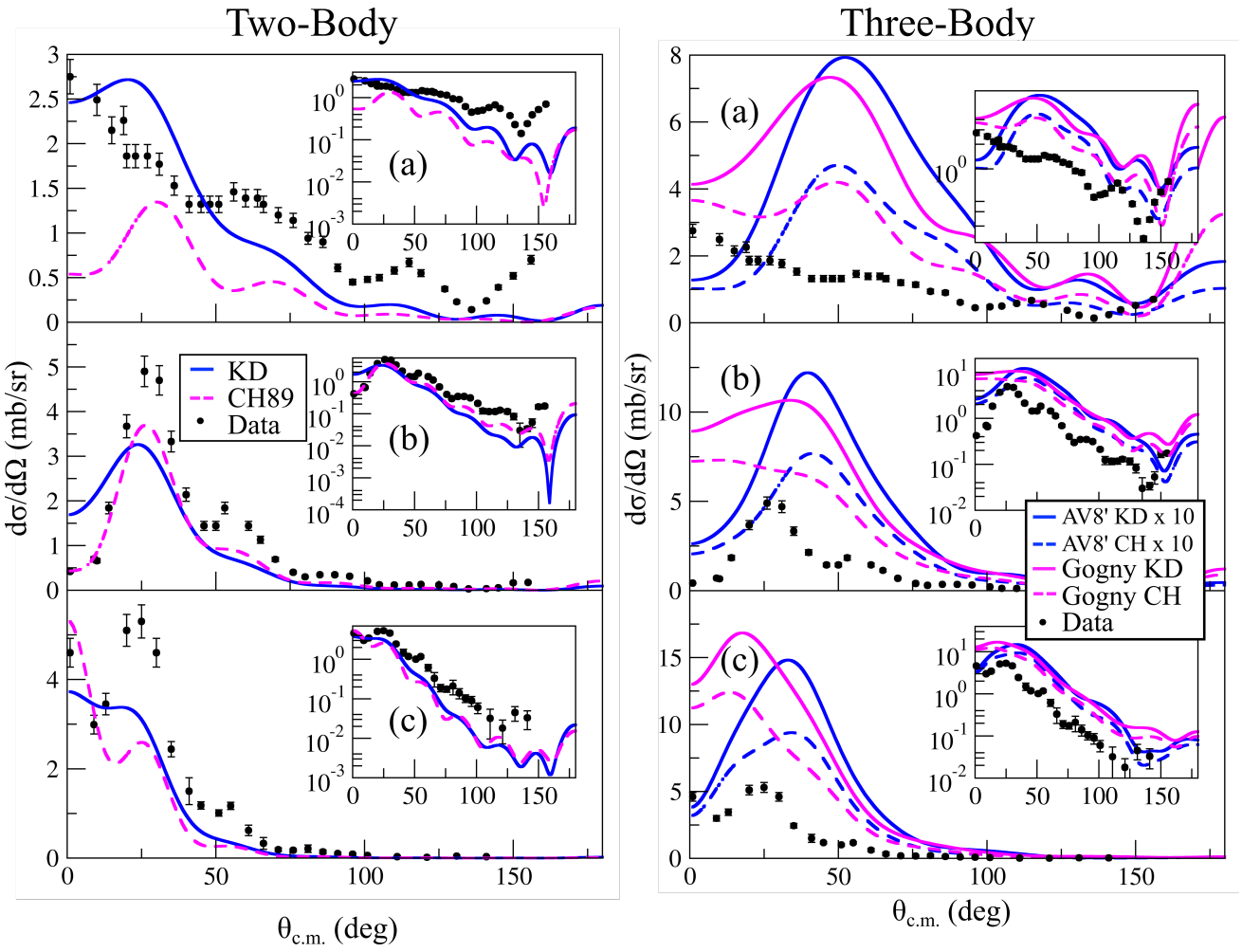

Figure 4.5: Charge-exchange cross sections for the ^{48}Ca(p,n)^{48}Sc^{IAS} transition at E_{lab} = 25 (a), 35 (b), and 45 (c) MeV. The left column shows the results for calculations using a two-body formalism with Lane potentials using OMP parameters from KD (solid blue) and CH89 (dashed pink). The right column shows the results for calculations using a three-body formalism. The solid/dashed blue lines utilized the AV8' NN interaction and distorted waves derived from KD/CH89. The solid/dashed pink lines utilized the Gogny NN interaction and distorted waves derived from KD/CH89. Insets show the same results in a log scale. Experimental data from [18] is shown in black.

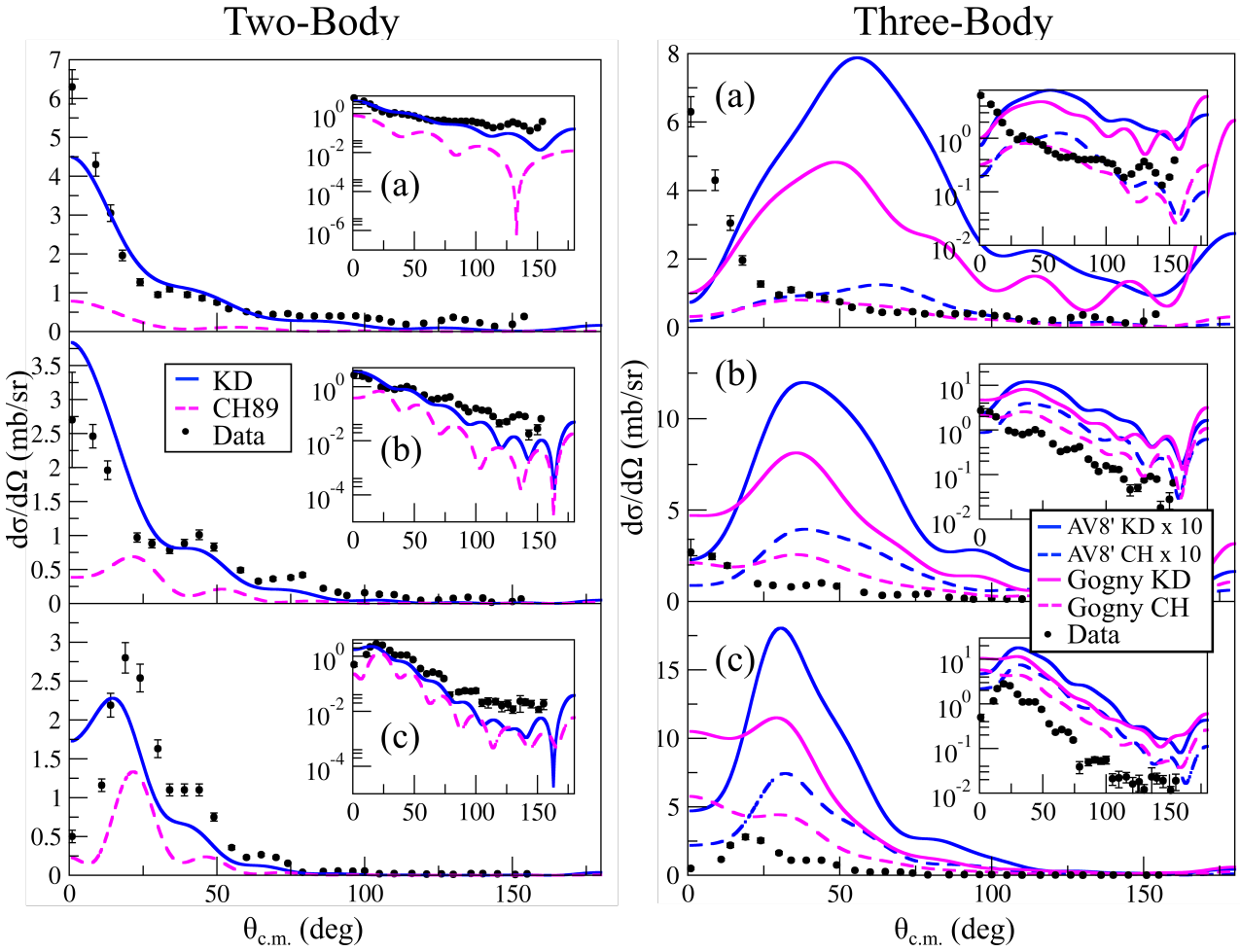

Figure 4.6: Charge-exchange cross sections for the ^{90}Zr(p,n)^{90}Nb^{IAS} transition at E_{lab} = 25 (a), 35 (b), and 45 (c) MeV. The left column shows the results for calculations using a two-body formalism with Lane potentials using OMP parameters from KD (solid blue) and CH89 (dashed pink). The right column shows the results for calculations using a three-body formalism. The solid/dashed blue lines utilized the AV8' NN interaction and distorted waves derived from KD/CH89. The solid/dashed pink lines utilized the Gogny NN interaction and distorted waves derived from KD/CH89. Insets show the same results in a log scale. Experimental data from [18]is shown in black.

Our two-body calculations can also be compared to experimental charge-exchange cross section data. As can be seen in panels (a)-(c) of Figures 4.4, 4.5, and 4.6, it is clear that the two-body charge-exchange calculations are able to capture the overall features of the charge-exchange data at small and large angles. Quantitatively, one option to explore the "goodness of fit" is through the traditional χ^2/N, defined as [67]

Reaction		Percent Difference Evaluated at θ_{peak}			
Target	E_{lab} (MeV)	2-Body Δ_{OMP}	Gogny Δ_{OMP}	AV8' Δ_{OMP}	3-Body Δ_{NN}
^{14}C	25	21	12	15	190
^{14}C	35	39	20	17	191
^{14}C	45	40	21	18	192
^{48}Ca	25	67	54	51	161
^{48}Ca	35	12	37	146	159
^{48}Ca	45	35	30	45	168
^{90}Zr	25	141	143	145	144
^{90}Zr	35	51	104	101	149
^{90}Zr	45	53	66	83	146

Table 4.3: Percent difference evaluated at the first peak for cross sections produced using different models.

$$\chi^2 = \sum_{i=1}^{N} \frac{(\sigma^{th}(i) - \sigma^{exp}(i))^2}{\Delta\sigma(i)^2}, \tag{4.2}$$

where i sums over all of the data points, and $\Delta\sigma(i)$ is the error in data point i and N is the number of data points. In the cases studied here, the typical experimental percent error was 10% for the reactions on ^{14}C and 7% for reactions on ^{48}Ca and ^{90}Zr. The second metric we will use is the percent of data, including experimental error bars, which falls between the normalized curves produced for each target/energy pair with differing choices of OMP. The rational is that two curves resulting from varied OMPs give a rough idea of the theoretical error, so this number represents that percent of the data which can be reproduced, within experimental and theoretical error bars. A summary of these values for the two-body calculations are given in Table 4.4.

The average χ^2/N and normalization values for two-body calculations produced with KD and CH89 OMP are very similar, implying that neither potential is preferable to describe the data. This notion is backed up by visual inspection of the cross section calculations in comparison to data. Although a particular potential may describe any specific data set

Reaction		2-Body KD		2-Body CH89		2-Body Δ_{OMP}
Target	E_{lab} (MeV)	χ^2/N	Norm	χ^2/N	Norm	% Data
^{14}C	25	5.20	0.60	1.67	0.80	33.33
^{14}C	35	8.33	0.60	5.73	0.60	33.33
^{14}C	45	0.86	0.50	0.51	0.60	70.00
^{48}Ca	25	16.02	1.00	16.87	2.30	13.89
^{48}Ca	35	22.05	0.50	5.94	1.40	30.30
^{48}Ca	45	3.22	1.40	5.63	1.40	24.00
^{90}Zr	25	13.87	1.10	21.40	7.10	24.24
^{90}Zr	35	15.10	1.10	22.87	2.90	16.67
^{90}Zr	45	8.34	1.00	5.28	3.70	34.38
Average						31.13

Table 4.4: Numerical comparison of two-body charge-exchange angular distributions to experimental data. The final column shows the percentage of the data, including experimental errors, which falls between the theoretical curves produced by two-body calculations with the KD and CH89 OMP.

better than the other, the opposite may be true for a different target/energy combination. This is unsurprising because OMPs are fit to large data sets and, while their fit might favor particular nuclei, they are optimized to best describe trends in elastic scattering data over a wide range of energies and target masses.

Finally, the percent of data captured by two-body calculations with various OMPs are shown in the final column of Table 4.4. The two-body calculations do a reasonable job of capturing trends in the data considering that these calculations included no free parameters, describing at least some data points in all cases. The percentage of captured data ranges from 13.89% for the case of ^{48}Ca(p,n) at 25 MeV, and 70.00% for the case of ^{14}C(p,n) at 45 MeV. The average percent of data captured among all data sets for our two-body calculations is 31.13%.

4.2.2 Three-Body Results

Next we present the results of our charge-exchange calculations utilizing the three-body formalism introduced in Section 2.4.2. For these calculations, we study the same IAS transitions in ^{14}C, ^{48}Ca, and ^{90}Zr at $E_{lab} = 25$, 35, and 45 MeV. For these calculations, the Lane potential operator is replaced by a NN operator which acts directly between the projectile and valence nucleons. For our study here, we considered the bare AV8' and in medium Gogny interactions (see Section 3.2.3) [75, 83, 82] . For the case of AV8', we included isospin contributions from the central, tensor, and spin-spin operators. For the Gogny interactions, we included isospin contributions from the central and spin-spin operators. Additionally, incoming and outgoing distorted waves were calculated using the KD and CH89 OMPs for all cases.

In the three-body formalism, we incorporate a bound state wave function for the valence nucleon in the target which will undergo charge-exchange. Each bound state is calculated using a real Woods-Saxson potential with quantum numbers, l and j. The angular momentum of each state, j, should match the spin of the core because we only consider transitions between 0^+ IAS in this work. The excitation energy of the bound state is an input to CHEX and the user then adjusts the depth of the Woods-Saxson potential (V_v) to reproduce the experimental binding energy. The other Woods-Saxon parameters, r_0 and a, are fixed at 1.25 fm and 0.65, respectively. There is also a spin-orbit term included in the bound state potential with a depth of 6.0 MeV. The parameters used to define the bound states used in these calculations are given in Table 4.5.

Charge-exchange reactions can involve a complicated admixture of transitions between initial and final states. In the work presented here, we only include a single transition

Nucleus	$E_x(MeV)$	l	j	Core Spin	Binding Energy (MeV)	V_v (MeV)
^{14}C	g.s.	1	0.5	0.5	8.17	48.6
^{14}N	2.31	1	0.5	0.5	5.24	48.7
^{48}Ca	g.s.	3	3.5	3.5	9.95	51.7
^{48}Sc	6.67	3	3.5	3.5	2.67	51.2
^{90}Zr	g.s.	4	4.5	4.5	11.97	46.6
^{90}Nb	5.01	4	4.5	4.5	0.07	58

Table 4.5: Bound state parameters used in the three-body calculations with CHEX.

between single particle states. While this is not, in general, a good approximation, here we study a limited set of cases involving transitions between 0^+ isobaric analog states. In each of the target nuclei, ^{14}C, ^{48}Ca, and ^{90}Zr, there is a shell closure or subshell closure for both proton and neutrons, indicating a simpler nuclear structure. To further test the validity of this assumption, we explicitly calculated the one body transition densities between ^{48}Ca and ^{48}Sc [101]. The one body transition density is defined as

$$OBTD = \frac{\langle f||[a^+_{k_\alpha,q'} \otimes \tilde{a}_{k_\beta,q}]^\lambda||i\rangle}{\sqrt{2\lambda+1}}, \tag{4.3}$$

where $\lambda = 1$ and $a^+_{k_\alpha,q'}$ is the creation operator which creates a particle with isospin projection $q = -1/2$ (neutron) with single particle quantum numbers, k_α. $\tilde{a}_{k_\beta,q}$ is the annihilation operator which destroys a particle with isospin projection $q = 1/2$ (proton) with single particle quantum numbers k_β. The calculation yielded a one body transition density very close to 1 (0.98648) for the $f_{7/2} \rightarrow f_{7/2}$ transition and gave negligible contributions for each other transition included in the calculation. Similar calculations were performed indicating the the ^{14}C transition was similarly dominated by a single $p_{1/2}$ transition. For the IAS in ^{90}Zr, the $g_{9/2} \rightarrow g_{9/2}$ transition is the most important configuration with a OBTD of 0.85, although there is a secondary $p_{1/2} \rightarrow p_{1/2}$ transition with a OBTD of 0.14 which is not included in

this work. However, as discussed later, we find that the cross section for a $p_{1/2} \rightarrow p_{1/2}$ transition is negligible compared to the cross section from the $g_{9/2} \rightarrow g_{9/2}$ configuration. This gives us confidence that the single-state approximation made throughout this work is valid these these specific transitions.

First we examine the three-body charge-exchange cross sections produced using the AV8' interaction, shown in Figure 4.7. Calculations for three-body cross sections with AV8' require about 10 partial waves to converge for all cases studied here, and typical run times range from about 1 min for the isospin central term to about 5-10 minutes for the isospin spin-spin term, although these calculations could be further optimized for speed. This quick convergence indicates that, even though our NN interactions have large radial form factors at $r_{12} = 0$, once the interaction is folded with our wave functions, the resulting T-matrix is well behaved. As with the two-body case, we observe that cross sections are peaked at relatively forward angles, consistent with the data which indicates a direct reaction process in all cases. In this figure, the cross section resulting from the isospin central, tensor, and spin-spin operators are shown separately, as well as the total cross section. We observe that, depending on the case, contributions from various components of the interaction can add constructively or destructively.

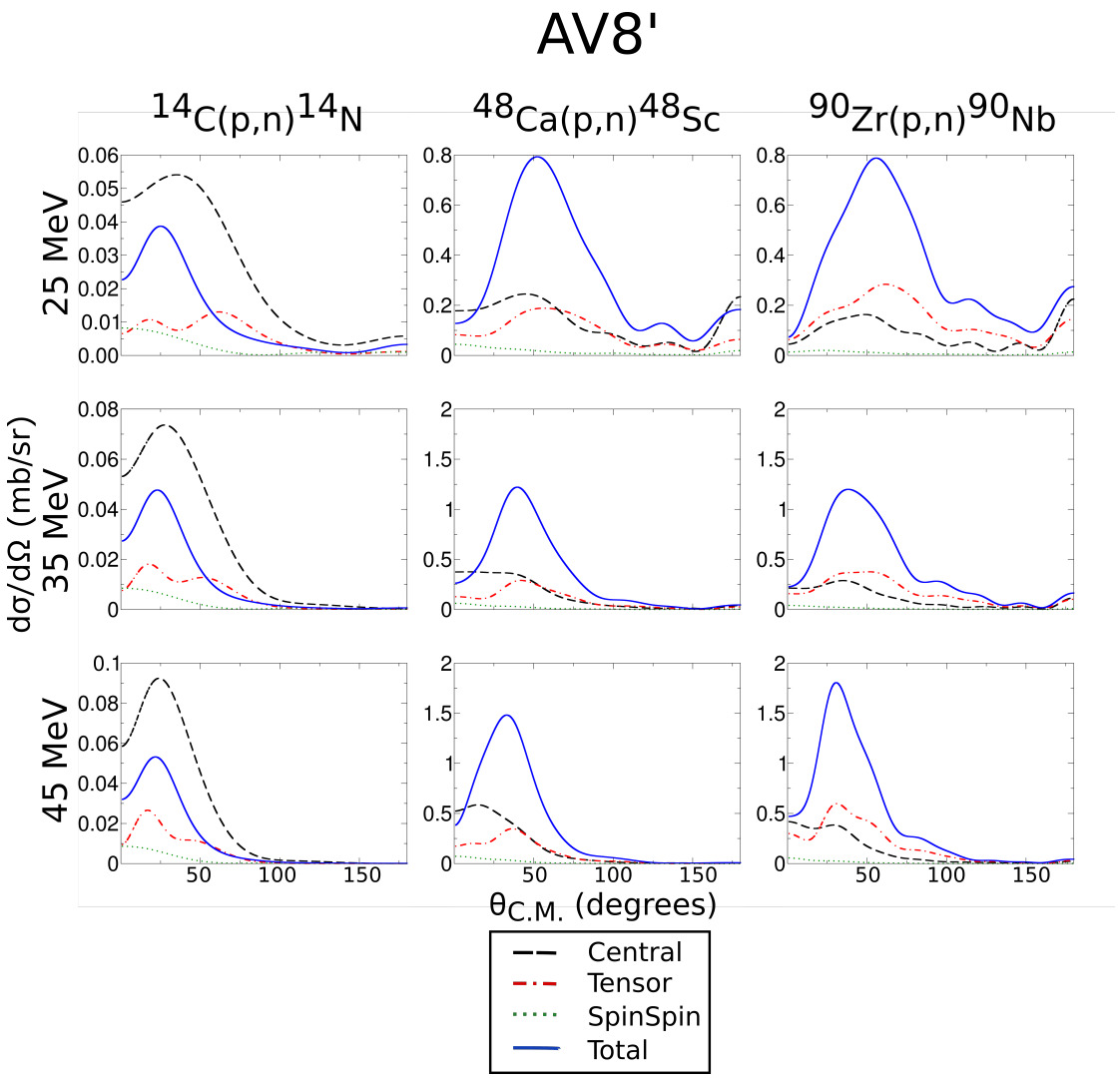

Figure 4.7: Charge-exchange cross sections for the ^{14}C(p,n)^{14}N^{IAS}, ^{48}Ca(p,n)^{48}Sc^{IAS}, and ^{90}Zr(p,n)^{90}Nb^{IAS} transitions at E_{lab} = 25, 35, and 45 MeV calculated using the AV8' potential. The contribution to the cross section from various potential operators are shown in dashed black for central, dotted green for spin-spin, dash-dotted red for tensor, and solid blue for the total cross section. Calculations shown here use the KD OMP for to calculate distorted waves.

As the beam energy increases, both the individual components of the cross sections and the total cross sections increase in magnitude and their first peaks shift to more forward angles. The location of the first peak of the total cross section increases with target mass, but in the cases chosen here, this also correlates to an increase in the angular momentum of the valence neutron, l. In order to try to disentangle these two effects, we ran a test calculation

of charge-exchange on ^{58}Fe which is heavier than ^{48}Ca, but has a valence nucleon with l=1, opposed to l=3 in ^{48}Ca or l=4 in ^{90}Zr. The results of this calculation are shown in Figure 4.8. The ^{58}Fe(p,n)^{58}Co cross section peaks around 30 degrees, compared to 52 degrees for ^{48}Ca(p,n)^{48}Sc and 25 degrees for ^{14}C(p,n)^{14}N. This indicates that the location of the first peak is a convolution of target mass and valence nucleon angular momentum.

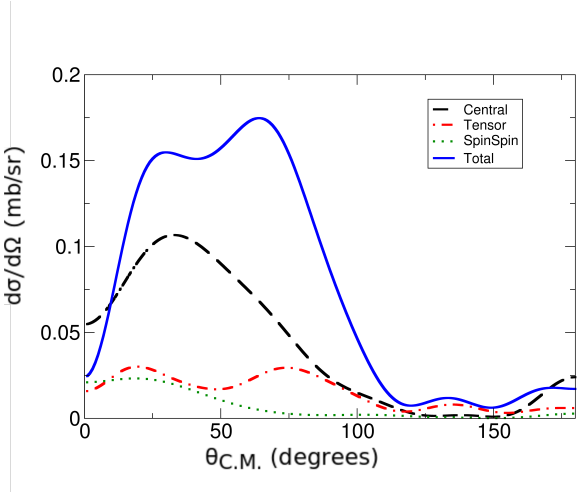

Figure 4.8: Charge-exchange cross sections for the ^{58}Fe(p,n)^{58}Co^{IAS} transitions at E_{lab} = 23 MeV calculated using the AV8' potential. The contribution to the cross section from various potential operators are shown in dashed black for central, dotted green for spin-spin, dash-dotted red for tensor, and solid blue for the total cross section. Calculations shown here use the KD OMP for to calculate distorted waves.

Contributions from the central term dominate the calculations at all energies in ^{14}C(p,n)^{14}N, but, expectedly, contributions from the tensor term grow with increased values of l, competing with the central term in ^{48}Ca (l=3) and dominating in ^{90}Zr (l=4). Calculations of ^{58}Fe(p,n)^{58}Co show a dominant contribution from the central term, indicating that the growth in the tensor term is, in fact, related to larger values of l, as opposed to target mass.

It is worth noting that while the spin-spin term is negligible in ^{48}Ca and ^{90}Zr, it represents a sizable contribution in ^{14}C l=1 . This can also be observed in ^{58}Fe. One possible explanation is related to the spin-spin operator's radial form factor which can be seen in

Figure 3.4. The spin-spin radial form is the only component of the NN interactions considered in this work which contains both an attractive and repulsive region, crossing through 0 MeV at around 0.5 fm. The degree to which various regions of the potential form factor will contribute to the cross section is related to the two dimensional radial integral of the potential along with the incoming and outgoing scattering and bound state wave functions. Because ^{58}Fe and ^{14}C have l=1, their bound state wave functions peak at lower values of the internal radial coordinate, r_{2c}. This could result in capturing a larger portion of the attractive spin-spin interaction, resulting in a larger contribution to the overall cross section.

Next we examine the three-body charge-exchange cross sections produced using the Gogny interaction, shown in Figure 4.9. Calculation time and convergence properties for calculations with the Gogny interaction are very similar to their counterparts in AV8' calculations. Again, we observe forward peaked cross sections, consistent with a direct reaction process in all cases. In this figure, the cross section resulting from the isospin central and spin-spin operators are shown separately, as well as the total cross section.

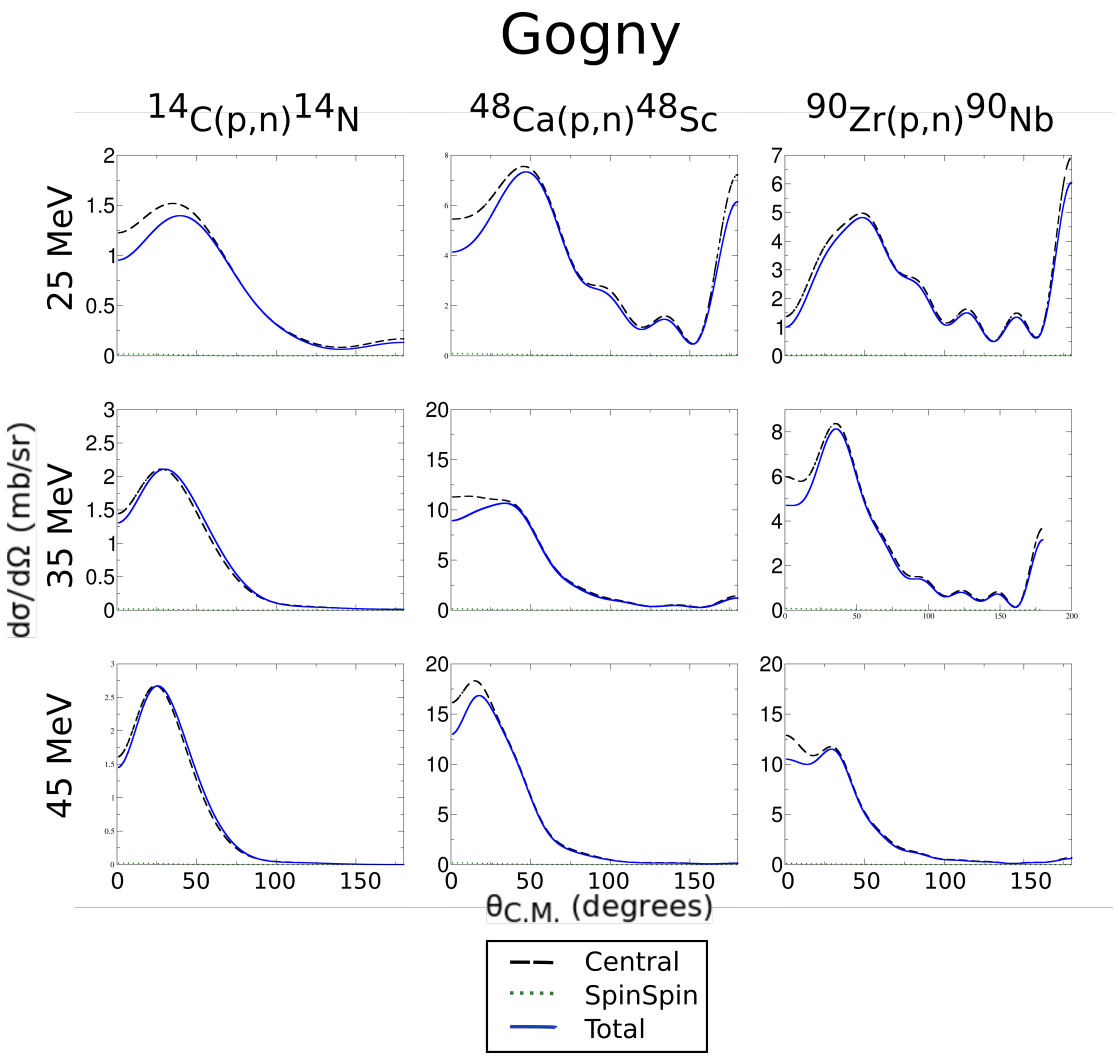

Figure 4.9: Charge-exchange cross sections for the ^{14}C(p,n)^{14}N^{IAS}, ^{48}Ca(p,n)^{48}Sc^{IAS}, and ^{90}Zr(p,n)^{90}Nb^{IAS} transitions at E_{lab} = 25, 35, and 45 MeV calculated using the Gogny potential. The contribution to the cross section from various potential operators are shown in dashed black for central, dotted green for spin-spin, and solid blue for the total cross section. Calculations shown here use the KD OMP for to calculate distorted waves.

As with the AV8' calculations, the cross sections produced using Gogny grow in magnitude and become more forward peaked with increased beam energy. Unlike the results from AV8', the central term of the Gogny interaction dominates for all target and energy combinations. This is unsurprising given that, in Figure 3.4, we see that the isospin central and spin-spin terms are both repulsive potentials with similar form factors, except that the central term is about 5 times larger in magnitude.

We next consider the effect of the choice of KD versus CH89 OMP for the distorted waves on the charge-exchange cross section in the three-body framework. These results, including contributions from all potential operator terms, can be seen in panels (d)-(f) of Figures 4.4, 4.5, and 4.6. Note that in these figures, the cross sections utilizing the AV8' interaction have been enhanced by a factor of 10 so they could be viewed on the same scale as the calculations using the Gogny interaction. The results for the calculations using AV8' are shown in solid lines, while the results utilizing Gogny are shown in dashed lines. It is clear that, while the choice of OMP can have significant effects on the magnitude of the cross section, the angular distributions are relatively similar, regardless of the choice of OMP. This is in contrast to results from the two-body formalism where changing the OMP could significantly change the shape of the cross sections, although in the two-body case, using a different OMP for distorted waves also corresponds to changing the Lane interaction. Additionally, in the two body case, we saw that in some cases using the KD parameters led to a larger magnitude in the cross sections, while sometimes the opposite was true and CH89 lead to the larger cross sections. However, in the three-body formalism, the KD OMP consistently produces the larger cross section. This is likely related to the fact that the CH89 parameter set is more absorptive, particularly at the surface, decreasing the contribution to the charge-exchange cross section. The percent difference between the cross sections produced with KD versus CH89, evaluated at the first peak, are given in the columns labeled "AV8' Δ_{OMP}" and "Gogny Δ_{OMP}" of Table 4.3. We note that the percent difference seems to be loosely correlated with the mass of the target, and has no observable trend with regards to the beam energies studied here. The average percent difference over all targets and energies is 58% for AV8' and 55% for Gogny, which is similar to the 50% demonstrated for the two-body calculations.

Comparing the results from AV8' to those obtained with the Gogny interaction, we note

that the cross sections produced with the Gogny interactions are consistently about an order of magnitude larger than those produced with AV8'. The percent difference between cross sections produced using these two NN interactions are given in the "3-Body Δ_{NN}" column of table 4.3. The average percent difference between calculations produced with the AV8' and Gogny interactions, across all cases studied here, is 167%, which represents a significantly larger variation than is introduced through the choice of OMP. This is easily understandable given the relative magnitudes of the Gogny and AV8' central terms in Figure 3.4. This mismatch in the radial form factor could be a result of Gogny being fit to observables which include in medium effects, as opposed to the bare AV8' NN interaction.

Finally, we can compare results from our three-body calculations to experimental data. As we can see in Figures 4.4, 4.5, and 4.6, calculations using both the AV8' and Gogny interaction do a poor job of describing the experimental data, with severe mismatches in both the magnitude and the shape of the distributions. As in the two-body case, we can normalize our calculations to the data and calculate the percent of data, within errors, captured by our normalized calculations. These results are shown in Tables 4.6 and 4.7 for AV8' and Gogny, respectively. For the case of ^{14}C(p,n), the cross sections utilizing the AV8' interactions needed to be enhanced by a factor of about 50 to match the magnitude of the data, while the magnitude of the cross section was similar to data in all other cases. The Gogny interaction produced results that is similar to the magnitude to the data in all cases, although it consistently overshoots experimental results.

Additionally, we can asses the quality of the calculation through the percentage of data captured inside the rough uncertainty band defined by the two curves corresponding to calculations with different OMPs. Visual inspection asserts that both AV8' and Gogny do a poor job reproducing experimental data and this is backed up with this metric. Both the

AV8' and Gogny interaction have one case where they capture none of the data within error. Additionally, the maximum percent of data reproduced by the AV8' calculation is 38% for the case of ^{14}C(p,n) at 35 MeV, with an average across all cases of just 13%. The picture is similar for the Gogny interaction, which has a maximum of 34% for the case of ^{90}Zr(p,n) at 45 MeV and an average across all data sets of 14%.

Reaction		3-Body KD		3-Body CH89		3-Body Δ_{OMP}
Target	E_{lab} (MeV)	χ^2/N	Norm	χ^2/N	Norm	% Data
^{14}C	25	4.84	58	5.51	63	0.00
^{14}C	35	7.35	34	6.78	45	37.50
^{14}C	45	1.95	25	1.71	32	3.13
^{48}Ca	25	12.17	2.10	12.66	3.90	0.00
^{48}Ca	35	6.85	1.80	7.24	2.70	15.63
^{48}Ca	45	6.26	1.60	5.84	2.50	12.50
^{90}Zr	25	13.81	1.00	18.89	6.20	9.38
^{90}Zr	35	9.39	0.23	9.69	2.00	9.38
^{90}Zr	45	6.91	0.50	6.62	1.20	25.00
Average						12.50

Table 4.6: Numerical comparison of three-body charge-exchange angular distributions to experimental data. The final column shows the percentage of the data, including experimental errors, which falls between the theoretical curves produced by three-body calculations with the AV8' NN interaction and the KD and CH89 OMP used for distorted waves.

The large variation in the magnitude and shape of charge-exchange cross sections that results from the implementation of different interactions implies that the charge-exchange cross section is very sensitive to the choice of interaction. With this in mind, we wished to explore whether or not charge-exchange across a range of target masses and beam energies, such as those explored in the work, could be well described by a potential with a simple form, such as the Gogny interaction. For this brief exploration, we tuned the 4 parameters which define the isospin central term of the Gogny interaction to best fit experimental data

Reaction		3-Body KD		3-Body CH89		3-Body Δ_{OMP}
Target	E_{lab} (MeV)	χ^2/N	Norm	χ^2/N	Norm	% Data
^{14}C	25	6.80	0.70	6.83	0.80	9.38
^{14}C	35	11.47	0.30	11.25	0.40	28.13
^{14}C	45	6.42	0.20	4.22	0.40	6.25
^{48}Ca	25	9.93	0.20	8.88	0.40	3.13
^{48}Ca	35	13.72	0.10	18.29	0.10	28.13
^{48}Ca	45	2.38	0.20	2.01	0.30	9.38
^{90}Zr	25	13.95	0.20	14.09	1.20	0.00
^{90}Zr	35	7.07	0.10	7.20	0.40	9.38
^{90}Zr	45	4.00	0.10	4.54	0.20	34.38
Average						14.24

Table 4.7: Numerical comparison of three-body charge-exchange angular distributions to experimental data. The final column shows the percentage of the data, including experimental errors, which falls between the theoretical curves produced by three-body calculations with the Gogny NN interaction and the KD and CH89 OMP used for distorted waves.

Parameter Set	μ_1 (fm)	μ_2 (fm)	H_1(MeV)	H_2(MeV)
Original Gogny	0.7	1.2	-469.2	37.37
Refit Gogny	0.71	1.2	-760	135

Table 4.8: Original and refit parameters for the central component of the Gogny NN interaction.

for the case of ^{48}Ca(p,n)^{48}Sc at 35 MeV. This was done qualitatively, just fitting the data by eye. We then fixed these values and calculated the charge-exchange cross sections for all other cases. The original Gogny parameters, and the refit parameters are shown in Table 4.8 and the results of these calculations are shown in Figure 4.10. We note that this fitting is not unique. Our refitting involved increasing the strength parameters, but it is likely that an equally good fit could be achieved through another combination parameters with decreased strength.

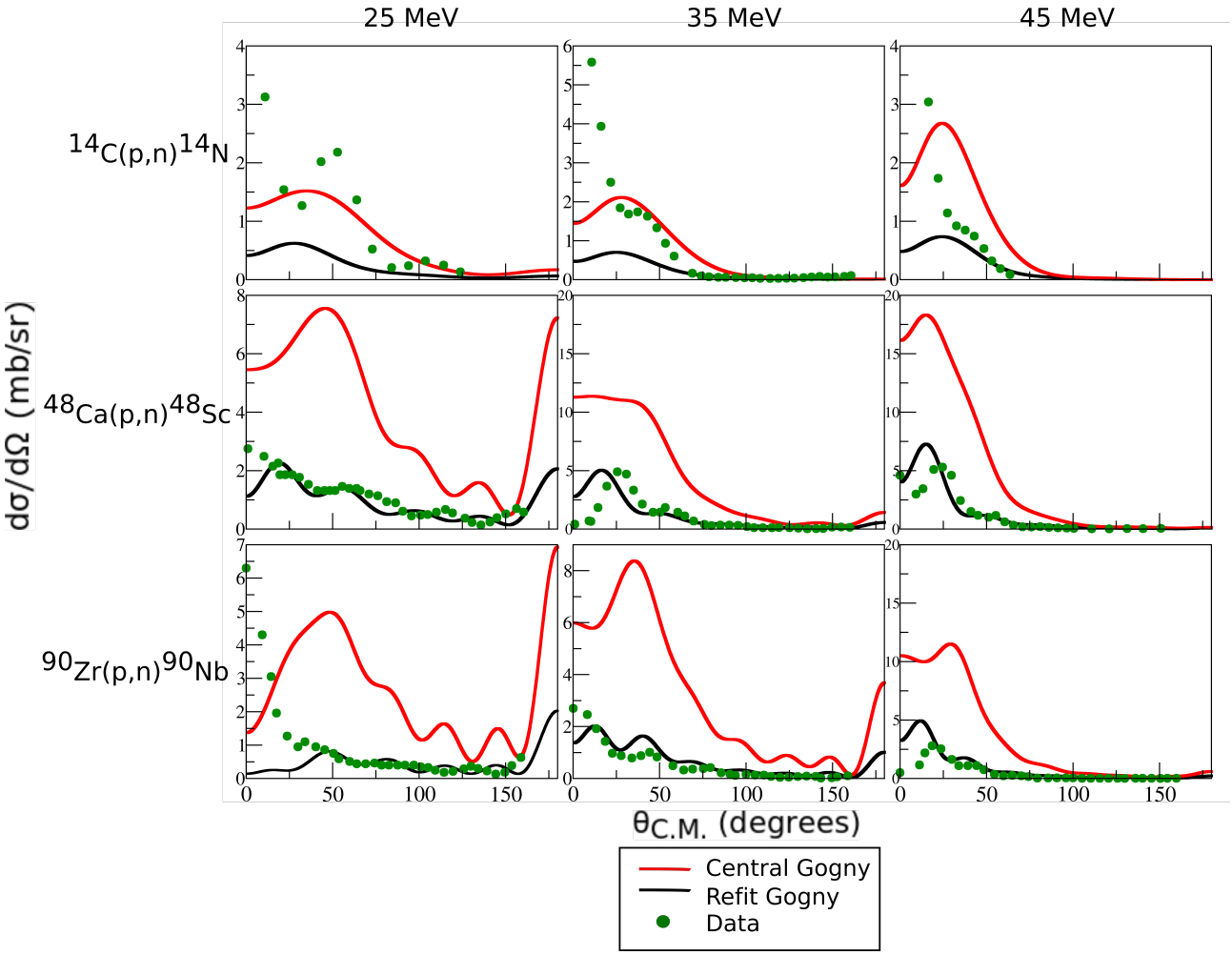

Figure 4.10: Charge-exchange cross sections for the ^{14}C(p,n)^{14}N^{IAS}, ^{48}Ca(p,n)^{48}Sc^{IAS}, and ^{90}Zr(p,n)^{90}Nb^{IAS} transitions at E_{lab} = 25, 35, and 45 MeV calculated using a refit Gogny potential with only a central contribution (back). The red curve shows the original calculation using the isospin central Gogny interaction.

Qualitatively, the refit Gogny interaction has better success describing the experimental data. The cross sections produced for all cases are similar in magnitude to the data and, in some cases, the description of the angular distribution is much better than for the unfit Gogny interaction. Additionally, the quality of the description does seem to improve with beam energy. Still, cross sections utilizing the refit interaction struggle to describe cross sections that peak at 0 degrees, suggesting that the assumed gaussian shape for the NN interaction is not physically adequate.

4.2.3 Comparing Reaction Formalisms

Now that we have examined results from both formalisms separately, we will comment on how results calculated in the two-body versus three-body formalisms compare. In particular, there are significant differences in the angular distributions between the two frameworks. First, in the three-body calculations, the angular diffraction at large angles are washed out for both NN interactions considered here relative to the two-body calculations.

Second, the angular distributions for the three-body calculations display a much smaller variation between the various target/beams energies explored in this work than their two-body counterparts. For almost every case, the three-body cross section is dominated by a single peak around 30-50 degrees, while the two-body calculations peak between 0 and 40 degrees and exhibit more complicated structures with multiple peaks. In order to understand this difference, we examined which partial waves were contributing most to the charge-exchange cross section for the two-body and three-body calculations.

Generally speaking, the shape of the angular distributions is created by combining the spherical harmonics used to describe the partial wave expansion of the cross section, weighted by factors that include angular momentum conservation and the radial behavior of the reactions. Lower values of scattering angular momentum, L, correspond to more central interactions with small impact parameters, while cross sections that more heavily weight larger L contributions are more peripheral. Figure 4.11 shows the angle integrated cross section as a function of scattering angular momentum, L, for the case of ^{90}Zr(p,n)^{90}Nb at 25 MeV, where the angular distributions produced by the two-body and three-body frameworks are severely mismatched. In this figure the three-body cross section with the Gogny interaction is scaled so that all contributions can be shown on the same plot. The cross sections for

the three-body formalisms peak at larger values of angular momentum, implying that the reaction mechanism mediated by the two-body Lane interactions is more central, and the charge-exchange reactions mediated by NN interaction in the three-body formalism are more peripheral.

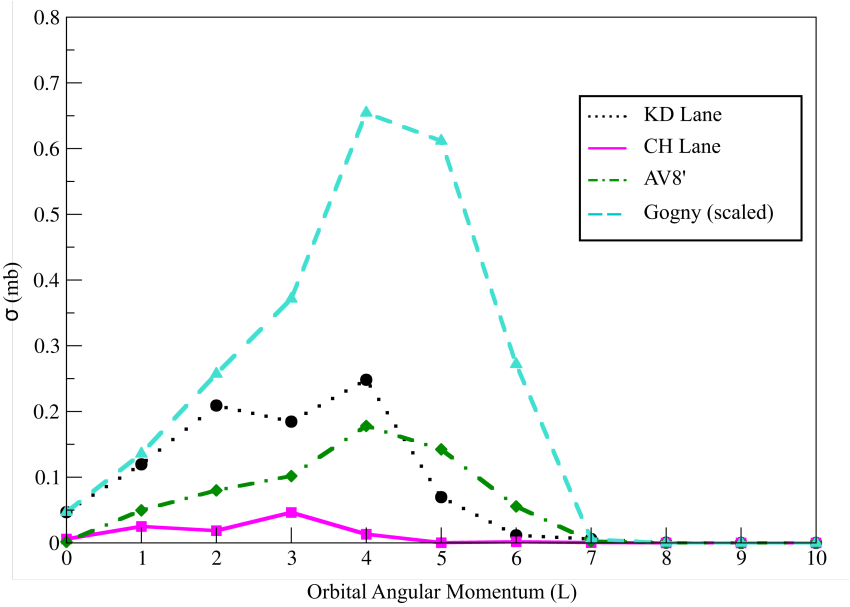

Figure 4.11: Angle integrated charge-exchange cross sections and a function of scattering angular momentum for ^{90}Zr(p,n)^{90}Nb at 25 MeV for the three-body formalism with the Gogny and AV8' interactions, and the two-body formalism with the Lane potential parameterized by KD and CH89.

To further explain this result, we can explore the radial parameter space to demonstrate which regions significantly contribute to the charge-exchange cross section. To do this, we calculate the radial integral of the interaction with the initial and final wave functions, including bound states for the three-body formalism, in different portions of the radial parameter space. For the two-body formalism, there is only one radial variable, R_{1A}, but for the three-body formalism, there are three radial variables, R_{1A}, r_{2c}, and r_{12}. Figure 4.12 shows the value of the radial integral as a function of an interior radial cut in each of the these variables for the AV8', Gogny, and Lane interactions. The specific case shown here is

for charge-exchange on ^{48}Ca at E_{lab}=35 MeV, although these results are consistent across different targets and beam energies.

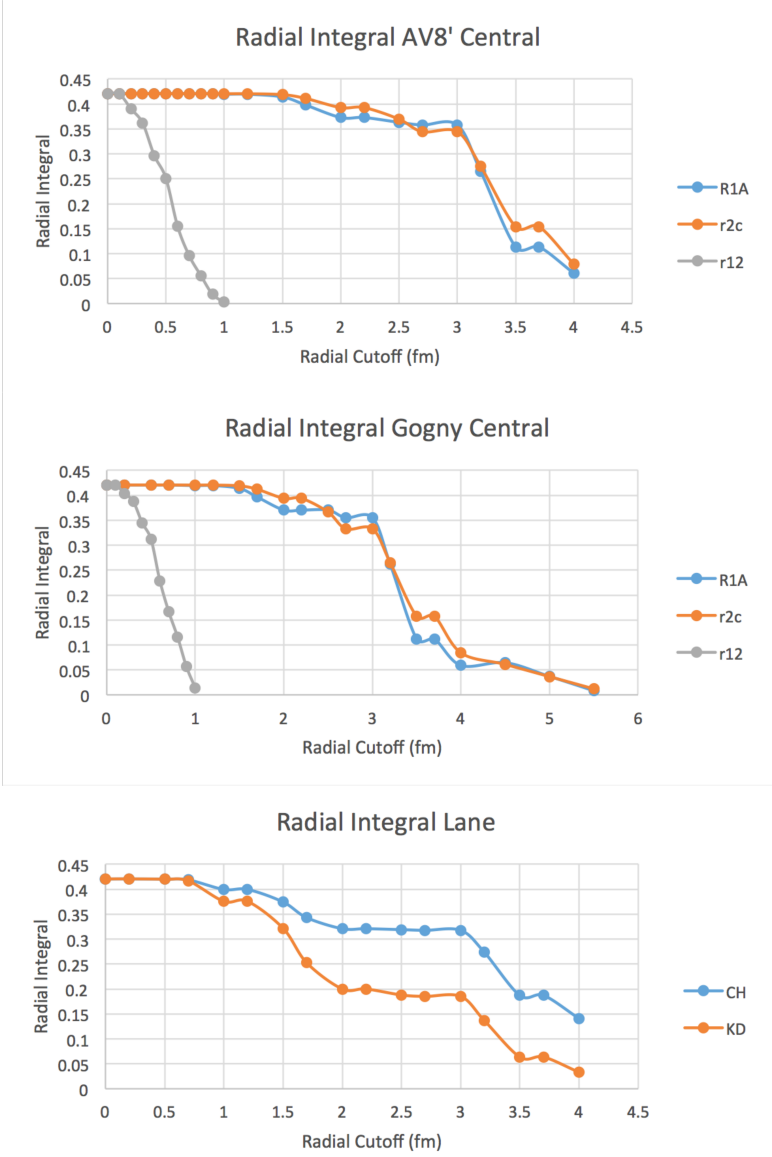

Figure 4.12: Dependence of radial integral on the range of various radial parameters. The x-axis shows the internal radial cut in each radial parameter.

As expected, for both of the short range NN interactions, the radial integral falls off quickly as a function of r_{12}, but when we make cuts in the r_{2c} and R_{1A} parameters, the radial integral does not significantly decrease until about 3 fm. The ^{47}Ca + n bound state

that describes the target has a radius of $R = r_0 A_T^{1/3}$ where, in this case, $r_0 = 1.25$ and $R = 4.5$. This indicates that, in the three-body formalism, the reaction is occurring near the surface of the target, where the proton and neutron are close together, resulting in small values of r_{12}. In the two-body formalism, however, there is only one scattering variable and the radial integral begins to drop off significantly around 1.5 fm, indicating a reaction that is involving much more of the nuclear interior. This reaffirms our prior assertion that the three-body framework results in a reaction concentrated closer to the surface region, modifying the resulting angular distribution compared to the two-body approach.

4.2.4 Discussion

Here, we comment on our study in the context of other methods which have been used to study charge-exchange reactions. First, we examine the theoretical calculations presented alongside the data sets used in the analysis. Doering et al. includes DWBA calculations for the ^{48}Ca(p,n) and ^{90}Zr(p,n) reactions considered here [18]. For their calculations, they used the OMP parameterized by Bechetti and Greenlees to calculate distorted waves [66]. In this work they considered a number of effective interactions, including two parameterizations of simple Yukawa potentials with a 1 fm range, and a realistic NN potential derived from the Reid soft core potential [78, 102]. Doering et al. included the direct and knock-on exchange contributions exactly. As mentioned before, we do not address knock-on exchange in our calculations. These calculations yielded a reasonably good description of the data, similar in quality to our two-body calculations. The methods used by Doering et al. are similar to our three-body formalism in the sense that they can describe microscopic transitions between single particle states in the initial and final nucleus and they describe their incoming and outgoing distorted waves using a separate scattering coordinate. However, it is unclear exactly

what approximations and methods they implement in their calculations, so it is difficult to draw more detailed comparison. Additionally, their choice of interaction is such that they do not see large contributions from non-central isospin terms, such as the isospin tensor and spin-orbit interactions. In contrast, we see increasing contributions from the tensor term as the value of l increases in our target. Finally, our current calculations only include one initial and final single particle state configuration. For the case of ^{48}Ca, Doering et al. also models the initial and final states as a pure $f_{7/2}$ to $f_{7/2}$ transition, so differences between the results presented here and their calculations arise solely from the different interactions and frameworks implemented in the two cases. However, for ^{90}Zr, the shell model configurations from Doering et al. are $0.8(1g_{9/2})^{10} + 0.6(1g_{g/2})^{8}(2p_{1/2})^{2}$. In our case, we used a pure $g_{9/2}$ configuration. We performed a preliminary calculation showing that the cross section for the $p_{1/2}$ transition is negligibly small compared to the $g_{9/2}$ transition, so our single orbital calculation for ^{90}Zr should be slightly larger than the calculation that uses the configuration from Doering et al.

Next, we can examine the results presented alongside the experimental data for ^{14}C(p,n) in Taddeucci et al. [17]. They, again, use an charge-exchange reactions framework similar to that presented in [27]. For the case of ^{14}C(p,n), Taddeucci et al. does not use a global parameterization to describe the incoming and scattering waves but, instead, uses an optical model parameterization fit specifically for that work. The parameterization was chosen by fitting a Lane-type interaction to their charge-exchange data to the isobaric analog state in ^{14}N. For the effective NN interaction, Taddeucci et al. employs the BBML interaction [103], which is based on the M3Y interaction [104]. Again, they calculated direct and knock-on exchange terms explicitly. In this work they found they were unable to describe the charge-exchange data accurately unless they modified the BBML interaction, demonstrating a high

sensitivity in the NN interactions as we observed in the work presented here.

Additionally, our two-body study employs a very similar methodology to that employed by Danielewicz et al. [10]. In that work, Danielewicz used an equivalent charge-exchange framework to calculate transition between 0^+ IAS using a Lane potential. Danielewicz et al. considered a wide range of targets, including ^{48}Ca(p,n) and ^{90}Zr(p,n), and used the KD optical model parameterization for their distorted waves and Lane interaction. Because of this, our two-body results using KD are almost identical to those presented in Danielewicz et al., although there is a slight variation owning to the fact that in Ref [10], the authors modified the KD to use the same geometry for proton and neutron scattering potentials. Danielewicz et al. simultaneously fit proton elastic scattering, neutron elastic scattering, and charge-exchange data in order to uncover differences between isovector and isoscalar potential geometries, which were then used to extract a neutron skin thickness. They determined that there was a significant difference between the geometries. However, their study only utilized one optical model parameterization, but our results indicate that using the CH98 parameterization can have a significant effect on both the magnitude and shape of angular distributions. We know that there are large parametric uncertainties arising from OMPs. It would be informative to explore how propagating these parametric uncertainties through this simultaneous fitting procedure effects the uncertainties associated with the resulting isovector skin predictions.

In our work, we chose a position space representation. However, the formalisms can equivalently be cast in a momentum space representation. Lenske et al. has developed a microscopic DWBA formalism which, in momentum space, separates into projectile and target transition form factors, with a distortion coefficient [105]. This model has been used to describe single charge-exchange using heavy ions (i.e. ^{18}O+^{40}Ca), as opposed to the (p,n)

reactions discussed here. In this formalisms, the ground states of the target and projectile nuclear densities are derived from Hartree-Fock-Bogolubov with excited states described by the Quasiparticle Random Phase Approximation. Lenske et al. [105] suggests that a similar factorization between structure and reaction dynamics as is used in Equation(1.1) for (p,n) Gamow-Teller transitions is appropriate. This factorizability could be possible for beam energies of a few 10s of MeV per particle in a heavy ion probe. This model was not applied to systems with light probes and, therefore, cannot be compared to our work.

Finally, the ^{48}Ca(p,n) and ^{90}Zr(p,n) data considered here has also been analyzed using a microscopic model by Khoa et al. [50]. In that work they looked at both (p,n) and (^{3}He,t) reactions using the folding model (double-folding model in the case of (^{3}He,t) reactions) which integrates over the nuclear density of the target and probe. This is in contrast to our work which does not incorporate nuclear densities and, instead, describes the projectile-target interaction with a global optical potential. In their work, they use a coupled channel formalism to describe elastic and charge-exchange reactions. The effective NN interaction is, in this case, density dependent (the CDM3Y6 interaction based on the M3Y interaction [106]). The goal of their work is to fit data by adjusting the isospin dependence of the NN interaction. This can be used to make realistic predictions about the density dependence of the symmetry energy. Their calculations were able to produce a good description of the data, which were improved by tuning the complex components of the OMPs to each individual target. Similar methods are used to analyze charge-exchange reactions in [52, 51, 48, 49].

4.2.5 Limitations of Current Work

Finally, this work represents a preliminary effort to study the reaction dynamics of charge-exchange reactions and there are a number of limitations in this current study. Perhaps

most importantly, all cross sections calculated in this work use a single step DWBA, however, at beam energies as low as 25 MeV, there are likely contributions to the charge-exchange cross section from higher order processes which are not included in our current model. Although there have been efforts to quantify possible effects from multistep processes in charge-exchange (i.e. [107]), here we will just note that these effects are likely significant and the reaction formalism should be extended to better understand the role that multistep process play in low energy charge-exchange reactions.

Additionally, as discussed in Section 2.4.2, this work does not include contributions from the isospin, spin-orbit term of the AV8' interaction. We did not include this component because of complications of expanding the angular momentum operator, $\hat{\boldsymbol{L}}$, in the coordinate system used to describe our framework. Although the contribution from this term is possibly small, it should be included explicitly and a derivation explaining how to do this can be found in Appendix C.4. This is particularly important because AV8' is a reprojection of the more complicated v_{18} interaction that reduces 14 operator terms to just 8 terms. This means that it is difficult to predict the effect of leaving out any particular term of the interaction.

Finally, the theoretical uncertainty quantification discussed in this work is very basic. In the future, a more robust uncertainty quantification study should be conducted in the realm of charge-exchange reactions using the Bayesian methods recently developed by other members of the reaction theory group at Michigan State University. These analysis tools for studying uncertainty from the OMPs are already in place for transfer reactions and extending this framework to charge-exchange reactions should be fairly straightforward, as CHEX already calculates the elastic scattering cross sections which are necessary for the analysis. Additionally, it would be illuminating to study the role that charge-exchange cross sections play in constraining the uncertainties in OMPs, given the demonstrated sensitivity

of charge-exchange to the choice of interaction.

Chapter 5

Conclusions and Outlook

5.1 Conclusions

Indirect reaction methods are an important tool for exploring the evolution of the elements in our universe, but they are only useful if we have reliable theories to link indirect reaction mechanisms with the astrophysical processes of interest. In this thesis we explored two indirect reaction methods, transfer and charge-exchange reactions, with an emphasis on the reaction theory models used to understand them.

We discussed several examples of using deuteron induced transfer reactions to probe the astrophysical proton capture reaction rate. We introduced a methodology that allows us to extract spectroscopic factors of low lying resonances of interest. These values then directly inform the astrophysical reaction rate via the resonance strength, $\omega\gamma$. These spectroscopic factors were extracted from angle integrated cross section measurements using transfer calculations which utilize the adiabatic distorted wave approximation. In many cases, a bound state approximation was used to simplify transfer calculations to low lying resonances with non-zero orbital angular momentum, l. We presented results of three transfer reaction studies. The study of ^{30}P(d,n) for applications to the ^{30}P(p,γ) reaction in classical novae marks the first experimental constraints on the ^{30}P(p,γ) reaction rate. In the study of ^{23}Al(d,n) for applications to the ^{23}Al(p,γ) reaction in type-I x-ray bursts, the uncertainty in the as-

trophysical ^{23}Al(p,γ) reaction rate was reduced by 3-4 orders of magnitude in the relevant temperature range. Finally, the work examining ^{56}Ni(d,n) for applications to the ^{56}Ni(p,γ) reaction, also important in x-ray bursts, constrained the ^{56}Ni(p,γ) reaction rate via the first measurement of the $7/2^-$ state in the ^{57}Ni mirror nucleus.

In the realm of charge-exchange reactions we conducted a systematic study of transitions to 0^+ isobaric analog states, over a range of target nuclei and beam energies. All charge-exchange calculations presented in this study were produced using the charge-exchange reaction code, CHEX, developed for this thesis. This study marks an initial investigation into how various aspects of the reaction model effect charge-exchange observables. We explored a two-body framework where the charge-exchange transition is mediated by a Lane potential. These types of interactions are described by a difference in proton+target and neutron+target optical potentials. We explored the impact of using two different optical model parameterizations (KD and CH89) on charge-exchange cross sections. This simple two-body model was reasonably successful in describing the shape and magnitude angular distribution of data. On average, there was a 50% difference in the cross sections produced by the two parameterizations, which is similar to the spread observed in other reactions. Finally, we examined the extent to which the data could be described, within error, by these calculations. We defined rudimentary theoretical error bands with the normalized cross sections produced by the KD and CH89 OMPs and calculated the percent of data captured by these bands. On average, 31% of data in our study was captured by our normalized two-body calculations.

Next we extended our description of charge-exchange to a three-body framework, which uses an NN interaction to describe charge-exchange between a scattering nucleon and a valence nucleon bound to an inert core. This model allows a valence nucleon to transition

between two well defined single-particle states. We explored the effect of using two different NN interactions: the AV8' [75, 83] and Gogny [82] interactions. We found that the three-body formalism, regardless of the choice interaction, was unsuccessful in reproducing either the shape or magnitude of the charge-exchange angular distribution data used in this study. Additionally, the normalized error bands for the AV8' and Gogny interactions only captured 13% and 14% of the data, respectively.

We noted that the three-body charge-exchange cross section is highly dependent on the choice of NN-interaction. The cross sections produced with the Gogny interaction are typically about an order of magnitude larger than those produced by the AV8' interaction and, on average, the choice of interaction results in a 167% difference between the cross sections at the first peak. This is significantly larger than deviations caused by the choice of OMP used to calculate the incoming and outgoing distorted waves, which lead to a 55% difference, on average.

Finally, we noted that the shape of the angular distributions in the three-body model, regardless of the choice of interaction, differ significantly from their two-body counterparts and from experimental data. We determined that the two-body formalism more heavily weighted lower partial waves in the cross section calculation, indicating a more central reaction that involves a significant portion of the nuclear interior. In contrast, the three-body formalism using the Gogny and AV8' interactions select higher partial waves, resulting in a reaction located near the surface of the target.

5.2 Outlook

This thesis presents initial findings regarding charge-exchange reactions in a two-body and three-body formalism, but there are a number of important limitations in this investigation, as well as a broad outlook regarding further studies. Because the two-body formalism presented here has a relatively straightforward implementation and short calculation time, it is a particularly good candidate for a more rigorous uncertainty quantification study. Our preliminary analysis shows that, on average, the charge-exchange cross section varies by 50%, depending on the choice of OMPs. In order to better understand how parametric uncertainties affect the precision of charge-exchange calculations, the Bayesian methods recently developed to quantify parametric uncertainties in transfer reactions should be extended to this reaction channel [61]. Additionally, all interactions considered for this work are purely local, but it has been demonstrated that including the effects of non-local interactions can have a large impact on the transfer cross section. The CHEX charge-exchange reaction code incorporates the non-local Schrödinger equation solver from the NLAT reaction code [81]. Although this effect was not investigated in our current study, CHEX allows for easy extension to examine the effect of non-local potentials in future studies.

There are also several opportunities to improve and expand on our study of the three-body formalism. As discussed in Section 2.4.2, we have implemented three of the four isospin operators in the AV8' interaction, but the isospin spin-orbit interaction is not included due to complications expressing the $\hat{\boldsymbol{L}}$ operator in the coordinate system used to describe scattering and bound states. Although the full implementation is outside of the scope of this thesis, a derivation outlining how to explicitly include this term can be found in Appendix C.4.

In this work, we implemented the AV8' and Gogny interaction, but CHEX is readily able

to include any position space nuclear interaction which is cast in an operator form. Most notably, the effective NN interaction developed by Love and Franey [59, 60] is commonly used to analyze charge-exchange reactions and has a parameterization for scattering energies ranging from 50-1000 MeV. The Love-Franey interaction was not included here because it is not parameterized for energies below 50 MeV and is considered to be less accurate at low energies. Additionally, there are complications involving the knock-on exchange term. Future developments to include this interaction with a knock-on exchange term would allow for a clearer comparison between charge-exchange calculations presented in this work and other models, such as in [17].

This thesis limited its study to charge-exchange transitions to 0^+ isobaric analog states. However, there are other important transitions that should be considered. Most notably, the Gamow-Teller transition (ΔL=0, ΔS=1, ΔT=1) is of particular physical interest as it is used to constrain electron-capture rates in supernovae. CHEX was designed to be generalizable, so this implementation should only require an extension of the spin-spin T-matrix expression to include ΔS=1 transitions. Additionally, we know that the structure of many nuclei are not well described by one single-particle state and, instead, are highly fragmented. In order to describe these nuclei accurately, the CHEX front end program would need to be modified to input transitions between multiple orbitals.

Finally, both the two and three-body frameworks presented in this thesis use single step DWBA. While the single-step approximation is a valid reaction model at medium to high beam energies, this study includes beam energies as low as 25 MeV, where there are likely contributions to the charge-exchange cross section from higher order processes. There have been efforts to quantify effects from multistep processes in charge-exchange, including work by Madsen et al. which proposes an energy dependent correction factor [107]. We note

that these effects are likely significant and it is crucial that future investigations of charge-exchange reaction models explicitly implement a formalism which accounts for multi-step processes.

APPENDICES

APPENDIX A

Summary of Additional Transfer Results

This appendix contains a summary of the methods and results used to analyze the ^{56}Ni(d,n)^{57}Cu and ^{56}Ni(d,p)^{57}Ni reactions for applications to astrophysical capture, as well as a brief introduction to a new method that has been proposed to utilize the Active Target Time Projection Chamber (AT-TPC) to more precisely extract the spectroscopic factor from transfer reactions.

A.1 ^{56}Ni(d,n)^{57}Cu

The ^{56}Ni(p,γ)^{57}Cu reaction plays a key role in the rp-process in XRBs, acting as a key waiting point that impedes flow along the proton drip line [108]. This characteristic is due to the unique structure of ^{56}Ni, which is doubly magic. This N=Z=28 isotope lies right on the edge of stability with a 6.08 day half-life. In order to reduce the uncertainty in this key reaction, the ^{56}Ni(d,n)^{57}Cu transfer reaction was measured using the same GRETINA/S800 setup described in Section 4.1, this time using 33.6 MeV/u beam. However, this experiment was unique in that it also measured the transfer reaction to the mirror nucleus of ^{57}Cu via ^{56}Ni(d,p)^{57}Ni. This measurement allows for a test of the isospin symmetry between these two nuclei. Additionally, information on excited states of the mirror nucleus, ^{57}Ni, can allow

for constraints on the astrophysical proton capture reaction rate to ^{57}Cu in cases where these states are not directly measured.

The theoretical cross sections for ^{56}Ni(d,n)^{57}Cu and ^{56}Ni(d,p)^{57}Ni were calculated according to the same process described in Section 3.1. In this case, the final states in ^{57}Ni are bound, so the final bound states can be modeled with a real Woods-Saxon potential where the depth is adjusted to reproduce the experimental binding energy. In the case of ^{57}Cu final states, we employ the bound state approximation to model the final resonance states. The shell model calculations which produced theoretical spectroscopic factors used the GPFX1A Hamiltonian [109] to describe the isospin-conserving strong interaction, along with the Coulomb and charge-dependent Hamiltonians from [110]. A brief summary of these results are given in Table A.1.

^{56}Ni(d,n)^{57}Cu								
E_x (MeV)	E_{res} (KeV)	J^π	σ_{exp} (mb)	σ_{th} (mb)	C^2S_{exp}	C^2S_{SM}	l	$\omega\gamma$
1.028	338	$5/2^-$	2.00(40)	2.62	0.76(28)	0.75	3	1.7×10^{-11}
1.109	418	$1/2^-$	0.28(6)	0.45	0.62(22)	0.71	1	1.9×10^{-7}
2.398	1708	$5/2^-$	<0.2	2.61	$< 8 \times 10^{-2}$	1.8×10^{-3}	3	1.0×10^{-2}
2.525	1835	$7/2^-$	<0.2	14.5		3.9×10^{-2}	3	2.7×10^{-2}
^{56}Ni(d,p)^{57}Ni								
E_x (MeV)		J^π	σ_{exp} (mb)	σ_{th} (mb)	C^2S_{exp}	C^2S_{SM}	l	
0.768		$5/2^-$	2.10(60)	2.77	0.77(31)	0.74	3	
1.122		$1/2^-$	0.50(15)	0.68	0.73(31)	0.69	1	
2.443		$5/2^-$	<0.4	2.61	<0.1	3×10^{-4}	3	
2.579		$7/2^-$	1.24(36)	14.9	$8(3) \times 10^{-2}$	4.1×10^{-2}	3	

Table A.1: Summary of results from [7] for the study of ^{56}Ni(p,γ)^{57}Cu via ^{56}Ni(d,n)^{57}Cu and the mirror reaction of ^{56}Ni(d,p)^{57}Ni. States which were not observed in this study are listed with upper limits in the experimental cross section. A large proton branching ratio in inferred for decay of the $7/2^-$ resonance at 1.835 MeV, so no experimental spectroscopic factor is listed for that state here.

By comparing experimental and theoretical spectroscopic factors, it is clear that the low

lying states in both ^{57}Cu and ^{57}Ni exhibit a strong single-particle nature, and agree well with the results of shell model calculations. Most importantly, charge-symmetry is preserved. For higher lying states, spectroscopic factors, either extracted from measurement or constrained by upper limits, are much smaller, consistent with the shell model predictions. Shell model predictions for spectroscopic factors for the $5/2^-$ state around 2.4 MeV in both final nuclei are small, consistent with their non observation in this case. Finally, the observation of the $7/2^-$ state in ^{57}Ni constitutes the first measurement of this state.

These results, including constraining the $7/2^-$ state in ^{57}Cu through the measurement in the ^{57}Ni mirror, can be used to calculate the reaction rate in the temperature range relevant for XRBs, as shown in Figure A.1. For temperatures below about 1 GK, the rate is dominated by the $l = 2$ state at 418 keV. However, at higher temperatures, the higher lying $l = 3$ states both contribute substantially and come to dominate the reaction rate. The rate calculated in [7] which incorporates the these newly constrained spectroscopic factors is significantly higher than the previous result from Zhou et al. [21] which used experimental excitation energies, but only theoretical widths. For lower temperatures, the result from [7] agrees well with the central value from Rehm et al. [20] which incorporated experimental spectroscopic factors for the lower-lying resonance strengths states derived from their study of the ^{56}Ni(d,p)^{57}Ni reaction. However, at higher temperatures the rate predicted by [7] begins to diverge from Rehm et al. because of the inclusion of the newly constrained spectroscopic factors for the higher-lying $l = 3$ states.

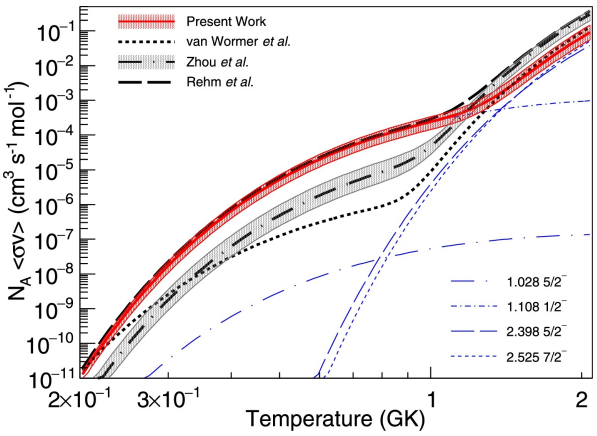

Figure A.1: The 1-σ uncertainty band of the reaction rate determined in [7] is shown in red, compared with the previous calculations from refs. [19, 20, 21]. Results match previous results from Rehm et al. at lower temperatures, but begin to diverge at higher temperatures because of the constraints imposed on higher lying states by this work. Figure from [7].

A.2 Using the ATTPC to Validate the Combined Method

Although it is common to directly extract spectroscopic factors by normalizing experimental cross sections to theoretical calculations, this practice produces a large uncertainty because of ambiguity in the single-particle potential used to create the final bound state wave function. The combined method, first put forth by Mukhamedzhanov et al. [111], proposes that measuring transfer reactions at both a high and low energy offers a way to constrain single-particle geometry and, therefore, the spectroscopic factor. Time projection chambers offer a unique opportunity to apply the combined method in one measurement.

A.2.1 Asymptotic Normalization Coefficients and the Combined Method

As mentioned before, the final bound state in transfer calculations is modeled as a nucleon in a mean-field, Woods-Saxon potential, where the depth of the potential is adjusted to reproduce the experimental binding energy for the final, $A + N$ nucleus. The radius and

diffuseness of the potential well, r_0 and a, are chosen to be realistic, but usually arbitrary values. However, if these values are adjusted, even within reasonable limits, they will directly impact the single-particle wave function produced in the calculation and can have a large impact on the cross section produced in DWBA (see Figure A.2). This will, in turn, introduce an uncertainty in the spectroscopic factor.

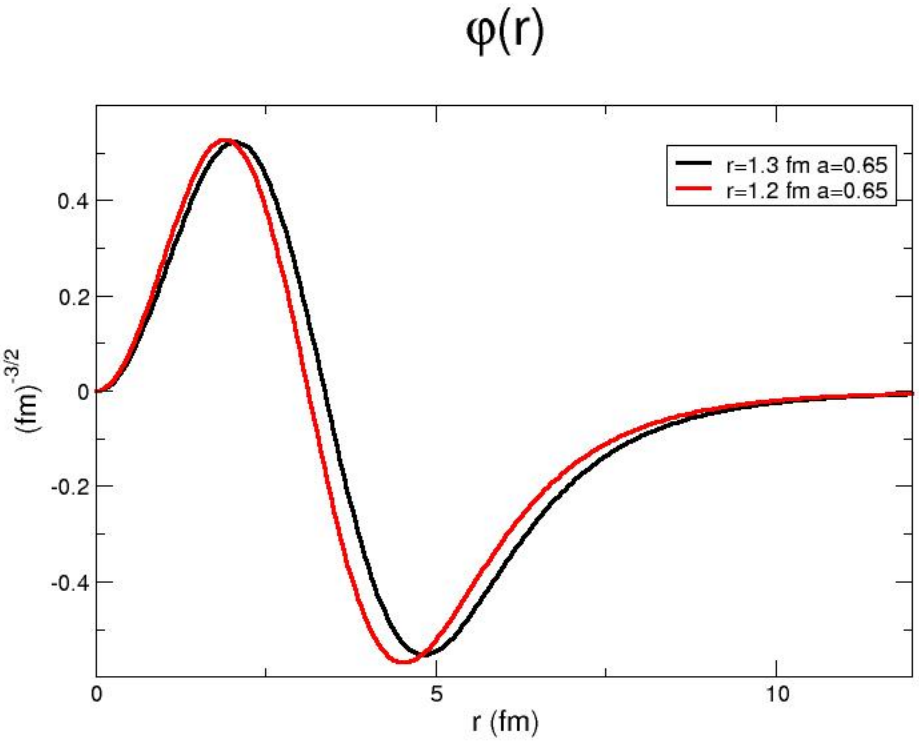

Figure A.2: Single-particle wave functions $\psi_{sp}(r_{AN})$, produced by changing the radius of the Woods-Saxon potential from $r_0 = 1.2$ to $r_0 = 1.3$. These values are both within a reasonable range for the single-particle geometry but create significant differences in the wave functions which, in turn, directly impact the cross section.

One way to improve this description is through the use of asymptotic normalization coefficients (ANCs). The ANC describes the strength of the tail of the exponentially decaying wave function. The many-body ANC (C_{lj}) describes the behavior of the full, many-body overlap function, $\phi(r_{AN}) = \langle \Psi_{A+1} | \Psi_A \rangle$, of the A+1 nucleons in the final state, which is usu-

ally not known, and the single-particle ANC (b_{lj}) describes the tail of the single-particle wave function, $\psi_{sp}(r_{AN})$ which is easy to calculate, but affected by the shape of the Woods-Saxon geometry (see Figure A.2). As mentioned in Section 2.3.2, in standard DWBA calculations $\phi(r_{AN})$ is often replaced by $S^{1/2}\psi_{sp}(r_{AN})$, an approximation of unknown validity. Although the many-body and single-particle wave functions can be very different in the interior region, they exhibit similar behavior at large distances (i.e. Whittaker functions), differing by only a normalization factor ($S^{1/2}$). Therefore outside the range of the nuclear interaction, the overlap function defined in Equation (2.29) can be written as:

$$\phi(r_{AN}) \overset{\mathrm{r>Rn}}{=} C_{lj} W_{-\eta,l+1/2}(2kr)/r = S^{1/2} b_{lj} W_{-\eta,l+1/2}(2kr)/r \tag{A.1}$$

where W is the Whittaker function. It is important to stress that this expression is only exact at large distances, where both the single-particle and many-body wave functions are described by the Whittaker form. Therefore, the spectroscopic factor can be defined as

$$S = \frac{C_{lj}^2}{b_{lj}^2}. \tag{A.2}$$

With this in mind, Mukhamedzhanov and Nunes [111] have proposed the combined method, which involves two measurements of the same transfer reaction, one at a low beam energy and one at a higher beam energy, to more efficiently constrain the spectroscopic factor. At low beam energies (<10MeV/u), the projectile can only probe the tail of the nuclear wave function, resulting in a peripheral reaction. Because the cross section is proportional to the square modulus of the overlap function, and the form factor of the overlap is well known at peripheral distances, the overall normalization C_{ij} can be extracted without sensitivity to the single-particle geometry. The second measurement, at higher energies, will probe deeper

into the nuclear wave function, and is sensitive to both the nuclear interior and exterior. However, the many-body ANC is a property of the structure of the target, not the beam energy, so it can be used to constrain the spectroscopic factor extracted from the high energy measurement. This will, in turn, constrain the single-particle geometry through the ANC.

In practice, the single-particle ANC is calculated directly from theory, (in our case, using the reaction code FRESCO) and for each b_{lj}, the spectroscopic factor is extracted by normalizing the corresponding theoretical cross section to experimental results. Because of the relation in Equation (A.2), this uniquely determines the many-body ANC. A cartoon demonstrating how this would work is shown in Figure A.3. Calculations can be repeated using a range of geometries, resulting in a range of single-particle ANCs and, therefore, spectroscopic factors. In the left plot, it is clear that depending on the single-particle geometry chosen (which translates to different values of b_{lj}), a wide range of spectroscopic factors can be extracted. However, the right plot demonstrates that at low energies, the reaction is peripheral and the many-body ANC (C_{lj}) is flat, meaning it is insensitive to the single-particle mean field geometry and, therefore, C_{lj} can be reliably obtained. Then at high energies, we use the previously established C_{lj} to fix the range for b_{lj} and are able to obtain a constrained spectroscopic factor.

This method was first validated by Walter et al. with an analysis of ^{86}Kr(d,p)^{87}Kr from two different experiments, one at 5.5 MeV/u [112] and one at 33 MeV/u [113]. This allowed for the extraction of a spectroscopic factor that was dominated by experimental errors, as opposed to theoretical uncertainties associated with the bound state geometry.

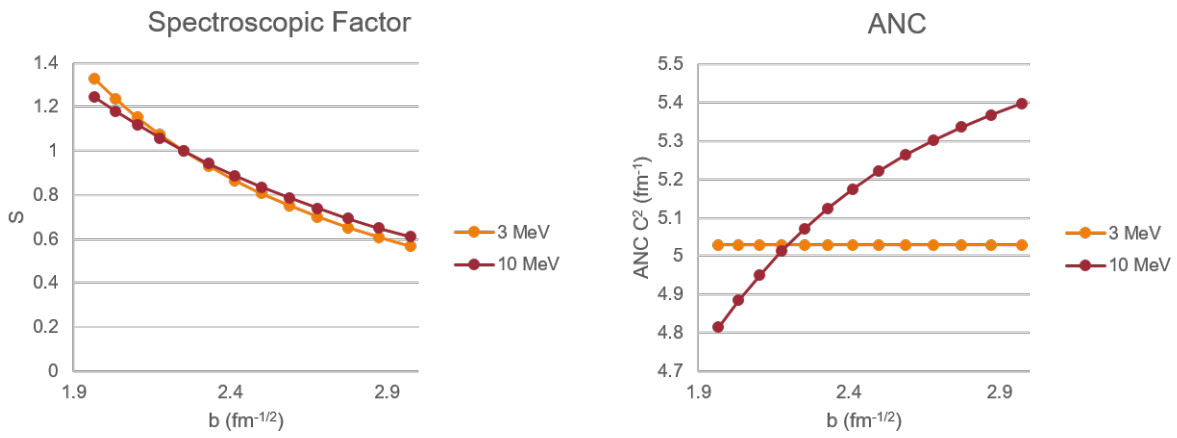

Figure A.3: Left: A cartoon of the spectroscopic factor as a function of single-particle ANC, b_{lj}, at two different beam energies. Right: A cartoon of the many-body ANC, C_{lj}, as a function of single-particle ANC b_{lj}, at two different beam energies.

A.2.2 Proposed Measurement and Preliminary Calculations

One practical drawback of the combined method is that it requires the combination of results from two different experiments, which introduces its own uncertainties and complications. Often different facilities and setups are necessary to make measurements at high and low energies, introducing different systematic errors across the measurements. In addition, obtaining the beam time necessary for two experiments can be a challenge. Thus, a new technique has been proposed to measure both a high and low energy transfer reaction in a single experiment. This would be accomplished through the use of a time projection chamber (TPC) with an active target configuration. The main benefit of this setup is that the detector gas which fills the TPC volume, for our purposes deuterium gas, also serves as the reaction target [114]. As a beam passes through the gas in the TPC, it will slow down. The beam can react anywhere within the TPC volume, allowing for a continuous reaction measurement at different energies, approaching 0 Mev/u at the far end of the chamber. Additionally, this method allows for a nearly 4π solid angle coverage which is important for

measuring reactions utilizing low-intensity rare isotope beams.

It has been proposed to perform this type of measurement using the Active Target Time Projection Chamber (AT-TPC) [115] at the National Superconducting Cyclotron Laboratory [116]. The initial experiment to validate this new method would measure ^{86}Kr(d,p)^{87}Kr, which is relevant to neutron capture in the weak r-process and has the advantage of a well know structure at low excitation energies. A beam would be introduced to the AT-TPC from the ReA6 facility at around 18 MeV (9 MeV/u). As the beam moves through the gas chamber, the energy is attenuated, allowing for the collection of transfer reaction data at a wide range of energies. Preliminary calculations for [116] indicate that, in the energy range currently available at the NSCL, it might be possible to implement the combined method in a single measurement.

The results of these calculations are shown in Figure A.4. The single particle ANC, b_{lj} is calculated using FRESCO for a range of mean-field geometries. The overall normalization is arbitrary: a transfer calculation with an reasonable choice of single-particle geometry, as described in Section 3.1, is chosen to act as the "data" that is used in the extraction of spectroscopic factors for the rest of the calculations. Once the spectroscopic factor is extracted, the many-body ANC can be determined using relation A.2. This process is repeated at a lower reaction energy (in this case, 5 MeV) and a higher energy (in this case, 8 MeV). These energies represent relatively conservative estimates of the energy window that could be attained with the AT-TPC at the NSCL. Ideally the lower energy many-body ANC will show little to no dependence on the mean field geometry, and the constrained mean field parameters can be determined by the crossing point of the calculations from different energies. The hope is to constrain, not only the ground state geometry as indicated in the left plot of Figure A.4, but also a number of excited states in ^{87}Kr, for example the $3/2^+$ state at 1.47

MeV excitation energy shown in the right plot of Figure A.4. If successful, this could be a powerful new tool in the realm of transfer spectroscopy.

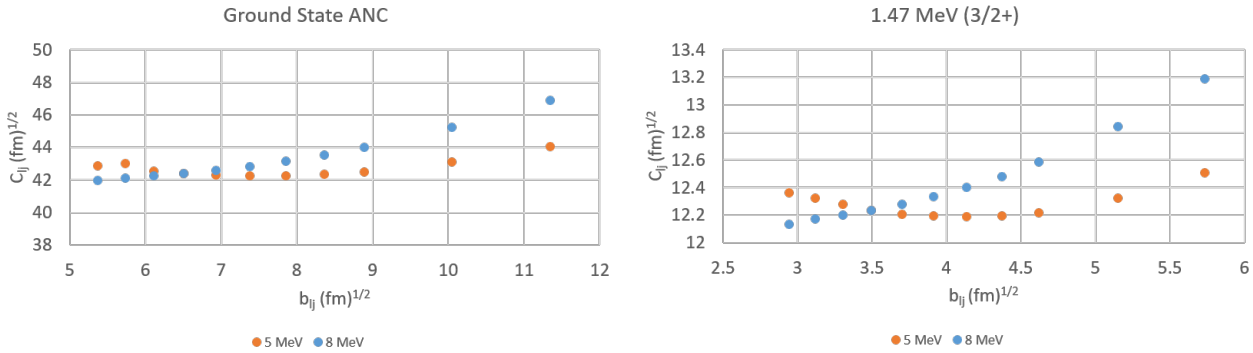

Figure A.4: Left: Preliminary calculations showing the many-body ANC, C_{lj}, as a function of single-particle ANC b_{lj}, for the ground state of ^{87}Kr. Left: Preliminary calculations showing the many-body ANC, C_{lj}, as a function of single-particle ANC b_{lj}, for the $3/2^+$ excited state of ^{87}Kr at 1.47 MeV excitation energy. The orange points correspond to calculations at 5 MeV/u and the blue points correspond to calculations at 8 MeV/u. These energies represent a conservative energy range attainable with the ATTPC.

APPENDIX B

Derivation of Charge-Exchange Two-Body T-Matrix

This derivation is for the simplified case of (p,n) charge-exchange with a two-body formalism. The target has mass A, N neutrons, and Z protons. For this study we are only looking at isobaric analog state transition on 0^+ targets. The scattering coordinate, R_{1A}, runs from the center of mass of the target to the scattering proton/neutron. The interaction is moderated through a bulk potential, in this case, the Lane Potential [47]. It is defined as

$$V_{Lane} = 2\frac{\sqrt{|N-Z|}}{A}\frac{A}{2(N-Z)}\Big[U_n(\boldsymbol{r}) - U_p(\boldsymbol{r})\Big] = \frac{1}{\sqrt{|N-Z|}}\Big[U_n(\boldsymbol{r}) - U_p(\boldsymbol{r})\Big], \quad \text{(B.1)}$$

where U_n and U_p are proton and neutron optical potentials. In our study we consider OMPs parameterized by Koning-Delaroche [1] and Varner et al. [2]. All angular momentum identities used here come from [117]. For this derivation we use the time reversed phase convention such that

$$Y_m^{l*}(\hat{r}) = (-1)^{l-m}Y_{-m}^{l}(\hat{r}). \quad \text{(B.2)}$$

In the incoming channel, the initial scattering state is

$$\chi_i^+ = \sum_{L_i} i^{L_i}(-1)^{L_i} e^{i\sigma_{L_i}} \chi_{L_i J_i}(R_{1A}) Y_0^{L_i}(\hat{R}_{1A}) \Xi_{I_1,\mu_1}(\xi_1) \frac{\sqrt{4\pi}\hat{L}_i}{k_i R_{1A}}, \tag{B.3}$$

where $\hat{L}_i = \sqrt{2L_i + 1}$ and we have set $M_i = 0$, which correspods to alligning the beam with the z axis. We can couple the spinor to the incoming spherical harmonic to get

$$\chi_i^+ = \sum_{L_i J_i} i^{L_i}(-1)^{L_i} e^{i\sigma_{L_i}} \frac{\sqrt{4\pi}\hat{L}_i}{k_i} \frac{\chi_{L_i J_i}(R_{1A})}{R_{1A}} C^{J_i \mu_1}_{L i 0 I_1 \mu_1} \left[Y^{L_i}(\hat{R}_{1A}) \Xi^{I_1}(\xi_1)\right]^{J_i}_{\mu_1}. \tag{B.4}$$

There is an equivalent expression for the outgoing channel, written as:

$$\begin{aligned} \chi_f^{*-} = \sum_{L_f J_f M_f} & i^{-L_f}(-1)^{-(M_f - \mu_1') + J_f - M_f} \frac{4\pi}{k_f} \frac{\chi^*_{L_f J_f}(R_{1A})}{R_{1A}} C^{J_f M_f}_{L_f (M_f - \mu_1') I_1 \mu_1'} \\ & \left[Y^{L_f}(\hat{R}_{1A}) \Xi^{I_1}(-\xi_1)\right]^{J_f}_{-M_f} Y^{L_f}_{-(M_f - \mu_1')}(\hat{k}_f), \end{aligned} \tag{B.5}$$

Where we have applied the phase convention from Equation (B.2). Combing the incoming and outgoing channels with the interaction, we the our T-matrix expression, written as

$$\begin{aligned} \langle \chi_f^{*-}(\boldsymbol{R_{1A}}) | V | \chi_i^+(\boldsymbol{R_{1A}}) \rangle = \int \sum_{L_f J_f M_f L_i J_i} & i^{L_i - L_f} e^{i\sigma_{L_i}} (-1)^{L_i - (M_f - \mu_1') + J_f - M_f} \frac{(4\pi)^{3/2} \hat{L}_i}{k_f k_i} \\ & \frac{\chi_{L_i J_i}(R_{1A}) V_L(R_{1A}) \chi^*_{L_f J_f}(R_{1A})}{R_{1A}^2} C^{J_i \mu_1}_{L i 0 I_1 \mu_1} C^{J_f M_f}_{L_f (M_f - \mu_1') I_1 \mu_1'} \left[Y^{L_f}(\hat{R}_{1A}) \Xi^{I_1}(-\xi_1)\right]^{J_f}_{-M_f} \\ & \left[Y^{L_i}(\hat{R}_{1A}) \Xi^{I_1}(\xi_1)\right]^{J_i}_{\mu_1} Y^{L_f}_{-(M_f - \mu_1')}(\hat{k}_f) d\Omega_{1A} d\xi_1 dR_{1A}. \end{aligned} \tag{B.6}$$

Next we can couple together the angular momentum in the initial and final channels:

$$\begin{aligned}&\left[Y^{L_f}(\hat{R}_{1A})\Xi^{I_1}(-\xi_1)\right]^{J_f}_{-M_f}\left[Y^{L_i}(\hat{R}_{1A})\Xi^{I_1}(\xi_1)\right]^{J_i}_{\mu_1}\\&=\sum_{JM}C^{JM}_{J_f-M_fJ_i\mu_1}\left\{\left[Y^{L_f}(\hat{R}_{1A})\Xi^{I_1}(-\xi_1)\right]^{J_f}\left[Y^{L_i}(\hat{R}_{1A})\Xi^{I_1}(\xi_1)\right]^{J_i}\right\}^{J}_{M}.\end{aligned}\tag{B.7}$$

But we know that the Lane potential is a scalar operator, so only terms that couple to total angular momentum 0 can contribute. This gives us

$$\begin{aligned}&=C^{00}_{J_f-M_fJ_i\mu_1}\left\{\left[Y^{L_f}(\hat{R}_{1A})\Xi^{I_1}(-\xi_1)\right]^{J_f}\left[Y^{L_i}(\hat{R}_{1A})\Xi^{I_1}(\xi_1)\right]^{J_i}\right\}^{0}_{0}\\&=\frac{(-1)^{J_f+M_f}}{\hat{J}_f}\delta_{J_iJ_f}\delta_{M_f\mu_1}\left\{\left[Y^{L_f}(\hat{R}_{1A})\Xi^{I_1}(-\xi_1)\right]^{J_f}\left[Y^{L_i}(\hat{R}_{1A})\Xi^{I_1}(\xi_1)\right]^{J_i}\right\}^{0}_{0}.\end{aligned}\tag{B.8}$$

Next, we couple the spinors and spherical harmonics together by rearranging the couplings using [117] pg. 70, Equation (11)

$$\{\{\boldsymbol{P}_a\otimes\boldsymbol{Q}_b\}_c\otimes\{\boldsymbol{R}_d\otimes\boldsymbol{S}_e\}_f\}_k=\sum_{gh}\hat{c}\hat{f}\hat{g}\hat{h}\begin{Bmatrix}a&b&c\\d&e&f\\g&h&k\end{Bmatrix}\{\{\boldsymbol{P}_a\otimes\boldsymbol{R}_d\}_g\otimes\{\boldsymbol{Q}_b\otimes\boldsymbol{S}_e\}_h\}_k,\tag{B.9}$$

giving us

$$
\begin{aligned}
&\left\{\left[Y^{L_f}(\hat{R}_{1A})\Xi^{I_1}(-\xi_1)\right]^{J_i}\left[Y^{L_i}(\hat{R}_{1A})\Xi^{I_1}(\xi_1)\right]^{J_i}\right\}_0^0 \\
&= \sum_{gh}\hat{g}\hat{h}\hat{J}_i^2 \begin{Bmatrix} L_f & I_1 & J_i \\ L_i & I_1 & J_f \\ g & h & 0 \end{Bmatrix} \left\{\left[Y^{L_f}(\hat{R}_{1A})Y^{L_i}(\hat{R}_{1A})\right]^g\left[\Xi^{I_1}(-\xi_1)\Xi^{I_1}(\xi_1)\right]^h\right\}_0^0 \\
&= \sum_{m_g m_h gh}\hat{g}\hat{h}\hat{J}_i^2 C^{00}_{gm_g hm_h} \begin{Bmatrix} L_f & I_1 & J_i \\ L_i & I_1 & J_f \\ g & h & 0 \end{Bmatrix} \left[Y^{L_f}(\hat{R}_{1A})Y^{L_i}(\hat{R}_{1A})\right]^g_{m_g}\left[\Xi^{I_1}(-\xi_1)\Xi^{I_1}(\xi_1)\right]^h_{m_h} \\
&= \sum_{m_g g}\hat{g}^2\hat{J}_i^2\frac{(-1)^{g-m_g}}{\hat{g}} \begin{Bmatrix} L_f & I_1 & J_i \\ L_i & I_1 & J_f \\ g & g & 0 \end{Bmatrix} \left[Y^{L_f}(\hat{R}_{1A})Y^{L_i}(\hat{R}_{1A})\right]^g_{m_g}\left[\Xi^{I_1}(-\xi_1)\Xi^{I_1}(\xi_1)\right]^g_{-m_g}.
\end{aligned}
\tag{B.10}
$$

The spinors must couple to 0 because the interaction is scalar. This leaves us with

$$
\begin{aligned}
&\hat{0}^2\hat{J}_i^2\frac{1}{\hat{0}} \begin{Bmatrix} L_f & I_1 & J_i \\ L_i & I_1 & J_f \\ 0 & 0 & 0 \end{Bmatrix} \left[Y^{L_f}(\hat{R}_{1A})Y^{L_i}(\hat{R}_{1A})\right]^0_0\left[\Xi^{I_1}(-\xi_1)\Xi^{I_1}(\xi_1)\right]^0_0 \\
&= \hat{J}_i^2\frac{\delta_{L_i L_f}\delta_{I_1 I_1}\delta_{J_i J_f}}{\hat{L}_f\hat{I}_1\hat{J}_i}\left[Y^{L_f}(\hat{R}_{1A})Y^{L_i}(\hat{R}_{1A})\right]^0_0\left[\Xi^{I_1}(-\xi_1)\Xi^{I_1}(\xi_1)\right]^0_0.
\end{aligned}
\tag{B.11}
$$

Integrating over the coupled spinors gives $\hat{I}_1$ and we can simplify the spherical harmonics with

$$\begin{aligned}\left[Y^{L_f}(\hat{R}_{1A})Y^{L_i}(\hat{R}_{1A})\right]_0^0 &= \sum_{m_i}\frac{(-1)^{L_i-m_i}}{\hat{L}_i}\delta_{L_iL_f}\delta_{m_i-m_f}Y^{L_f}_{-m_i}(\hat{R}_{1A})Y^{L_i}_{m_i}(\hat{R}_{1A}) \\ &= \sum_{m_i}\frac{(-1)^{L_i-m_i}}{\hat{L}_i}Y^{L_i}_{-m_i}(\hat{R}_{1A})Y^{L_i}_{m_i}(\hat{R}_{1A}).\end{aligned} \tag{B.12}$$

Then we integrate over the $\hat{R}_{1A}$ variable using [117] pg. 148 Equation (3) to get

$$\int_0^{2\pi}\int_0^{\pi} Y^{L_i}_{-m_i}(\hat{R}_{1A})Y^{L_i}_{m_i}(\hat{R}_{1A})d\Omega_{1A} = \delta_{L_iL_i}\delta_{m_i-m_i}(-1)^{m_i}. \tag{B.13}$$

Putting that all together, we have

$$\left[Y^{L_f}(\hat{R}_{1A})Y^{L_i}(\hat{R}_{1A})\right]_0^0 = \sum_{m_i}\frac{(-1)^{L_i}}{\hat{L}_i} = \hat{L}_i(-1)^{L_i}. \tag{B.14}$$

Combining all of these expressions, we get

$$\begin{aligned}&\left\{\left[Y^{L_f}(\hat{R}_{1A})\Xi^{I_1}(-\xi_1)\right]^{J_i}\left[Y^{L_i}(\hat{R}_{1A})\Xi^{I_1}(\xi_1)\right]^{J_i}\right\}_0^0 \\ &\qquad = \hat{J}_i^2\frac{\delta_{L_iL_f}\delta_{I_1I_1}\delta_{J_iJ_i}}{\hat{L}_f\hat{I}_1\hat{J}_i}\left[Y^{L_f}(\hat{R}_{1A})Y^{L_i}(\hat{R}_{1A})\right]_0^0\left[\Xi^{I_1}(-\xi_1)\Xi^{I_1}(\xi_1)\right]_0^0. = (-1)^{L_i}\hat{J}_i.\end{aligned} \tag{B.15}$$

Inserting this back into our T-matrix and simplifying all phases and prefactors, our final result is

$$\langle \chi_f^{*-}(\boldsymbol{R_{1A}})|V|\chi_i^{+}(\boldsymbol{R_{1A}})\rangle = \int \sum_{L_i J_i} e^{i\sigma_{L_i}} \frac{(4\pi)^{3/2}}{k_f k_i} \hat{L}_i \frac{\chi_{L_i J_i}(R_{1A}) V_L(R_{1A}) \chi^*_{L_f J_f}(R_{1A})}{R_{1A}^2}$$
$$C^{J_i \mu_1}_{Li0 I_1 \mu_1} C^{J_i \mu_1}_{L_i(\mu_1 - \mu_1') I_1 \mu_1'} Y^{L_i}_{\mu_1 - \mu_1'}(\hat{k}_f) dR_{1A}. \tag{B.16}$$

To get the cross section, we note that

$$\frac{d\sigma}{d\Omega} = \sum_{\mu_1 \mu_1' \mu_A \mu_B} \frac{k_f}{k_i} \frac{\mu_1 \mu_f}{4\pi^2 (\hbar c)^4} \frac{1}{\hat{J}_A \hat{\mu}_1} |T^{\mu_1}_{\mu_1'}|^2 \tag{B.17}$$

where J_A and J_B are the initial and final spin of the target.

APPENDIX C

Derivation of Charge-Exchange Three-Body T-Matrix

This appendix contains the derivations for various terms of the three-body, (p,n) charge-exchange T-matrix. In this framework, the interaction is mediated by an NN-potential with various isospin operators. For this study, we consider the isospin central, tensor, spin-spin, and spin-orbit operators. All derivation use the coordinate system described in Figure 2.3.

C.1 Central T-Matrix Derivation

This derivation is for (p,n) charge-exchange with a three-body formalism and a central NN potential. The potential only acts between the projectile proton and the target's valence neutron. This derivation uses the Condon-Shortly phase convention which can be expressed as

$$Y_m^l(\theta)^* = (-1)^m Y_{-m}^l(\theta). \tag{C.1}$$

The isospin central NN potential is directed along the r_{12} coordinate which runs from the projectile proton to the valence neutron and has the form

$$t_{NN} = V(r_{12})\boldsymbol{\tau_1} \cdot \boldsymbol{\tau_2}. \tag{C.2}$$

The isospin operators will give a factor of $\frac{1}{2}$ and we will also add a factor of $(2j+1)$ to account for all available neutrons in the valence shell. This leaves us with

$$t_{NN} = V(r_{12})\frac{(2j+1)}{2}. \tag{C.3}$$

Additionally the central potential, $V(r_{12})$, is not directed along either of the coordinates used to describe our systems, so we express the radial form factor using an expansion in our current coordinates using the method from [67]. The relationship between the two coordinate vectors and $\boldsymbol{r}_{12}$ is expressed as

$$\boldsymbol{r}_{12} = \boldsymbol{R}_{1A} - \frac{m_c}{m_A}\boldsymbol{r}_{2c}. \tag{C.4}$$

The potential only depends on the magnitude of $\boldsymbol{r}_{12}$, so we can calculate r_{12}^2

$$r_{12}^2 = R_{1A}^2 + \frac{m_c^2}{m_A^2}r_{2c}^2 - \frac{2m_c}{m_A}R_{1A}r_{2c}z, \tag{C.5}$$

where $z = \cos\theta_{12}$ and θ_{12} is the angle between $\boldsymbol{R}_{1A}$ and $\boldsymbol{r}_{2c}$. Then we can build a multipole function, F_λ, using the potential so that:

$$F_\lambda(R_{1A}, r_{2c}) = \frac{1}{2}\int_{-1}^{1} V(r_{12})P_\lambda(z)dz, \tag{C.6}$$

where P_λ are Legendre Polynomials. Inserting this into a full expression for the potential, leaves us with

$$V(r_{12}) = \sum_{\lambda}(2\lambda+1)F_{\lambda}(R,r)\frac{4\pi}{2\lambda+1}\sum_{m_\lambda}Y_{\lambda,m_\lambda}(\hat{r}_{2c})^{*}Y_{\lambda,m_\lambda}(\hat{R}_{1A}). \tag{C.7}$$

Then, our final potential is

$$t_{NN} = V(r_{12})\frac{(2j+1)}{2} = \sum_{\lambda}(2\lambda+1)F_{\lambda}(R,r)\frac{4\pi}{2\lambda+1}\sum_{m_\lambda}Y_{\lambda,m_\lambda}(\hat{r}_{2c})^{*}Y_{\lambda,m_\lambda}(\hat{R}_{1A})\frac{(2j+1)}{2}. \tag{C.8}$$

The initial scattering wave function can be expressed, in this phase convention, as

$$\chi_i = \sum_{L_i} i^{-L_i}(-1)^{L_i}\frac{\sqrt{4\pi}}{k_i R_{1A}}\hat{L}_i e^{i\sigma_{L_i}}F_{L_i}(R_{1A})Y_0^{L_i}(\hat{R}_{1A}) \tag{C.9}$$

and including spin-orbit effects we have

$$\chi_i = \sum_{L_i J_i} i^{-L_i}(-1)^{L_i}\frac{\sqrt{4\pi}}{k_i R_{1A}}\hat{L}_i e^{i\sigma_{L_i}}F_{L_i J_i}(R_{1A})C^{J_i\mu_1}_{L_i 0 I_1\mu_1}\left[Y^{L_i}(\hat{R}_{1A})\Xi^{I_1}(\xi_1)\right]^{J_i}_{\mu_1} \tag{C.10}$$

and our entire incoming channel wave function can be expressed as

$$\begin{aligned}|\psi^{\mu_1}_{\mu_A A}\rangle = \sum_{L_i J_i} i^{-L_i}(-1)^{L_i}\frac{\sqrt{4\pi}}{k_i R_{1A}}\hat{L}_i e^{i\sigma_{L_i}}\phi_{j_i}(r_{2c})F_{L_i J_i}(R_{1A})C^{J_i\mu_1}_{L_i 0 I_1\mu_1}\left[Y^{L_i}(\hat{R}_{1A})\Xi^{I_1}(\xi_1)\right]^{J_i}_{\mu_1} \\ \left\{\left[Y^{l_i}(\hat{r}_{2c})\Xi^{I_2}(\xi_2)\right]^{j_i}\Xi^{I_c}(\xi_c)\right\}^{J_A}_{\mu_A},\end{aligned} \tag{C.11}$$

where $\psi^{\mu_1}_{\mu_A A} = \chi_i(R_{1A})\Phi_{I_c:I_2}(\xi_c,\xi_2,r_{2c})$. We can create a similar expression for the outgoing

scattering wave function

$$\chi^f = \sum_{L_f J_f M_f} i^{-L_f}(-1)^{L_f - M_f} \frac{4\pi}{k_f R_{1A}} F^*_{L_f J_f}(R_{1A}) Y^{L_f}_{-M_f}(\hat{k}_f) C^{J_f M_f + \mu'_1}_{L_f M_f I_1 \mu'_1} \\ \left[Y^{L_f}(\hat{R}_{1A}) \Xi^{I_1}(\xi_1)\right]^{J_f}_{M_f + \mu'_1}. \tag{C.12}$$

So the entire outgoing wave function can be expressed as

$$|\psi^{\mu'_1}_{\mu_B}\rangle = \sum_{L_f J_f M_f} i^{-L_f}(-1)^{L_f - M_f} \frac{4\pi}{k_f R_{1A}} \phi_{j_f}(r_{2c}) F^*_{L_f J_f}(R_{1A}) Y^{L_f}_{-M_f}(\hat{k}_f) C^{J_f M_f + \mu'_1}_{L_f M_f I_1 \mu'_1} \\ \left[Y^{L_f}(\hat{R}_{1A}) \Xi^{I_1}(\xi_1)\right]^{J_f}_{M_f + \mu'_1} \left\{ \left[Y^{l_f}(\hat{r}_{2c}) \Xi^{I_2}(\xi_2)\right]^{j_f} \Xi^{I_c}(\xi_c) \right\}^{J_B}_{\mu_B}, \tag{C.13}$$

where $\psi^{\mu'_1}_{\mu_B} = \chi_f(R_{1A}) \Phi_{I_c : I_{2'}}(\xi_c, \xi_2, r_{2c})$ But we need $\langle \psi^{\mu'_1}_{\mu_B}|$. After taking the appropriate complex conjugates, we are left with

$$\langle \psi^{\mu'_1}_{\mu_B}| = \sum_{L_f J_f M_f} i^{L_f}(-1)^{L_f} \frac{4\pi}{k_f R_{1A}} \phi_{j_f}(r_{2c}) F_{L_f J_f}(R_{1A}) Y^{L_f}_{M_f}(\hat{k}_f) C^{J_f M_f + \mu'_1}_{L_f M_f I_1 \mu'_1} \\ \left[Y^{L_f}(\hat{R}_{1A}) \Xi^{I_1}(\xi_1)\right]^{*J_f}_{M_f + \mu'_1} \left\{ \left[Y^{l_f}(\hat{r}_{2c}) \Xi^{I_2}(\xi_2)\right]^{j_f} \Xi^{I_c}(\xi_c) \right\}^{*J_B}_{\mu_B}. \tag{C.14}$$

The first step is to free the core from its coupling because it will be unchanged by the interaction and can be immediately integrated out:

$$\langle\psi^{\mu_1'}_{\mu_B}| = \sum_{L_f J_f M_f m_{j_f} \mu_c'} i^{L_f}(-1)^{L_f}\frac{4\pi}{k_f R_{1A}}\phi_{j_f}(r_{2c})F_{L_f J_f}(R_{1A})Y^{L_f}_{M_f}(\hat{k}_f)C^{J_f M_f+\mu_1'}_{L_f M_f I_1 \mu_1'}$$
$$\left[Y^{L_f}(\hat{R}_{1A})\Xi^{I_1}(\xi_1)\right]^{*J_f}_{M_f+\mu_1'} C^{J_B \mu_B}_{j_f m_{j_f} I_c \mu_c'}\left[Y^{l_f}(\hat{r}_{2c})\Xi^{I_2}(\xi_2)\right]^{*j_f}_{m_{j_f}}\Xi^{*I_c}_{\mu_c'}(\xi_c). \tag{C.15}$$

$$|\psi^{\mu_1}_{\mu_A}\rangle = \sum_{L_i J_i m_{j_i} \mu_c} i^{-L_i}(-1)^{L_i}\frac{\sqrt{4\pi}}{k_i R_{1A}}\hat{L}_i e^{i\sigma_{L_i}}\phi_{j_i}(r_{2c})F_{L_i J_i}(R_{1A})C^{J_i \mu_1}_{L_i 0 I_1 \mu_1}$$
$$\left[Y^{L_i}(\hat{R}_{1A})\Xi^{I_1}(\xi_1)\right]^{J_i}_{\mu_1} C^{J_A \mu_A}_{j_i m_{j_i} I_c \mu_c}\left[Y^{l_i}(\hat{r}_{2c})\Xi^{I_2}(\xi_2)\right]^{j_i}_{m_{j_i}}\Xi^{I_c}_{\mu_c}(\xi_c). \tag{C.16}$$

Now we can note that, in our phase convention,

$$\left[Y^{L_f}(\hat{R}_{1A})\Xi^{I_1}(\xi_1)\right]^{*J_f}_{M_f+\mu_1'} = (-1)^{M_f+\mu_1'}\left[Y^{L_f}(\hat{R}_{1A})\Xi^{I_1}(-\xi_1)\right]^{J_f}_{-(M_f+\mu_1')} \tag{C.17}$$

and

$$\left[Y^{l_f}(\hat{r}_{2c})\Xi^{I_2}(\xi_2)\right]^{*j_f}_{m_{j_f}} = (-1)^{m_{j_f}}\left[Y^{l_f}(\hat{r}_{2c})\Xi^{I_2}(-\xi_2)\right]^{j_f}_{-m_{j_f}}. \tag{C.18}$$

This leaves us with a total T-matrix expression of

$$\langle\psi^{\mu_1'}_{\mu_B}|t_{NN}|\psi^{\mu_1}_{\mu_A}\rangle = \int \sum_{\substack{L_f J_f M_f L_i J_i \\ m_{j_i} m_{j_f} \mu_c \mu_c'}} k_1\; Y^{L_f}_{M_f}(\hat{k}_f) C^{J_f M_f+\mu_1'}_{L_f M_f I_1 \mu_1'} C^{J_i \mu_1}_{L_i 0 I_1 \mu_1} C^{J_A \mu_A}_{j_i m_{j_i} I_c \mu_c} C^{J_B \mu_B}_{j_f m_{j_f} I_c \mu_c'}$$

$$\left[Y^{L_f}(R_{1A})\Xi^{I_1}(-\xi_1)\right]^{J_f}_{-(M_f+\mu_1')} \left[Y^{l_f}(r_{2c})\Xi^{I_2}(-\xi_2)\right]^{j_f}_{-m_{j_f}} \left[Y^{L_i}(R_{1A})\Xi^{I_1}(\xi_1)\right]^{J_i}_{\mu_1}$$

$$\left[Y^{l_i}(r_{2c})\Xi^{I_2}(\xi_2)\right]^{j_i}_{m_{j_i}} \Xi^{*I_c}_{\mu_c'}(\xi_c)\Xi^{I_c}_{\mu_c}(\xi_c) \frac{\phi_{j_f}(r_{2c}) F_{L_f J_f}(R_{1A}) t_{NN} \phi_{j_i}(r_{2c}) F_{L_i J_i}(R_{1A})}{R^2_{1A}}$$

$$R^2_{1A} r^2_{2c} dR_{1A} dr_{2c} d\Omega_{2c} d\Omega_{1A} d\xi_1 d\xi_2 d\xi_c, \tag{C.19}$$

where

$$k_1 = i^{L_f - L_i}(-1)^{L_i + L_f + M_f + \mu_1' + m_{j_f}} e^{i\sigma_{L_i}} \frac{\hat{L}_i (4\pi)^{\frac{3}{2}}}{k_f k_i}. \tag{C.20}$$

Immediately, we see that

$$\int \Xi^{*I_c}_{\mu_c'}(\xi_c)\Xi^{I_c}_{\mu_c}(\xi_c) d\xi_c = \delta_{\mu_c \mu_c'} \tag{C.21}$$

leaving us with

$$\langle\psi^{\mu_1'}_{\mu_B}|t_{NN}|\psi^{\mu_1}_{\mu_A}\rangle = \int \sum_{\substack{L_f J_f M_f L_i J_i \\ m_{j_i} m_{j_f} \mu_c}} k_1 \; Y^{L_f}_{M_f}(\hat{k}_f) C^{J_f M_f+\mu_1'}_{L_f M_f I_1 \mu_1'} C^{J_i \mu_1}_{L_i 0 I_1 \mu_1} C^{J_A \mu_A}_{j_i m_{j_i} I_c \mu_c} C^{J_B \mu_B}_{j_f m_{j_f} I_c \mu_c}$$

$$\left[Y^{L_f}(R_{1A})\Xi^{I_1}(-\xi_1)\right]^{J_f}_{-(M_f+\mu_1')} \left[Y^{l_f}(r_{2c})\Xi^{I_2}(-\xi_2)\right]^{j_f}_{-m_{j_f}} \left[Y^{L_i}(R_{1A})\Xi^{I_1}(\xi_1)\right]^{J_i}_{\mu_1}$$

$$\left[Y^{l_i}(r_{2c})\Xi^{I_2}(\xi_2)\right]^{j_i}_{m_{j_i}} \frac{\phi_{j_f}(r_{2c}) F_{L_f J_f}(R_{1A}) t_{NN} \phi_{j_i}(r_{2c}) F_{L_i J_i}(R_{1A})}{R^2_{1A}}$$

$$R^2_{1A} r^2_{2c} dR_{1A} dr_{2c} d\Omega_{2c} d\Omega_{1A} d\xi_1 d\xi_2 \tag{C.22}$$

The central isospin operator is a scalar, so all of the angular momentum must couple to 0 to contribute. To achieve this, we will couple all the angular momentum operators together.

$$\langle\psi^{\mu_1'}_{\mu_B}|t_{NN}|\psi^{\mu_1}_{\mu_A}\rangle = \int \sum_{\substack{L_f J_f M_f L_i J_i \\ J M_J j m_j m_{j_i} m_{j_f} \mu_c}} k_1 \; Y^{L_f}_{M_f}(\hat{k}_f) C^{J_f M_f+\mu_1'}_{L_f M_f I_1 \mu_1'} C^{J_i \mu_1}_{L_i 0 I_1 \mu_1} C^{J M_J}_{J_f -(M_f+\mu_1') J_i \mu_1}$$

$$C^{j m_j}_{j_f -m_{j_f} j_i m_{j_i}} C^{J_A \mu_A}_{j_i m_{j_i} I_c \mu_c} C^{J_B \mu_B}_{j_f m_{j_f} I_c \mu_c} \left\{ \left[Y^{L_f}(R_{1A})\Xi^{I_1}(-\xi_1)\right]^{J_f} \left[Y^{L_i}(R_{1A})\Xi^{I_1}(\xi_1)\right]^{J_i} \right\}^{J}_{M_J}$$

$$\left\{ \left[Y^{l_f}(r_{2c})\Xi^{I_2}(-\xi_2)\right]^{j_f} \left[Y^{l_i}(r_{2c})\Xi^{I_2}(\xi_2)\right]^{j_i} \right\}^{j}_{m_j}$$

$$\frac{\phi_{j_f}(r_{2c}) F_{L_f J_f}(R_{1A}) t_{NN} \phi_{j_i}(r_{2c}) F_{L_i J_i}(R_{1A})}{R^2_{1A}} R^2_{1A} r^2_{2c} dR_{1A} dr_{2c} d\Omega_{2c} d\Omega_{1A} d\xi_1 d\xi_2. \tag{C.23}$$

Now we can rearrange the spin and angular momentum components using Equation (B.9). Applying this identity gives

$$\sum_{\substack{JM_J \\ jm_j}} C^{JM_J}_{J_f-(M_f+\mu_1')J_i\mu_1} C^{jm_j}_{j_f-m_{j_f}j_im_{j_i}} \left\{ \left[Y^{L_f}(R_{1A})\Xi^{I_1}(-\xi_1)\right]^{J_f} \left[Y^{L_i}(R_{1A})\Xi^{I_1}(\xi_1)\right]^{J_i} \right\}^J_{M_J}$$
$$\left\{ \left[Y^{l_f}(r_{2c})\Xi^{I_2}(-\xi_2)\right]^{j_f} \left[Y^{l_i}(r_{2c})\Xi^{I_2}(\xi_2)\right]^{j_i} \right\}^j_{m_j}$$
$$= \sum_{JM_Jjm_jgh} \hat{J}_i\hat{J}_f\hat{g}\hat{h} \begin{Bmatrix} L_f & I_1 & J_f \\ L_i & I_1 & J_i \\ g & h & J \end{Bmatrix} C^{JM_J}_{J_f-(M_f+\mu_1')J_i\mu_1} C^{jm_j}_{j_f-m_{j_f}j_im_{j_i}}$$
$$\left\{ \left[Y^{L_f}(R_{1A})Y^{L_i}(R_{1A})\right]^g \left[\Xi^{I_1}(-\xi_1)\Xi^{I_1}(\xi_1)\right]^h \right\}^J_{M_J}$$
$$\left\{ \left[Y^{l_f}(r_{2c})\Xi^{I_2}(-\xi_2)\right]^{j_f} \left[Y^{l_i}(r_{2c})\Xi^{I_2}(\xi_2)\right]^{j_i} \right\}^j_{m_j}. \tag{C.24}$$

The spinors must couple to 0 because the interaction is scalar in spin space. This leaves us with

$$= \sum_{JM_Jjm_jg} \hat{J}_i\hat{J}_f\hat{g} \begin{Bmatrix} L_f & I_1 & J_f \\ L_i & I_1 & J_i \\ g & 0 & J \end{Bmatrix} C^{JM_J}_{J_f-(M_f+\mu_1')J_i\mu_1} C^{jm_j}_{j_fm_{j_f}j_im_{j_i}}$$
$$\left\{ \left[Y^{L_f}(R_{1A})Y^{L_i}(R_{1A})\right]^g \left[\Xi^{I_1}(-\xi_1)\Xi^{I_1}(\xi_1)\right]^0 \right\}^J_{M_J}$$
$$\left\{ \left[Y^{l_f}(r_{2c})\Xi^{I_2}(-\xi_2)\right]^{j_f} \left[Y^{l_i}(r_{2c})\Xi^{I_2}(\xi_2)\right]^{j_i} \right\}^j_{m_j}. \tag{C.25}$$

Now we can perform the exact analogy for the internal angular momentum variables, l and j, leaving us with

$$= \sum_{JM_J j m_j g h} \hat{J}_i \hat{J}_f \hat{j}_i \hat{j}_f \hat{g} \hat{h} \begin{Bmatrix} L_f & I_1 & J_f \\ L_i & I_1 & J_i \\ g & 0 & J \end{Bmatrix} \begin{Bmatrix} l_f & I_2 & j_f \\ l_i & I_2 & j_i \\ h & 0 & j \end{Bmatrix} C^{JM_J}_{J_f-(M_f+\mu_1')J_i\mu_1} C^{jm_j}_{j_f-m_j f j_i m_{j_i}}$$
$$\left\{ \left[Y^{L_f}(R_{1A}) Y^{L_i}(R_{1A}) \right]^g \left[\Xi^{I_1}(-\xi_1) \Xi^{I_1}(\xi_1) \right]^0 \right\}^J_{M_J}$$
$$\left\{ \left[Y^{l_f}(r_{2c}) Y^{l_i}(r_{2c}) \right]^h \left[\Xi^{I_2}(-\xi_2) \Xi^{I_2}(\xi_2) \right]^0 \right\}^j_{m_j}. \tag{C.26}$$

Next, we couple everything together, allowing us to ultimately couple all of the angular momentum operators together.

$$= \sum_{JM_J j m_j g h T M_T} \hat{J}_i \hat{J}_f \hat{j}_i \hat{j}_f \hat{g} \hat{h} \begin{Bmatrix} L_f & I_1 & J_f \\ L_i & I_1 & J_i \\ g & 0 & J \end{Bmatrix} \begin{Bmatrix} l_f & I_2 & j_f \\ l_i & I_2 & j_i \\ h & 0 & j \end{Bmatrix} C^{JM_J}_{J_f-(M_f+\mu_1')J_i\mu_1} C^{jm_j}_{j_f-m_j f j_i m_{j_i}}$$
$$C^{TM_T}_{JM_J j m_j} \left[\left\{ \left[Y^{L_f}(R_{1A}) Y^{L_i}(R_{1A}) \right]^g \left[\Xi^{I_1}(-\xi_1) \Xi^{I_1}(\xi_1) \right]^0 \right\}^J \right.$$
$$\left. \left\{ \left[Y^{l_f}(r_{2c}) Y^{l_i}(r_{2c}) \right]^h \left[\Xi^{I_2}(-\xi_2) \Xi^{I_2}(\xi_2) \right]^0 \right\}^j \right]^T_{M_T}. \tag{C.27}$$

Again, rearranging using Equation(B.9) gives us

$$= \sum_{JM_J j m_j g h T M_T x y} \hat{J}\hat{j}\hat{x}\hat{y}\hat{J}_i\hat{J}_f\hat{j}_i\hat{j}_f\hat{g}\hat{h} \begin{Bmatrix} L_f & I_1 & J_f \\ L_i & I_1 & J_i \\ g & 0 & J \end{Bmatrix} \begin{Bmatrix} l_f & I_2 & j_f \\ l_i & I_2 & j_i \\ h & 0 & j \end{Bmatrix} \begin{Bmatrix} g & 0 & J \\ h & 0 & j \\ x & y & T \end{Bmatrix}$$

$$C^{JM_J}_{J_f-(M_f+\mu_1')J_i\mu_1} C^{jm_j}_{j_f-m_{j_f}j_i m_{j_i}} C^{TM_T}_{JM_J j m_j} \left[\left\{ \left[Y^{L_f}(R_{1A}) Y^{L_i}(R_{1A}) \right]^g \left[Y^{l_f}(r_{2c}) Y^{l_i}(r_{2c}) \right]^h \right\}^x \right.$$

$$\left. \left\{ \left[\Xi^{I_1}(-\xi_1)\Xi^{I_1}(\xi_1) \right]^0 \left[\Xi^{I_2}(-\xi_2)\Xi^{I_2}(\xi_2) \right]^0 \right\}^y \right]^T_{M_T} .$$

(C.28)

It is immediately clear that y must equal 0. If we uncouple the spin operators and apply this simplification we get

$$= \sum_{JM_J jm_j ghTM_T xm_x} \hat{J}\hat{j}\hat{x}\hat{J}_i\hat{J}_f\hat{j}_i\hat{j}_f\hat{g}\hat{h} \begin{Bmatrix} L_f & I_1 & J_f \\ L_i & I_1 & J_i \\ g & 0 & J \end{Bmatrix} \begin{Bmatrix} l_f & I_2 & j_f \\ l_i & I_2 & j_i \\ h & 0 & j \end{Bmatrix} \begin{Bmatrix} g & 0 & J \\ h & 0 & j \\ x & 0 & T \end{Bmatrix}$$

$$C^{JM_J}_{J_f-(M_f+\mu_1')J_i\mu_1} C^{jm_j}_{j_f-m_{j_f}j_i m_{j_i}} \Big\{ \big[Y^{L_f}(R_{1A})Y^{L_i}(R_{1A})\big]^g \big[Y^{l_f}(r_{2c})Y^{l_i}(r_{2c})\big]^h \Big\}^x_{m_x}$$

$$C^{TM_T}_{JM_J jm_j} C^{TM_T}_{xm_x 00} \Big\{ \big[\Xi^{I_1}(-\xi_1)\Xi^{I_1}(\xi_1)\big]^0 \big[\Xi^{I_2}(-\xi_2)\Xi^{I_2}(\xi_2)\big]^0 \Big\}^0_0$$

$$= \sum_{JM_J jm_j TM_T} \hat{J}_i\hat{J}_f\hat{j}_i\hat{j}_f\hat{J}\hat{j} \begin{Bmatrix} L_f & I_1 & J_f \\ L_i & I_1 & J_i \\ J & 0 & J \end{Bmatrix} \begin{Bmatrix} l_f & I_2 & j_f \\ l_i & I_2 & j_i \\ j & 0 & j \end{Bmatrix}$$

$$C^{JM_J}_{J_f-(M_f+\mu_1')J_i\mu_1} C^{jm_j}_{j_f-m_{j_f}j_i m_{j_i}} C^{TM_T}_{JM_J jm_j} \Big\{ \big[Y^{L_f}(R_{1A})Y^{L_i}(R_{1A})\big]^J \big[Y^{l_f}(r_{2c})Y^{l_i}(r_{2c})\big]^j \Big\}^T_{M_T}$$

$$\Big\{ \big[\Xi^{I_1}(-\xi_1)\Xi^{I_1}(\xi_1)\big]^0 \big[\Xi^{I_2}(-\xi_2)\Xi^{I_2}(\xi_2)\big]^0 \Big\}^0_0 \tag{C.29}$$

We can now integrate over the ξ_1 and ξ_2 variables, giving us a factor of $\hat{I}_1\hat{I}_2$. As discussed before, we need the total angular momentum, T, to be equal to 0 because of our scalar operator. This leaves us with

$$
= \sum_{\substack{JM_J jm_j \\ TM_T}} \hat{I}_1 \hat{I}_2 \hat{J}_i \hat{J}_f \hat{j}_i \hat{j}_f \hat{J} \hat{j} \begin{Bmatrix} L_f & I_1 & J_f \\ L_i & I_1 & J_i \\ J & 0 & J \end{Bmatrix} \begin{Bmatrix} l_f & I_2 & j_f \\ l_i & I_2 & j_i \\ j & 0 & j \end{Bmatrix} C^{JM_J}_{J_f-(M_f+\mu_1')J_i\mu_1} C^{jm_j}_{j_f-m_{j_f}j_i m_{j_i}}
$$

$$
C^{TM_T}_{JM_J jm_j} \left\{ \left[Y^{L_f}(R_{1A}) Y^{L_i}(R_{1A}) \right]^J \left[Y^{l_f}(r_{2c}) Y^{l_i}(r_{2c}) \right]^j \right\}^T_{M_T}
$$

$$
= \sum_{JM_J jm_j} \hat{I}_1 \hat{I}_2 \hat{J}_i \hat{J}_f \hat{j}_i \hat{j}_f \hat{J} \hat{j} \begin{Bmatrix} L_f & I_1 & J_f \\ L_i & I_1 & J_i \\ J & 0 & J \end{Bmatrix} \begin{Bmatrix} l_f & I_2 & j_f \\ l_i & I_2 & j_i \\ j & 0 & j \end{Bmatrix} C^{JM_J}_{J_f-(M_f+\mu_1')J_i\mu_1} C^{jm_j}_{j_f-m_{j_f}j_i m_{j_i}}
$$

$$
C^{00}_{JM_J jm_j} \left\{ \left[Y^{L_f}(R_{1A}) Y^{L_i}(R_{1A}) \right]^J \left[Y^{l_f}(r_{2c}) Y^{l_i}(r_{2c}) \right]^j \right\}^0_0
$$

$$
= \sum_{JM_J jm_j} \frac{(-1)^{J-M_J} \delta_{Jj} \delta_{M_J - m_j}}{\hat{J}} \hat{I}_1 \hat{I}_2 \hat{J}_i \hat{J}_f \hat{j}_i \hat{j}_f \hat{J} \hat{j} \begin{Bmatrix} L_f & I_1 & J_f \\ L_i & I_1 & J_i \\ J & 0 & J \end{Bmatrix} \begin{Bmatrix} l_f & I_2 & j_f \\ l_i & I_2 & j_i \\ j & 0 & j \end{Bmatrix}
$$

$$
C^{JM_J}_{J_f-(M_f+\mu_1')J_i\mu_1} C^{jm_j}_{j_f-m_{j_f}j_i m_{j_i}} \left\{ \left[Y^{L_f}(R_{1A}) Y^{L_i}(R_{1A}) \right]^J \left[Y^{l_f}(r_{2c}) Y^{l_i}(r_{2c}) \right]^j \right\}^0_0
$$

$$
= \sum_{JM_J} (-1)^{J-M_J} \hat{I}_1 \hat{I}_2 \hat{J}_i \hat{J}_f \hat{j}_i \hat{j}_f \hat{J} \begin{Bmatrix} L_f & I_1 & J_f \\ L_i & I_1 & J_i \\ J & 0 & J \end{Bmatrix} \begin{Bmatrix} l_f & I_2 & j_f \\ l_i & I_2 & j_i \\ J & 0 & J \end{Bmatrix}
$$

$$
C^{JM_J}_{J_f-(M_f+\mu_1')J_i\mu_1} C^{JM_J}_{j_f-m_{j_f}j_i m_{j_i}} \left\{ \left[Y^{L_f}(R_{1A}) Y^{L_i}(R_{1A}) \right]^J \left[Y^{l_f}(r_{2c}) Y^{l_i}(r_{2c}) \right]^J \right\}^0_0. \tag{C.30}
$$

We can use [117], pg. 357 Equation (2) to simplify the 9j symbols

$$\begin{Bmatrix} d & c & e \\ a & c & b \\ g & 0 & g \end{Bmatrix} = \frac{(-1)^{b+d+c+g}}{\hat{c}\hat{g}} \begin{Bmatrix} a & b & c \\ e & d & g \end{Bmatrix}, \tag{C.31}$$

leaving us with

$$= \sum_{JM_J} (-1)^{J-M_J+J_i+L_f+I_1+j_i+l_f+I_2} \hat{J}_i \hat{J}_f \hat{j}_i \hat{j}_f \frac{1}{\hat{J}} \begin{Bmatrix} L_i & J_i & I_1 \\ J_f & L_f & J \end{Bmatrix} \begin{Bmatrix} l_i & j_i & I_2 \\ j_f & l_f & J \end{Bmatrix} \tag{C.32}$$
$$C^{JM_J}_{J_f-(M_f+\mu_1')J_i\mu_1} C^{JM_J}_{j_f-m_{j_f}j_i m_{j_i}} \left\{ \left[Y^{L_f}(R_{1A}) Y^{L_i}(R_{1A}) \right]^J \left[Y^{l_f}(r_{2c}) Y^{l_i}(r_{2c}) \right]^J \right\}_0^0.$$

We can now take advantage of the rotational invariance of the integrand. The value of the interaction is unchanged by a rotation of the reference frame and we can align R_{1A} with the z axis. In this configuration, r_{2c} forms the angle θ_{2c} with the z axis. This simplifies $Y^{L_f/L_i}_{M_i/M_f}(R_{1A})$ to $\frac{\hat{L}}{\sqrt{4\pi}}$ and results in a factor of $8\pi^2$ from the integration over θ_{1A}, ϕ_{1A}, and ϕ_{2c}. This results in an overall factor of $8\pi^2$. So we have

$$= \sum_{JM_J m_f} (-1)^{J-M_J+J_i+L_f+I_1+j_i+l_f+I_2} C^{00}_{J0J0} C^{J0}_{L_i 0 L_f 0} C^{J0}_{l_f m_f l_i - m_f} 2\pi \hat{L}_i \hat{L_f} \hat{J}_i \hat{J}_f \hat{j}_i \hat{j_f} \frac{1}{\hat{J}}$$

$$\begin{Bmatrix} L_i & J_i & I_1 \\ J_f & L_f & J \end{Bmatrix} \begin{Bmatrix} l_i & j_i & I_2 \\ j_f & l_f & J \end{Bmatrix} C^{JM_J}_{J_f -(M_f+\mu_1')J_i\mu_1} C^{JM_J}_{j_f -m_{j_f} j_i m_{j_i}} Y^{l_f}_{m_f}(\hat{r}_{2c}) Y^{l_i}_{-m_f}(\hat{r}_{2c})$$

$$= \sum_{JM_J m_f} (-1)^{-M_J+J_i+L_f+I_1+j_i+l_f+I_2} C^{J0}_{L_i 0 L_f 0} C^{J0}_{l_f m_f l_i - m_f} 2\pi \hat{L}_i \hat{L_f} \hat{J}_i \hat{J}_f \hat{j}_i \hat{j_f} \frac{1}{\hat{J^2}}$$

$$\begin{Bmatrix} L_i & J_i & I_1 \\ J_f & L_f & J \end{Bmatrix} \begin{Bmatrix} l_i & j_i & I_2 \\ j_f & l_f & J \end{Bmatrix} C^{JM_J}_{J_f -(M_f+\mu_1')J_i\mu_1} C^{JM_J}_{j_f -m_{j_f} j_i m_{j_i}} Y^{l_f}_{m_f}(\hat{r}_{2c}) Y^{l_i}_{-m_f}(\hat{r}_{2c}).$$

(C.33)

Combining this result with our full T-matrix expression, we have

$$\langle \psi^{\mu_1'}_{\mu_B} | t_{NN} | \psi^{\mu_1}_{\mu_A} \rangle = \int \sum_{\substack{L_f J_f M_f L_i J_i \\ J M_J m_f m_{j_i} m_{j_f} \mu_c}} k_2 \; Y^{L_f}_{M_f}(\hat{k}_f) C^{J_f M_f + \mu_1'}_{L_f M_f I_1 \mu_1'} C^{J_i \mu_1}_{L_i 0 I_1 \mu_1} C^{JM_J}_{J_f -(M_f+\mu_1')J_i\mu_1}$$

$$C^{JM_J}_{j_f -m_{j_f} j_i m_{j_i}} C^{J0}_{L_i 0 L_f 0} C^{J0}_{l_f m_f l_i - m_f} C^{J_A \mu_A}_{j_i m_{j_i} I_c \mu_c} C^{J_B \mu_B}_{j_f m_{j_f} I_c \mu_c}$$

$$\begin{Bmatrix} L_i & J_i & I_1 \\ J_f & L_f & J \end{Bmatrix} \begin{Bmatrix} l_i & j_i & I_2 \\ j_f & l_f & J \end{Bmatrix} Y^{l_f}_{m_f}(\hat{r}_{2c}) Y^{l_i}_{-m_f}(\hat{r}_{2c})$$

$$\frac{\phi_{j_f}(r_{2c}) F_{L_f J_f}(R_{1A}) t_{NN} \phi_{j_i}(r_{2c}) F_{L_i J_i}(R_{1A})}{R^2_{1A}} R^2_{1A} r^2_{2c} dR_{1A} dr_{2c} \sin\theta_{2c} d\theta_{2c},$$

(C.34)

where, noting that $(-1)^{2L_f} = 1$ and $i^{-L_i}(-1)^{L_i} = i^{L_i}$,

$$k_2 = i^{L_f+L_i}(-1)^{M_f+\mu_1'+m_{j_f}-M_J+J_i+I_1+j_i+l_f+I_2} e^{i\sigma_{L_i}} \frac{2\pi(4\pi)^{\frac{3}{2}}}{k_f k_i} \frac{\hat{L_i}^2 \hat{L_f} \hat{J_i} \hat{J_f} \hat{j_i} \hat{j_f}}{\hat{J}^2}. \quad \text{(C.35)}$$

Now we can look more closely at the form of our potential:

$$t_{NN} = V(r_{12})\frac{(2j+1)}{2} = \sum_{\lambda}(2\lambda+1)F_\lambda(R,r)\frac{4\pi}{2\lambda+1}\sum_{m_\lambda} Y_{\lambda,m_\lambda}(\hat{r}_{2c})^* Y_{\lambda,m_\lambda}(\hat{R}_{1A})\frac{(2j+1)}{2}$$
$$= \sum_{\lambda m_\lambda} F_\lambda(R,r)2\pi(2j_i+1)Y^*_{\lambda,m_\lambda}(\hat{r}_{2c})Y_{\lambda,m_\lambda}(\hat{R}_{1A}). \quad \text{(C.36)}$$

Because we aligned the R_{1A} coordinate with the z axis, Equation (C.36) simplifies to

$$t_{NN} = \sum_{\lambda} F_\lambda(R,r)\frac{\hat{\lambda}2\pi(2j_i+1)}{\sqrt{4\pi}}Y_0^\lambda(\hat{r}_{2c}). \quad \text{(C.37)}$$

We can now complete the simplification of the angular variables. First, we use [117] pg. 144 Equation (9):

$$Y_{l_1m_1}(\theta)Y_{l_2m_2}(\theta) = \sum_{LM}\frac{\hat{l}_1\hat{l}_2}{\sqrt{4\pi}\hat{L}}C^{L0}_{l_10l_20}C^{LM}_{l_1m_1l_2m_2}Y_{LM}.(\theta) \quad \text{(C.38)}$$

Applying this gives

$$Y^{l_f}_{m_f}(\hat{r}_{2c})Y^{l_i}_{-m_f}(\hat{r}_{2c})Y_0^\lambda(\hat{r}_{2c}) = \sum_L \frac{\hat{l_i}\hat{l_f}}{\hat{L}\sqrt{4\pi}}C^{L0}_{l_f0l_i0}C^{L0}_{l_fm_fl_i-m_f}Y_0^L(\hat{r}_{2c})Y_0^\lambda(\hat{r}_{2c}). \quad \text{(C.39)}$$

Next, we can use [117] pg. 149 Equation (10):

$$\int Y^*_{lm}(\theta) Y_{l'm}(\theta) \sin\theta d\theta = \frac{\delta_{ll'}}{2\pi}, \tag{C.40}$$

giving us the T-matrix expression:

$$\begin{aligned}
\langle \psi^{\mu'_1}_{\mu_B} | t_{NN} | \psi^{\mu_1}_{\mu_A} \rangle = \int & \sum_{\substack{L_f J_f M_f L_i J_i \\ J M_J m_f \lambda m_{j_i} m_{j_f} \mu_c}} k_3 \; Y^{L_f}_{M_f}(\hat{k}_f) C^{J_f M_f + \mu'_1}_{L_f M_f I_1 \mu'_1} C^{J_i \mu_1}_{L_i 0 I_1 \mu_1} C^{J M_J}_{J_f - (M_f + \mu'_1) J_i \mu_1} \\
& C^{J M_J}_{j_f - m_{j_f} j_i m_{j_i}} C^{J0}_{L_i 0 L_f 0} C^{J0}_{l_f m_f l_i - m_f} C^{J_A \mu_A}_{j_i m_{j_i} I_c \mu_c} C^{J_B \mu_B}_{j_f m_{j_f} I_c \mu_c} \\
& \begin{Bmatrix} L_i & J_i & I_1 \\ J_f & L_f & J \end{Bmatrix} \begin{Bmatrix} l_i & j_i & I_2 \\ j_f & l_f & J \end{Bmatrix} C^{\lambda 0}_{l_f 0 l_i 0} C^{\lambda 0}_{l_f m_f l_i - m_f} \\
& \frac{\phi_{j_f}(r_{2c}) F_{L_f J_f}(R_{1A}) F_\lambda(R, r) \phi_{j_i}(r_{2c}) F_{L_i J_i}(R_{1A})}{R^2_{1A}} R^2_{1A} r^2_{2c} dR_{1A} dr_{2c},
\end{aligned} \tag{C.41}$$

where

$$k_3 = i^{L_f + L_i} (-1)^{M_f + \mu'_1 + m_{j_f} - M_J + J_i + I_1 + j_i + l_f + I_2} e^{i\sigma_{L_i}} (2j_i + 1) \frac{(4\pi)^{\frac{3}{2}}}{2 k_f k_i} \frac{\hat{L_i}^2 \hat{L_f} \hat{J_i} \hat{J_f} \hat{j_i} \hat{j_f} \hat{l_i} \hat{l_f}}{\hat{J}^2}. \tag{C.42}$$

Finally, we can simplify

$$\sum_{m_f} C^{J0}_{l_f m_f l_i - m_f} C^{\lambda 0}_{l_f m_f l_i - m_f} = \delta_{J\lambda} \delta_{00}, \tag{C.43}$$

giving a final result of

$$\langle\psi^{\mu'_1}_{\mu_B}|t_{NN}|\psi^{\mu_1}_{\mu_A}\rangle = \int \sum_{\substack{L_f J_f M_f L_i J_i \\ M_J \lambda m_{j_i} m_{j_f} \mu_c}} k_4\, Y^{L_f}_{M_f}(\hat{k}_f) C^{J_f M_f + \mu'_1}_{L_f M_f I_1 \mu'_1} C^{J_i \mu_1}_{L_i 0 I_1 \mu_1} C^{\lambda M_J}_{J_f - (M_f+\mu'_1) J_i \mu_1}$$

$$C^{\lambda M_J}_{j_f - m_{j_f} j_i m_{j_i}} C^{\lambda 0}_{L_i 0 L_f 0} C^{\lambda 0}_{l_f 0 l_i 0} C^{J_A \mu_A}_{j_i m_{j_i} I_c \mu_c} C^{J_B \mu_B}_{j_f m_{j_f} I_c \mu_c} \begin{Bmatrix} L_i & J_i & I_1 \\ J_f & L_f & \lambda \end{Bmatrix}$$

$$\begin{Bmatrix} l_i & j_i & I_2 \\ j_f & l_f & \lambda \end{Bmatrix} \frac{\phi_{j_f}(r_{2c}) F_{L_f J_f}(R_{1A}) F_\lambda(R,r) \phi_{j_i}(r_{2c}) F_{L_i J_i}(R_{1A})}{R^2_{1A}} R^2_{1A} r^2_{2c} dR_{1A} dr_{2c}, \tag{C.44}$$

where

$$k_4 = i^{L_f + L_i} (-1)^{M_f + \mu'_1 + m_{j_f} - M_J + J_i + I_1 + j_i + l_f + I_2} e^{i\sigma_{L_i}} (2j_i + 1) \frac{(4\pi)^{\frac{3}{2}}}{2k_f k_i} \frac{\hat{L_i}^2 \hat{L_f} \hat{J_i} \hat{J_f} \hat{j_i} \hat{j_f} \hat{l_i} \hat{l_f}}{\hat{\lambda}^2}. \tag{C.45}$$

The total cross section expression is

$$\frac{d\sigma}{d\Omega} = \sum_{\mu_1 \mu'_1 \mu_A \mu_B} \frac{k_f}{k_i} \frac{\mu_1 \mu_f}{4\pi^2 (\hbar c)^4} \frac{1}{\hat{J}^2_A \hat{\mu}^2_1} |\langle\psi^{\mu'_1}_{\mu_B}|t_{NN}|\psi^{\mu_1}_{\mu_A}\rangle|^2, \tag{C.46}$$

and J_A and J_B are the initial and final spin of the target.

C.2 Tensor T-Matrix Derivation

This derivation is for the isospin tensor interaction for Fermi, (p,n) charge-exchange reactions.

The interaction is defined as:

$$V_{TEN} = \sqrt{\frac{24\pi}{5}}(\boldsymbol{\tau_1}\cdot\boldsymbol{\tau_1})V_t(r_{12})\Big[\boldsymbol{Y_{(2)}}\cdot[\boldsymbol{\sigma_1}\otimes\boldsymbol{\sigma_2}]_{\boldsymbol{(2)}}\Big] \tag{C.47}$$

where $\boldsymbol{Y_{(2)}}$ is a tensor whose components are the spherical harmonics Y_{2m}, $\boldsymbol{\tau_1}\cdot\boldsymbol{\tau_2}$ is the isospin operator, $V_t(r_{12})$ is a form factor for the radial dependence of the isospin tensor interaction, and $[\boldsymbol{\sigma_1}\otimes\boldsymbol{\sigma_2}]_{\boldsymbol{(2)}}$ is the tensor represented by the cross product of the proton and neutron spin functions. Just as in the central case, the isospin operator will give a factor of $\frac{1}{2}$ and there will be a factor of $(2j+1)$ to account for the number of nucleons in the valence shell. This can be inserted in the same T-matrix expression used for the isospin central interaction, giving us

$$\begin{aligned}
&\langle\psi^{\mu_1'}_{\mu_B}|t_{NN}|\psi^{\mu_1}_{\mu_A}\rangle = \int \sum_{\substack{L_fJ_fM_fL_iJ_i\\ m_{j_i}m_{j_f}\mu_c\mu_c'}} k_1\; Y^{L_f}_{M_f}(\hat{k}_f)C^{J_fM_f+\mu_1'}_{L_fM_fI_1\mu_1'}C^{J_i\mu_1}_{L_i0I_1\mu_1}C^{J_A\mu_A}_{j_im_{j_i}I_c\mu_c}C^{J_B\mu_B}_{j_fm_{j_f}I_c\mu_c'}\\
&\big[Y^{L_f}(R_{1A})\Xi^{I_1}(-\xi_1)\big]^{J_f}_{-(M_f+\mu_1')}\big[Y^{l_f}(r_{2c})\Xi^{I_2}(-\xi_2)\big]^{j_f}_{-m_{j_f}}\\
&\big[Y^{L_i}(R_{1A})\Xi^{I_1}(\xi_1)\big]^{J_i}_{\mu_1}\big[Y^{l_i}(r_{2c})\Xi^{I_2}(\xi_2)\big]^{j_i}_{m_{j_i}}\Xi^{*I_c}_{\mu_c'}(\xi_c)\Xi^{I_c}_{\mu_c}(\xi_c)\\
&\frac{\phi_{j_f}(r_{2c})F_{L_fJ_f}(R_{1A})t_{NN}\phi_{j_i}(r_{2c})F_{L_iJ_i}(R_{1A})}{R^2_{1A}}R^2_{1A}r^2_{2c}dR_{1A}dr_{2c}d\Omega_{2c}d\Omega_{1A}d\xi_1d\xi_2d\xi_c
\end{aligned} \tag{C.48}$$

where

$$k_1 = i^{L_f-L_i}(-1)^{L_i+L_f+M_f+\mu_1'+m_{j_f}}e^{i\sigma_{L_i}}\frac{\hat{L}_i(4\pi)^{\frac{3}{2}}\sqrt{24\pi}}{k_fk_i}. \tag{C.49}$$

and

$$t_{NN} = \frac{(2j_i+1)}{2} V(r_{12}) \Big[\boldsymbol{Y_{(2)}} [\boldsymbol{\sigma_1} \otimes \boldsymbol{\sigma_2}]_{\boldsymbol{(2)}} \Big]_0^0 \tag{C.50}$$

,

where we have used [117] pg. 65 Equation (35):

$$(M_J \cdot N_J) = (-1)^{-J} \hat{J} \{ M_J \otimes N_J \}_{00}. \tag{C.51}$$

Immediately, we see that

$$\int \Xi^{*I_c}_{\mu'_c}(\xi_c) \Xi^{I_c}_{\mu_c}(\xi_c) d\xi_c, = \delta_{\mu_c \mu'_c} \tag{C.52}$$

leaving us with

$$\begin{aligned}
\langle \psi^{\mu'_1}_{\mu_B} | t_{NN} | \psi^{\mu_1}_{\mu_A} \rangle = \int \sum_{\substack{L_f J_f M_f L_i J_i \\ m_{j_i} m_{j_f} \mu_c}} & k_1 \; Y^{L_f}_{M_f}(\hat{k}_f) C^{J_f M_f + \mu'_1}_{L_f M_f I_1 \mu'_1} C^{J_i \mu_1}_{L_i 0 I_1 \mu_1} C^{J_A \mu_A}_{j_i m_{j_i} I_c \mu_c} C^{J_B \mu_B}_{j_f m_{j_f} I_c \mu_c} \\
& \big[Y^{L_f}(R_{1A}) \Xi^{I_1}(-\xi_1) \big]^{J_f}_{-(M_f + \mu'_1)} \big[Y^{l_f}(r_{2c}) \Xi^{I_2}(-\xi_2) \big]^{j_f}_{-m_{j_f}} \\
& \big[Y^{L_i}(R_{1A}) \Xi^{I_1}(\xi_1) \big]^{J_i}_{\mu_1} \big[Y^{l_i}(r_{2c}) \Xi^{I_2}(\xi_2) \big]^{j_i}_{m_{j_i}} \\
& \frac{\phi_{j_f}(r_{2c}) F_{L_f J_f}(R_{1A}) t_{NN} \phi_{j_i}(r_{2c}) F_{L_i J_i}(R_{1A})}{R^2_{1A}} R^2_{1A} r^2_{2c} dR_{1A} dr_{2c} d\Omega_{2c} d\Omega_{1A} d\xi_1 d\xi_2.
\end{aligned} \tag{C.53}$$

The central isopin operator is a scalar, so the total angular momentum must couple to 0 to contribute. To achieve this, we will couple all the angular momentum operators together:

$$\sum_{J_T} C^{J_T-(M_f+\mu_1')+\mu_1}_{J_f-(M_f+\mu_1')J_i\mu_1} \left\{ \left[Y^{L_f}(R_{1A})\Xi^{I_1}(-\xi_1)\right]^{J_f} \left[Y^{L_i}(R_{1A})\Xi^{I_1}(\xi_1)\right]^{J_i} \right\}^{J_T}_{-(M_f+\mu_1')+\mu_1}. \tag{C.54}$$

Now we can rearrange the spin and angular momentum components using Equation (B.9), giving us

$$\sum_{J_T,g,h} \hat{J}_i\hat{J}_f\hat{g}\hat{h} C^{J_T-(M_f+\mu_1')+\mu_1}_{J_f-(M_f+\mu_1')J_i\mu_1} \begin{Bmatrix} L_f & I_1 & J_f \\ L_i & I_1 & J_i \\ g & h & J_T \end{Bmatrix} \left\{ \left[Y^{L_f}(R_{1A})Y^{L_i}(R_{1A})\right]^g \right. \\ \left. \left[\Xi^{I_1}(-\xi_1)\Xi^{I_1}(\xi_1)\right]^h \right\}^{J_T}_{-(M_f+\mu_1')+\mu_1}. \tag{C.55}$$

In this case, the spinors must couple to 1 in order to couple to a rank two tensor. Applying this, and also making the replacement that $M_{J_f} = M_f + \mu_1'$, we are left with

$$\sum_{J_T,g} \hat{J}_i\hat{J}_f\hat{g}\hat{1} C^{J_T-M_{J_f}+\mu_1}_{J_f-M_{J_f}J_i\mu_1} \begin{Bmatrix} L_f & I_1 & J_f \\ L_i & I_1 & J_i \\ g & 1 & J_T \end{Bmatrix} \left\{ \left[Y^{L_f}(R_{1A})Y^{L_i}(R_{1A})\right]^g \right. \\ \left. \left[\Xi^{I_1}(-\xi_1)\Xi^{I_1}(\xi_1)\right]^1 \right\}^{J_T}_{-M_{J_f}+\mu_1}. \tag{C.56}$$

We can perform the exact analogy for the internal angular momentum variables, leaving us with

$$\sum_{j_t,h} \hat{j}_i \hat{j}_f \hat{h} \hat{1} C^{j_t m_{j_i} - m_{j_f}}_{j_f - m_{j_f} j_i m_{j_i}} \begin{Bmatrix} l_f & I_2 & j_f \\ l_i & I_2 & j_i \\ h & 1 & j_t \end{Bmatrix} \left\{ \left[Y^{l_f}(r_{2c}) Y^{l_i}(r_{2c}) \right]^h \left[\Xi^{I_2}(-\xi_2) \Xi^{I_2}(\xi_2) \right]^1 \right\}^{j_t}_{m_{j_i} - m_{j_f}}. \tag{C.57}$$

To deal with the operator, we can break up the tensor operator into its spin and isospin parts:

$$\begin{aligned} &\left[\boldsymbol{Y_{(2)}} [\boldsymbol{\sigma_1} \otimes \boldsymbol{\sigma_2}]_{(2)} \right]^0_0 \\ &\quad = \sum_{m_2 m_2'} C^{00}_{2 m_2 2 m_2'} Y^2_{m_2}(\hat{r}_{12}) S^2_{m_2'}(\xi_1 \xi_2) = \sum_{m_2} \frac{(-1)^{-m_2}}{\hat{2}} Y^2_{m_2}(\hat{r}_{12}) S^2_{-m_2}(\xi_1 \xi_2), \end{aligned} \tag{C.58}$$

and couple all angular momentum operators:

$$\begin{aligned} &= \sum_{T M_T} C^{T M_T}_{J_T - M_{J_f} + \mu_1 j_t - m_{j_f} + m_{j_i}} \Bigg[\left\{ \left[Y^{L_f}(R_{1A}) Y^{L_i}(R_{1A}) \right]^g \left[\Xi^{I_1}(-\xi_1) \Xi^{I_1}(\xi_1) \right]^1 \right\}^{J_T} \\ &\left\{ \left[Y^{l_f}(r_{2c}) Y^{l_i}(r_{2c}) \right]^h \left[\Xi^{I_2}(-\xi_2) \Xi^{I_2}(\xi_2) \right]^1 \right\}^{j_t} \Bigg]^T_{M_T}. \end{aligned} \tag{C.59}$$

Rearranging using Equation (B.9) gives us

$$= \sum_{TM_T xy} \hat{J_T}\hat{j_t}\hat{x}\hat{y} \begin{Bmatrix} g & 1 & J_T \\ h & 1 & j_t \\ x & y & T \end{Bmatrix} C^{TM_T}_{J_T - M_{J_f} + \mu_1 j_t - m_{j_f} + m_{j_i}} \Bigg[\Big\{ \big[Y^{L_f}(R_{1A}) Y^{L_i}(R_{1A})\big]^g$$
$$\big[Y^{l_f}(r_{2c}) Y^{l_i}(r_{2c})\big]^h \Big\}^x \Big\{ \big[\Xi^{I_1}(-\xi_1)\Xi^{I_1}(\xi_1)\big]^1 \big[\Xi^{I_2}(-\xi_2)\Xi^{I_2}(\xi_2)\big]^1 \Big\}^y \Bigg]^T_{M_T}. \tag{C.60}$$

As mentioned before, because the operator is a scalar, we need the total spin components to couple to 2, forcing $y = 2$. If we uncouple the spinors operators and apply this simplification we get

$$= \sum_{TM_T x m_x m'_2} \hat{J_T}\hat{j_t}\hat{x}\hat{2} \begin{Bmatrix} g & 1 & J_T \\ h & 1 & j_t \\ x & 2 & T \end{Bmatrix} C^{TM_T}_{x m_x 2 m'_2} C^{TM_T}_{J_T - M_{J_f} + \mu_1 j_t - m_{j_f} + m_{j_i}}$$
$$\Big[\big[Y^{L_f}(R_{1A}) Y^{L_i}(R_{1A})\big]^g \big[Y^{l_f}(r_{2c}) Y^{l_i}(r_{2c})\big]^h \Big]^x_{m_x}$$
$$\Big[\big[\Xi^{I_1}(-\xi_1)\Xi^{I_1}(\xi_1)\big]^1 \big[\Xi^{I_2}(-\xi_2)\Xi^{I_2}(\xi_2)\big]^1 \Big]^2_{m'_2}. \tag{C.61}$$

Finally we rearrange the spinor components one more time using Equation (B.9) to have a projectile and target nucleon coupled together in each channel giving us

$$
\begin{aligned}
&= \sum_{TM_T x m_x m_2' \alpha\beta} \hat{J_T}\hat{j_t}\hat{x}\hat{2}\hat{1}\hat{1}\hat{\alpha}\hat{\beta} \begin{Bmatrix} g & 1 & J_T \\ h & 1 & j_t \\ x & 2 & T \end{Bmatrix} \begin{Bmatrix} \frac{1}{2} & \frac{1}{2} & 1 \\ \frac{1}{2} & \frac{1}{2} & 1 \\ \alpha & \beta & 2 \end{Bmatrix} \\
&C^{TM_T}_{xm_x 2m_2'} C^{TM_T}_{J_T - M_{J_f} + \mu_1 j_t - m_{j_f} + m_{j_i}} \Big[\big[Y^{L_f}(R_{1A}) Y^{L_i}(R_{1A}) \big]^g \big[Y^{l_f}(r_{2c}) Y^{l_i}(r_{2c}) \big]^h \Big]^x_{m_x} \\
&\Big[\big[\Xi^{I_1}(-\xi_1) \Xi^{I_2}(-\xi_2) \big]^1 \big[\Xi^{I_2}(\xi_2) \Xi^{I_1}(\xi_1) \big]^1 \Big]^2_{m_2'}.
\end{aligned}
\tag{C.62}
$$

The 9j symbol simplifies to to $\delta_{\alpha\beta}\delta_{\alpha 1}\frac{1}{9}$. This will can cancel out the $\hat{\alpha}\hat{\beta}\hat{1}\hat{1}$ factor, leaving us with

$$
\begin{aligned}
&= \sum_{TM_T x m_x m_2'} \hat{J_T}\hat{j_t}\hat{x}\hat{2} \begin{Bmatrix} g & 1 & J_T \\ h & 1 & j_t \\ x & 2 & T \end{Bmatrix} C^{TM_T}_{xm_x 2m_2'} C^{TM_T}_{J_T - M_{J_f} + \mu_1 j_t - m_{j_f} + m_{j_i}} \\
&\Big[\big[Y^{L_f}(R_{1A}) Y^{L_i}(R_{1A}) \big]^g \big[Y^{l_f}(r_{2c}) Y^{l_i}(r_{2c}) \big]^h \Big]^x_{m_x} \\
&\Big[\big[\Xi^{I_1}(-\xi_1) \Xi^{I_2}(-\xi_2) \big]^1 \big[\Xi^{I_2}(\xi_2) \Xi^{I_1}(\xi_1) \big]^1 \Big]^2_{m_2'}.
\end{aligned}
\tag{C.63}
$$

Because we have the angular momentum operators and spin operators coupled separately, it is clear how to impose conservation of the projection of the angular momentum in both spaces separately. Including the projections from the tensor operator, we are left with the relations

$$m_2' - m_2 = 0 \qquad\qquad m_x + m_2 = 0$$

$$m_2' = m_2 \qquad\qquad m_x = -m_2.$$

We see from the Clebsch-Gordan coefficient that $M_T = m_x + m_2'$. Using the substitutions from above, we notice that $M_T = 0$. Incorporating all of these changes into the T-matrix expression, we are left with

$$\langle \psi^{\mu_1'}_{\mu_B} | t_{NN} | \psi^{\mu_1}_{\mu_A} \rangle = \int \sum_{\substack{L_f J_f M_{J_f} L_i J_i \\ m_{j_i} m_{j_f} \mu_c g h \\ J_T j_t m_2 x T}} k_2 \; Y^{L_f}_{M_{J_f} - \mu_1'}(\hat{k}_f) C^{J_f M_{J_f}}_{L_f M_{J_f} - \mu_1' I_1 \mu_1'} C^{J_i \mu_1}_{L_i 0 I_1 \mu_1} C^{J_A \mu_A}_{j_i m_{j_i} I_c \mu_c}$$
$$C^{J_B \mu_B}_{j_f m_{j_f} I_c \mu_c} C^{J_T - M_{J_f} + \mu_1}_{J_f - M_{J_f} J_i \mu_1} C^{j_t - m_{j_f} + m_{j_i}}_{j_f - m_{j_f} j_i m_{j_i}} C^{T0}_{x - m_2 2 m_2} C^{T0}_{J_T - M_{J_f} + \mu_1 j_t - m_{j_f} + m_{j_i}}$$
$$Y^2_{m_2}(\hat{r}_{12}) S^2_{-m_2}(\xi_1 \xi_2) \begin{Bmatrix} l_f & I_2 & j_f \\ l_i & I_2 & j_i \\ h & 1 & j_t \end{Bmatrix} \begin{Bmatrix} L_f & I_1 & J_f \\ L_i & I_1 & J_i \\ g & 1 & J_T \end{Bmatrix} \begin{Bmatrix} g & 1 & J_T \\ h & 1 & j_t \\ x & 2 & T \end{Bmatrix}$$
$$\Big[\big[Y^{L_f}(R_{1A}) Y^{L_i}(R_{1A}) \big]^g \big[Y^{l_f}(r_{2c}) Y^{l_i}(r_{2c}) \big]^h \Big]^x_{-m_2}$$
$$\Big[\big[\Xi^{I_1}(-\xi_1) \Xi^{I_2}(-\xi_2) \big]^1 \big[\Xi^{I_2}(\xi_2) \Xi^{I_1}(\xi_1) \big]^1 \Big]^2_{m_2}$$
$$\frac{\phi_{j_f}(r_{2c}) F_{L_f J_f}(R_{1A}) t_{NN} \phi_{j_i}(r_{2c}) F_{L_i J_i}(R_{1A})}{R^2_{1A}} R^2_{1A} r^2_{2c} dR_{1A} dr_{2c} d\Omega_{2c} d\Omega_{1A} d\xi_1 d\xi_2. \tag{C.64}$$

where

$$k_2 = i^{L_i - L_f}(-1)^{L_i + L_f + M_{J_f} + m_{j_f} - m_2} e^{i\sigma_{L_i}} \hat{L}_i \hat{J}_i \hat{J}_f \hat{g} \hat{h} \hat{1}^2 \hat{j_i}^3 \hat{j_f} \hat{J}_T \hat{j}_t \hat{x} \frac{\sqrt{24\pi}}{2} \frac{(4\pi)^{\frac{3}{2}}}{k_i k_f} \quad \text{(C.65)}$$

and

$$t_{NN} = \sum_{\lambda m_\lambda} F_\lambda(R_{1A}, r_{2c}) 4\pi Y^\lambda_{m_\lambda}(R_{1A}) Y^\lambda_{m_\lambda}(r_{2c})^*, \quad \text{(C.66)}$$

where F_λ contains the interaction over the r_{12} coordinate expressed as a function of the other two coordinates. We can then apply the spin operator:

$$\sum_{m_q m_Q} \int \left[\Xi^{I_1}(-\xi_1)\Xi^{I_2}(-\xi_2)\right]^1_{m_q} \left[\Xi^{I_2}(\xi_2)\Xi^{I_1}(\xi_1)\right]^1_{m_Q} C^{2m_2}_{1m_q 1m_Q} S^2_{-m_2}(\xi_1 \xi_2). \quad \text{(C.67)}$$

This is equivalent to

$$\sum_{m_q m_Q} C^{2m_2}_{1m_q 1m_Q} \langle \frac{1}{2}\frac{1}{2} 1 m_q | \{\sigma_1 \otimes \sigma_2\}^2_{-m_2} | \frac{1}{2}\frac{1}{2} 1 m_Q \rangle, \quad \text{(C.68)}$$

which can be simplified using [117] pg. 479 Equation (28):

$$\langle n_1' j_1' n_2' j_2' j' m' | \{\hat{P}_a(1) \otimes \hat{Q}_b(2)\}_{c\gamma} | n_1 j_1 n_2 j_2 j m \rangle$$
$$= (-1)^{2c} \hat{c}\hat{j} C^{j'm'}_{jmc\gamma} \begin{Bmatrix} a & b & c \\ j_1' & j_2' & j' \\ j_1 & j_2 & j \end{Bmatrix} \langle n_1' j_1' || \hat{\boldsymbol{P}}_{\boldsymbol{a}}(1) || n_1 j_1 \rangle \langle n_2' j_2' || \hat{\boldsymbol{Q}}_{\boldsymbol{b}}(2) || n_2 j_2 \rangle. \tag{C.69}$$

In our case, this gives us

$$\sum_{m_q m_Q} C^{2m_2}_{1m_q 1m_Q} \langle \frac{1}{2}\frac{1}{2} 1 m_q | \{\sigma_1 \otimes \sigma_2\}^2_{-m_2} | \frac{1}{2}\frac{1}{2} 1 m_Q \rangle =$$
$$\sum_{m_q m_Q} C^{2m_2}_{1m_q 1m_Q} \hat{2}\hat{1} C^{1m_q}_{1M_Q 2-m_2} \begin{Bmatrix} 1 & 1 & 2 \\ \frac{1}{2} & \frac{1}{2} & 1 \\ \frac{1}{2} & \frac{1}{2} & 1 \end{Bmatrix} \langle \frac{1}{2} || \sigma_p || \frac{1}{2} \rangle \langle \frac{1}{2} || \sigma_n || \frac{1}{2} \rangle. \tag{C.70}$$

The reduced matrix elements can be evaluated using [117] pg. 495 Equation (95):

$$\langle s' || \hat{\boldsymbol{S}}_{\boldsymbol{1}} || s \rangle = \delta_{ss'} \sqrt{s(s+1)(2s+1)}, \tag{C.71}$$

keeping in mind that $2\hat{S} = \hat{\sigma}$. The sum over Clebsch-Gordan coefficients can also be evaluated explicitly, giving us

$$
\begin{aligned}
&= \sum_{m_q m_Q} C^{2m_2}_{1m_q 1m_Q} \hat{2}\hat{1} C^{1m_q}_{1M_Q 2-m_2} \begin{Bmatrix} 1 & 1 & 2 \\ \frac{1}{2} & \frac{1}{2} & 1 \\ \frac{1}{2} & \frac{1}{2} & 1 \end{Bmatrix} \langle \frac{1}{2} || \sigma_p || \frac{1}{2} \rangle \langle \frac{1}{2} || \sigma_n || \frac{1}{2} \rangle \\
&= \frac{\sqrt{3}\sqrt{5}}{\sqrt{15}} \frac{1}{9} 4 \sqrt{\frac{1}{2}(\frac{1}{2}+1)(2\frac{1}{2}+1)} \\
&= \frac{2}{3}
\end{aligned}
\tag{C.72}
$$

Substituting this into the T-matrix expression gives

$$
\begin{aligned}
&\langle \psi^{\mu_1'}_{\mu_B} | t_{NN} | \psi^{\mu_1}_{\mu_A} \rangle = \int \sum_{\substack{L_f J_f M_{J_f} L_i J_i \\ m_{j_i} m_{j_f} \mu_c g h \\ J_T j_t m_2 x T}} k_3 \; Y^{L_f}_{M_{J_f} - \mu_1'}(\hat{k}_f) C^{J_f M_{J_f}}_{L_f M_{J_f} - \mu_1' I_1 \mu_1'} C^{J_i \mu_1}_{L_i 0 I_1 \mu_1} C^{J_A \mu_A}_{j_i m_{j_i} I_c \mu_c} \\
&C^{J_B \mu_B}_{j_f m_{j_f} I_c \mu_c} C^{J_T - M_{J_f} + \mu_1}_{J_f - M_{J_f} J_i \mu_1} C^{j_t - m_{j_f} + m_{j_i}}_{j_f - m_{j_f} j_i m_{j_i}} C^{T0}_{x-m_2 2 m_2} C^{T0}_{J_T - M_{J_f} + \mu_1 j_t - m_{j_f} + m_{j_i}} Y^2_{m_2}(\hat{r}_{12}) \\
&\begin{Bmatrix} l_f & I_2 & j_f \\ l_i & I_2 & j_i \\ h & 1 & j_t \end{Bmatrix} \begin{Bmatrix} L_f & I_1 & J_f \\ L_i & I_1 & J_i \\ g & 1 & J_T \end{Bmatrix} \begin{Bmatrix} g & 1 & J_T \\ h & 1 & j_t \\ x & 2 & T \end{Bmatrix} \Big[\big[Y^{L_f}(R_{1A}) Y^{L_i}(R_{1A}) \big]^g \\
&\big[Y^{l_f}(r_{2c}) Y^{l_i}(r_{2c}) \big]^h \Big]^x_{-m_2} \frac{\phi_{j_f}(r_{2c}) F_{L_f J_f}(R_{1A}) t_{NN} \phi_{j_i}(r_{2c}) F_{L_i J_i}(R_{1A})}{R^2_{1A}} \\
&R^2_{1A} r^2_{2c} dR_{1A} dr_{2c} d\Omega_{2c} d\Omega_{1A},
\end{aligned}
\tag{C.73}
$$

where

$$k_3 = i^{L_i - L_f}(-1)^{L_i + L_f + M_{J_f} + m_{j_f} - m_2} e^{i\sigma_{L_i}} \hat{L}_i \hat{J}_i \hat{J}_f \hat{g} \hat{h} \hat{j}_i^3 \hat{j}_f \hat{J}_T \hat{j}_t \hat{x} \sqrt{24\pi} \frac{(4\pi)^{\frac{3}{2}}}{k_i k_f}, \tag{C.74}$$

and

$$t_{NN} = \sum_{\lambda m_\lambda} F_\lambda(R_{1A}, r_{2c}) 4\pi Y^\lambda_{m_\lambda}(R_{1A}) Y^\lambda_{m_\lambda}(r_{2c})^*. \tag{C.75}$$

Next we can simplify the angular momentum operators. Because the tensor operator is a scalar operator, all of the angular momentum operators must couple to 0.

$$\begin{aligned} &C^{00}_{x-m_2 2 m_2} \left\{ \left[\left[Y^{L_f}(R_{1A}) Y^{L_i}(R_{1A}) \right]^g \left[Y^{l_f}(r_{2c}) Y^{l_i}(r_{2c}) \right]^h \right]^x Y^2(\hat{r}_{12}) \right\}^0_0 = \\ &\frac{(-1)^{2+m_2}}{\hat{2}} \delta_{x2} \delta_{m_2 m_2} \left[\left[Y^{L_f}(R_{1A}) Y^{L_i}(R_{1A}) \right]^g \left[Y^{l_f}(r_{2c}) Y^{l_i}(r_{2c}) \right]^h \right]^2_{-m_2} Y^2_{m_2}(\hat{r}_{12}). \end{aligned} \tag{C.76}$$

As in the central case, we have the freedom to choose the $\hat{R}_{1A}$ direction to be along the $\hat{z}$ axis, meaning that M_i and M_f are 0 and the initial and final scattering spherical harmonics reduce to $\frac{\hat{L}_i \hat{L}_f}{4\pi}$. We can also perform the integration over $\sin\theta_{1A} d\theta_{1A} d\phi_{1A} d\phi_{2c}$, giving a factor of $8\pi^2$. Incorporating these simplifications, Equation (C.76) becomes

$$\begin{aligned} &\frac{(-1)^{2+m_2}}{\hat{2}} \delta_{x2} \delta_{m_2 m_2} \left[\left[Y^{L_f}(R_{1A}) Y^{L_i}(R_{1A}) \right]^g \left[Y^{l_f}(r_{2c}) Y^{l_i}(r_{2c}) \right]^h \right]^2_{-m_2} Y^2_{m_2}(\hat{r}_{12}) \\ &= \sum_{\substack{m_2 m_h m_g \\ m_i m_f}} \frac{(-1)^{2+m_2}}{\hat{2}} C^{00}_{2-m_2 2 m_2} C^{2-m_2}_{g m_g h m_h} C^{h m_h}_{l_f m_f l_i m_i} C^{g m_g}_{L_f 0 L_i 0} \frac{\hat{L}_i \hat{L}_f}{4\pi} \\ &Y^{l_f}_{m_f}(\hat{r}_{2c}) Y^{l_i}_{m_i}(\hat{r}_{2c}) Y^2_{m_2}(\hat{r}_{12}) 8\pi^2. \end{aligned} \tag{C.77}$$

It is immediately clear that $m_g = 0$ and, therefore, $m_h = -m_2$. Also, the Clebsch-Gordan coefficient coupled to 0 can again be simplified. Finally, we can make the substitution at $m_i = -m_2 - m_f$. Combining these simplifications, we are left with

$$\sum_{m_2 m_f} \frac{(-1)^{2(2+m_2)}}{\hat{2}^2} C^{2-m_2}_{g0h-m_2} C^{h-m_2}_{l_f m_f l_i - m_2 - m_f} C^{g0}_{L_f 0 L_i 0} \hat{L}_i \hat{L}_f \\ Y^{l_f}_{m_f}(\hat{r}_{2c}) Y^{l_i}_{-m_2-m_f}(\hat{r}_{2c}) Y^2_{m_2}(\hat{r}_{12}) 2\pi. \tag{C.78}$$

The T-matrix expression is now given by

$$\langle \psi^{\mu_1'}_{\mu_B} | t_{NN} | \psi^{\mu_1}_{\mu_A} \rangle = \int \sum_{\substack{L_f J_f M_{J_f} L_i J_i \\ m_{j_i} m_{j_f} \mu_c g h \\ J_T j_t m_2 m_f T}} k_4 \; Y^{L_f}_{M_{J_f} - \mu_1'}(\hat{k}_f) C^{J_f M_{J_f}}_{L_f M_{J_f} - \mu_1' I_1 \mu_1'} C^{J_i \mu_1}_{L_i 0 I_1 \mu_1} C^{J_A \mu_A}_{j_i m_{j_i} I_c \mu_c} \\ C^{J_B \mu_B}_{j_f m_{j_f} I_c \mu_c} C^{J_T - M_{J_f} + \mu_1}_{J_f - M_{J_f} J_i \mu_1} C^{j_t - m_{j_f} + m_{j_i}}_{j_f - m_{j_f} j_i m_{j_i}} C^{T0}_{x - m_2 2 m_2} C^{T0}_{J_T - M_{J_f} + \mu_1 j_t - m_{j_f} + m_{j_i}} \\ C^{2-m_2}_{g0h-m_2} C^{h-m_2}_{l_f m_f l_i - m_2 - m_f} C^{g0}_{L_f 0 L_i 0} \begin{Bmatrix} l_f & I_2 & j_f \\ l_i & I_2 & j_i \\ h & 1 & j_t \end{Bmatrix} \begin{Bmatrix} L_f & I_1 & J_f \\ L_i & I_1 & J_i \\ g & 1 & J_T \end{Bmatrix} \begin{Bmatrix} g & 1 & J_T \\ h & 1 & j_t \\ 2 & 2 & T \end{Bmatrix} \\ Y^{l_f}_{m_f}(r_{2c}) Y^{l_i}_{-m_2-m_f}(r_{2c}) Y^2_{m_2}(\hat{r}_{12}) \\ \frac{\phi_{j_f}(r_{2c}) F_{L_f J_f}(R_{1A}) t_{NN} \phi_{j_i}(r_{2c}) F_{L_i J_i}(R_{1A})}{R^2_{1A}} R^2_{1A} r^2_{2c} dR_{1A} dr_{2c} \sin\theta_{2c} d\theta_{2c}, \tag{C.79}$$

where

$$k_4 = i^{L_i - L_f}(-1)^{L_i+L_f+M_{J_f}+m_{j_f}-m_2} e^{i\sigma_{L_i}} \hat{L_i}^2 \hat{L_f} \hat{J}_i \hat{J}_f \hat{g} \hat{h} \hat{j_i}^3 \hat{j_f} \hat{J_T} \hat{jt} \frac{2\pi\sqrt{24\pi}}{\hat{2}^2} \frac{(4\pi)^{\frac{3}{2}}}{k_i k_f}. \quad \text{(C.80)}$$

Additionally, aligning R_{1A} with the z-axis will mean that $m_\lambda = 0$ in the t_{NN} operator, and the spherical harmonic over the scattering angle simplifies to $\frac{\hat{\lambda}}{\sqrt{4\pi}}$:

$$t_{NN} = \sum_\lambda F_\lambda(R_{1A}, r_{2c}) 4\pi Y_0^\lambda(r_{2c}) \frac{\lambda}{\sqrt{4\pi}}. \quad \text{(C.81)}$$

Explicitly, F_λ is

$$\frac{1}{2}\int_{-1}^{1} V(r_{12}) P_\lambda(z) dz. \quad \text{(C.82)}$$

$Y^2_{m_2}(\hat{r}_{12})$ needs to be expanded in terms of the coordinate used within the problem using [117] pg. 167 Equation (35):

$$r^L Y_{LM}(\theta,\phi) = \sqrt{4\pi(2L+1)!} \sum_{\substack{l_1,l_2=0 \\ l_2-l_1=L}}^{L} (-1)^{l_2} \frac{r_1^{l_1} r_2^{l_2}}{\sqrt{(2l_1+1)!(2l_2+1)!}} \{Y_{l_1}(\Omega_1) \otimes Y_{l_2}(\Omega_2)\}_{LM}. \quad \text{(C.83)}$$

Applying this to our system gives us

$$Y^2_{m_2}(\hat{r}_{12}) = \sum_{n=0}^{2} \hat{n} \left(\frac{120}{\hat{n^2}! \hat{(2-n)}^2!} \right)^{\frac{1}{2}} \Big(- \frac{m_c}{m_A} r_{2c} \Big)^n R_{1A}^{2-n} \frac{1}{r_{12}^2} C^{2m_2}_{(2-n)m_2 n 0} Y^{2-n}_{m_2}(\hat{r}_{2c}). \quad \text{(C.84)}$$

Now the four spherical harmonics over the internal angle can be simplified using Equation(C.38

twice, giving us

$$Y^{l_f}_{m_f}(\hat{r}_{2c})Y^{l_i}_{-m_2-m_f}(\hat{r}_{2c})Y^{\lambda}_{0}(\hat{r}_{2c})Y^{2-n}_{m_2}(\hat{r}_{2c}) = \sum_{L'L} \frac{\hat{l_i}\hat{l_f}(\hat{2-n})\hat{\lambda}}{\hat{L}\hat{L'}4\pi} C^{L0}_{l_f 0 l_i 0} C^{L-m_2}_{l_f m_f l_i -m_2-m_f}$$
$$C^{L'0}_{2-n0\lambda 0} C^{L'm_2}_{(2-n)m_2\lambda 0} Y^{L}_{-m_2}(\hat{r}_{2c})Y^{L'}_{m_2}(\hat{r}_{2c}). \tag{C.85}$$

Next, we can use Equation (C.40), giving us

$$= \sum_{L} \frac{\hat{l_i}\hat{l_f}(\hat{2-n})\hat{\lambda}}{\hat{L}^2 8\pi^2} C^{L0}_{l_f 0 l_i 0} C^{L-m_2}_{l_f m_f l_i -m_2-m_f} C^{L0}_{2-n0\lambda 0} C^{Lm_2}_{(2-n)m_2\lambda 0}. \tag{C.86}$$

Putting it all together, along with the simplification that

$$\sum_{m_f} C^{h-m_2}_{l_f m_f l_i -m_2-m_f} C^{L-m_2}_{l_f m_f l_i -m_2-m_f} = \delta_{Lh}\delta_{m_2 m_2}, \tag{C.87}$$

leaves us with the final T-matrix expression:

$$\langle\psi^{\mu_1'}_{\mu_B}|t_{NN}|\psi^{\mu_1}_{\mu_A}\rangle = \int \sum_{\substack{L_f J_f M_{J_f} L_i J_i \\ m_{j_i} m_{j_f} \mu_c g h \\ J_T j_t m_2 m_f T\lambda}} k_5\; Y^{L_f}_{M_{J_f}-\mu_1'}(\hat{k}_f) C^{J_f M_{J_f}}_{L_f M_{J_f}-\mu_1' I_1 \mu_1'} C^{J_i\mu_1}_{L_i 0 I_1 \mu_1} C^{J_A\mu_A}_{j_i m_{j_i} I_c \mu_c}$$
$$C^{J_B\mu_B}_{j_f m_{j_f} I_c \mu_c} C^{J_T - M_{J_f}+\mu_1}_{J_f - M_{J_f} J_i \mu_1} C^{j_t - m_{j_f}+m_{j_i}}_{j_f - m_{j_f} j_i m_{j_i}} C^{T0}_{x-m_2 2 m_2} C^{T0}_{J_T - M_{J_f}+\mu_1 j_t - m_{j_f}+m_{j_i}}$$
$$C^{2-m_2}_{g0h-m_2} C^{g0}_{L_f 0 L_i 0} \begin{Bmatrix} l_f & I_2 & j_f \\ l_i & I_2 & j_i \\ h & 1 & j_t \end{Bmatrix} \begin{Bmatrix} L_f & I_1 & J_f \\ L_i & I_1 & J_i \\ g & 1 & J_T \end{Bmatrix} \begin{Bmatrix} g & 1 & J_T \\ h & 1 & j_t \\ 2 & 2 & T \end{Bmatrix} C^{h0}_{l_f 0 l_i 0}$$
$$C^{h0}_{2-n0\lambda 0} C^{hm_2}_{(2-n)m_2\lambda 0} \frac{\phi_{j_f}(r_{2c}) F_{L_f J_f}(R_{1A}) t_{NN} \phi_{j_i}(r_{2c}) F_{L_i J_i}(R_{1A})}{R^2_{1A}} R^2_{1A} r^2_{2c} dR_{1A} dr_{2c}, \tag{C.88}$$

where

$$k_5 = i^{L_i - L_f} (-1)^{L_i + L_f + M_{J_f} + m_{j_f}} e^{i\sigma_{L_i}} \frac{\hat{L_i}^2 \hat{L_f} \hat{J_i} \hat{J_f} \hat{g} \hat{j_i}^3 \hat{j_f} \hat{J_T} \hat{j_t} \hat{l_i} \hat{l_f} (2\hat{-}n) \hat{\lambda}}{\hat{h}^2} \frac{8\sqrt{6}}{5} \frac{(\pi)^{\frac{3}{2}}}{k_i k_f} \tag{C.89}$$

and

$$t_{NN} = \frac{1}{2} \int_{-1}^{1} \frac{V(r_{12})}{r^2_{12}} P_\lambda(z) dz \sum_{n=0}^{2} \hat{n} \left(\frac{120}{\hat{n}^2 ! (2\hat{-}n)^2 !} \right)^{\frac{1}{2}} \left(-\frac{m_c}{m_A} r_{2c}\right)^n R^{2-n}_{1A} C^{2m_2}_{(2-n)m_2 n0}. \tag{C.90}$$

The total cross section expression is

$$\frac{d\sigma}{d\Omega} = \sum_{\mu_1\mu_1'\mu_A\mu_B} \frac{k_f}{k_i}\frac{\mu_1\mu_f}{4\pi^2(\hbar c)^4}\frac{1}{\hat{J}_A^2\hat{\mu}_1^2}\left|\langle\psi_{\mu_B}^{\mu_1'}|t_{NN}|\psi_{\mu_A}^{\mu_1}\rangle\right|^2, \tag{C.91}$$

where J_A and J_B are the initial and final spin of the target.

C.3 Spin-Spin T-matrix Derivation

This derivation is for (p,n) charge-exchange with a three-body formalism and an NN potential. The potential only acts between the projectile proton and the target's valence neutron. This derivation uses the Condon-Shortly phase convention from Equation (C.1). The isospin spin-spin NN potential is directed along the r_{12} coordinate which runs from the projectile proton to the valence neutron and has the form

$$t_{NN} = V(r_{12})(\boldsymbol{\tau_1}\cdot\boldsymbol{\tau_2})(\boldsymbol{\sigma_1}\cdot\boldsymbol{\sigma_2}). \tag{C.92}$$

The isospin operators will give a factor of $\frac{1}{2}$ and we will also add a $(2j_i+1)$ factor to account for all available neutrons in the valence shell. This leaves us with

$$t_{NN} = V(r_{12})\boldsymbol{\sigma_1}\cdot\boldsymbol{\sigma_2}\frac{(2j_i+1)}{2}. \tag{C.93}$$

As with the central and tensor cases, $V(r_{12})$ is expanded in terms of R_{1A} and r_{2c}, giving the full expression for the interaction:

$$
\begin{aligned}
t_{NN} &= V(r_{12})\boldsymbol{\sigma_1}\cdot\boldsymbol{\sigma_2}\frac{(2j_i+1)}{2} \\
&= \sum_{\lambda}(2\lambda+1)F_\lambda(R,r)\frac{4\pi}{2\lambda+1}\sum_{m_\lambda}Y_{\lambda,m_\lambda}(\hat{r}_{2c})^* Y_{\lambda,m_\lambda}(\hat{R}_{1A})\frac{\boldsymbol{\sigma_1}\cdot\boldsymbol{\sigma_2}(2j_i+1)}{2}.
\end{aligned}
\tag{C.94}
$$

Similarly to the central and tensor cases, we can create a T-matrix expressing using the incoming and outgoing wave functions:

$$
\begin{aligned}
&\langle\psi^{\mu_1'}_{\mu_B}|t_{NN}|\psi^{\mu_1}_{\mu_A}\rangle = \int \sum_{\substack{L_f J_f M_f L_i J_i \\ m_{j_i} m_{j_f} \mu_c}} k_1\; Y^{L_f}_{M_f}(\hat{k}_f) C^{J_f M_f+\mu_1'}_{L_f M_f I_1 \mu_1'} C^{J_i \mu_1}_{L_i 0 I_1 \mu_1} C^{J_A \mu_A}_{j_i m_{j_i} I_c \mu_c} C^{J_B \mu_B}_{j_f m_{j_f} I_c \mu_c} \\
&\left[Y^{L_f}(R_{1A})\Xi^{I_1}(-\xi_1)\right]^{J_f}_{-(M_f+\mu_1')} \left[Y^{l_f}(r_{2c})\Xi^{I_2}(-\xi_2)\right]^{j_f}_{-m_{j_f}} \\
&\left[Y^{L_i}(R_{1A})\Xi^{I_1}(\xi_1)\right]^{J_i}_{\mu_1} \left[Y^{l_i}(r_{2c})\Xi^{I_2}(\xi_2)\right]^{j_i}_{m_{j_i}} \\
&\frac{\phi_{j_f}(r_{2c})F_{L_f J_f}(R_{1A}) t_{NN} \phi_{j_i}(r_{2c}) F_{L_i J_i}(R_{1A})}{R^2_{1A}} R^2_{1A} r^2_{2c} dR_{1A} dr_{2c} d\Omega_{2c} d\Omega_{1A} d\xi_1 d\xi_2,
\end{aligned}
\tag{C.95}
$$

where

$$
k_1 = i^{L_f - L_i}(-1)^{L_i+L_f} e^{i\sigma_{L_i}} \frac{\hat{L}_i (4\pi)^{\frac{3}{2}}}{k_f k_i} \frac{2j_i+1}{2}. \tag{C.96}
$$

We couple the initial and final angular momentum and spin operators together to get

$$\langle \psi^{\mu_1'}_{\mu_B} | t_{NN} | \psi^{\mu_1}_{\mu_A} \rangle = \int \sum_{\substack{L_f J_f M_f L_i J_i \\ J_T M_{J_T} J_T' M_{J_T'} m_{j_i} m_{j_f} \mu_c}} k_1 Y^{L_f}_{M_f}(\hat{k}_f)$$

$$C^{J_f M_f + \mu_1'}_{L_f M_f I_1 \mu_1'} C^{J_i \mu_1}_{L_i 0 I_1 \mu_1} C^{J_T' M_{J_T'}}_{J_f - (M_f + \mu_1') j_f - m_{j_f}} C^{J_T M_{J_T}}_{J_i \mu_1 j_i m_{j_i}} C^{J_A \mu_A}_{j_i m_{j_i} I_c \mu_c} C^{J_B \mu_B}_{j_f m_{j_f} I_c \mu_c}$$

$$\left\{ \left[Y^{L_f}(R_{1A}) \Xi^{I_1}(-\xi_1) \right]^{J_f} \left[Y^{l_f}(r_{2c}) \Xi^{I_2}(-\xi_2) \right]^{j_f} \right\}^{J_T'}_{M_{J_T'}} \tag{C.97}$$

$$\left\{ \left[Y^{L_i}(R_{1A}) \Xi^{I_1}(\xi_1) \right]^{J_i} \left[Y^{l_i}(r_{2c}) \Xi^{I_2}(\xi_2) \right]^{j_i} \right\}^{J_T}_{M_{J_T}}$$

$$\frac{\phi_{j_f}(r_{2c}) F_{L_f J_f}(R_{1A}) t_{NN} \phi_{j_i}(r_{2c}) F_{L_i J_i}(R_{1A})}{R^2_{1A}} R^2_{1A} r^2_{2c} dR_{1A} dr_{2c} d\Omega_{2c} d\Omega_{1A} d\xi_1 d\xi_2.$$

Now we can rearrange the spin and angular momentum components using Equation (B.9) for both the scattering and bound states, giving us

$$\sum_{J_T M_{J_T} J'_T M_{J'_T}} C^{J'_T M_{J'_T}}_{J_f-(M_f+\mu'_1)j_f-m_{j_f}} \left\{ \left[Y^{L_f}(R_{1A})\Xi^{I_1}(-\xi_1)\right]^{J_f} \left[Y^{l_f}(r_{2c})\Xi^{I_2}(-\xi_2)\right]^{j_f} \right\}^{J'_T}_{M_{J'_T}}$$

$$C^{J_T M_{J_T}}_{J_i \mu_1 j_i m_{j_i}} \left\{ \left[Y^{L_i}(R_{1A})\Xi^{I_1}(\xi_1)\right]^{J_i} \left[Y^{l_i}(r_{2c})\Xi^{I_2}(\xi_2)\right]^{j_i} \right\}^{J_T}_{M_{J_T}}$$

$$= \sum_{\substack{J_T M_{J_T} J'_T \\ M_{J'_T} g h g' h'}} \hat{J}_f \hat{j}_f \hat{J}_i \hat{j}_i \hat{g} \hat{h} \hat{g}' \hat{h}' C^{J'_T M_{J'_T}}_{J_f-(M_f+\mu'_1)j_f-m_{j_f}} C^{J_T M_{J_T}}_{J_i \mu_1 j_i m_{j_i}} \begin{Bmatrix} L_i & I_1 & J_i \\ l_i & I_2 & j_i \\ g & h & J_T \end{Bmatrix} \begin{Bmatrix} L_f & I_1 & J_f \\ l_f & I_2 & j_f \\ g' & h' & J'_T \end{Bmatrix}$$

$$\left\{ \left[Y^{L_f}(R_{1A})Y^{l_f}(r_{2c})\right]^{g'} \left[\Xi^{I_1}(-\xi_1)\Xi^{I_2}(-\xi_2)\right]^{h'} \right\}^{J'_T}_{M_{J'_T}}$$

$$\left\{ \left[Y^{L_i}(R_{1A})Y^{l_i}(r_{2c})\right]^{g} \left[\Xi^{I_1}(\xi_1)\Xi^{I_2}(\xi_2)\right]^{h} \right\}^{J_T}_{M_{J_T}}.$$

(C.98)

Then we break the coupling to J_T so we can apply the spin-spin operator:

$$= \sum_{\substack{J_T M_{J_T} J'_T M_{J'_T} g h \\ g' h' m_g m_h m'_g m'_h}} \hat{J}_f \hat{j}_f \hat{J}_i \hat{j}_i \hat{g} \hat{h} \hat{g}' \hat{h}' C^{J'_T M_{J'_T}}_{J_f-(M_f+\mu'_1)j_f-m_{j_f}} C^{J_T M_{J_T}}_{J_i \mu_1 j_i m_{j_i}} C^{J'_T M_{J'_T}}_{g' m'_g h' m'_h} C^{J_T M_{J_T}}_{g m_g h m_h}$$

$$\begin{Bmatrix} L_i & I_1 & J_i \\ l_i & I_2 & j_i \\ g & h & J_T \end{Bmatrix} \begin{Bmatrix} L_f & I_1 & J_f \\ l_f & I_2 & j_f \\ g' & h' & J'_T \end{Bmatrix} \left[Y^{L_f}(R_{1A})Y^{l_f}(r_{2c})\right]^{g'}_{m'_g} \left[\Xi^{I_1}(-\xi_1)\Xi^{I_2}(-\xi_2)\right]^{h'}_{m'_h}$$

$$\left[Y^{L_i}(R_{1A})Y^{l_i}(r_{2c})\right]^{g}_{m_g} \left[\Xi^{I_1}(\xi_1)\Xi^{I_2}(\xi_2)\right]^{h}_{m_h}.$$

(C.99)

The spin and position operators from t_{NN} act on independent operators, so we can evaluate the spin space first. Collecting the relevant operators gives us

$$\int \sum_{hh'm_hm'_h} \hat{h}\hat{h}' C^{J'_T M_{J'_T}}_{g'm'_g h'm'_h} C^{J_T M_{J_T}}_{gm_g hm_h} \begin{Bmatrix} L_i & I_1 & J_i \\ l_i & I_2 & j_i \\ g & h & J_T \end{Bmatrix} \begin{Bmatrix} L_f & I_1 & J_f \\ l_f & I_2 & j_f \\ g' & h' & J'_T \end{Bmatrix} \tag{C.100}$$
$$\left[\Xi^{I_1}(-\xi_1)\Xi^{I_2}(-\xi_2)\right]^{h'}_{m'_h} \boldsymbol{\sigma_p}\cdot\boldsymbol{\sigma_n} \left[\Xi^{I_1}(\xi_1)\Xi^{I_2}(\xi_2)\right]^{h}_{m_h} d\xi_1 d\xi_2,$$

which is equivalent to

$$\begin{aligned} &= \sum_{\substack{hh'm_hm'_hm_1 \\ m_2m'_1m'_2}} \hat{h}\hat{h}' C^{h'm'_h}_{I_1m'_1I_1m'_2} C^{hm_h}_{I_1m_1I_2m_2} C^{J'_T M_{J'_T}}_{g'm'_g h'm'_h} C^{J_T M_{J_T}}_{gm_g hm_h} \\ &\begin{Bmatrix} L_i & I_1 & J_i \\ l_i & I_2 & j_i \\ g & h & J_T \end{Bmatrix} \begin{Bmatrix} L_f & I_1 & J_f \\ l_f & I_2 & j_f \\ g' & h' & J'_T \end{Bmatrix} \langle I_1 m_1 I_2 | \boldsymbol{\sigma_p}\cdot\boldsymbol{\sigma_n} | I_1 m'_1 I_2 m'_2\rangle. \end{aligned} \tag{C.101}$$

The matrix element can be simplified using [117]pg. 479 Equation (26):

$$\begin{aligned} &\langle n'_1 j'_1 m'_1 n'_2 j'_2 m'_2 | (\hat{\boldsymbol{P}}_{\boldsymbol{a}}(\mathbf{1})\cdot\hat{\boldsymbol{Q}}_{\boldsymbol{a}}(\mathbf{2})) | n_1 j_1 m_1 n_2 j_2 m_2\rangle \\ &= \frac{1}{\hat{j}'_1\hat{j}'_2} \sum_\alpha (-1)^{-\alpha} C^{j'_1 m'_1}_{j_1 m_1 a\alpha} C^{j'_2 m'_2}_{j_2 m_2 a-\alpha} \langle n'_1 j'_1 || \hat{\boldsymbol{P}}_{\boldsymbol{a}}(\mathbf{1}) || n_1 j_1\rangle \langle n'_2 j'_2 || \hat{\boldsymbol{Q}}_{\boldsymbol{a}}(\mathbf{2}) || n_2 j_2\rangle. \end{aligned} \tag{C.102}$$

In this work, we are only considering the case of Fermi transitions, where there is no spin flip between the projectile and target nucleon. This restricts us to $\alpha = 0$ in the expression

above and insists that $m_1 = m_1'$ and $m_2 = m_2'$. Applying this, we get

$$= \sum_{hh'm_h m_h' m_1 m_2} \hat{h}\hat{h}' C^{h'm_h'}_{I_1 m_1 I_2 m_2} C^{hm_h}_{I_1 m_1 I_2 m_2} C^{J_T' M_{J_T'}}_{g' m_g' h' m_h'} C^{J_T M_{J_T}}_{g m_g h m_h} \begin{Bmatrix} L_i & I_1 & J_i \\ l_i & I_2 & j_i \\ g & h & J_T \end{Bmatrix} \begin{Bmatrix} L_f & I_1 & J_f \\ l_f & I_2 & j_f \\ g' & h' & J_T' \end{Bmatrix} \frac{1}{\hat{I}_1 \hat{I}_2} C^{I_1 m_1}_{I_1 m_1 1 0} C^{I_2 m_2}_{I_2 m_2 1 0} \langle \frac{1}{2} || \boldsymbol{\sigma_p} || \frac{1}{2} \rangle \langle \frac{1}{2} || \boldsymbol{\sigma_n} || \frac{1}{2} \rangle. \tag{C.103}$$

Summing over the projections of the spins and the Clebsch-Gordon coefficients gives $\frac{(-1)^{1+m_h}}{3} \delta_{hh'} \delta_{m_h m_h'}$. This reduces the expression to

$$= \sum_{hm_h} \frac{\hat{h}^2}{6} C^{J_T' M_{J_T'}}_{g' m_g' h m_h} C^{J_T M_{J_T}}_{g m_g h m_h} \begin{Bmatrix} L_i & I_1 & J_i \\ l_i & I_2 & j_i \\ g & h & J_T \end{Bmatrix} \begin{Bmatrix} L_f & I_1 & J_f \\ l_f & I_2 & j_f \\ g' & h & J_T' \end{Bmatrix} \langle \frac{1}{2} || \boldsymbol{\sigma_p} || \frac{1}{2} \rangle \langle \frac{1}{2} || \boldsymbol{\sigma_n} || \frac{1}{2} \rangle. \tag{C.104}$$

These matrix elements can be simplified using [117] pg. 495 Equation (95):

$$\langle s' || \hat{\boldsymbol{S}}_{\mathbf{1}} || s \rangle = \delta_{ss'} \sqrt{s(s+1)(2s+1)}. \tag{C.105}$$

Applying this, the final expression for the spin operators is

$$= \sum_{hm_h} \frac{\hat{h}^2}{4} C^{J'_T M_{J'_T}}_{g' m'_g h m_h} C^{J_T M_{J_T}}_{g m_g h m_h} \begin{Bmatrix} L_i & I_1 & J_i \\ l_i & I_2 & j_i \\ g & h & J_T \end{Bmatrix} \begin{Bmatrix} L_f & I_1 & J_f \\ l_f & I_2 & j_f \\ g' & h & J'_T \end{Bmatrix}. \tag{C.106}$$

Recombining this in the T-matrix expression gives

$$\begin{aligned} \langle \psi^{\mu'_1}_{\mu_B} | t_{NN} | \psi^{\mu_1}_{\mu_A} \rangle = \int & \sum_{\substack{L_f J_f M_f L_i J_i J_T M_{J_T} J'_T M_{J'_T} \\ g g' m_g m'_g m_{j_i} m_{j_f} \mu_c h m_h}} k_2 \; Y^{L_f}_{M_f}(\hat{k}_f) C^{J_f M_f + \mu'_1}_{L_f M_f I_1 \mu'_1} C^{J_i \mu_1}_{L_i 0 I_1 \mu_1} \\ & C^{J_A \mu_A}_{j_i m_{j_i} I_c \mu_c} C^{J_B \mu_B}_{j_f m_{j_f} I_c \mu_c} C^{J'_T M_{J'_T}}_{g' m'_g h m_h} C^{J_T M_{J_T}}_{g m_g h m_h} C^{J'_T M_{J'_T}}_{J_f - (M_f + \mu'_1) j_f - m_{j_f}} C^{J_T M_{J_T}}_{J_i \mu_1 j_i m_{j_i}} \\ & \begin{Bmatrix} L_i & I_1 & J_i \\ l_i & I_2 & j_i \\ g & h & J_T \end{Bmatrix} \begin{Bmatrix} L_f & I_1 & J_f \\ l_f & I_2 & j_f \\ g' & h & J'_T \end{Bmatrix} \left[Y^{L_f}(R_{1A}) Y^{l_f}(r_{2c}) \right]^{g'}_{m'_g} \left[Y^{L_i}(R_{1A}) Y^{l_i}(r_{2c}) \right]^{g}_{m_g} \\ & \frac{\phi_{j_f}(r_{2c}) F_{L_f J_f}(R_{1A}) t_{NN} \phi_{j_i}(r_{2c}) F_{L_i J_i}(R_{1A})}{R^2_{1A}} R^2_{1A} r^2_{2c} dR_{1A} dr_{2c} d\Omega_{2c} d\Omega_{1A}, \end{aligned} \tag{C.107}$$

where

$$k_2 = i^{L_f - L_i} (-1)^{L_i + L_f + M_f + \mu'_1 + m_{j_f}} e^{i\sigma_{L_i}} \frac{1}{4} \hat{J}_f \hat{j}_f \hat{J}_i \hat{j}_i \hat{g} \hat{h}^2 \hat{g}' \frac{\hat{L}_i (4\pi)^{\frac{3}{2}}}{k_f k_i}, \tag{C.108}$$

and

$$t_{NN} = \sum_{\lambda}(2\lambda+1)F_{\lambda}(R,r)\frac{4\pi}{2\lambda+1}\sum_{m_\lambda}Y_{\lambda,m_\lambda}(\hat{r}_{2c})^{*}Y_{\lambda,m_\lambda}(\hat{R}_{1A})\frac{(2j_i+1)}{2}. \tag{C.109}$$

Now we can deal with the angular momentum operators. Because the interaction is scalar, we want all of the angular momentum variables to couple to total angular momentum 0. Applying this produces

$$\begin{aligned}&\sum_{gg'm_gm'_gTM_T} C^{TM_T}_{gm_gg'm'_g}\Big\{\big[Y^{L_f}(R_{1A})Y^{l_f}(r_{2c})\big]^{g'}\big[Y^{L_i}(R_{1A})Y^{l_i}(r_{2c})\big]^{g}\Big\}^{T}_{M_T}\\ &=\sum_{gm_g}\frac{(-1)^{g-m_g}\delta_{gg'}\delta_{m_g-m'_g}}{\hat{g}}\Big\{\big[Y^{L_f}(R_{1A})Y^{l_f}(r_{2c})\big]^{g}\big[Y^{L_i}(R_{1A})Y^{l_i}(r_{2c})\big]^{g}\Big\}^{0}_{0}.\end{aligned} \tag{C.110}$$

We can now take advantage of the rotational invariance of the integrand, as in the central and tensor interactions. The value of the interaction is unchanged by a rotation of the reference frame and we can align R_{1A} with the z axis. Once we integrate over $\Omega_{1A}\phi_{2c}$, we gain an overall factor of $8\pi^2$. So we have

$$\begin{aligned}&\Big\{\big[Y^{L_f}(R_{1A})Y^{l_f}(r_{2c})\big]^{g}\big[Y^{L_i}(R_{1A})Y^{l_i}(r_{2c})\big]^{g}\Big\}^{0}_{0}=\sum_{m'_gm''_gm_fm_i}C^{00}_{gm'_ggm''_g}C^{gm'_g}_{L_f0l_fm_f}\\ &C^{gm''_g}_{L_i0l_im_i}8\pi^2\frac{\hat{L}_i\hat{L}_f}{4\pi}Y^{l_i}_{m_i}(\hat{r}_{2c})Y^{l_f}_{m_f}(\hat{r}_{2c})\\ &=\sum_{m_i}\frac{(-1)^{g-m_i}}{\hat{g}}C^{g-m_i}_{L_f0l_f-m_i}C^{gm_i}_{L_i0l_im_i}2\pi\hat{L}_i\hat{L}_fY^{l_i}_{m_i}(\hat{r}_{2c})Y^{l_f}_{-m_i}(\hat{r}_{2c}).\end{aligned} \tag{C.111}$$

Combining this result with our full T-matrix expression, we have

$$\langle\psi^{\mu_1'}_{\mu_B}|t_{NN}|\psi^{\mu_1}_{\mu_A}\rangle = \int \sum_{\substack{L_f J_f M_f L_i J_i J_T M_{J_T} \\ m_i J_T' M_{J_T'} g m_g m_{j_i} m_{j_f} \mu_c h m_h}} k_3\ Y^{L_f}_{M_f}(\hat{k}_f) C^{J_f M_f+\mu_1'}_{L_f M_f I_1 \mu_1'} C^{J_i \mu_1}_{L_i 0 I_1 \mu_1}$$

$$C^{J_A \mu_A}_{j_i m_{j_i} I_c \mu_c} C^{J_B \mu_B}_{j_f m_{j_f} I_c \mu_c} C^{J_T' M_{J_T'}}_{g -m_g h m_h} C^{J_T M_{J_T}}_{g m_g h m_h} C^{J_T' M_{J_T'}}_{J_f -(M_f+\mu_1') j_f - m_{j_f}} C^{J_T M_{J_T}}_{J_i \mu_1 j_i m_{j_i}}$$

$$C^{g-m_i}_{L_f 0 l_f -m_i} C^{g m_i}_{L_i 0 l_i m_i} \begin{Bmatrix} L_i & I_1 & J_i \\ l_i & I_2 & j_i \\ g & h & J_T \end{Bmatrix} \begin{Bmatrix} L_f & I_1 & J_f \\ l_f & I_2 & j_f \\ g & h & J_T' \end{Bmatrix} Y^{l_i}_{m_i}(\hat{r}_{2c}) Y^{l_f}_{-m_i}(\hat{r}_{2c})$$

$$\frac{\phi_{j_f}(r_{2c}) F_{L_f J_f}(R_{1A}) t_{NN} \phi_{j_i}(r_{2c}) F_{L_i J_i}(R_{1A})}{R^2_{1A}} R^2_{1A} r^2_{2c} dR_{1A} dr_{2c} sin(\theta_{2c}) d\theta_{2c}, \tag{C.112}$$

where

$$k_3 = i^{L_f - L_i} (-1)^{L_i + L_f + M_f + \mu_1' + m_{j_f} - m_i - m_g} e^{i\sigma_{L_i}} \frac{1}{4} \hat{J}_f \hat{j}_f \hat{J}_i \hat{j}_i \hat{h}^2 \frac{\hat{L}_i^2 \hat{L}_f (4\pi)^{\frac{3}{2}}}{k_f k_i}. \tag{C.113}$$

Now we can look more closely at the form of our potential:

$$t_{NN} = \sum_\lambda (2\lambda+1) F_\lambda(R,r) \frac{4\pi}{2\lambda+1} \sum_{m_\lambda} Y_{\lambda, m_\lambda}(\hat{r}_{2c})^* Y_{\lambda, m_\lambda}(\hat{R}_{1A}) \frac{(2j_i+1)}{2}. \tag{C.114}$$

After aligning R_{1A} with the z axis, t_{NN} simplifies to

$$t_{NN} = \sum_\lambda F_\lambda(R,r) \frac{\hat{\lambda} 2\pi (2j_i+1)}{\sqrt{4\pi}} Y^\lambda_0(\hat{r}_{2c}). \tag{C.115}$$

We can now complete the simplification of the angular variables using Equations (C.38) and (C.40):

$$Y^{l_i}_{m_i}(\hat{r}_{2c})Y^{l_f}_{-m_i}(\hat{r}_{2c})Y^{\lambda}_0(\hat{r}_{2c}) = \sum_L \frac{\hat{l}_i\hat{l_f}}{\hat{L}\sqrt{4\pi}} C^{L0}_{l_f0l_i0} C^{L0}_{l_f-m_il_im_i} Y^L_0(\hat{r}_{2c})Y^{\lambda}_0(\hat{r}_{2c}) \tag{C.116}$$

and

$$\int Y^L_0(\hat{r}_{2c})Y^{\lambda}_0(\hat{r}_{2c})\sin\theta_{2c}d\theta_{2c} = \frac{\delta_{L\lambda}}{2\pi}. \tag{C.117}$$

Combining everything gives us

$$\begin{aligned}
\langle\psi^{\mu'_1}_{\mu_B}|t_{NN}|\psi^{\mu_1}_{\mu_A}\rangle = \int \sum_{\substack{L_fJ_fM_fL_iJ_iJ_TM_{J_T}\lambda \\ m_iJ'_TM_{J'_T}gm_gm_{j_i}m_{j_f}\mu_chm_h}} & k_4\ Y^{L_f}_{M_f}(\hat{k}_f) C^{J_fM_f+\mu'_1}_{L_fM_fI_1\mu'_1} C^{J_i\mu_1}_{L_i0I_1\mu_1} \\
& C^{J_A\mu_A}_{j_im_{j_i}I_c\mu_c} C^{J_B\mu_B}_{j_fm_{j_f}I_c\mu_c} C^{J'_TM_{J'_T}}_{g-m_ghm_h} C^{J_TM_{J_T}}_{gm_ghm_h} C^{J'_TM_{J'_T}}_{J_f-(M_f+\mu'_1)j_f-m_{j_f}} C^{J_TM_{J_T}}_{J_i\mu_1j_im_{j_i}} \\
& C^{g-m_i}_{L_f0l_f-m_i} C^{gm_i}_{L_i0l_im_i} C^{g-m_i}_{L_f0l_f-m_i} C^{gm_i}_{L_i0l_im_i} C^{\lambda0}_{l_f0l_i0} C^{\lambda0}_{l_f-m_il_im_i} \begin{Bmatrix} L_i & I_1 & J_i \\ l_i & I_2 & j_i \\ g & h & J_T \end{Bmatrix} \begin{Bmatrix} L_f & I_1 & J_f \\ l_f & I_2 & j_f \\ g & h & J'_T \end{Bmatrix} \\
& \frac{\phi_{j_f}(r_{2c})F_{L_fJ_f}(R_{1A})t_{NN}\phi_{j_i}(r_{2c})F_{L_iJ_i}(R_{1A})}{R^2_{1A}} R^2_{1A}r^2_{2c}dR_{1A}dr_{2c},
\end{aligned} \tag{C.118}$$

where

$$k_4 = i^{L_f - L_i}(-1)^{L_i+L_f+M_f+\mu_1'+m_{j_f}-m_i-m_g} e^{i\sigma_{L_i}} \frac{1}{4}\hat{J}_f\hat{j}_f\hat{J}_i\hat{j}_i^3\hat{h}^2\hat{l}_i\hat{l}_f \frac{\hat{L}_i^2\hat{L}_f(4\pi)^{\frac{3}{2}}}{2k_f k_i}. \quad \text{(C.119)}$$

We can simplify some of the Clebsch-Gordan coefficients by implementing equation 12 on pg. 260 of [117]:

$$\sum_{\alpha\beta\delta} C^{c\gamma}_{a\alpha b\beta} C^{e\epsilon}_{d\delta b\beta} C^{d\delta}_{a\alpha f\phi} = (-1)^{b+c+d+f}\hat{c}\hat{d} C^{e\epsilon}_{c\gamma f\phi} \begin{Bmatrix} a & b & c \\ e & f & d \end{Bmatrix}. \quad \text{(C.120)}$$

First, however, we have to rearrange some Clebsch-Gordan coefficients using expressions from equation 10 on page 245:

$$C^{c\gamma}_{a\alpha b\beta} = (-1)^{a+b-c} C^{c\gamma}_{b\beta a\alpha} = (-1)^{b+\beta}\frac{\hat{c}}{\hat{a}} C^{a-\alpha}_{c-\gamma b\beta}. \quad \text{(C.121)}$$

Applying this we get

$$\begin{aligned} \sum_{m_i} C^{g-m_i}_{L_f 0 l_f -m_i} C^{gm_i}_{L_i 0 l_i m_i} C^{\lambda 0}_{l_f -m_i l_i m_i} = \\ (-)^{l_i+m_i+L_f+l_f-g}\frac{\hat{g}}{\hat{L_i}} C^{\lambda 0}_{l_f -m_i l_i m_i} C^{L_i 0}_{g-m_i l_i m_i} C^{g-m_i}_{l_f -m_i L_f 0} \\ = (-)^{l_i+m_i+2L_f+l_f-g+g+l_i+\lambda}\frac{\hat{g}}{\hat{L_i}} C^{L_i 0}_{\lambda 0 L_f 0} \begin{Bmatrix} l_f & l_i & \lambda \\ L_i & L_f & g \end{Bmatrix}. \end{aligned} \quad \text{(C.122)}$$

Taking into account that $(-1)^{2L_f} = 1$ and $(-1)^{2l_i} = 1$ we obtain, as our final T-matrix expression,

$$\langle\psi^{\mu'_1}_{\mu_B}|t_{NN}|\psi^{\mu_1}_{\mu_A}\rangle = \int \sum_{\substack{L_f J_f M_f L_i J_i J_T M_{J_T} \lambda \\ J'_T M_{J'_T} g m_g m_{j_i} m_{j_f} \mu_c h m_h}} k_5\; Y^{L_f}_{M_f}(\hat{k}_f) C^{J_f M_f+\mu'_1}_{L_f M_f I_1 \mu'_1} C^{J_i \mu_1}_{L_i 0 I_1 \mu_1}$$

$$C^{J_A \mu_A}_{j_i m_{j_i} I_c \mu_c} C^{J_B \mu_B}_{j_f m_{j_f} I_c \mu_c} C^{J'_T M_{J'_T}}_{g -m_g h m_h} C^{J_T M_{J_T}}_{g m_g h m_h} C^{J'_T M_{J'_T}}_{J_f -(M_f+\mu'_1) j_f - m_{j_f}} C^{J_T M_{J_T}}_{J_i \mu_1 j_i m_{j_i}}$$

$$C^{\lambda 0}_{l_f 0 l_i 0} C^{L_i 0}_{\lambda 0 L_f 0} \begin{Bmatrix} l_f & l_i & \lambda \\ L_i & L_f & g \end{Bmatrix} \begin{Bmatrix} L_i & I_1 & J_i \\ l_i & I_2 & j_i \\ g & h & J_T \end{Bmatrix} \begin{Bmatrix} L_f & I_1 & J_f \\ l_f & I_2 & j_f \\ g & h & J'_T \end{Bmatrix} \tag{C.123}$$

$$\frac{\phi_{j_f}(r_{2c}) F_{L_f J_f}(R_{1A}) t_{NN} \phi_{j_i}(r_{2c}) F_{L_i J_i}(R_{1A})}{R^2_{1A}} R^2_{1A} r^2_{2c} dR_{1A} dr_{2c},$$

where

$$k_5 = i^{L_f - L_i} (-1)^{L_i + L_f + M_f + \mu'_1 + m_{j_f} - m_g + l_f + \lambda} e^{i\sigma_{L_i}} \frac{1}{4} \hat{J}_f \hat{j}_f \hat{J}_i \hat{j}_i^3 \hat{h}^2 \hat{g} \hat{l}_i \hat{l}_f \frac{\hat{L}_i \hat{L}_f (4\pi)^{\frac{3}{2}}}{2 k_f k_i}. \tag{C.124}$$

The total cross section expression is

$$\frac{d\sigma}{d\Omega} = \sum_{\mu_1 \mu'_1 \mu_A \mu_B} \frac{k_f}{k_i} \frac{\mu_1 \mu_f}{4\pi^2 (\hbar c)^4} \frac{1}{\hat{J}^2_A \hat{\mu}^2_1} |\langle\psi^{\mu'_1}_{\mu_B}|t_{NN}|\psi^{\mu_1}_{\mu_A}, \rangle|^2 \tag{C.125}$$

where J_A and J_B are the initial and final spin of the target.

C.4 Spin-Orbit T-Matrix

This derivation is for (p,n) charge-exchange with a three-body formalism and an NN potential. The potential only acts between the projectile proton and the target's valence neutron. This derivation uses the Condon-Shortly phase convention from Equation (C.1). The isospin spin-orbit NN potential is directed along the r_{12} coordinate which runs from the projectile proton to the valence neutron and has the form

$$V_{LS} = (\boldsymbol{\tau_1} \cdot \boldsymbol{\tau_2}) V_L S(r_{12}) \boldsymbol{L} \cdot \boldsymbol{S}. \tag{C.126}$$

Here, we note that the $\boldsymbol{L}$ and $\boldsymbol{S}$ operators act between the two active nucleons on our system. This presents a challenge because our coordinate system is defined with by $L_{i/f}$ and $l_{i/f}$, so $\boldsymbol{L}$ cannot act directly on these angular momentum operators, making this operator particularly difficult to implement. In this section we will first present a derivation for a full implementation of the spin-orbit interaction in our system, and then we will discuss some simplifications which we considered for this work.

Just as in the central case, the isospin operator will give a factor of $\frac{1}{2}$ and there will be a factor of $(2j+1)$ to account for the number of nucleons in the valence shell. This can be inserted in the same T-matrix expression used for the isospin central interaction, giving us

$$\langle\psi^{\mu_1'}_{\mu_B}|t_{NN}|\psi^{\mu_1}_{\mu_A}\rangle = \int \sum_{\substack{L_f J_f M_f L_i J_i \\ m_{j_i} m_{j_f} \mu_c \mu_c'}} k_1\; Y^{L_f}_{M_f}(\hat{k}_f) C^{J_f M_f+\mu_1'}_{L_f M_f I_1 \mu_1'} C^{J_i \mu_1}_{L_i 0 I_1 \mu_1} C^{J_A \mu_A}_{j_i m_{j_i} I_c \mu_c} C^{J_B \mu_B}_{j_f m_{j_f} I_c \mu_c'}$$

$$\left[Y^{L_f}(R_{1A})\Xi^{I_1}(-\xi_1)\right]^{J_f}_{-(M_f+\mu_1')} \left[Y^{l_f}(r_{2c})\Xi^{I_2}(-\xi_2)\right]^{j_f}_{-m_{j_f}}$$

$$\left[Y^{L_i}(R_{1A})\Xi^{I_1}(\xi_1)\right]^{J_i}_{\mu_1} \left[Y^{l_i}(r_{2c})\Xi^{I_2}(\xi_2)\right]^{j_i}_{m_{j_i}} \Xi^{*I_c}_{\mu_c'}(\xi_c)\Xi^{I_c}_{\mu_c}(\xi_c)$$

$$\frac{\phi_{j_f}(r_{2c})F_{L_f J_f}(R_{1A}) t_{NN} \phi_{j_i}(r_{2c})F_{L_i J_i}(R_{1A})}{R^2_{1A}} R^2_{1A} r^2_{2c} dR_{1A} dr_{2c} d\Omega_{2c} d\Omega_{1A} d\xi_1 d\xi_2 d\xi_c, \tag{C.127}$$

where

$$k_1 = i^{L_f - L_i}(-1)^{L_i+L_f+M_f+\mu_1'+m_{j_f}} e^{i\sigma_{L_i}} \frac{\hat{L}_i (4\pi)^{\frac{3}{2}}}{k_f k_i}, \tag{C.128}$$

and

$$t_{NN} = \frac{(2j_i+1)}{2} V(r_{12}) \boldsymbol{L}\cdot\boldsymbol{S}. \tag{C.129}$$

Immediately, we see that

$$\int \Xi^{*I_c}_{\mu_c'}(\xi_c)\Xi^{I_c}_{\mu_c}(\xi_c) d\xi_c = \delta_{\mu_c \mu_c'}, \tag{C.130}$$

leaving us with

$$\langle\psi^{\mu_1'}_{\mu_B}|t_{NN}|\psi^{\mu_1}_{\mu_A}\rangle = \int \sum_{\substack{L_f J_f M_f L_i J_i \\ m_{j_i} m_{j_f} \mu_c}} k_1 \; Y^{L_f}_{M_f}(\hat{k}_f) C^{J_f M_f+\mu_1'}_{L_f M_f I_1 \mu_1'} C^{J_i \mu_1}_{L_i 0 I_1 \mu_1} C^{J_A \mu_A}_{j_i m_{j_i} I_c \mu_c} C^{J_B \mu_B}_{j_f m_{j_f} I_c \mu_c}$$

$$\left[Y^{L_f}(R_{1A})\Xi^{I_1}(-\xi_1)\right]^{J_f}_{-(M_f+\mu_1')} \left[Y^{l_f}(r_{2c})\Xi^{I_2}(-\xi_2)\right]^{j_f}_{-m_{j_f}}$$

$$\left[Y^{L_i}(R_{1A})\Xi^{I_1}(\xi_1)\right]^{J_i}_{\mu_1} \left[Y^{l_i}(r_{2c})\Xi^{I_2}(\xi_2)\right]^{j_i}_{m_{j_i}}$$

$$\frac{\phi_{j_f}(r_{2c}) F_{L_f J_f}(R_{1A}) t_{NN} \phi_{j_i}(r_{2c}) F_{L_i J_i}(R_{1A})}{R^2_{1A}} R^2_{1A} r^2_{2c} dR_{1A} dr_{2c} d\Omega_{2c} d\Omega_{1A} d\xi_1 d\xi_2. \tag{C.131}$$

The spin-orbit operator is a scalar, so all of the angular momentum must couple to 0 to contribute. To achieve this, we will couple together all the angular momentum operators:

$$\sum_{J_T} C^{J_T-(M_f+\mu_1')+\mu_1}_{J_f-(M_f+\mu_1')J_i\mu_1} \left\{ \left[Y^{L_f}(R_{1A})\Xi^{I_1}(-\xi_1)\right]^{J_f} \left[Y^{L_i}(R_{1A})\Xi^{I_1}(\xi_1)\right]^{J_i} \right\}^{J_T}_{-(M_f+\mu_1')+\mu_1}. \tag{C.132}$$

Now we can rearrange the spin and angular momentum components using Equation (B.9) and make the replacement that $M_{J_f} = M_f + \mu_1'$, giving us giving us

$$\sum_{J_T,g,h} \hat{J}_i \hat{J}_f \hat{g} \hat{h} C^{J_T-M_{J_f}+\mu_1}_{J_f-M_{J_f}J_i\mu_1} \begin{Bmatrix} L_f & I_1 & J_f \\ L_i & I_1 & J_i \\ g & h & J_T \end{Bmatrix} \left\{ \left[Y^{L_f}(R_{1A})Y^{L_i}(R_{1A})\right]^g \left[\Xi^{I_1}(-\xi_1)\Xi^{I_1}(\xi_1)\right]^h \right\}^{J_T}_{-M_{J_f}+\mu_1}. \tag{C.133}$$

We can perform the analogous couplings and rearrangements for the internal angular momentum variables, leaving us with

$$\sum_{j_t,\tilde{g},\tilde{h}} \hat{j}_i\hat{j}_f\hat{\tilde{h}}\hat{\tilde{g}} C^{j_t-m_{j_f}+m_{j_i}}_{j_f-m_{j_f}j_i m_{j_i}} \begin{Bmatrix} l_f & I_2 & j_f \\ l_i & I_2 & j_i \\ \tilde{h} & \tilde{g} & j_t \end{Bmatrix} \left\{ \left[Y^{l_f}(r_{2c})Y^{l_i}(r_{2c})\right]^{\tilde{h}} \left[\Xi^{I_2}(-\xi_2)\Xi^{I_2}(\xi_2)\right]^{\tilde{g}} \right\}^{j_t}_{-m_{j_f}+m_{j_i}}. \tag{C.134}$$

Also, we can break up the spin-orbit operator into its spin and angular momentum parts:

$$\begin{aligned} \boldsymbol{L}\cdot\boldsymbol{S} &= (-1)^1\hat{1}\{\boldsymbol{L}^1\boldsymbol{S}^1\}^0_0 \\ &= \sum_{m_L m_S} (-1)^1\hat{1}C^{00}_{1m_L1m_S}\boldsymbol{L}_{1m_L}\boldsymbol{S}_{1m_L} \\ &= \sum_{m_L}(-1)^{-m_L}\boldsymbol{L}_{1m_L}\boldsymbol{S}_{1-m_L}. \end{aligned} \tag{C.135}$$

Next, we couple all of the operators together so we can ultimately apply conservation of spin and angular momentum:

$$\sum_{TM_T} C^{TM_T}_{J_T-M_{J_f}+\mu_1 j_t-m_{j_f}+m_{j_i}} \left[\left\{ \left[Y^{L_f}(R_{1A})Y^{L_i}(R_{1A})\right]^g \left[\Xi^{I_1}(-\xi_1)\Xi^{I_1}(\xi_1)\right]^h \right\}^{J_T} \left\{ \left[Y^{l_f}(r_{2c})Y^{l_i}(r_{2c})\right]^{\tilde{h}} \left[\Xi^{I_2}(-\xi_2)\Xi^{I_2}(\xi_2)\right]^{\tilde{g}} \right\}^{j_t} \right]^T_{M_T}. \tag{C.136}$$

We, again, rearrange these operators using Equation (B.9), giving

$$= \sum_{TM_T xy} \hat{J_T} \hat{j_t} \hat{x} \hat{y} \begin{Bmatrix} g & h & J_T \\ \tilde{h} & \tilde{g} & j_t \\ x & y & T \end{Bmatrix} C^{TM_T}_{J_T - M_{J_f} + \mu_1 j_t - m_{j_f} + m_{j_i}} \Bigg[\Big\{ \big[Y^{L_f}(R_{1A}) Y^{L_i}(R_{1A}) \big]^g$$

$$\big[Y^{l_f}(r_{2c}) Y^{l_i}(r_{2c}) \big]^h \Big\}^x \Big\{ \big[\Xi^{I_1}(-\xi_1) \Xi^{I_1}(\xi_1) \big]^{\tilde{g}} \big[\Xi^{I_2}(-\xi_2) \Xi^{I_2}(\xi_2) \big]^{\tilde{h}} \Big\}^y \Bigg]^T_{M_T}. \tag{C.137}$$

As mentioned before, because the operator is a scalar, we need the spin components to couple to 1, so they can couple with the $\boldsymbol{S}$ operator to give 0. This constraint implies that y=1. If we uncouple the spin operators and apply this simplification we get

$$= \sum_{TM_T x m_x m_1'} \hat{J_T} \hat{j_t} \hat{x} \hat{1} \begin{Bmatrix} g & h & J_T \\ \tilde{h} & \tilde{g} & j_t \\ x & 1 & T \end{Bmatrix} C^{TM_T}_{x m_x 1 m_1'} C^{TM_T}_{J_T - M_{J_f} + \mu_1 j_t - m_{j_f} + m_{j_i}} \tag{C.138}$$

$$\Big[\big[Y^{L_f}(R_{1A}) Y^{L_i}(R_{1A}) \big]^g \big[Y^{l_f}(r_{2c}) Y^{l_i}(r_{2c}) \big]^h \Big]^x_{m_x}$$

$$\Big[\big[\Xi^{I_1}(-\xi_1) \Xi^{I_1}(\xi_1) \big]^{\tilde{g}} \big[\Xi^{I_2}(-\xi_2) \Xi^{I_2}(\xi_2) \big]^{\tilde{h}} \Big]^1_{m_1'}.$$

Finally we rearrange the spinor components using Equation(B.9 once again more time to have a projectile and target nucleon coupled together in each channel giving us

$$= \sum_{TM_T x m_x m_1' \alpha\beta} \hat{J}_T \hat{j}_t \hat{x} \hat{1} \hat{\tilde{g}} \hat{\tilde{h}} \hat{\alpha} \hat{\beta} \begin{Bmatrix} g & 1 & J_T \\ h & 1 & j_t \\ x & 2 & T \end{Bmatrix} \begin{Bmatrix} \frac{1}{2} & \frac{1}{2} & \tilde{g} \\ \frac{1}{2} & \frac{1}{2} & \tilde{h} \\ \alpha & \beta & 1 \end{Bmatrix} C^{TM_T}_{xm_x 1 m_1'} C^{TM_T}_{J_T - M_{J_f} + \mu_1 j_t - m_{j_f} + m_{j_i}}$$
$$\Big[\big[Y^{L_f}(R_{1A}) Y^{L_i}(R_{1A}) \big]^g \big[Y^{l_f}(r_{2c}) Y^{l_i}(r_{2c}) \big]^h \Big]^x_{m_x}$$
$$\Big[\big[\Xi^{I_1}(-\xi_1) \Xi^{I_2}(-\xi_2) \big]^\alpha \big[\Xi^{I_2}(\xi_2) \Xi^{I_1}(\xi_1) \big]^\beta \Big]^1_{m_1'}. \tag{C.139}$$

Because we have the angular momentum operators and spin operators coupled separately, we can impose conservation of the projection of the angular momentum in both spaces separately. Including the projections from the spin-orbit operator, we are left with the relations

$$m_1' - m_L = 0 \qquad\qquad m_x + m_L = 0$$
$$m_1' = m_L \qquad\qquad m_x = -m_L.$$

Also, we see from the Clebsch-Gordan coefficient in Equation (C.139) that $M_T = m_x + m_1'$. Using the substitutions from above, we notice that $M_T = 0$. Incorporating all of these changes into the T-matrix expression, we are left with

$$\langle\psi^{\mu_1'}_{\mu_B}|t_{NN}|\psi^{\mu_1}_{\mu_A}\rangle = \int \sum_{\substack{L_f J_f M_{J_f} L_i J_i \\ m_{j_i} m_{j_f} \mu_c g h \tilde{g} \tilde{h} \\ J_T j_t m_L x T \alpha \beta}} k_2\; Y^{L_f}_{M_{J_f}-\mu_1'}(\hat{k}_f) C^{J_f M_{J_f}}_{L_f M_{J_f}-\mu_1' I_1 \mu_1'} C^{J_i \mu_1}_{L_i 0 I_1 \mu_1} C^{J_A \mu_A}_{j_i m_{j_i} I_c \mu_c}$$
$$C^{J_B \mu_B}_{j_f m_{j_f} I_c \mu_c} C^{J_T - M_{J_f}+\mu_1}_{J_f - M_{J_f} J_i \mu_1} C^{j_t - m_{j_f} + m_{j_i}}_{j_f - m_{j_f} j_i m_{j_i}} C^{T0}_{x-m_L 1 m_1} C^{T0}_{J_T - M_{J_f}+\mu_1 j_t - m_{j_f}+m_{j_i}}$$
$$\boldsymbol{L}_{1 m_L} \boldsymbol{S}_{1 - m_L} \begin{Bmatrix} l_f & I_2 & j_f \\ l_i & I_2 & j_i \\ \tilde{h} & \tilde{g} & j_t \end{Bmatrix} \begin{Bmatrix} L_f & I_1 & J_f \\ L_i & I_1 & J_i \\ g & h & J_T \end{Bmatrix} \begin{Bmatrix} g & h & J_T \\ \tilde{h} & \tilde{g} & j_t \\ x & 1 & T \end{Bmatrix} \begin{Bmatrix} \frac{1}{2} & \frac{1}{2} & \tilde{g} \\ \frac{1}{2} & \frac{1}{2} & \tilde{h} \\ \alpha & \beta & 1 \end{Bmatrix}$$
$$\Big[\big[Y^{L_f}(R_{1A}) Y^{L_i}(R_{1A})\big]^g \big[Y^{l_f}(r_{2c}) Y^{l_i}(r_{2c})\big]^h\Big]^x_{-m_L}$$
$$\Big[\big[\Xi^{I_1}(-\xi_1)\Xi^{I_2}(-\xi_2)\big]^\alpha \big[\Xi^{I_2}(\xi_2)\Xi^{I_1}(\xi_1)\big]^\beta\Big]^1_{m_L}$$
$$\frac{\phi_{j_f}(r_{2c}) F_{L_f J_f}(R_{1A}) t_{NN} \phi_{j_i}(r_{2c}) F_{L_i J_i}(R_{1A})}{R^2_{1A}} R^2_{1A} r^2_{2c} dR_{1A} dr_{2c} d\Omega_{2c} d\Omega_{1A} d\xi_1 d\xi_2, \tag{C.140}$$

where

$$k_2 = i^{L_i - L_f} (-1)^{L_i + L_f + M_{J_f} + m_{j_f} - m_L} e^{i\sigma_{L_i}} \hat{L}_i \hat{J}_i \hat{J}_f \hat{g} \hat{h} \hat{1} \hat{j}_i^{\,3} \hat{j}_f \hat{J}_T \hat{j}_t \hat{x} \hat{\alpha} \hat{\beta} \hat{\tilde{g}} \hat{\tilde{h}} \frac{(4\pi)^{\frac{3}{2}}}{2 k_i k_f}, \tag{C.141}$$

and

$$t_{NN} = \sum_{\lambda m_\lambda} F_\lambda(R_{1A}, r_{2c}) 4\pi Y^\lambda_{m_\lambda}(R_{1A}) Y^\lambda_{m_\lambda}(r_{2c})^*. \tag{C.142}$$

F_λ contains the interaction over the r_{12} coordinate expressed as a function of the other two

coordinates. We can then apply the spin operator. This amounts to calculating

$$\sum_{m_\alpha m_\beta} C^{1m_L}_{qmqrm_r} \langle I_1 I_2 \alpha m_\alpha | S_{1,-m_L} | I_1 I_2 \beta m_\beta \rangle, \tag{C.143}$$

which gives a factor of $-\frac{1}{\sqrt{2}}\delta\alpha\beta\delta_{1\alpha}$. Substituting this in gives us

$$\begin{aligned}
\langle \psi^{\mu_1'}_{\mu_B} | t_{NN} | \psi^{\mu_1}_{\mu_A} \rangle = \int \sum_{\substack{L_f J_f M_{J_f} L_i J_i \\ m_{j_i} m_{j_f} \mu_c g h \tilde{g} \tilde{h} \\ J_T j_t m_L x T}} & k_3 \; Y^{L_f}_{M_{J_f} - \mu_1'}(\hat{k}_f) C^{J_f M_{J_f}}_{L_f M_{J_f} - \mu_1' I_1 \mu_1'} C^{J_i \mu_1}_{L_i 0 I_1 \mu_1} C^{J_A \mu_A}_{j_i m_{j_i} I_c \mu_c} \\
& C^{J_B \mu_B}_{j_f m_{j_f} I_c \mu_c} C^{J_T - M_{J_f} + \mu_1}_{J_f - M_{J_f} J_i \mu_1} C^{j_t - m_{j_f} + m_{j_i}}_{j_f - m_{j_f} j_i m_{j_i}} C^{T0}_{x - m_L 1 m_1} C^{T0}_{J_T - M_{J_f} + \mu_1 j_t - m_{j_f} + m_{j_i}} \\
& \boldsymbol{L}_{1 m_L} \begin{Bmatrix} l_f & I_2 & j_f \\ l_i & I_2 & j_i \\ \tilde{h} & \tilde{g} & j_t \end{Bmatrix} \begin{Bmatrix} L_f & I_1 & J_f \\ L_i & I_1 & J_i \\ g & h & J_T \end{Bmatrix} \begin{Bmatrix} g & h & J_T \\ \tilde{h} & \tilde{g} & j_t \\ x & 1 & T \end{Bmatrix} \begin{Bmatrix} \frac{1}{2} & \frac{1}{2} & \tilde{g} \\ \frac{1}{2} & \frac{1}{2} & \tilde{h} \\ 1 & 1 & 1 \end{Bmatrix} \\
& \Big[\big[Y^{L_f}(R_{1A}) Y^{L_i}(R_{1A}) \big]^g \big[Y^{l_f}(r_{2c}) Y^{l_i}(r_{2c}) \big]^h \Big]^x_{-m_L} \\
& \frac{\phi_{j_f}(r_{2c}) F_{L_f J_f}(R_{1A}) t_{NN} \phi_{j_i}(r_{2c}) F_{L_i J_i}(R_{1A})}{R^2_{1A}} R^2_{1A} r^2_{2c} dR_{1A} dr_{2c} d\Omega_{2c} d\Omega_{1A},
\end{aligned} \tag{C.144}$$

where

$$k_3 = i^{L_i - L_f} (-1)^{L_i + L_f + M_{J_f} + m_{j_f} - m_L} e^{i\sigma_{L_i}} \hat{L}_i \hat{J}_i \hat{J}_f \hat{g} \hat{h} \hat{j}_i^3 \hat{j}_f \hat{J}_T \hat{j}_t \hat{x} \hat{\tilde{g}} \hat{\tilde{h}} \frac{3\sqrt{\frac{3}{2}}(4\pi)^{\frac{3}{2}}}{k_i k_f}. \tag{C.145}$$

Next we can simplify the angular momentum operators by coupling to total angular momen-

tum 0:

$$C^{00}_{x-m_L 1 m_L}\left\{\left[\left[Y^{L_f}(R_{1A})Y^{L_i}(R_{1A})\right]^g\left[Y^{l_f}(r_{2c})Y^{l_i}(r_{2c})\right]^h\right]^x \boldsymbol{L}^1\right\}_0^0$$
$$= \frac{(-1)^{1+m_L}}{\hat{1}}\delta_{x1}\delta_{m_L m_L}\left[\left[Y^{L_f}(R_{1A})Y^{L_i}(R_{1A})\right]^g\left[Y^{l_f}(r_{2c})Y^{l_i}(r_{2c})\right]^h\right]^1_{-m_L}\boldsymbol{L}^1_{m_L}. \tag{C.146}$$

If we now align the R_{1A} coordinate along the $\hat{z}$ axis, the spherical harmonics over $\hat{R}_{1A}$ reduce to $\frac{\hat{L}_i\hat{L}_f}{4\pi}$. This is additionally helpful, because in this configuration, $\theta_{2c} = \theta_{12}$ and $\phi_{12} = \pi + \phi_{2c}$. Finally, we can perform the integration over $\sin\theta_{1A}d\theta_{1A}d\phi_{1A}$ gives a factor of 4π. Applying this and uncoupling the angular momentum operators, we are left with

$$= \sum_{m_L m_h m_g m_i m_f} \frac{(-1)^{1+m_L}}{\hat{1}} C^{00}_{1-m_L 1 m_L} C^{1-m_L}_{g m_g h m_h} C^{h m_h}_{l_f m_f l_i m_i} C^{g m_g}_{L_f 0 L_i 0} \frac{\hat{L}_i\hat{L}_f}{4\pi}$$
$$Y^{l_f}_{m_f}(\hat{r}_{2c})Y^{l_i}_{m_i}(\hat{r}_{2c})\boldsymbol{L}^1_{m_L}4\pi. \tag{C.147}$$

It is immediately clear that $m_g = 0$ and, therefore, $m_h = -m_L$. Also, the Clebsch-Gordan coefficient coupled to 0 can again be simplified. Finally, we can make the substitution at $m_i = -m_L - m_f$. Combining these simplifications, we are left with

$$\sum_{m_L m_f} \frac{(-1)^{2(1+m_L)}}{\hat{1}^2} C^{1-m_L}_{g 0 h - m_L} C^{h-m_L}_{l_f m_f l_i - m_L - m_f} C^{g0}_{L_f 0 L_i 0} \hat{L}_i\hat{L}_f Y^{l_f}_{m_f}(\hat{r}_{2c})Y^{l_i}_{-m_2-m_f}(\hat{r}_{2c})\boldsymbol{L}^1_{m_L} \tag{C.148}$$

The T-matrix expression is now

$$\langle\psi^{\mu_1'}_{\mu_B}|t_{NN}|\psi^{\mu_1}_{\mu_A}\rangle = \int \sum_{\substack{L_f J_f M_{J_f} L_i J_i \\ m_{j_i} m_{j_f} \mu_c g h \tilde{g} \tilde{h} m_f \\ J_T j_t m_L x T}} k_4\, Y^{L_f}_{M_{J_f}-\mu_1'}(\hat{k}_f) C^{J_f M_{J_f}}_{L_f M_{J_f}-\mu_1' I_1 \mu_1'} C^{J_i \mu_1}_{L_i 0 I_1 \mu_1} C^{J_A \mu_A}_{j_i m_{j_i} I_c \mu_c}$$
$$C^{J_B \mu_B}_{j_f m_{j_f} I_c \mu_c} C^{J_T - M_{J_f}+\mu_1}_{J_f - M_{J_f} J_i \mu_1} C^{j_t - m_{j_f}+m_{j_i}}_{j_f - m_{j_f} j_i m_{j_i}} C^{T0}_{x-m_L 1 m_1} C^{T0}_{J_T - M_{J_f}+\mu_1 j_t - m_{j_f}+m_{j_i}}$$
$$\begin{Bmatrix} l_f & I_2 & j_f \\ l_i & I_2 & j_i \\ \tilde{h} & \tilde{g} & j_t \end{Bmatrix} \begin{Bmatrix} L_f & I_1 & J_f \\ L_i & I_1 & J_i \\ g & h & J_T \end{Bmatrix} \begin{Bmatrix} g & h & J_T \\ \tilde{h} & \tilde{g} & j_t \\ x & 1 & T \end{Bmatrix} \begin{Bmatrix} \frac{1}{2} & \frac{1}{2} & \tilde{g} \\ \frac{1}{2} & \frac{1}{2} & \tilde{h} \\ 1 & 1 & 1 \end{Bmatrix}$$
$$C^{1-m_L}_{g0h-m_L} C^{h-m_L}_{l_f m_f l_i - m_L - m_f} C^{g0}_{L_f 0 L_i 0} Y^{l_f}_{m_f}(\hat{r}_{2c}) Y^{l_i}_{-m_L-m_f}(\hat{r}_{2c}) \boldsymbol{L}^1_{m_L}$$
$$\frac{\phi_{j_f}(r_{2c}) F_{L_f J_f}(R_{1A}) t_{NN} \phi_{j_i}(r_{2c}) F_{L_i J_i}(R_{1A})}{R^2_{1A}} R^2_{1A} r^2_{2c} dR_{1A} dr_{2c} \sin\theta_{2c} d\theta_{2c} d\phi_{2c}, \tag{C.149}$$

where

$$k_4 = i^{L_i - L_f} (-1)^{L_i + L_f + M_{J_f} + m_{j_f} - m_L} e^{i\sigma_{L_i}} \hat{L_i}^2 \hat{L}_f \hat{J}_i \hat{J}_f \hat{g} \hat{h} \hat{j_i}^3 \hat{j_f} \hat{J}_T \hat{j}_t \hat{x} \hat{\tilde{g}} \hat{\tilde{h}} \frac{\sqrt{\frac{3}{2}} (4\pi)^{\frac{3}{2}}}{k_i k_f} \tag{C.150}$$

and, in the t_{NN} operator, $m_\lambda = 0$ and the spherical harmonic over $\hat{R}_{1A}$ simplifies to $\frac{\hat{\lambda}}{\sqrt{4\pi}}$. Incorporating this, the expression becomes

$$t_{NN} = \sum_\lambda F_\lambda(R_{1A}, r_{2c}) 4\pi Y^\lambda_0(r_{2c}) \frac{\hat{\lambda}}{\sqrt{4\pi}}. \tag{C.151}$$

Explicitly, F_λ is

$$\frac{1}{2}\int_{-1}^{1} V(r_{12})P_{\lambda}(z)dz. \tag{C.152}$$

To implement this expression, one could apply the angular momentum operator, $L^1_{m_L}$, the the spherical harmonics in the initial channel and then perform the remaining angular integral over the this result and all other remaining spherical harmonics. Explicitly, L can be represented by Equation (18) from pg. 41 of [117]:

$$\begin{aligned} L_{1,+1} &= -\frac{1}{\sqrt{2}}e^{i\phi}\Big\{\frac{\partial}{\partial\theta} + icot\theta\frac{\partial}{\partial\phi}\Big\} \\ L_{1,0} &= -i\frac{\partial}{\partial\phi} \\ L_{1,-1} &= -\frac{1}{\sqrt{2}}e^{-i\phi}\Big\{\frac{\partial}{\partial\theta} - icot\theta\frac{\partial}{\partial\phi}\Big\}. \end{aligned} \tag{C.153}$$

However, CHEX is not currently set up to handle these angular integrals, so we hoped to find an approximation that could give us an idea of the shape and magnitude of the spin-orbit contribution without this explicit integration. The first simplification we considered was a zero-range approximation for the valence nucleon and core. In this approximation, the valence particle would sit directly on top of the core, collapsing the r_{2c} coordinate. In this configuration, $r_{12} = R_{1A}$ and applying $\boldsymbol{L}\cdot\boldsymbol{S}$ is straightforward.

While this would simplify the T-matrix expression considerably, Figure C.1 demonstrates the dependence of the radial integral over the NN potential and both scattering and bound state wave functions on the various radial variables. The case shown is for the central term of the AV8' potential for the ^{48}Ca(p,n)^{48}Sc reaction, but the behavior is similar across all terms of both NN potentials studied here. The x-axis shows the cutoff on the lower bound of the radial integral for each radial variable. As expected, we see that the radial integral

quickly goes to zero if we cut out contributions from even $r_{12} < 1$ fm. This is reflected in the geometry of the NN potentials which are all peaked in magnitude at 0 fm and approach 0 in the range of 2-3 fm. However, we can see that a similar radial cut in the bound state coordinate, r_{2c} or the scattering coordinate, R_{1A} does not cause a large decrease to the radial integral until about 2 fm and the fall-off is less steep. This indicates that the reaction is occurring near or just below the surface of the target nucleon when the scattering and valence nucleons are in close proximity, as opposed to in the internal region of the core.

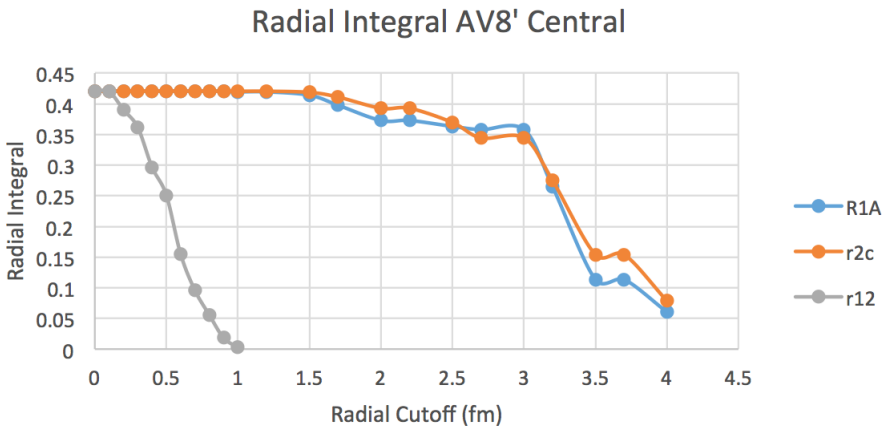

Figure C.1: Dependence of radial integral to the range of various radial parameters for the case of ^{48}Ca(p,n)^{48}Sc. The x-axis shows the internal radial cut in each parameter.

Based on this, we experimented with applying an approximation that is a hybrid of a zero-range approximation in the r_{12} coordinate. The zero-range approximation would model the projectile/valence potential as a delta function with a weighing factor, $V_{NN}(r_{12})\phi(r_{12}) \sim D_0\delta(r_{12})$. The strength of D_0 can be found by taking the integral of the proton-neutron wave function and the NN potential.

Additionally, we need to adjust our integrals over the bound state and scattering state variables to reflect the fact that we are only considering contributions in a limited region of the nuclear volume. Instead of integrating over the entire length of r_{12} and R_{1A}, we weight

the interaction by only including an integral over these wave functions in the region near the nuclear surface. The strength of the radial interaction will depend on the cutoffs chosen for this approximation and the choice should depend on the size of the target considered in the reaction. After studying the response in targets of various size, we chose a weighting factor which included contributions from the bound and scattering wave functions between $\frac{r_0 A^{1/3}}{2.5}$ to $r_0 A^{1/3}$, where r_0 is the radius parameter of the Woods-Saxon potential that describes the bound state.

The biggest challenge to this approximation is that our coordinates do not contain a natural wave-function to describe the relative motion between proton and neutron. The form of this wave function will directly impact the magnitude of D_0 in the zero range approximation, and, therefore, the magnitude of the cross section. We considered several different forms of this wave function, including a simple deuteron wave function parameterized by the sum of exponentials from [118]. This wave function has both an s-wave and d-wave component. However, the spin-orbit contribution from from relative angular momentum $L = 0$ is 0, so we only consider the d-wave contribution and, thus, will only consider L=2 contributions to the spin-orbit potential. Strictly speaking, the zero-range approximation would only include L=0, but we allow for this deviation in order to explore the possible effect of including a spin-orbit term from the NN interaction.

We also considered simpler forms, like r^L or a gaussian form factor. Because D_0 was so sensitive to the choice of wave function, and we had no consistent way of choosing an appropriate factor given our representation, we felt we could neither conclude that the spin-orbit contribution is small enough to disregard nor be convinced that any of our approximations would give an accurate representation of the magnitude or shape. Thus, we decided it was best to refrain from implementing an approximate spin-orbit contribution and leave this

problem as an area of future investigation.

APPENDIX D

Benchmarking and Testing CHEX

The charge-exchange code, CHEX, was developed to calculate charge-exchange cross sections in both the two and three-body formalisms presented in this thesis. Throughout its development, CHEX was benchmarked and tested against other reaction codes for several cases in order to ensure it was working properly. Additionally, we compared analytic forms with known solutions, for specific simplified cases. Some of those tests are presented and discussed here. Wave functions and elastic scattering cross sections were compare to results from the reaction code FRESCO [76]. Charge-exchange cross sections in the two-body formalism are compared to results from the unpublished charge-exchange code developed for the IAS analysis work in [10].

Scattering Wave Functions

First, we verify that the scattering wave functions produced by CHEX are correct. This is demonstrated in Fig. D.1 for the case of the reaction ^{48}Ca(p,p)^{48}Ca at E_p=30 MeV. The solid black (blue) lines show the real (imaginary) part of the scattering wave function for the L=0, J=0.5 partial wave calculated in CHEX. These calculations are compared to results from FRESCO shown by the dashed red (green) lines. For these calculations, we used a step size of 0.05 fm, a matching radius of 30 fm, and the OMP parameterized by Koning-Delaroche [1]. The calculation is fully converged using these parameters. Scattering wave functions

calculated by CHEX agree with Fresco within 1%, with an average percent difference of 0.33% for the real scattering wave function and 0.46% for the imaginary scattering wave function in the region shown here.

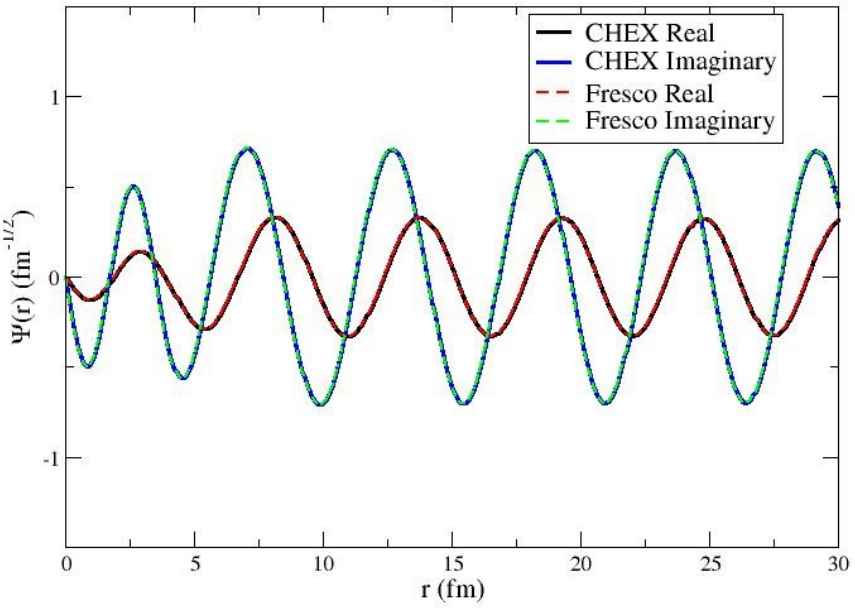

Figure D.1: Real and Imaginary parts of the scattering wave function as a function of scattering radius for the L=0, J=0.5 partial wave for ^{48}Ca(p, p)^{48}Ca at E_p = 30.0 MeV. The solid black (blue) lines show the real (imaginary) part of scattering wave function calculated in CHEX, the dashed red (green) lines show the same result produced by FRESCO.

Elastic Scattering

Next, we demonstrated that the elastic scattering cross sections calculated by CHEX reproduce results from FRESCO. This can be seen in Fig. D.2, again for the case of the reaction ^{48}Ca(p,p)^{48}Ca at E_p=30 MeV. The solid black line shows the differential elastic scattering cross section relative to Rutherford calculated in CHEX. This is compared to the

result from FRESCO shown by the dashed red line. For this calculation, we used the same input parameters as for the scattering wave function benchmarking tests (stepsize of 0.05 fm, matching radius of 30 fm, and optical model parameterized by Koning-Delaroche [1]) and the calculation is fully converged using these parameters. Elastic scattering cross sections produced by CHEX agree with Fresco within 1%, for small angles, with a slight divergence at large scattering angles. The average percent different over all angles shown in Figure D.2 is 1.84%.

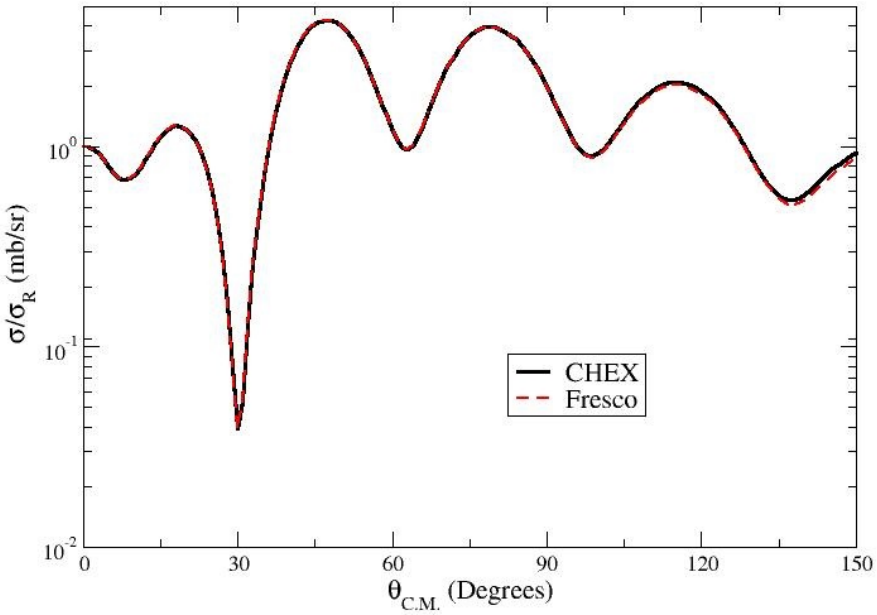

Figure D.2: Differential elastic scattering relative to Rutherford as a function of scattering angle for ^{48}Ca(p, p)^{48}Ca at $E_p = 30.0$ MeV. The solid black line shows the elastic scattering cross section calculated in CHEX, the dashed red line shows the same result produced by FRESCO.

Bound States

Calculations performed in the three-body formalism require the calculation of a bound state wave function. These wave functions have been benchmarked with bound state calculations in FRESCO. Fig. D.3 shows the n+^{47}Ca (left) and p+^{47}Ca (right) bound state wave functions which correlate to the target and residual of the ^{48}Ca(p,n)^{48}Sc. The cross section calculated using CHEX is shown in solid black and the result from FRESCO is shown in dashed red. In this case, the n+^{47}Ca bound state corresponds to the $f_{7/2}$ ground state in ^{48}Ca, and the p+^{47}Ca bound state corresponds to the the IAS in ^{48}Sc. The calculation used a step size of 0.5 fm, a matching radius of 2.5 fm and a maximum radius of 30 fm and the calculation is fully converged with these parameters. Bound state wave functions produced by CHEX agree with results from FRESCO well within 1%, with an average percent difference of 0.03% within the region shown if Figure D.3.

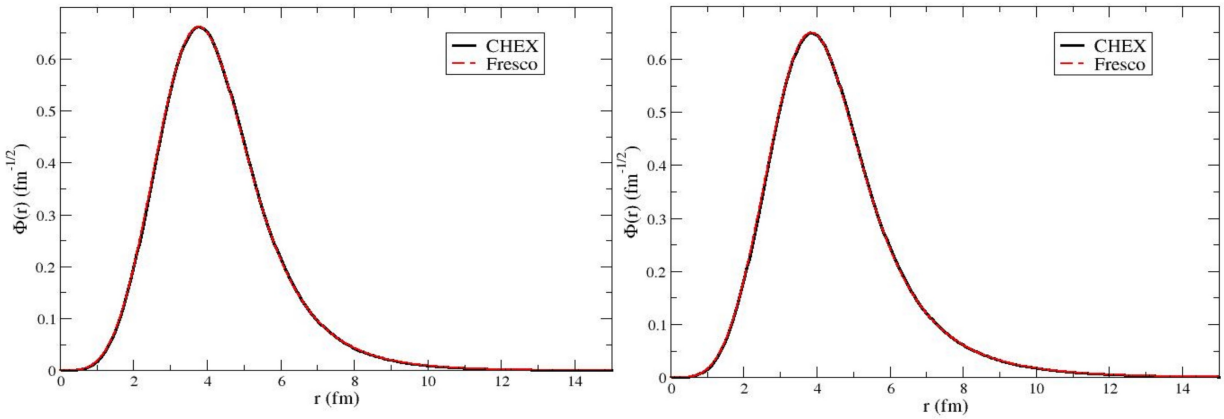

Figure D.3: Bound state wave functions as a function of radius. The left plot shows n+^{47}Ca bound state wave function and the right plot shows the p+^{47}Ca bound state wave function, which correlate to the in the initial and final states of the ^{48}Ca(p,n)^{48}Sc reaction. The solid black line shows results from CHEX, the dashed red line shows the same result produced by FRESCO.

Two-Body Charge-Exchange

Two-body calculations performed using CHEX can be directly compared to results from [10]. Before checking the implementation in CHEX, we first verified that the expressions we developed for the charge-exchange T-matrix and cross sections, shown in Equations (2.41) and (2.42), give the same result as the expression presented in [10]. This task was not trivial, as the expressions were developed using sums over different parameters. The cross section expression from [10] gives

$$\frac{d\sigma_{(p,n)}}{d\Omega} = \frac{1}{k_p^2}\frac{1}{2s+1}\sum_L (2L+1)A_L^{(p,n)}P_L(\cos\theta), \tag{D.1}$$

where

$$\begin{aligned} A_L^{(p,n)} =& 4\mu_p\mu_n k_p k_n \sum_{J'l'}(2J'+1)(2l'+1)\sum_{Jl}(2J+1)(2l+1) \\ & \begin{pmatrix} l & l' & L \\ 0 & 0 & 0 \end{pmatrix}^2 \begin{Bmatrix} l & l' & L \\ J' & J & s \end{Bmatrix}^2 Re[I^*_{J'l'}I_{lJ}], \end{aligned} \tag{D.2}$$

and

$$I_{lj} = 2\frac{\sqrt{|N-Z|}}{A}\int_0^\infty dr r^2 u^+_{nJl}(r)U_1^{Jl}(r)u^+_{pJl}(r). \tag{D.3}$$

In this formulation, $u(r)$ are the radial scattering wave functions, U_1 is the charge-exchange term from the Lane potential shown in Equation (2.35). In these expressions, J/J' and l/l' do not correlate to the initial and final angular momentum values from our definition but, instead, correspond to the different indexes used while taking the modulus squared of the

reaction amplitude. There is no direct correlation between L in the expression above, and our Equation (2.41). To prove equivalence of these two expressions, we can demonstrate that they give the same results for particular partial waves, as well as an arbitrary sum of partial waves. We do this by setting the values of the integrals to 1 (I_{lj} in the expression above) and checking the analytical forms of the expressions using Mathematica. It is worth noting that the wave functions in [10] include a factor of $\frac{1}{k_{i/f}}$ and, for the case of proton distorted waves, include the Coulomb phase shift. Excluding these factors, the first three partial waves, in both expressions, have the analytical forms shown in Table (D.1).

L value	Analytic Expression
0	$\frac{40k_f\mu_f\mu_i}{k_i(\hbar c)^4}$
1	$\frac{360k_f\mu_f\mu_i Cos(\theta)^2}{k_i(\hbar c)^4}$
2	$\frac{250k_f\mu_f\mu_i}{k_i(\hbar c)^4} - \frac{1500k_f\mu_f\mu_i Cos(\theta)^2}{k_i(\hbar c)^4} + \frac{2250k_f\mu_f\mu_i Cos(\theta)^4}{k_i(\hbar c)^4}$
0+1+2	$\frac{90k_f\mu_f\mu_i}{k_i(\hbar c)^4} - \frac{360k_f\mu_f\mu_i Cos(\theta)}{k_i(\hbar c)^4} - \frac{540k_f\mu_f\mu_i Cos(\theta)^2}{k_i(\hbar c)^4} + \frac{1800k_f\mu_f\mu_i Cos(\theta)^3}{k_i(\hbar c)^4} + \frac{2250k_f\mu_f\mu_i Cos(\theta)^4}{k_i(\hbar c)^4}$

Table D.1: Analytic result for the first few partial waves for the two-body charge-exchange cross sections calculated using the T-matrix from Equations (2.42) and (D.1). In the expressions above, the radial integrals are set to 1.

Once we determined that our expressions for the two-body T-matrix and cross sections are sound, we could check that the implementation in CHEX was correct by directly comparing charge-exchange cross sections with those produced by Danielewicz et al. In making this comparison, we found there was a slight difference in the way that the spin-orbit term is included in the Lane interaction (see Figure D.4(a)). In the work by Danielewicz et al., they varied parameters to create best fits to charge-exchange data and, as a result, their code initialized the spin-orbit parameters at slightly different values than the standard KD values. Figure D.4(b) shows that, if this small spin-orbit term is neglected, the cross sections agree well within 1% difference.

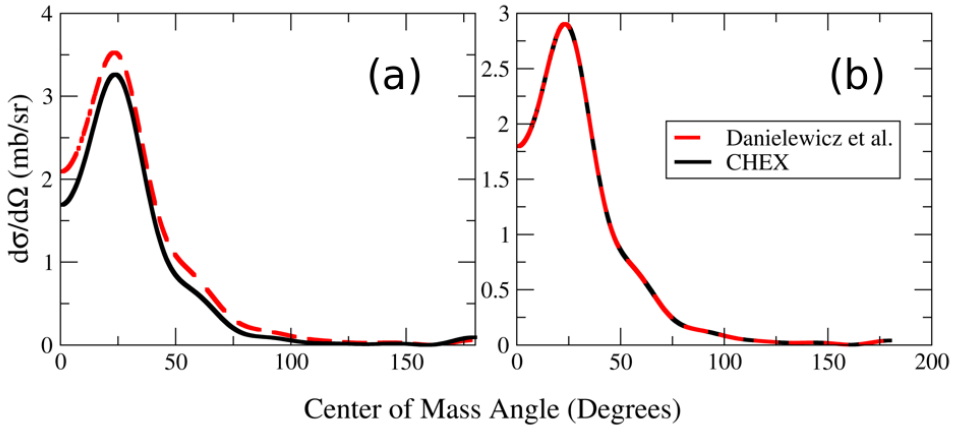

Figure D.4: Comparing the charge-exchange cross sections for ^{48}Ca(p,n)^{48}Sc at 35 MeV, produced by [10] and by CHEX. (a): there is a small difference resulting from the way spin-orbit was included. (b): once this spin-orbit contribution is neglected, the two calculations match exactly.

Three-Body Charge-Exchange

Benchmarking the three-body formalism presented in this thesis, as well as its implementation in CHEX, presents a unique challenge because there is no option for direct comparisons with another charge-exchange code (this is the first implementation of its kind). Still, we took many steps to ensure that the resulting calculations in CHEX were correct. These tests generally fell into one of two categories: tests which ensured that components were implemented accurately in CHEX, and limiting cases that simplify the T-matrix expressions and allow us to verify our results.

While implementing the formalism for each operator's T-matrix expression, sums in CHEX were checked numerically against the same sums coded in Mathematica. This ensures that errors were not introduced to the code through FORTRAN syntax errors or through issues calling subroutines that compute algebraic factors, such as 6 and 9-j factors. Additionally, we could use Mathematica to ensure that our numerical integrals, including those

that utilize a multipole expansion, were working properly. We did this by importing the wave functions and potentials produced by CHEX into Mathematica and using its interpolation and numerical integration functions to calculate integrals. When we compared these integrals to those produced by CHEX, they were in agreement.

We noticed that in cases where the magnitude of the potential integral was very small, the value of the integral could be sensitive to the radial cut-off and number of integration points used in the calculation. This was resulting from adding many small contributions from regions where the potential should be, effectively, zero. This problem was solved by adding a routine which sets the value of the integrant to 0 if its magnitude drops below a certain tolerance value, which depends on the strength of the potential.

Finally, we were able to check components of the CHEX implementation, as well simplified cases with the reaction code DW81 [79]. These cases included replacing incoming and outgoing distorted waves and our NN interaction with simple Yukawa interaction. However, a detailed comparison of charge-exchange cross sections was hindered by differences in the reaction formalism.

We also performed a number of analytical checks to ensure that our T-matrix expressions behave as we expect in limiting cases. These tests included using spin=0 for the projectile and the valence nucleon, which results in $L_{i/f} = J_{i/f}$ and $l_{i/f} = j_{i/f}$, greatly reducing the number of sums and reducing 6 and 9-j symbols to simpler expressions. We also checked, for each T-matrix, the results when the partial wave expansion was reduced to just L=0 or L=1. Finally, we checked our T-matrix expression for the limiting case where the T-matrix operator is assumed to be unity, V_{NN}=1. In this case, you would expect $\delta_{Li,Lf}\delta_{l_i,l_f}\delta_{J_i,J_f}\delta_{j_i,j_f}$. CHEX passed each of these tests.

BIBLIOGRAPHY

BIBLIOGRAPHY

[1] A. Koning and J. Delaroche, "Local and global nucleon optical models from 1 kev to 200 MeV," *Nuclear Physics A*, vol. 713, no. 3, pp. 231 – 310, 2003.

[2] R. Varner, W. Thompson, T. McAbee, E. Ludwig, and T. Clegg, "A global nucleon optical model potential," *Physics Reports*, vol. 201, no. 2, pp. 57 – 119, 1991.

[3] A. Kankainen, P. Woods, H. Schatz, T. Poxon-Pearson, D. Doherty, V. Bader, T. Baugher, D. Bazin, B. Brown, J. Browne, A. Estrade, A. Gade, J. JosÃl', A. Kontos, C. Langer, G. Lotay, Z. Meisel, F. Montes, S. Noji, F. Nunes, G. Perdikakis, J. Pereira, F. Recchia, T. Redpath, R. Stroberg, M. Scott, D. Seweryniak, J. Stevens, D. Weisshaar, K. Wimmer, and R. Zegers, "Measurement of key resonance states for the p30(p,γ)s31 reaction rate, and the production of intermediate-mass elements in nova explosions," *Physics Letters B*, vol. 769, pp. 549 – 553, 2017.

[4] B. A. Brown and W. A. Richter, "New "usd" hamiltonians for the *sd* shell," *Phys. Rev. C*, vol. 74, p. 034315, Sep 2006.

[5] E. K. Warburton and B. A. Brown, "Effective interactions for the 0p1s0d nuclear shell-model space," *Phys. Rev. C*, vol. 46, pp. 923–944, Sep 1992.

[6] C. Wolf, C. Langer, F. Montes, J. Pereira, W.-J. Ong, T. Poxon-Pearson, S. Ahn, S. Ayoub, T. Baumann, D. Bazin, P. C. Bender, B. A. Brown, J. Browne, H. Crawford, R. H. Cyburt, E. Deleeuw, B. Elman, S. Fiebiger, A. Gade, P. Gastis, S. Lipschutz, B. Longfellow, Z. Meisel, F. M. Nunes, G. Perdikakis, R. Reifarth, W. A. Richter, H. Schatz, K. Schmidt, J. Schmitt, C. Sullivan, R. Titus, D. Weisshaar, P. J. Woods, J. C. Zamora, and R. G. T. Zegers, "Constraining the neutron star compactness: Extraction of the ^{23}Al(p,γ) reaction rate for the *rp* process," *Phys. Rev. Lett.*, vol. 122, p. 232701, Jun 2019.

[7] D. Kahl, P. Woods, T. Poxon-Pearson, F. Nunes, B. Brown, H. Schatz, T. Baumann, D. Bazin, J. Belarge, P. Bender, B. Elman, A. Estrade, A. Gade, A. Kankainen, C. Lederer-Woods, S. Lipschutz, B. Longfellow, S.-J. Lonsdale, E. Lunderberg, F. Montes, W. Ong, G. Perdikakis, J. Pereira, C. Sullivan, R. Taverner, D. Weisshaar, and R. Zegers, "Single-particle shell strengths near the doubly magic nucleus 56ni and the 56ni(p,γ)57cu reaction rate in explosive astrophysical burning," *Physics Letters B*, vol. 797, p. 134803, 2019.

[8] N. R. Council, *Nuclear Physics: Exploring the Heart of Matter*. Washington, DC: The National Academies Press, 2013.

[9] F. Nunes, G. Potel, T. Poxon-Pearson, and J. Cizewski, "Nuclear reactions in astrophysics: A review of useful probes for extracting reaction rates," *Annual Review of Nuclear and Particle Science*, vol. 70, 2020. Accepted for Publication.

[10] P. Danielewicz, P. Singh, and J. Lee, "Symmetry energy iii: Isovector skins," *Nuclear Physics A*, vol. 958, pp. 147 – 186, 2017.

[11] I. Tews, T. Krüger, K. Hebeler, and A. Schwenk, "Neutron matter at next-to-next-to-next-to-leading order in chiral effective field theory," *Phys. Rev. Lett.*, vol. 110, p. 032504, Jan 2013.

[12] L.-W. Chen, C. M. Ko, B.-A. Li, and J. Xu, "Density slope of the nuclear symmetry energy from the neutron skin thickness of heavy nuclei," *Phys. Rev. C*, vol. 82, p. 024321, Aug 2010.

[13] A. W. Steiner, J. M. Lattimer, and E. F. Brown, "The equation of state from observed masses and radii of neutron stars," *The Astrophysical Journal*, vol. 722, pp. 33–54, sep 2010.

[14] M. Kortelainen, T. Lesinski, J. Moré, W. Nazarewicz, J. Sarich, N. Schunck, M. V. Stoitsov, and S. Wild, "Nuclear energy density optimization," *Phys. Rev. C*, vol. 82, p. 024313, Aug 2010.

[15] M. B. Tsang, J. R. Stone, F. Camera, P. Danielewicz, S. Gandolfi, K. Hebeler, C. J. Horowitz, J. Lee, W. G. Lynch, Z. Kohley, R. Lemmon, P. Möller, T. Murakami, S. Riordan, X. Roca-Maza, F. Sammarruca, A. W. Steiner, I. Vidaña, and S. J. Yennello, "Constraints on the symmetry energy and neutron skins from experiments and theory," *Phys. Rev. C*, vol. 86, p. 015803, Jul 2012.

[16] R. H. Cyburt, A. M. Amthor, R. Ferguson, Z. Meisel, K. Smith, S. Warren, A. Heger, R. D. Hoffman, T. Rauscher, A. Sakharuk, H. Schatz, F. K. Thielemann, and M. Wiescher, "The jina reaclib database: Its recent updates and impact on type-I X-ray bursts," *The Astrophysical Journal Supplement Series*, vol. 189, pp. 240–252, June 2010.

[17] T. N. Taddeucci, R. R. Doering, A. Galonsky, and S. M. Austin, "(p,n) reactions on ^{14}C and ^{14}N and the effective nucleon-nucleon interaction," *Phys. Rev. C*, vol. 29, pp. 764–776, Mar 1984.

[18] R. R. Doering, D. M. Patterson, and A. Galonsky, "Microscopic description of isobaric-analog-state transitions induced by 25-, 35-, and 45-MeV protons," *Phys. Rev. C*, vol. 12, pp. 378–389, Aug 1975.

[19] L. van Wormer, J. Goerres, C. Iliadis, M. Wiescher, and F. Thielemann, "Reaction rates and reaction sequences in the rp-process," *The Astrophysical Journal*, vol. 432, pp. 326–350, 08 1994.

[20] K. E. Rehm, F. Borasi, C. L. Jiang, D. Ackermann, I. Ahmad, B. A. Brown, F. Brumwell, C. N. Davids, P. Decrock, S. M. Fischer, J. Görres, J. Greene, G. Hackmann, B. Harss, D. Henderson, W. Henning, R. V. F. Janssens, G. McMichael, V. Nanal, D. Nisius, J. Nolen, R. C. Pardo, M. Paul, P. Reiter, J. P. Schiffer, D. Seweryniak, R. E. Segel, M. Wiescher, and A. H. Wuosmaa, "Study of the ^{56}Ni$(d,p)^{57}$Ni reaction and the astrophysical ^{56}Ni$(p,\gamma)^{57}$Cu reaction rate," *Phys. Rev. Lett.*, vol. 80, pp. 676–679, Jan 1998.

[21] X. G. Zhou, H. Dejbakhsh, C. A. Gagliardi, J. Jiang, L. Trache, and R. E. Tribble, "Low-lying levels in ^{57}Cu and the rp process," *Phys. Rev. C*, vol. 53, pp. 982–988, Feb 1996.

[22] S. Starrfield, C. Iliadis, and W. R. Hix, "The thermonuclear runaway and the classical nova outburst," *Publications of the Astronomical Society of the Pacific*, vol. 128, p. 051001, April 2016.

[23] H. Schatz, A. Aprahamian, J. GÃűrres, M. Wiescher, T. Rauscher, J. Rembges, F.-K. Thielemann, B. Pfeiffer, P. MÃűller, K.-L. Kratz, H. Herndl, B. Brown, and H. Rebel, "rp-process nucleosynthesis at extreme temperature and density conditions," *Physics Reports*, vol. 294, no. 4, pp. 167 – 263, 1998.

[24] E. M. Burbidge, G. R. Burbidge, W. A. Fowler, and F. Hoyle, "Synthesis of the elements in stars," *Rev. Mod. Phys.*, vol. 29, pp. 547–650, Oct 1957.

[25] B. P. Abbott, R. Abbott, T. D. Abbott, F. Acernese, K. Ackley, C. Adams, T. Adams, P. Addesso, R. X. Adhikari, V. B. Adya, C. Affeldt, M. Afrough, B. Agarwal, M. Agathos, K. Agatsuma, N. Aggarwal, O. D. Aguiar, L. Aiello, A. Ain, P. Ajith, B. Allen, G. Allen, A. Allocca, P. A. Altin, A. Amato, A. Ananyeva, S. B. Anderson, W. G. Anderson, S. V. Angelova, S. Antier, S. Appert, K. Arai, M. C. Araya, J. S. Areeda, N. Arnaud, K. G. Arun, S. Ascenzi, G. Ashton, M. Ast, S. M. Aston, P. Astone, D. V. Atallah, P. Aufmuth, C. Aulbert, K. AultONeal, C. Austin, A. Avila-Alvarez, S. Babak, P. Bacon, M. K. M. Bader, S. Bae, M. Bailes, P. T. Baker, F. Baldaccini, G. Ballardin, S. W. Ballmer, S. Banagiri, J. C. Barayoga, S. E. Barclay, B. C. Barish, D. Barker, K. Barkett, F. Barone, B. Barr, L. Barsotti, M. Barsuglia, D. Barta, S. D. Barthelmy, J. Bartlett, I. Bartos, R. Bassiri, A. Basti, J. C. Batch, M. Bawaj, J. C. Bayley, M. Bazzan, B. Bécsy, C. Beer, M. Bejger, I. Belahcene, A. S. Bell, B. K. Berger, G. Bergmann, S. Bernuzzi, J. J. Bero, C. P. L. Berry, D. Bersanetti, A. Bertolini, J. Betzwieser, S. Bhagwat, R. Bhandare, I. A. Bilenko, G. Billingsley, C. R. Billman, J. Birch, R. Birney, O. Birnholtz, S. Biscans, S. Biscoveanu, A. Bisht, M. Bitossi, C. Biwer, M. A. Bizouard, J. K. Blackburn, J. Blackman, C. D. Blair, D. G. Blair, R. M. Blair, S. Bloemen, O. Bock, N. Bode, M. Boer, G. Bogaert, A. Bohe,

F. Bondu, E. Bonilla, R. Bonnand, B. A. Boom, R. Bork, V. Boschi, S. Bose, K. Bossie, Y. Bouffanais, A. Bozzi, C. Bradaschia, P. R. Brady, M. Branchesi, J. E. Brau, T. Briant, A. Brillet, M. Brinkmann, V. Brisson, P. Brockill, J. E. Broida, A. F. Brooks, D. A. Brown, D. D. Brown, S. Brunett, C. C. Buchanan, A. Buikema, T. Bulik, H. J. Bulten, A. Buonanno, D. Buskulic, C. Buy, R. L. Byer, M. Cabero, L. Cadonati, G. Cagnoli, C. Cahillane, J. Calderón Bustillo, T. A. Callister, E. Calloni, J. B. Camp, M. Canepa, P. Canizares, K. C. Cannon, H. Cao, J. Cao, C. D. Capano, E. Capocasa, F. Carbognani, S. Caride, M. F. Carney, G. Carullo, J. Casanueva Diaz, C. Casentini, S. Caudill, M. Cavaglià, F. Cavalier, R. Cavalieri, G. Cella, C. B. Cepeda, P. Cerdá-Durán, G. Cerretani, E. Cesarini, S. J. Chamberlin, M. Chan, S. Chao, P. Charlton, E. Chase, E. Chassande-Mottin, D. Chatterjee, K. Chatziioannou, B. D. Cheeseboro, H. Y. Chen, X. Chen, Y. Chen, H.-P. Cheng, H. Chia, A. Chincarini, A. Chiummo, T. Chmiel, H. S. Cho, M. Cho, J. H. Chow, N. Christensen, Q. Chu, A. J. K. Chua, S. Chua, A. K. W. Chung, S. Chung, G. Ciani, R. Ciolfi, C. E. Cirelli, A. Cirone, F. Clara, J. A. Clark, P. Clearwater, F. Cleva, C. Cocchieri, E. Coccia, P.-F. Cohadon, D. Cohen, A. Colla, C. G. Collette, L. R. Cominsky, M. Constancio, L. Conti, S. J. Cooper, P. Corban, T. R. Corbitt, I. Cordero-Carrión, K. R. Corley, N. Cornish, A. Corsi, S. Cortese, C. A. Costa, M. W. Coughlin, S. B. Coughlin, J.-P. Coulon, S. T. Countryman, P. Couvares, P. B. Covas, E. E. Cowan, D. M. Coward, M. J. Cowart, D. C. Coyne, R. Coyne, J. D. E. Creighton, T. D. Creighton, J. Cripe, S. G. Crowder, T. J. Cullen, A. Cumming, L. Cunningham, E. Cuoco, T. Dal Canton, G. Dálya, S. L. Danilishin, S. D'Antonio, K. Danzmann, A. Dasgupta, C. F. Da Silva Costa, V. Dattilo, I. Dave, M. Davier, D. Davis, E. J. Daw, B. Day, S. De, D. DeBra, J. Degallaix, M. De Laurentis, S. Deléglise, W. Del Pozzo, N. Demos, T. Denker, T. Dent, R. De Pietri, V. Dergachev, R. De Rosa, R. T. DeRosa, C. De Rossi, R. DeSalvo, O. de Varona, J. Devenson, S. Dhurandhar, M. C. Díaz, T. Dietrich, L. Di Fiore, M. Di Giovanni, T. Di Girolamo, A. Di Lieto, S. Di Pace, I. Di Palma, F. Di Renzo, Z. Doctor, V. Dolique, F. Donovan, K. L. Dooley, S. Doravari, I. Dorrington, R. Douglas, M. Dovale Álvarez, T. P. Downes, M. Drago, C. Dreissigacker, J. C. Driggers, Z. Du, M. Ducrot, R. Dudi, P. Dupej, S. E. Dwyer, T. B. Edo, M. C. Edwards, A. Effler, H.-B. Eggenstein, P. Ehrens, J. Eichholz, S. S. Eikenberry, R. A. Eisenstein, R. C. Essick, D. Estevez, Z. B. Etienne, T. Etzel, M. Evans, T. M. Evans, M. Factourovich, V. Fafone, H. Fair, S. Fairhurst, X. Fan, S. Farinon, B. Farr, W. M. Farr, E. J. Fauchon-Jones, M. Favata, M. Fays, C. Fee, H. Fehrmann, J. Feicht, M. M. Fejer, A. Fernandez-Galiana, I. Ferrante, E. C. Ferreira, F. Ferrini, F. Fidecaro, D. Finstad, I. Fiori, D. Fiorucci, M. Fishbach, R. P. Fisher, M. Fitz-Axen, R. Flaminio, M. Fletcher, H. Fong, J. A. Font, P. W. F. Forsyth, S. S. Forsyth, J.-D. Fournier, S. Frasca, F. Frasconi, Z. Frei, A. Freise, R. Frey, V. Frey, E. M. Fries, P. Fritschel, V. V. Frolov, P. Fulda, M. Fyffe, H. Gabbard, B. U. Gadre, S. M. Gaebel, J. R. Gair, L. Gammaitoni, M. R. Ganija, S. G. Gaonkar, C. Garcia-Quiros, F. Garufi, B. Gateley, S. Gaudio, G. Gaur, V. Gayathri, N. Gehrels, G. Gemme, E. Genin, A. Gennai, D. George, J. George, L. Gergely, V. Germain, S. Ghonge, A. Ghosh, A. Ghosh, S. Ghosh, J. A. Giaime, K. D. Giardina, A. Giazotto, K. Gill, L. Glover, E. Goetz, R. Goetz, S. Gomes, B. Goncharov, G. González, J. M. Gonzalez Castro, A. Gopakumar, M. L. Gorodetsky, S. E. Gossan, M. Gosselin, R. Gouaty, A. Grado, C. Graef,

M. Granata, A. Grant, S. Gras, C. Gray, G. Greco, A. C. Green, E. M. Gretarsson, P. Groot, H. Grote, S. Grunewald, P. Gruning, G. M. Guidi, X. Guo, A. Gupta, M. K. Gupta, K. E. Gushwa, E. K. Gustafson, R. Gustafson, O. Halim, B. R. Hall, E. D. Hall, E. Z. Hamilton, G. Hammond, M. Haney, M. M. Hanke, J. Hanks, C. Hanna, M. D. Hannam, O. A. Hannuksela, J. Hanson, T. Hardwick, J. Harms, G. M. Harry, I. W. Harry, M. J. Hart, C.-J. Haster, K. Haughian, J. Healy, A. Heidmann, M. C. Heintze, H. Heitmann, P. Hello, G. Hemming, M. Hendry, I. S. Heng, J. Hennig, A. W. Heptonstall, M. Heurs, S. Hild, T. Hinderer, W. C. G. Ho, D. Hoak, D. Hofman, K. Holt, D. E. Holz, P. Hopkins, C. Horst, J. Hough, E. A. Houston, E. J. Howell, A. Hreibi, Y. M. Hu, E. A. Huerta, D. Huet, B. Hughey, S. Husa, S. H. Huttner, T. Huynh-Dinh, N. Indik, R. Inta, G. Intini, H. N. Isa, J.-M. Isac, M. Isi, B. R. Iyer, K. Izumi, T. Jacqmin, K. Jani, P. Jaranowski, S. Jawahar, F. Jiménez-Forteza, W. W. Johnson, N. K. Johnson-McDaniel, D. I. Jones, R. Jones, R. J. G. Jonker, L. Ju, J. Junker, C. V. Kalaghatgi, V. Kalogera, B. Kamai, S. Kandhasamy, G. Kang, J. B. Kanner, S. J. Kapadia, S. Karki, K. S. Karvinen, M. Kasprzack, W. Kastaun, M. Katolik, E. Katsavounidis, W. Katzman, S. Kaufer, K. Kawabe, F. Kéfélian, D. Keitel, A. J. Kemball, R. Kennedy, C. Kent, J. S. Key, F. Y. Khalili, I. Khan, S. Khan, Z. Khan, E. A. Khazanov, N. Kijbunchoo, C. Kim, J. C. Kim, K. Kim, W. Kim, W. S. Kim, Y.-M. Kim, S. J. Kimbrell, E. J. King, P. J. King, M. Kinley-Hanlon, R. Kirchhoff, J. S. Kissel, L. Kleybolte, S. Klimenko, T. D. Knowles, P. Koch, S. M. Koehlenbeck, S. Koley, V. Kondrashov, A. Kontos, M. Korobko, W. Z. Korth, I. Kowalska, D. B. Kozak, C. Krämer, V. Kringel, B. Krishnan, A. Królak, G. Kuehn, P. Kumar, R. Kumar, S. Kumar, L. Kuo, A. Kutynia, S. Kwang, B. D. Lackey, K. H. Lai, M. Landry, R. N. Lang, J. Lange, B. Lantz, R. K. Lanza, S. L. Larson, A. Lartaux-Vollard, P. D. Lasky, M. Laxen, A. Lazzarini, C. Lazzaro, P. Leaci, S. Leavey, C. H. Lee, H. K. Lee, H. M. Lee, H. W. Lee, K. Lee, J. Lehmann, A. Lenon, E. Leon, M. Leonardi, N. Leroy, N. Letendre, Y. Levin, T. G. F. Li, S. D. Linker, T. B. Littenberg, J. Liu, X. Liu, R. K. L. Lo, N. A. Lockerbie, L. T. London, J. E. Lord, M. Lorenzini, V. Loriette, M. Lormand, G. Losurdo, J. D. Lough, C. O. Lousto, G. Lovelace, H. Lück, D. Lumaca, A. P. Lundgren, R. Lynch, Y. Ma, R. Macas, S. Macfoy, B. Machenschalk, M. MacInnis, D. M. Macleod, I. Magaña Hernandez, F. Magaña Sandoval, L. Magaña Zertuche, R. M. Magee, E. Majorana, I. Maksimovic, N. Man, V. Mandic, V. Mangano, G. L. Mansell, M. Manske, M. Mantovani, F. Marchesoni, F. Marion, S. Márka, Z. Márka, C. Markakis, A. S. Markosyan, A. Markowitz, E. Maros, A. Marquina, P. Marsh, F. Martelli, L. Martellini, I. W. Martin, R. M. Martin, D. V. Martynov, J. N. Marx, K. Mason, E. Massera, A. Masserot, T. J. Massinger, M. Masso-Reid, S. Mastrogiovanni, A. Matas, F. Matichard, L. Matone, N. Mavalvala, N. Mazumder, R. McCarthy, D. E. McClelland, S. McCormick, L. McCuller, S. C. McGuire, G. McIntyre, J. McIver, D. J. McManus, L. McNeill, T. McRae, S. T. McWilliams, D. Meacher, G. D. Meadors, M. Mehmet, J. Meidam, E. Mejuto-Villa, A. Melatos, G. Mendell, R. A. Mercer, E. L. Merilh, M. Merzougui, S. Meshkov, C. Messenger, C. Messick, R. Metzdorff, P. M. Meyers, H. Miao, C. Michel, H. Middleton, E. E. Mikhailov, L. Milano, A. L. Miller, B. B. Miller, J. Miller, M. Millhouse, M. C. Milovich-Goff, O. Minazzoli, Y. Minenkov, J. Ming, C. Mishra, S. Mitra, V. P. Mitrofanov, G. Mitselmakher, R. Mittleman, D. Moffa, A. Moggi, K. Mogushi, M. Mohan, S. R. P. Mohapatra, I. Molina, M. Mon-

tani, C. J. Moore, D. Moraru, G. Moreno, S. Morisaki, S. R. Morriss, B. Mours, C. M. Mow-Lowry, G. Mueller, A. W. Muir, A. Mukherjee, D. Mukherjee, S. Mukherjee, N. Mukund, A. Mullavey, J. Munch, E. A. Muñiz, M. Muratore, P. G. Murray, A. Nagar, K. Napier, I. Nardecchia, L. Naticchioni, R. K. Nayak, J. Neilson, G. Nelemans, T. J. N. Nelson, M. Nery, A. Neunzert, L. Nevin, J. M. Newport, G. Newton, K. K. Y. Ng, P. Nguyen, T. T. Nguyen, D. Nichols, A. B. Nielsen, S. Nissanke, A. Nitz, A. Noack, F. Nocera, D. Nolting, C. North, L. K. Nuttall, J. Oberling, G. D. O'Dea, G. H. Ogin, J. J. Oh, S. H. Oh, F. Ohme, M. A. Okada, M. Oliver, P. Oppermann, R. J. Oram, B. O'Reilly, R. Ormiston, L. F. Ortega, R. O'Shaughnessy, S. Ossokine, D. J. Ottaway, H. Overmier, B. J. Owen, A. E. Pace, J. Page, M. A. Page, A. Pai, S. A. Pai, J. R. Palamos, O. Palashov, C. Palomba, A. Pal-Singh, H. Pan, H.-W. Pan, B. Pang, P. T. H. Pang, C. Pankow, F. Pannarale, B. C. Pant, F. Paoletti, A. Paoli, M. A. Papa, A. Parida, W. Parker, D. Pascucci, A. Pasqualetti, R. Passaquieti, D. Passuello, M. Patil, B. Patricelli, B. L. Pearlstone, M. Pedraza, R. Pedurand, L. Pekowsky, A. Pele, S. Penn, C. J. Perez, A. Perreca, L. M. Perri, H. P. Pfeiffer, M. Phelps, O. J. Piccinni, M. Pichot, F. Piergiovanni, V. Pierro, G. Pillant, L. Pinard, I. M. Pinto, M. Pirello, M. Pitkin, M. Poe, R. Poggiani, P. Popolizio, E. K. Porter, A. Post, J. Powell, J. Prasad, J. W. W. Pratt, G. Pratten, V. Predoi, T. Prestegard, M. Prijatelj, M. Principe, S. Privitera, R. Prix, G. A. Prodi, L. G. Prokhorov, O. Puncken, M. Punturo, P. Puppo, M. Pürrer, H. Qi, V. Quetschke, E. A. Quintero, R. Quitzow-James, F. J. Raab, D. S. Rabeling, H. Radkins, P. Raffai, S. Raja, C. Rajan, B. Rajbhandari, M. Rakhmanov, K. E. Ramirez, A. Ramos-Buades, P. Rapagnani, V. Raymond, M. Razzano, J. Read, T. Regimbau, L. Rei, S. Reid, D. H. Reitze, W. Ren, S. D. Reyes, F. Ricci, P. M. Ricker, S. Rieger, K. Riles, M. Rizzo, N. A. Robertson, R. Robie, F. Robinet, A. Rocchi, L. Rolland, J. G. Rollins, V. J. Roma, J. D. Romano, R. Romano, C. L. Romel, J. H. Romie, D. Rosińska, M. P. Ross, S. Rowan, A. Rüdiger, P. Ruggi, G. Rutins, K. Ryan, S. Sachdev, T. Sadecki, L. Sadeghian, M. Sakellariadou, L. Salconi, M. Saleem, F. Salemi, A. Samajdar, L. Sammut, L. M. Sampson, E. J. Sanchez, L. E. Sanchez, N. Sanchis-Gual, V. Sandberg, J. R. Sanders, B. Sassolas, B. S. Sathyaprakash, P. R. Saulson, O. Sauter, R. L. Savage, A. Sawadsky, P. Schale, M. Scheel, J. Scheuer, J. Schmidt, P. Schmidt, R. Schnabel, R. M. S. Schofield, A. Schönbeck, E. Schreiber, D. Schuette, B. W. Schulte, B. F. Schutz, S. G. Schwalbe, J. Scott, S. M. Scott, E. Seidel, D. Sellers, A. S. Sengupta, D. Sentenac, V. Sequino, A. Sergeev, D. A. Shaddock, T. J. Shaffer, A. A. Shah, M. S. Shahriar, M. B. Shaner, L. Shao, B. Shapiro, P. Shawhan, A. Sheperd, D. H. Shoemaker, D. M. Shoemaker, K. Siellez, X. Siemens, M. Sieniawska, D. Sigg, A. D. Silva, L. P. Singer, A. Singh, A. Singhal, A. M. Sintes, B. J. J. Slagmolen, B. Smith, J. R. Smith, R. J. E. Smith, S. Somala, E. J. Son, J. A. Sonnenberg, B. Sorazu, F. Sorrentino, T. Souradeep, A. P. Spencer, A. K. Srivastava, K. Staats, A. Staley, M. Steinke, J. Steinlechner, S. Steinlechner, D. Steinmeyer, S. P. Stevenson, R. Stone, D. J. Stops, K. A. Strain, G. Stratta, S. E. Strigin, A. Strunk, R. Sturani, A. L. Stuver, T. Z. Summerscales, L. Sun, S. Sunil, J. Suresh, P. J. Sutton, B. L. Swinkels, M. J. Szczepańczyk, M. Tacca, S. C. Tait, C. Talbot, D. Talukder, D. B. Tanner, M. Tápai, A. Taracchini, J. D. Tasson, J. A. Taylor, R. Taylor, S. V. Tewari, T. Theeg, F. Thies, E. G. Thomas, M. Thomas, P. Thomas, K. A. Thorne, K. S. Thorne, E. Thrane, S. Tiwari, V. Tiwari, K. V. Tok-

makov, K. Toland, M. Tonelli, Z. Tornasi, A. Torres-Forné, C. I. Torrie, D. Töyrä, F. Travasso, G. Traylor, J. Trinastic, M. C. Tringali, L. Trozzo, K. W. Tsang, M. Tse, R. Tso, L. Tsukada, D. Tsuna, D. Tuyenbayev, K. Ueno, D. Ugolini, C. S. Unnikrishnan, A. L. Urban, S. A. Usman, H. Vahlbruch, G. Vajente, G. Valdes, M. Vallisneri, N. van Bakel, M. van Beuzekom, J. F. J. van den Brand, C. Van Den Broeck, D. C. Vander-Hyde, L. van der Schaaf, J. V. van Heijningen, A. A. van Veggel, M. Vardaro, V. Varma, S. Vass, M. Vasúth, A. Vecchio, G. Vedovato, J. Veitch, P. J. Veitch, K. Venkateswara, G. Venugopalan, D. Verkindt, F. Vetrano, A. Viceré, A. D. Viets, S. Vinciguerra, D. J. Vine, J.-Y. Vinet, S. Vitale, T. Vo, H. Vocca, C. Vorvick, S. P. Vyatchanin, A. R. Wade, L. E. Wade, M. Wade, R. Walet, M. Walker, L. Wallace, S. Walsh, G. Wang, H. Wang, J. Z. Wang, W. H. Wang, Y. F. Wang, R. L. Ward, J. Warner, M. Was, J. Watchi, B. Weaver, L.-W. Wei, M. Weinert, A. J. Weinstein, R. Weiss, L. Wen, E. K. Wessel, P. Weßels, J. Westerweck, T. Westphal, K. Wette, J. T. Whelan, S. E. Whitcomb, B. F. Whiting, C. Whittle, D. Wilken, D. Williams, R. D. Williams, A. R. Williamson, J. L. Willis, B. Willke, M. H. Wimmer, W. Winkler, C. C. Wipf, H. Wittel, G. Woan, J. Woehler, J. Wofford, K. W. K. Wong, J. Worden, J. L. Wright, D. S. Wu, D. M. Wysocki, S. Xiao, H. Yamamoto, C. C. Yancey, L. Yang, M. J. Yap, M. Yazback, H. Yu, H. Yu, M. Yvert, A. Zadrożny, M. Zanolin, T. Zelenova, J.-P. Zendri, M. Zevin, L. Zhang, M. Zhang, T. Zhang, Y.-H. Zhang, C. Zhao, M. Zhou, Z. Zhou, S. J. Zhu, X. J. Zhu, A. B. Zimmerman, M. E. Zucker, and J. Zweizig, "Gw170817: Observation of gravitational waves from a binary neutron star inspiral," *Phys. Rev. Lett.*, vol. 119, p. 161101, Oct 2017.

[26] K. Langanke and G. Martínez-Pinedo, "Nuclear weak-interaction processes in stars," *Rev. Mod. Phys.*, vol. 75, pp. 819–862, Jun 2003.

[27] T. Taddeucci, C. Goulding, T. Carey, R. Byrd, C. Goodman, C. Gaarde, J. Larsen, D. Horen, J. Rapaport, and E. Sugarbaker, "The (p, n) reaction as a probe of beta decay strength," *Nuclear Physics A*, vol. 469, no. 1, pp. 125 – 172, 1987.

[28] M. Sasano, H. Sakai, K. Yako, T. Wakasa, S. Asaji, K. Fujita, Y. Fujita, M. B. Greenfield, Y. Hagihara, K. Hatanaka, T. Kawabata, H. Kuboki, Y. Maeda, H. Okamura, T. Saito, Y. Sakemi, K. Sekiguchi, Y. Shimizu, Y. Takahashi, Y. Tameshige, and A. Tamii, "Gamow-teller unit cross sections of the (p, n) reaction at 198 and 297 MeV on medium-heavy nuclei," *Phys. Rev. C*, vol. 79, p. 024602, Feb 2009.

[29] R. G. T. Zegers, H. Akimune, S. M. Austin, D. Bazin, A. M. d. Berg, G. P. A. Berg, B. A. Brown, J. Brown, A. L. Cole, I. Daito, Y. Fujita, M. Fujiwara, S. Galès, M. N. Harakeh, H. Hashimoto, R. Hayami, G. W. Hitt, M. E. Howard, M. Itoh, J. Jänecke, T. Kawabata, K. Kawase, M. Kinoshita, T. Nakamura, K. Nakanishi, S. Nakayama, S. Okumura, W. A. Richter, D. A. Roberts, B. M. Sherrill, Y. Shimbara, M. Steiner, M. Uchida, H. Ueno, T. Yamagata, and M. Yosoi, "The $(t,{}^3\mathrm{He})$ and $({}^3\mathrm{He}, t)$ reactions as probes of Gamow-Teller strength," *Phys. Rev. C*, vol. 74, p. 024309, Aug 2006.

[30] G. Perdikakis, R. G. T. Zegers, S. M. Austin, D. Bazin, C. Caesar, J. M. Deaven, A. Gade, D. Galaviz, G. F. Grinyer, C. J. Guess, C. Herlitzius, G. W. Hitt, M. E. Howard, R. Meharchand, S. Noji, H. Sakai, Y. Shimbara, E. E. Smith, and C. Tur, "Gamow-Teller unit cross sections for $(t,^3\mathrm{He})$ and $(^3\mathrm{He},t)$ reactions," *Phys. Rev. C*, vol. 83, p. 054614, May 2011.

[31] K. Jackson, A. Celler, W. Alford, K. Raywood, R. Abegg, R. Azuma, C. Campbell, S. El-Kateb, D. Frekers, P. Green, O. HÃd'usser, R. Helmer, R. Henderson, K. Hicks, R. Jeppesen, P. Lewis, C. Miller, A. Moalem, M. Moinester, R. Schubank, G. Shute, B. Spicer, M. Vetterli, A. Yavin, and S. Yen, "The (n, p) reaction as a probe of Gamow-Teller strength," *Physics Letters B*, vol. 201, no. 1, pp. 25 – 28, 1988.

[32] S. Rakers, C. Bäumer, D. Frekers, R. Schmidt, A. M. van den Berg, V. M. Hannen, M. N. Harakeh, M. A. de Huu, H. J. Wörtche, D. De Frenne, M. Hagemann, J. Heyse, E. Jacobs, and Y. Fujita, "Gamow-Teller matrix elements from the $^{12}\mathrm{C}(d,^2\mathrm{He})$ and $^{24}\mathrm{Mg}(d,^2\mathrm{He})$ reactions at 170 MeV," *Phys. Rev. C*, vol. 65, p. 044323, Apr 2002.

[33] E. W. Grewe, C. Bäumer, A. M. van den Berg, N. Blasi, B. Davids, D. De Frenne, D. Frekers, P. Haefner, M. N. Harakeh, M. Huynyadi, E. Jacobs, B. Junk, A. Korff, A. Negret, P. von Neumann-Cosel, L. Popescu, S. Rakers, and H. J. Wörtche, "Gamow-teller transitions to $^{32}\mathrm{P}$ studied through the $^{32}\mathrm{S}(d,^2\,\mathrm{He})$ reaction at $E_d = 170$ MeV," *Phys. Rev. C*, vol. 69, p. 064325, Jun 2004.

[34] R. G. T. Zegers, T. Adachi, H. Akimune, S. M. Austin, A. M. van den Berg, B. A. Brown, Y. Fujita, M. Fujiwara, S. Galès, C. J. Guess, M. N. Harakeh, H. Hashimoto, K. Hatanaka, R. Hayami, G. W. Hitt, M. E. Howard, M. Itoh, T. Kawabata, K. Kawase, M. Kinoshita, M. Matsubara, K. Nakanishi, S. Nakayama, S. Okumura, T. Ohta, Y. Sakemi, Y. Shimbara, Y. Shimizu, C. Scholl, C. Simenel, Y. Tameshige, A. Tamii, M. Uchida, T. Yamagata, and M. Yosoi, "Extraction of weak transition strengths via the (^{3}He, t) reaction at 420 MeV," *Phys. Rev. Lett.*, vol. 99, p. 202501, Nov 2007.

[35] T. Annakkage, J. JÃd'necke, J. Winfield, G. Berg, J. Brown, G. Crawley, S. Danczyk, M. Fujiwara, D. Mercer, K. Pham, D. Roberts, J. Stasko, and G. Yoo, "Isovector giant resonances in ^{6}He, ^{12}B, ^{90}Y, ^{120}In, and ^{208}Tl observed in the $(^7\mathrm{Li},^7\mathrm{Be})$ charge-exchange reaction," *Nuclear Physics A*, vol. 648, no. 1, pp. 3 – 44, 1999.

[36] R. G. T. Zegers, R. Meharchand, Y. Shimbara, S. M. Austin, D. Bazin, B. A. Brown, C. A. Diget, A. Gade, C. J. Guess, M. Hausmann, G. W. Hitt, M. E. Howard, M. King, D. Miller, S. Noji, A. Signoracci, K. Starosta, C. Tur, C. Vaman, P. Voss, D. Weisshaar, and J. Yurkon, "$^{34}\mathrm{P}(^7\mathrm{Li},^7\,\mathrm{Be}+\gamma)$ reaction at $100a$ MeV in inverse kinematics," *Phys. Rev. Lett.*, vol. 104, p. 212504, May 2010.

[37] C. Sullivan, E. O'Connor, R. G. T. Zegers, T. Grubb, and S. M. Austin, "The sensitivity of core-collapse supernovae to nuclear electron capture," *The Astrophysical Journal*, vol. 816, p. 44, Dec 2015.

[38] S. Furusawa, H. Nagakura, K. Sumiyoshi, C. Kato, and S. Yamada, "Dependence of weak interaction rates on the nuclear composition during stellar core collapse," *Phys. Rev. C*, vol. 95, p. 025809, Feb 2017.

[39] A. Pascal, S. Giraud, A. Fantina, F. Gulminelli, J. Novak, M. Oertel, and A. Raduta, "Impact of electron capture rates on nuclei far from stability on core-collapse supernovae," 2019.

[40] R. Titus, E. M. Ney, R. G. T. Zegers, D. Bazin, J. Belarge, P. C. Bender, B. A. Brown, C. M. Campbell, B. Elman, J. Engel, A. Gade, B. Gao, E. Kwan, S. Lipschutz, B. Longfellow, E. Lunderberg, T. Mijatović, S. Noji, J. Pereira, J. Schmitt, C. Sullivan, D. Weisshaar, and J. C. Zamora, "Constraints for stellar electron-capture rates on ^{86}Kr via the ^{86}Kr(t,^{3} He+γ)^{86}Br reaction and the implications for core-collapse supernovae," *Phys. Rev. C*, vol. 100, p. 045805, Oct 2019.

[41] S. Richers, C. D. Ott, E. Abdikamalov, E. O'Connor, and C. Sullivan, "Equation of state effects on gravitational waves from rotating core collapse," *Phys. Rev. D*, vol. 95, p. 063019, Mar 2017.

[42] G. M. Fuller, W. A. Fowler, and M. J. Newman, "Stellar weak interaction rates for intermediate-mass nuclei II A=21 to A=60," *The Astrophysical Journal*, vol. 252, pp. 715–740, Jan 1982.

[43] A. Krasznahorkay, M. Fujiwara, P. van Aarle, H. Akimune, I. Daito, H. Fujimura, Y. Fujita, M. N. Harakeh, T. Inomata, J. Jänecke, S. Nakayama, A. Tamii, M. Tanaka, H. Toyokawa, W. Uijen, and M. Yosoi, "Excitation of isovector spin-dipole resonances and neutron skin of nuclei," *Phys. Rev. Lett.*, vol. 82, pp. 3216–3219, Apr 1999.

[44] J. M. Lattimer and M. Prakash, "The equation of state of hot, dense matter and neutron stars," *Physics Reports*, vol. 621, pp. 127 – 164, 2016. Memorial Volume in Honor of Gerald E. Brown.

[45] C. J. Horowitz and J. Piekarewicz, "Neutron star structure and the neutron radius of ^{208}Pb," *Phys. Rev. Lett.*, vol. 86, pp. 5647–5650, Jun 2001.

[46] S. Yoshida and H. Sagawa, "Neutron skin thickness and equation of state in asymmetric nuclear matter," *Phys. Rev. C*, vol. 69, p. 024318, Feb 2004.

[47] A. Lane, "Isobaric spin dependence of the optical potential and quasi-elastic (p, n) reactions," *Nuclear Physics*, vol. 35, pp. 676 – 685, 1962.

[48] D. T. Khoa and H. S. Than, "Isospin dependence of ^{6}He + p optical potential and the symmetry energy," *Phys. Rev. C*, vol. 71, p. 044601, Apr 2005.

[49] D. T. Khoa, H. S. Than, and D. C. Cuong, "Folding model study of the isobaric analog excitation: Isovector density dependence, lane potential, and nuclear symmetry energy," *Phys. Rev. C*, vol. 76, p. 014603, Jul 2007.

[50] D. T. Khoa, B. M. Loc, and D. N. Thang, "Folding model study of the charge-exchange scattering to the isobaric analog state and implication for the nuclear symmetry energy," *The European Physical Journal A*, vol. 50, p. 34, Feb 2014.

[51] B. M. Loc, D. T. Khoa, and R. G. T. Zegers, "Charge-exchange scattering to the isobaric analog state at medium energies as a probe of the neutron skin," *Phys. Rev. C*, vol. 89, p. 024317, Feb 2014.

[52] B. M. Loc, N. Auerbach, and D. T. Khoa, "Single-charge-exchange reactions and the neutron density at the surface of the nucleus," *Phys. Rev. C*, vol. 96, p. 014311, Jul 2017.

[53] S. Lipschutz, *The (p,n) charge-exchange reaction in inverse kinematics as a probe for isovector giant resonances in exotic nuclei.* PhD thesis, Michigan State University, 2018.

[54] P. Capel, H. Esbensen, and F. M. Nunes, "Comparing nonperturbative models of the breakup of neutron-halo nuclei," *Phys. Rev. C*, vol. 85, p. 044604, Apr 2012.

[55] L. J. Titus, F. M. Nunes, and G. Potel, "Explicit inclusion of nonlocality in (d, p) transfer reactions," *Phys. Rev. C*, vol. 93, p. 014604, Jan 2016.

[56] W. Li, G. Potel, and F. Nunes, "Nonlocal interactions in the (d, p) surrogate method for (n, γ) reactions," *Phys. Rev. C*, vol. 98, p. 044621, Oct 2018.

[57] A. Deltuva, A. C. Fonseca, and P. U. Sauer, "Calculation of proton-deuteron breakup reactions including the coulomb interaction between the two protons," *Phys. Rev. Lett.*, vol. 95, p. 092301, Aug 2005.

[58] L. Hlophe, J. Lei, C. Elster, A. Nogga, F. M. Nunes, D. Jurčiukonis, and A. Deltuva, "Deuteron-α scattering: Separable versus nonseparable faddeev approach," *Phys. Rev. C*, vol. 100, p. 034609, Sep 2019.

[59] W. G. Love and M. A. Franey, "Effective nucleon-nucleon interaction for scattering at intermediate energies," *Phys. Rev. C*, vol. 24, pp. 1073–1094, Sep 1981.

[60] M. A. Franey and W. G. Love, "Nucleon-nucleon t-matrix interaction for scattering at intermediate energies," *Phys. Rev. C*, vol. 31, pp. 488–498, Feb 1985.

[61] A. E. Lovell, F. M. Nunes, J. Sarich, and S. M. Wild, "Uncertainty quantification for optical model parameters," *Phys. Rev. C*, vol. 95, p. 024611, Feb 2017.

[62] J. Rotureau, P. Danielewicz, G. Hagen, F. M. Nunes, and T. Papenbrock, "Optical potential from first principles," *Phys. Rev. C*, vol. 95, p. 024315, 2017.

[63] H. Feshbach, "Unified theory of nuclear reactions," *Annals of Physics*, vol. 5, no. 4, pp. 357 – 390, 1958.

[64] P. Fraser, K. Amos, S. Karataglidis, L. Canton, G. Pisent, and J. P. Svenne, "Two causes of nonlocalities in nucleon-nucleus potentials and their effects in nucleon-nucleus scattering," *The European Physical Journal A*, vol. 35, no. 1, pp. 69–80, 2008.

[65] G. H. Rawitscher, D. Lukaszek, R. S. Mackintosh, and S. G. Cooper, "Local representation of the exchange nonlocality in n-^{16}O scattering," *Phys. Rev. C*, vol. 49, pp. 1621–1629, Mar 1994.

[66] F. D. Becchetti and G. W. Greenlees, "Nucleon-nucleus optical-model parameters, $A > 40$, $E < 50$ MeV," *Phys. Rev.*, vol. 182, pp. 1190–1209, Jun 1969.

[67] I. J. Thompson and F. M. Nunes, *Nuclear Reactions for Astrophysics : Principles, Calculation and Applications of Low-Energy Reactions.* Cambridge University Press, 2009.

[68] A. E. Lovell and F. M. Nunes, "Constraining transfer cross sections using Bayes' theorem," *Phys. Rev. C*, vol. 97, p. 064612, Jun 2018.

[69] J. D. Harvey and R. C. Johnson, "Influence of breakup channels on the analysis of deuteron stripping reactions," *Phys. Rev. C*, vol. 3, pp. 636–645, Feb 1971.

[70] R. Johnson and P. Tandy, "An approximate three-body theory of deuteron stripping," *Nuclear Physics A*, vol. 235, no. 1, pp. 56 – 74, 1974.

[71] R. C. Johnson and P. J. R. Soper, "Contribution of deuteron breakup channels to deuteron stripping and elastic scattering," *Phys. Rev. C*, vol. 1, pp. 976–990, Mar 1970.

[72] S. Weinberg, "Quasiparticles and the born series," *Phys. Rev.*, vol. 131, pp. 440–460, Jul 1963.

[73] D. Y. Pang, N. K. Timofeyuk, R. C. Johnson, and J. A. Tostevin, "Rapid convergence of the weinberg expansion of the deuteron stripping amplitude," *Phys. Rev. C*, vol. 87, p. 064613, Jun 2013.

[74] C. Iliadis, *Nuclear physics of stars.* Wiley-VCH, 2007.

[75] B. S. Pudliner, V. R. Pandharipande, J. Carlson, S. C. Pieper, and R. B. Wiringa, "Quantum monte carlo calculations of nuclei with $A <\sim 7$," *Phys. Rev. C*, vol. 56, pp. 1720–1750, Oct 1997.

[76] I. Thompson, "Computer code fresco." University of Surrey, www.fresco.org.uk, 2006.

[77] M. Tostevin. private communication, 2014. University of Surrey modified version of the code TWOFNR (M. Igarashi, N. Kishida) and FRONT.

[78] R. V. Reid, "Local phenomenological nucleon-nucleon potentials," *Annals of Physics*, vol. 50, no. 3, pp. 411 – 448, 1968.

[79] R. Schaeffer and J. Raynal, "Computer code DWBA70." (unpublished) extended version DW81 by J.R. Comfort.

[80] J. Cook and J. A. Carr, "Computer code fold." Florida State University, (unpublished).

[81] L. Titus, A. Ross, and F. Nunes, "Transfer reaction code with nonlocal interactions," *Computer Physics Communications*, vol. 207, pp. 499 – 517, 2016.

[82] J. Dechargé and D. Gogny, "Hartree-fock-bogolyubov calculations with the $D1$ effective interaction on spherical nuclei," *Phys. Rev. C*, vol. 21, pp. 1568–1593, Apr 1980.

[83] R. B. Wiringa, V. G. J. Stoks, and R. Schiavilla, "Accurate nucleon-nucleon potential with charge-independence breaking," *Phys. Rev. C*, vol. 51, pp. 38–51, Jan 1995.

[84] J. Kelly, W. Bertozzi, T. N. Buti, F. W. Hersman, C. Hyde, M. V. Hynes, B. Norum, F. N. Rad, A. D. Bacher, G. T. Emery, C. C. Foster, W. P. Jones, D. W. Miller, B. L. Berman, W. G. Love, and F. Petrovich, "Signatures of density dependence in the two-nucleon effective interaction near 150 MeV," *Phys. Rev. Lett.*, vol. 45, pp. 2012–2015, Dec 1980.

[85] T. Udagawa, A. Schulte, and F. Osterfeld, "Antisymmetric distorted wave impulse approximation calculations for composite particle scattering," *Nuclear Physics A*, vol. 474, no. 1, pp. 131 – 154, 1987.

[86] R. B. Wiringa, "Argonne v18 and vn' and super-soft core potential package." Argonne National Laboratory.

[87] J. José and S. N. Shore, *Observational mysteries and theoretical challenges for abundance studies*, pp. 121âĂŞ140. Cambridge Astrophysics, Cambridge University Press, 2 ed., 2008.

[88] C. Iliadis, A. Champagne, J. Jose, S. Starrfield, and P. Tupper, "The effects of thermonuclear reaction-rate variations on nova nucleosynthesis: A sensitivity study," *The Astrophysical Journal Supplement Series*, vol. 142, pp. 105–137, sep 2002.

[89] M. B. Bennett, C. Wrede, B. A. Brown, S. N. Liddick, D. Pérez-Loureiro, D. W. Bardayan, A. A. Chen, K. A. Chipps, C. Fry, B. E. Glassman, C. Langer, N. R.

Larson, E. I. McNeice, Z. Meisel, W. Ong, P. D. O'Malley, S. D. Pain, C. J. Prokop, H. Schatz, S. B. Schwartz, S. Suchyta, P. Thompson, M. Walters, and X. Xu, "Isospin mixing reveals ^{30}P$(p,\gamma)^{31}$S resonance influencing nova nucleosynthesis," *Phys. Rev. Lett.*, vol. 116, p. 102502, Mar 2016.

[90] D. T. Doherty, G. Lotay, P. J. Woods, D. Seweryniak, M. P. Carpenter, C. J. Chiara, H. M. David, R. V. F. Janssens, L. Trache, and S. Zhu, "Key resonances in the ^{30}P$(p,\gamma)^{31}$S gateway reaction for the production of heavy elements in one novae," *Phys. Rev. Lett.*, vol. 108, p. 262502, Jun 2012.

[91] A. Parikh, K. Wimmer, T. Faestermann, R. Hertenberger, J. José, R. Longland, H.-F. Wirth, V. Bildstein, S. Bishop, A. A. Chen, J. A. Clark, C. M. Deibel, C. Herlitzius, R. Krücken, D. Seiler, K. Straub, and C. Wrede, "Improving the ^{30}P$(p,\gamma)^{31}$S rate in oxygen-neon novae: Constraints on J^π values for proton-threshold states in ^{31}S," *Phys. Rev. C*, vol. 83, p. 045806, Apr 2011.

[92] B. A. Brown, W. A. Richter, and C. Wrede, "Shell-model studies of the astrophysical rapid-proton-capture reaction ^{30}P$(p,\gamma)^{31}$S," *Phys. Rev. C*, vol. 89, p. 062801, Jun 2014.

[93] B. A. Brown, W. A. Richter, and C. Wrede, "Erratum: Shell-model studies of the astrophysical rapid-proton-capture reaction ^{30}P$(p,\gamma)^{31}$S [Phys. Rev. C 89, 062801(R) (2014)]," *Phys. Rev. C*, vol. 92, p. 069901, Dec 2015.

[94] A. Kankainen, P. J. Woods, F. Nunes, C. Langer, H. Schatz, V. Bader, T. Baugher, D. Bazin, B. A. Brown, J. Browne, D. T. Doherty, A. Estrade, A. Gade, A. Kontos, G. Lotay, Z. Meisel, F. Montes, S. Noji, G. Perdikakis, J. Pereira, F. Recchia, T. Redpath, R. Stroberg, M. Scott, D. Seweryniak, J. Stevens, D. Weisshaar, K. Wimmer, and R. Zegers, "Angle-integrated measurements of the ^{26}Al (d, n)^{27}Si reaction cross section: a probe of spectroscopic factors and astrophysical resonance strengths," *The European Physical Journal A*, vol. 52, p. 6, Jan 2016.

[95] S. Paschalis, I. Lee, A. Macchiavelli, C. Campbell, M. Cromaz, S. Gros, J. Pavan, J. Qian, R. Clark, H. Crawford, D. Doering, P. Fallon, C. Lionberger, T. Loew, M. Petri, T. Stezelberger, S. Zimmermann, D. Radford, K. Lagergren, D. Weisshaar, R. Winkler, T. Glasmacher, J. Anderson, and C. Beausang, "The performance of the gamma-ray energy tracking in-beam nuclear array gretina," *Nuclear Instruments and Methods in Physics Research Section A: Accelerators, Spectrometers, Detectors and Associated Equipment*, vol. 709, pp. 44 – 55, 2013.

[96] D. Bazin, J. Caggiano, B. Sherrill, J. Yurkon, and A. Zeller, "The S800 spectrograph," *Nuclear Instruments and Methods in Physics Research Section B: Beam Interactions with Materials and Atoms*, vol. 204, pp. 629 – 633, 2003. 14th International Conference on Electromagnetic Isotope Separators and Techniques Related to their Applications.

[97] R. H. Cyburt, A. M. Amthor, A. Heger, E. Johnson, L. Keek, Z. Meisel, H. Schatz, and K. Smith, "Dependence of X-ray burst models on nuclear reaction rates," *The Astrophysical Journal*, vol. 830, p. 55, oct 2016.

[98] A. Parikh, J. José, F. Moreno, and C. Iliadis, "The effects of variations in nuclear processes on type I X-ray burst nucleosynthesis," *The Astrophysical Journal Supplement Series*, vol. 178, pp. 110–136, sep 2008.

[99] P. Capel and Y. Nollet, "Reconciling coulomb breakup and neutron radiative capture," *Phys. Rev. C*, vol. 96, p. 015801, Jul 2017.

[100] F. M. Nunes, A. Deltuva, and J. Hong, "Improved description of ^{34,36,46}Ar(p, d) transfer reactions," *Phys. Rev. C*, vol. 83, p. 034610, Mar 2011.

[101] B. Brown and W. Rae, "The shell-model code NuShellX@MSU," *Nuclear Data Sheets*, vol. 120, pp. 115 – 118, 2014.

[102] J. Borysowicz, H. McManus, and G. Bertsch, "Michigan State University Cyclotron Laboratory report," 1974. (Unpublished).

[103] G. Bertsch, J. Borysowicz, H. McManus, and W. Love, "Interactions for inelastic scattering derived from realistic potentials," *Nuclear Physics A*, vol. 284, no. 3, pp. 399 – 419, 1977.

[104] W. G. Love, "Properties and applications of effective interactions derived from free nucleon-nucleon forces," in *The (p,n) Reaction and the Nucleon-Nucleon Force* (C. Goodman, S. Austin, B. S., J. Rapaport, and G. Satchler, eds.), ch. 1, pp. 23–55, New Tork: Plenum Press, 1980.

[105] H. Lenske, J. I. Bellone, M. Colonna, and J.-A. Lay, "Theory of single-charge exchange heavy-ion reactions," *Phys. Rev. C*, vol. 98, p. 044620, Oct 2018.

[106] D. T. Khoa, G. R. Satchler, and W. von Oertzen, "Nuclear incompressibility and density dependent NN interactions in the folding model for nucleus-nucleus potentials," *Phys. Rev. C*, vol. 56, pp. 954–969, Aug 1997.

[107] V. A. Madsen and V. Brown, "Properties of multistep amplitudes in charge-exchange reactions," in *The (p,n) Reaction and the Nucleon-Nucleon Force* (C. Goodman, S. Austin, B. S., J. Rapaport, and G. Satchler, eds.), ch. 5, pp. 433–449, New Tork: Plenum Press, 1980.

[108] R. K. Wallace and S. E. Woosley, "Explosive hydrogen burning," *The Astrophysical Journal Supplement Series*, vol. 45, pp. 389–420, Feb 1981.

[109] M. Honma, T. Otsuka, B. A. Brown, and T. Mizusaki, "Shell-model description of neutron-rich pf-shell nuclei with a new effective interaction GXPF 1," *The European Physical Journal A - Hadrons and Nuclei*, vol. 25, pp. 499–502, Sep 2005.

[110] W. Ormand and B. Brown, "Empirical isospin-nonconserving hamiltonians for shell-model calculations," *Nuclear Physics A*, vol. 491, no. 1, pp. 1 – 23, 1989.

[111] A. M. Mukhamedzhanov and F. M. Nunes, "Combined method to extract spectroscopic information," *Phys. Rev. C*, vol. 72, p. 017602, Jul 2005.

[112] K. Haravu, C. L. Hollas, P. J. Riley, and W. R. Coker, "^{86}Kr$(d,p)^{87}$Kr reaction," *Phys. Rev. C*, vol. 1, pp. 938–944, Mar 1970.

[113] D. Walter, S. D. Pain, J. A. Cizewski, F. M. Nunes, S. Ahn, T. Baugher, D. W. Bardayan, T. Baumann, D. Bazin, S. Burcher, K. A. Chipps, G. Cerizza, K. L. Jones, R. L. Kozub, S. J. Lonsdale, B. Manning, F. Montes, P. D. O'Malley, S. Ota, J. Pereira, A. Ratkiewicz, P. Thompson, C. Thornsberry, and S. Williams, "Constraining spectroscopic factors near the r-process path using combined measurements: ^{86}Kr $(d,p)^{87}$Kr," *Phys. Rev. C*, vol. 99, p. 054625, May 2019.

[114] S. Beceiro-Novo, T. Ahn, D. Bazin, and W. Mittig, "Active targets for the study of nuclei far from stability," *Progress in Particle and Nuclear Physics*, vol. 84, pp. 124 – 165, 2015.

[115] J. Bradt, D. Bazin, F. Abu-Nimeh, T. Ahn, Y. Ayyad, S. B. Novo, L. Carpenter, M. Cortesi, M. Kuchera, W. Lynch, W. Mittig, S. Rost, N. Watwood, and J. Yurkon, "Commissioning of the active-target time projection chamber," *Nuclear Instruments and Methods in Physics Research Section A: Accelerators, Spectrometers, Detectors and Associated Equipment*, vol. 875, pp. 65 – 79, 2017.

[116] J. Pereira, T. Poxon-Pearson, Y. Ayyad, and F. Nunes, "New approach to determine neutron-capture reaction rates relevant for the astrophysical r-process using the AT-TPC." Proprosal for ReA-PAC at the NSCL, (unpublished).

[117] D. A. Varshalovicz, A. N. Moskalev, and V. Khersonskii, *Quantum Theory of Angular Momuntum*. World Scientific, 1988.

[118] H. Kottler and K. Kowalski, "Analytic deuteron wave functions," *Nuclear Physics*, vol. 53, pp. 334 – 336, 1964.